TESE DE DOUTORAMENTO

REMOTELY ACTIVATED NANOSYSTEMS FOR INTRACELLULAR OPERATIONS

Raquel Martínez González

ESCOLA DE DOUTORAMENTO INTERNACIONAL
PROGRAMA DE DOUTORAMENTO EN CIENCIA E TECNOLOXÍA DE MATERIAIS

SANTIAGO DE COMPOSTELA

ANO 2020

USC
UNIVERSIDADE
DE SANTIAGO
DE COMPOSTELA

DECLARACIÓN DA AUTORA DA TESE
Remotely activated nanosystems for intracellular operations

Dna. Raquel Martínez González

Presento a miña tese, seguindo o procedemento axeitado ao Regulamento, e declaro que:

1) A tese abarca os resultados da elaboración do meu traballo.
2) De ser o caso, na tese faise referencia ás colaboracións que tivo este traballo.
3) A tese é a versión definitiva presentada para a súa defensa e coincide coa versión enviada en formato electrónico.
4) Confirmo que a tese non incorre en ningún tipo de plaxio doutros autores nin de traballos presentados por min para a obtención doutros títulos.

En Santiago de Compostela, 1 de Xuño de 2020

Asdo. Raquel Martínez González

USC
UNIVERSIDADE
DE SANTIAGO
DE COMPOSTELA

AUTORIZACIÓN DO DIRECTOR/TITOR DA TESE
Remotely activated nanosystems for intracellular operations

D. Pablo Taboada Antelo
D. Pablo Alfonso del Pino González de la Higuera

INFORMAN:

Que a presente tese, correspóndese co traballo realizado por Dna. Raquel Martínez González, baixo a nosa dirección, e autorizamos a súa presentación, considerando que reúne os requisitos esixidos no Regulamento de Estudos de Doutoramento da USC, e que como directores desta non incorre nas causas de abstención establecidas na Lei 40/2015.

En Santiago de Compostela, 1 de Xuño de 2020

Asdo. Pablo Taboada Antelo

Asdo. Pablo Alfonso del Pino González de la Higuera

USC
UNIVERSIDADE
DE SANTIAGO
DE COMPOSTELA

To my sister, Paula.
Because some humans emit sunshine

USC
UNIVERSIDADE
DE SANTIAGO
DE COMPOSTELA

CONTENTS

CONTENTS I

LIST OF FIGURES V

LIST OF TABLES IX

LIST OF ABBREVIATIONS XI

LIST OF PUBLICATIONS XIII

AGRADECEMENTOS XV

SUMMARY XVII

RESUMO XXV

1. INTRODUCTION 1

1.1. Nanoworld. Properties, Materials and Applications 1

1.1.1. What is nanoscale and nanotechnology? 1

1.1.2. Physics at the nanoscale 3

1.1.3. Materials in the nanoscale 6

1.1.4. Applications of nanoscale materials 8

1.2. Inorganic Nanoparticles preparation for biological applications 9

1.2.1. Nanoparticle fabrication, general considerations 10

1.2.2. NP characterization 12

1.2.3. Concentration determination. 18

1.2.4. Protein corona and NPs physicochemical properties if biological media 19

1.2.5. Stability and degradation in biologically relevant media 20

1.3. Nanomedicine and Smart Materials. 22

1.3.1. Application of nanosystems in medicine 22

1.3.2. Exogenous stimuli for nanomaterials activation 27

1.4. Main objectives 43

1.4.1. Upconverting nanoparticles (UCNPs) 43

1.4.2. Inorganic NP-MOFs nanocomposites (NC) 45

1.4.3. Plasmonic NC: gold nanostars (NS)-ZIF8 46

1.4.4. Catalytic NR: palladium nanocube (Pd-NP)-ZIF8 47

2. UPCONVERTING NPS MEDIATED PHOTODYNAMIC THERAPY 49

2.1. Introduction 49

2.2. Results and Discussion 51

2.3. Materials and Methods 60

2.4. Conclusions **67**

3. PLASMONIC NCS FOR NIR TRIGGERED RELEASE **69**

3.1. Introduction **69**

3.2. Results and Discussion **70**

3.3. Materials and Methods **77**

3.4. Conclusions **80**

4. PLASMONIC NCS FOR NIR TRIGGERED REACTIONS **83**

4.1. Introduction **83**

4.2. Results and Discussion **85**

4.3. Materials and Methods **94**

4.4. Conclusions **99**

5. PALLADIUM NCS FOR CONTROLLED CATALYTIC REACTIONS **101**

5.1. Introduction **101**

5.2. Results and Discussion **104**

Design and synthesis of Pd/ZIF8 NCs. 104

5.3. Materials and Methods **117**

5.4. Conclusions **122**

6. APPENDIX **125**

6.1. Chapter 2 Appendix **125**

6.1.1. Synthesis of 808 nm-activable core-multishell upconversion nanoparticles ... 125

6.1.2. Characterization of 808 nm-activable upconversion core-multishell UCNPs ... 125

6.1.3. Synthesis and characterization of water dispersable UCNPs after click chemistry onto the surface 131

6.1.4. Photodynamic therapy activation by 808 nm irradiation and ROS production 136

6.2. Chapter 3 Appendix **139**

6.2.1. Synthesis and characterization of gold nanostars 139

6.2.2. Synthesis of core-shell NS/ZIF8 NC (NC) 141

6.2.3. Encapsulation of HOE molecules in NS/ZIF8 nanocomposite (NC-HOE) 142

6.2.4. Post-functionalization of the NC with poly[isobutylene–alt–maleic anhydride]–graft–dodecyl (NC-HOE-PMA) 143

6.2.5. Characterization of the NC particles 145

6.2.6. Cell studies 155

6.3. Chapter 4 Appendix **159**

6.3.1. Synthesis and characterization of the probes 159

6.3.2. Synthesis of PMA-modified NS/ZIF8 nanoreactors 160

6.3.3. Morphological/structural characterization of NRs 161
6.3.4. Thermoplasmonic properties of NRs 163
6.3.5. Performance of NR particles as nanocontainer versus nanoreactor 166
6.3.6. Thermal-promoted nucleophilic substitutions by NRs 167
6.3.7. Photostability and reusability of the NRs 168
6.3.8. Cell studies 171
6.4. Chapter 5 Appendix 175
6.4.1. Synthesis and characterization of the probes and palladium complexes 175
6.4.2. Synthesis of PMA-modified Pd/ZIF8 NCs (NRs) 177
6.4.3. Morphological/structural characterization of NRs 178
6.4.4. Quantification of Pd by inductively coupled plasma mass spectrometry (ICP-MS) and estimation of potentially active Pd 182
6.4.5. Evaluation of porous accessibility/porosity of NRs 185
6.4.6. General procedures of the propargyl uncaging reactions 186
6.4.7. Performance of the reactions in the presence of bio-additives 192
6.4.8. Cells studies 194
7. REFERENCES 201

USC
UNIVERSIDADE
DE SANTIAGO
DE COMPOSTELA

LIST OF FIGURES

Figure 1.1. Nanosystems lye between the macroscopic and the atomic worlds. 2
Figure 1.2. Surface area and storage efficiency of nanostructures. 3
Figure 1.3. Surface to volume ratio as a function of NP radius. 4
Figure 1.4. Quantum confinement effect. 5
Figure 1.5. Different examples of inorganic and organic nanomaterials. 6
Figure 1.6. Schematic representation of inert, active and activatable nanomaterials. 7
Figure 1.7. Different examples of nanomaterials applications. 8
Figure 1.8. Brownian motion measurements by NTA. 12
Figure 1.9. Mie scattering examples due to colloidal NPs in nature. 13
Figure 1.10. EDL scheme. 14
Figure 1.11. Semliki Forest viruses under *cryo*-TEM. 16
Figure 1.12. Timeline of AFM key inventions. 17
Figure 1.13. PEGylated NPs and PEG structure. 19
Figure 1.14. NP functionalities in nanomedicine. 22
Figure 1.15. Illustration of the EPR effect. 25
Figure 1.16. Hemodynamic-based tumour targeting.[76] 26
Figure 1.17. Different external stimuli to activate nanosystems for therapeutic and diagnostic purposes in nanomedicine 27
Figure 1.18. Electromagnetic transversal wave. 28
Figure 1.19. Complete electromagnetic spectrum classified in terms of wavelengths. 29
Figure 1.20. Absorption spectrum of human skin. 30
Figure 1.21. Localized Surface Plasmon Resonance in plasmonics nanomaterials. 31
Figure 1.22. Jablonski diagrams. 33
Figure 1.23. Stokes and anti-Stokes shift in photoactive materials. 35
Figure 1.24. Magnetization effects in magnetic nanomaterials. 37
Figure 1.25. Biological differences between T_1 and T_2 contrast agents. 39
Figure 1.26. Brain images obtained by magnetic imaging techniques. 40
Figure 1.27. Longitudinal waves. 41
Figure 1.28. Direct piezoelectric effect. 42
Figure 1.29. Schematic representation of ultrasound interacting with body. 42
Figure 1.30. Multicolor emission UCNPs. 44
Figure 1.31. Core-multishell UCNP TEM image 44
Figure 1.32. Plasmonic core-shell NS/ZIF8 nanocomposite. 46
Figure 1.33. Plasmonic core-shell Pd-NP/ZIF8 NC. 48
Figure 2.1. UCNP based nanoplatform. 50
Figure 2.2. Photodynamic therapy activation using UCNPs. 51
Figure 2.3.TEM micrographs of the UC layer by layer process. 52
Figure 2.4. Core@multishell UCNP compositions and emission. 53
Figure 2.5. Absorbances of UCNP and PS. 54
Figure 2.6. UC-PMA water characterization. 55
Figure 2.7. *In vitro* behavior of the UCNPs. 56
Figure 2.8. Cell irradiation controls. 57
Figure 2.9. Photodynamic therapy efficiency studies. 57
Figure 2.10. Intracellular location of UCNPs platforms. 58
Figure 2.11. Photodynamic therapy test tubes. 59
Figure 2.12. PDT evaluation by confocal microscopy. 60
Figure 2.13. Scheme of the synthetic process for the PS. 62
Figure 2.14. PMA(DBCO) preparation. 63

Figure 2.15. Degradation of DPBF, raw data. 64
Figure 2.16. Laser irradiation setup. 65
Figure 3.1. Intracellular cargo protection and release using NS-ZIF8-PMA nanocomposites. 69
Figure 3.2. SEM micrographs of NCs; images acquired at different voltages and different detectors. 70
Figure 3.3. NCs characterization: SERS, TGA, N_2 absorption isotherms and colloidal stability in aqueous medium. 71
Figure 3.4. NC degradation on water. 73
Figure 3.5. HOE release after NIR illumination. 74
Figure 3.6. Cell viability using the resazurin assay 75
Figure 3.7. SERS cell studies. 76
Figure 3.8. Collage confocal microscopy images for NC-HOE-PMA(rhodamine) system. 77
Figure 3.9.NIR irradiation confocal cells studies with NC-HOE-PMA. 77
Figure 4.1. Core-shell MOF-based plasmonic NR for intracellular photothermal reactions. 83
Figure 4.2. Reacting probes used in this study (substrates 1 and 3), and fluorescent products (2 and 4). 84
Figure 4.3. Schematic illustration of the synthetic procedure of PMA-modified NS/ZIF8 nanoreactors (NRs). 86
Figure 4.4. Heating/cooling cycles and reaction yields with/without substrates encapsulation. 87
Figure 4.5. Yield of 2 after irradiations: heatmap and cumulative yield. 88
Figure 4.6. Cell viability of cells exposed to increasing concentrations of reactant(s), NRs and/or FBS-stabilized NSs. 90
Figure 4.7. Cytometry NRs internalization studies. 91
Figure 4.8. NR-preloaded cells before and after NIR pointer irradiation. 92
Figure 4.9. Intracellular thermocyclation performance in NR-preloaded cells 93
Figure 4.10. CTCF per cell intracellularly generated after 1 or 3 application. 93
Figure 4.11. Diagram of the synthetic method to produce substrates 1 and 3, and the corresponding thermal-promoted thermocyclization reactions. 94
Figure 4.12. NIR irradiation set-up (a), collimation/zoom system (b) and beam diameter (c). 95
Figure 5.1. Core-Shell Pd/ZIF8 nanoreactor for intracellular uncaging chemistry and caged probes. 102
Figure 5.2.Intracellular uncaging reactions scheme. 103
Figure 5.3. Electron microscopy characterization of core-shell Pd/ZIF8 NRs. 104
Figure 5.4. NR stability over time in different aqueous-based media. 105
Figure 5.5. Characterization of the Pd-promoted (NR or Pd-NP) uncaging of coumarin 1 in aqueous solution. 106
Figure 5.6. Photographs of NRs (or Pd-NPs) solutions before and after incubation with 5.107
Figure 5.7. Characterization of the Pd-promoted (NR or Pd-NP) generation of fluorophores 2 or 6 in biological media. 109
Figure 5.8. Cell viability of HeLa cells exposed to increasing concentrations of reactant(s) and/or NRs and/or Pd-NPs. 110
Figure 5.9. NR intracellular localization evaluation using confocal microscopy. 111
Figure 5.10. NR-promoted intracellular uncaging chemistry. 112
Figure 5.11. NR-preloaded cells working as recurrent “flow” nanoreactors. 114
Figure 5.12. NR-preloaded 3D spheroids working as recurrent flow tissue-like reactor. 116
Figure 5.13. Intracellular recycling with NRs preloaded cells methodology. 120
Figure 5.14. Brightfield images of 3D HeLa spheroids. 121

APPENDIX

Figure S2.1. Experimental setup for UCNP's synthesis 125
Figure S2.2. SEM characterization of UCNP cores and core@multishell. 126
Figure S2.3. TEM characterization of UCNP cores and core@multishell. 127
Figure S2.4. X-ray spectra from core UCNPs 127
Figure S2.5.Fluorescence spectra of UCNPs. 132
Figure S2.6. UC-PMA-RB,Ce6 133
Figure S2.7. Calibration curves of modified PS. 133
Figure S2.8. SEM micrographs of the final nanoplatform dispersed in water. 134
Figure S2.9. Intensity/number DLS population and ξ-potential distributions for different platforms. 134
Figure S2.10. Raw intensity and number DLS values for UC platforms. 135
Figure S2.11. Intracellular location of UC-PMA-RB,Ce6 in HeLa cells after 3 h of incubation (2.5 nM of NPs) 137
Figure S2.12. Intracellular location of UC-PMA-RB,Ce6 in HeLa cells (z-scan, 4 images) after 3 h of incubation (2.5 nM of NPs). 137
Figure S2.13. Intracellular colocation of UC-PMA-RB and lysosomes and mitochondria in HeLa cells after 3 h of incubation. 138
Figure S2.14. TMRE confocal experiments for PDT efficiency evaluation. 138

Figure S3.1. NS characterization. 140
Figure S3.2. SEM images of the NC particles taken at different magnifications and at two different voltages 141
Figure S3.3. Calibration curves of HOE in MeOH (A) and water (B). 142
Figure S3.4. Scheme of PMA–functionalization procedure of NC. 143
Figure S3.5. SEM images of NC-PMA particles. 144
Figure S3.6.TEM images of NC-HOE-PMA particles. 144
Figure S3.7. SEM images of NC-HOE and NC-HOE-PMA. 145
Figure S3.8. Characterization of NC particles. 146
Figure S3.9. DLS characterization of NC-HOE and NC-HOE-PMA. 146
Figure S3.10. PXRD spectra of ZIF8 (grey), NC (orange) and NC-PMA (blue). 147
Figure S3.11. PXRD spectra of the TGA residues. 150
Figure S3.12. HK pore volume distribution of selected samples. 151
Figure S3.13. DLS characterization of NC-HOE and NC-HOE-PMA over time. 153
Figure S3.14. Study of HOE release under laser irradiation with NC-HOE-PMA. 154
Figure S3.15. SEM images of NP-HOE-PMA after irradiation. 155
Figure S3.16. Collage confocal microscopy images for NC-HOE-PMA(rhodamine) system. 155
Figure S3.17. Collage confocal microscopy images for NC-HOE-PMA system. 156
Figure S3.18. Collage confocal microscopy images for NC-HOE system. 157
Figure S3.19. Collage confocal microscopy images for NC-HOE-PMA system after NIR treatment 158

Figure S4.1. PL spectra of substrate 1 and 3. 160
Figure S4.2. Representative SEM images of the NRs taken at different magnifications and different voltages 162
Figure S4.3. UV-Vis absorption spectrum and DLS number-weighted distribution of NR. .. 163
Figure S4.4. Test tube irradiation experiments. 164
Figure S4.5. Reproducibility of the photothermal conversion in three successive cycles. ... 164
Figure S4.6. SEM images of NRs after irradiation. 165
Figure S4.7. Calibration curves of fluorescent products. 167
Figure S4.8. Yields of different reactions under different conditions and substrates. 168
Figure S4.9. Cumulative yields of 2 and NR reusability experiments. 169

Figure S4.10. Internalization of TAMRA-labelled NRs. 171
Figure S4.11. NR@1 preloaded cells before and after NIR pointer irradiation. 171
Figure S4.12. NR@3 preloaded cells before and after NIR pointer irradiation. 172
Figure S4.13. NR preloaded cells incubated with 3 before and after NIR pointer irradiation. 172
Figure S4.14. Controls with freely incubated probes 1 or 2 (10 μM, 30 min), and without NIR. 173
Figure S4.15. Particle-loaded cells with substrate 1 and NIR. 173
Figure S4.16. Controls with probes 3 or 4 (10 mM, 30 min), and without NIR. 174
Figure S4.17. Particle-loaded cells with substrate 3 and NIR. 174

Figure S5.1.UV and fluorescence spectra of 1 and 2. 175
Figure S5.2. UV and fluorescence spectra of 3 (up) and 4. (down) 176
Figure S5.3. UV and fluorescence spectra of 5 and 6. 176
Figure S5.4. Calibration curves of 2, 4 and 6. 177
Figure S5.5. SEM characterization of Pd-NPs. 179
Figure S5.6. SEM characterization of NRs. 179
Figure S5.7. PXRD spectrum of Pd-ZIF8 NCs 180
Figure S5.8. DLS spectra of NRs 181
Figure S5.9. Calibration curves of TAMRA (A) and DOX (B) 186
Figure S5.10. Kinetics of the coumarin 2 uncaging reaction. 190
Figure S5.11. 6 production with NR-preloaded cells (using 2.5 μM of 5). 194
Figure S5.12. 6 production with NR-preloaded cells (using 10 μM of 5). 195
Figure S5.13. 6 production with NR-preloaded cells after 3 hours of incubation. 195
Figure S5.14. 6 production with NR-preloaded cells after 6 hours of incubation. 196
Figure S5.15. 6 production with NR-preloaded cells after 24 hours of incubation 196
Figure S5.16. Cell controls incubated with 6 197
Figure S5.17. 6 production comparison with different catalysts. 197
Figure S5.18. Intracellular recycling. 198
Figure S5.19. NR-TAMRA labeled loaded cell spheroid 199
Figure S5.20. Intracellular recycling in 3D cell spheroids. 200

LIST OF TABLES

Table 1.1. Different characteristic lengths that affect physico-chemical properties at the nanoscale.[6] 5
Table 1.2. Average timescales for radiative and non-radiative processes.[116] 34
Table 4.1. Ex./Em. wavelengths used for confocal imaging. 98

APPENDIX
Table S2.1. Sequence of reactants injections 125
Table S2.2. List of major peaks identified x-ray spectra of the cores. 127
Table S2.3. Experimental concentrations of each element in three different syntheses of core UCNPs 128
Table S2.4. Experimental concentrations of each element. 129
Table S2.5. Experimental values obtained by ICP-MS after performing statistical calculations. 129
Table S2.6. Dopants percentages and dopants ratios within the shells. 130
Table S2.7. Characteristic values for the final core@shell$_1$@shell$_2$@shell$_3$ UCNPs. 130
Table S2.8. NPs concentration for final samples. 130
Table S2.9. Raw hydrodynamic diameter values (number-weighted) 136
Table S2.10. Internalized UCNPs per cell determined by ICP-MS analysis. 136

Table S3.1.Hydrodynamic diameters of the NC-HOE and NC-HOE-PMA 147
Table S3.2. Major peaks (relative intensity > 6%) identified in the ZIF8 diffractogram. 148
Table S3.3. Major peaks (relative intensity > 6%) identified in the NC diffractogram. 148
Table S3.4. Major peaks (relative intensity > 9%) identified in the NC-PMA diffractogram. 148
Table S3.5. TGA characterization of selected samples. 150
Table S3.6. Data extracted from the N_2 isotherms analysis. 151
Table S3.7. Hydrodynamic diameters of NC-HOE and NC-HOE-PMA over time. 154

Table S4.1. DLS measurements of the NRs dispersed in water and cell medium. 163
Table S4.2. Fitting parameters for heating (Box-Lucas function) and cooling (exponential) simulation curves of NRs in water (Figure S4.4). 165
Table S4.3. Fitting parameters for heating (Box-Lucas function) and cooling (exponential) simulation curves in Figure S4.5 and Figure 4.4. 165
Table S4.4. Thermal reaction yields of substrate 1 to generate the fluorescent product 2 promoted by NRs (1 nM). 169
Table S4.5. Reaction yields of substrates (1 and 3) to generate the fluorescent products (2 and 4) promoted by NRs 170

Table S5.1.PXRD peaks. 180
Table S5.2. DLS measurements of the NRs and Pd-NPs overtime in different media. 182
Table S5.3. Amount of Pd per reaction as derived from ICP-MS measurements. 183
Table S5.4. Amounts of Pd (total and surface) per reaction as derived from ICP-MS measurements. 185
Table S5.5. Determination of loading percentage of two fluorescent probes into NRs after 4 h of incubation. 186
Table S5.6. Depropargylation reaction yields. 187
Table S5.7. Influence of the washing step after reaction. 188
Table S5.8. Leakage of Pd during the depropargylation reaction of 1. 189
Table S5.9. TON values for the depropargylation reaction of 1 and 5. 189

Table S5.10. Hydrodynamic diameters of NR after uncaging reactions. 191
Table S5.11. Depropargylation yields of two different substrates promoted by NRs or Pd-NPs after successive runs of the catalyst. 191
Table S5.12. Cumulative depropargylation yield of 5 promoted by NRs after successive reuses of the catalyst. 192
Table S5.13.Depropargylation reaction yields of 5 and 6 promoted by NRs or Pd-NPs in the presence of different bioadditives. 193
Table S5.14. Amounts of Pd per cell and particle uptake % (measured-to-added) as derived from ICP-MS measurements. 194

LIST OF ABBREVIATIONS

A	
AA	L-ascorbic acid
AC-DC	Alternating current-Direct current
AFM	Atomic Force Microscopy
ALF	artificial lysosomal fluid
AMF	Alternating Magnetic Field
B	
BSA	Bovine Serum Albumin
C	
Ce6	Chlorin e6
CTAB	hexadecyltrimethylammonium bromide
CTCF	corrected total cell fluorescence
CW	continuous wave
D	
DBCO	dibenzocyclooctyne
DDA	dodecylamine
DLS	Dynamic Light Scattering
DMEM	Dulbecco's modified Eagle's medium
DMF	Dimethylformamide
DNA	Deoxyribonucleic acid
DOX	Doxorubicin
DPBF	1,3-diphenylisobenzofuran
E	
EDC	1-ethyl-3-(3-dimethylaminopropyl)carbodiimide
EDL	Electric Double Layer
EM	Electromagnetic
EPR	Enhanced Permeability Effect
F	
FDA	Food and Drug Administration
FBS	Fetal Bovine Serum
H	
HOE	Hoechst H 33258
I	
IC50	half maximal inhibitory concentration
ICP-MS	Inductively Coupled Plasma Mass Spectroscopy
IR/NIR	Infrared/Near-Infrared
L	
LDA	Localized Surface Plasmon Resonance
LSPR	Laser Doppler Anemometry
M	
MFI	Mean fluorescence intensity
miRNA	Micro-RNA
MNP	Magnetic Nanoparticle
MOF	Metal-Organic-Framework
MRI	Magnetic Resonance Imaging
MW	Molecular weight
N	
NC	Nanocomposite
NR	Nanoreactor
NS	Gold Nanostars
NTA	Nanoparticle Tracking Analysis
NP	Nanoparticle
O	
OA	1-octadecene
ODE	oleic acid
P	
PBS	Phosphate buffer saline
Pd	Palladium
Pd-NP	Palladium Nanocube
PDI	polydispersity index
PDT	Photodynamic therapy
PEG	poly-Ethylene Glycol
PET	Positron Emission Tomography
PL	Photoluminescence
PMA	poly(isobutylene–alt–maleic anhydride)–graft–dodecyl
P/S	Penicillin Streptomycin
PS	Photosensitizer
PTT	Photothermal therapy
PXRD	powder X-ray diffraction
Q	
QD	Quantum Dot
QY	Quantum Yield

R

RB	Rose Bengal
RCF	relative centrifugal force
RE	rare-earth
RF	Radiofrequency
RNA	Ribonucleic acid
ROS	Reactive Oxygen Species
RPM	revolutions per minute
RT	room temperature

S

SBB	sodium borate buffer
SEM	Scanning Electron Microscopy
SERS	Surface-enhanced Raman Spectroscopy
siRNA	Small Interfering RNA
s-NHS	N-hydroxysulfosuccinimide
SPION	SuperParamagnetic Iron Oxide Nanoparticles
SPM	Scanning Probe Microscopy
STED	Stimulated Emission Depletion

T

TAMRA	Tetramethylrhodamine 5(and 6) carboxamide cadaverine
TEM	Transmission Electron Microscopy
TGA	thermogravimetric analysis
THF	tetrahydrofuran
TMRE	tetramethylrhodamine ethyl ester
TON	turnover number

U

UC	Upconversion
UCNP	Upconverting Nanoparticles
US	Ultrasound
UV-Vis	Ultraviolet-Visible

Z

ZIF8	Zeolitic imidazolate framework-8

LIST OF PUBLICATIONS

This thesis work has led to the following publications:

1. Raquel Martínez, María F. Navarro Poupard, Aitor Álvarez, Enrica Soprano, Martina Migliavacca, Carolina Carrillo-Carrión, Ester Polo, Beatriz Pelaz and Pablo del Pino. *Chapter 2 - Nanoparticle behavior and stability in biological environments.* Book Chapter in Nanoparticles for Biomedical Applications (Micro and Nano Technologies, Elsevier) 2020, Pages 5-18, ISBN 9780128166628, DOI B978-0-12-816662-8.00002-3. Main contributions of this thesis´s author:

Manuscript: Figure preparation; literature search and writing regarding state-of-the-art optically active nanosystems and their physicochemical characterization.

2. Raquel Martínez*, Ester Polo, Silvia Barbosa, Pablo Taboada, Pablo del Pino and Beatriz Pelaz. *808 nm-activable core@multishell upconverting nanoparticles with enhanced stability for efficient photodynamic therapy.* J. Nanobiotechnol. 2020, accepted. Main contributions of this thesis´s author:

Experimental: Entire experimental work.

Manuscript: Figure preparation and data processing.

3. Carolina Carrillo-Carrión,* **Raquel Martínez**,* María F. Navarro Poupard, Beatriz Pelaz, Ester Polo, Alessandro Olgiati, Pablo Taboada, Mahmoud G. Soliman, Ana Arenas-Vivo, Ursula Catalán, Sara Fernández-Castillejo, Rosa Solà, Wolfgang Parak, Patricia Horcajada, Ramon Alvarez-Puebla and Pablo del Pino. *Aqueous Stable Gold Nanostar/ZIF8 Nanocomposites for Light Triggered Release of Active Cargo Inside Living Cells.* Angew. Chem. Int. Ed., 58, 7078 (2019). Main contributions of this thesis´s author:

Experimental: Photothermal characterization of the nanoasystems and the entire experimental work involving cells.

Manuscript: Figure preparation and data processing of cell work.

Note: experimental work involving synthesis and physicochemical characterization of the nanoprobes is part of the PhD thesis of María F. Navarro Poupard (Ongoing).

4. Carolina Carrillo-Carrión*, **Raquel Martínez,*** Paolo Destito, María Tomás-Gamasa, Beatriz Pelaz, Fernando Lopez, José L. Mascareñas, Pablo del Pino. *Plasmonic-assisted thermocyclization using MOF-based nanoreactors in living cells*). Manuscript in preparation. Main contributions of this thesis´s author:

Experimental: Photothermal characterization of the nanosystems and the entire experimental work involving cells.

Manuscript: Figure preparation and data processing of cell work.

5. Raquel Martínez,* Carolina Carrillo-Carrión,* Paolo Destito, Aitor Alvarez, María Tomás-Gamasa, Beatriz Pelaz, Fernando Lopez, José L. Mascareñas, Pablo del Pino. *Core-Shell Palladium/MOF Platforms as Diffusion-Controlled Nanoreactors in Living Cells and Tissue Models*. Cell Rep. Phys. Sci., 2020, Accepted. Main contributions of this thesis´s author:

Experimental: Entire experimental work involving cells.

Manuscript: Figure preparation and data processing of cell work.

Note: experimental work involving synthesis and physicochemical characterization of the nanoprobes is part of the PhD thesis of Aitor Alvarez (Ongoing).

AGRADECEMENTOS

Primeiro, gustaríame agradecer aos meus directores de tesis, Pablo Taboada and Pablo del Pino. Síntome moi afortunada porque me ofrecerades a oportunidade de poder aprender todo o que aprendín durante estes cinco anos de formación. Por suposto, isto non tería ocorrido sen o apoio de Silvia Barbosa e Beatriz Pelaz.

En segundo lugar quero darlle as grazas a todos os meus compañeiros de laboratorio, tanto de Física como do Ciqus. Por suposto, a vosa axuda forma parte deste traballo e do meu aprendizaxe. Unha mención especial para o grupo de Prof. José Luis Mascareñas, que foi fundamental no deseño, síntese e caracterización de moitas das sondas utilizadas neste traballo. Tamén quero incluír a todos os técnicos da universidade así como do persoal do Ciqus, por axudar en todo o que puideron a obter os resultados deste traballo e ter a paciencia de aturar todas as miñas preguntas curiosas. Grazas por responderme sempre e ofrecerme coñecementos.

Ademais, agradezo moito a oportunidade e axuda económica que me ofreceu a Rede Galega de Nanomedicina para realizar a estancia de tres meses en Marburg, así como a Wolfgang Parak por permitirme traballar no seu laboratorio. Por suposto, quero destacar a Neus Feliu neste período xa que o seu apoio, optimismo foron clave neses tres meses. Quero incluír aquí a grandísima experiencia de acudir ao Nanax19. Grazas ao meus xefes por darme esa perspectiva que necesitaba do mundo científico así como facer que a ciencia me apaixone un pouco máis aínda.

Quero agradecer a Universidade de Santiago de Compostela por darme os medios para poder facer iso posible. Sen material, equipos e instalacións esta tese sería algo etéreo.

Por suposto, a miña familia e amigos foron do máis importante neste proceso. En todos os sentidos. De todas formas, non creo que sexa necesario poñer aquí todo o que xa vos digo continuamente.

Quero facer unha mención especial a todas esas mulleres que pasaron pola miña vida nestes cinco anos e que me axudaron a ser un pouco máis forte e libre. Todas axudaches dalgunha maneira, ofrecéndome perspectiva e sororidade.

Por último, as grazallas máis enormes para todas esas persoas que fomentaron a miña creatividade ao longo destes anos así como ao lector. Deixarei o "meu toque persoal" deste traballo no meu ResearchGate, por se tes curiosidade.

USC
UNIVERSIDADE
DE SANTIAGO
DE COMPOSTELA

SUMMARY

The context of this work is in the field of *nanotechnology*, which may be defined as the creation of functional materials, devices and systems through the control of matter at the nanometre length scale. The subsequent exploitation of derived novel phenomena and properties (physical, chemical and biological) at that length scale is the focus of this field of knowledge. *Nanosystems,* which are engineered at the nanoscale, may show new phenomena and properties in comparison with the corresponding bulk materials at the macroscopic scale. This provides them with a new variety of properties that can be exploited to produce the next generation devices. Different types of nanosystems are going to be designed, synthesized and implemented in this work, trying to exploit their unique 'nano-properties' for different objectives that are going to be summarized in the following.

In general, nanosystems can be classified considering different characteristic properties. The first classification, and the most obvious one, can be established in terms of the nature of the materials that compose the nanosystem. In this line, we can talk about organic and inorganic nanomaterials. Specially, in this work we are going to exploit different kinds of *inorganic nanoparticles*: gold nanostars, upconverting ceramic nanoparticles as well as palladium ones. The second classification can be given in terms of the nanosystems functionality and/or their characteristic properties, such as plasmonic (gold nanostars), photoluminescent (upconverting ceramic nanoparticles), porosity (metal-organic-frameworks, MOFs) and/or catalytic behaviour (palladium nanoparticles). To conclude within the context of my PhD work, an interesting classification may be proposed in terms of whether and how to control the nanomaterial's properties or not. In this manner, nanomaterials can be classified as inert, active and activatable nanomaterials. *Inert materials* have inherent properties that cannot be switched on or off like, for example, porosity, biocompatibility or electrical and thermal properties. They are referred as *non-working systems*. On the other hand, *working systems* have properties that may be activated, switched on/off or vice versa, by an endogenous or exogenous specific stimulus. Active systems by endogenous stimuli will change their conformation or functionality as a response to the physico-chemical properties of their surrounding environment such as pH and temperature variations, chemical gradients, molecular crowdedness and so forth. Lastly, exogenously activated nanosystems are those than can be activated with spatiotemporal control by external stimuli. Examples are electromagnetic radiation, sound waves, magnetic fields or the presence /application of an external molecule (catalytic controlled systems). *Activatable nanomaterials* have been the focus of this work, since the ability of a material to be stimulated in a controlled manner

is an obvious advantage in order to improve classical therapies and diagnosis techniques in the biomedical arena.

Next step refers to nanosystems application. These can be performed in many different fields of knowledge. Among this work, we will focus on the application of our nanosystems in the *nanomedicine field*. The main aim is to design new systems capable of interacting with biological entities (cells and ultimately, with animals and the human body) in a safer way (biocompatibility) than other state of the art approaches. Once nanosystems are immersed in living environments, different responses can be obtained. Nowadays one of the most important areas of nanomedicine is focused on designing platforms with the aim of both combining therapy and diagnosis capabilities, that is, *theranostic nanosystems*.

Eventually, in order to apply our proposed nanosystems in nanomedicine, it is quite important to note that nanoparticle design and synthesis should be carefully carried out. On the contrary, the expected outcomes within this field will not follow our expectations and even leading to unwanted and dangerous side effects. For this goal, we are going to discuss our synthesized nanosystems behaviour and stability in the context of biology and medicine. The focus will be on controlling the most important factors influencing nanoparticles' interactions when they are immersed in biological environments: nanoparticle integrity, colloidal stability and performance among others. Towards this end, we will study all the important factors and details of proposed nanosystems fabrication as well as a providing a detailed characterization for all of them.

Apart from the previous considerations, nanomaterials present some advantages in comparison with current treatments and diagnosis tools due to their characteristic nano-properties. Shortly, the first advantage arises from the size-difference ratios between nanoparticles and molecules. Nanotherapeutic platforms are much bigger in size than most of the molecular tools used in medicine, and therefore, the latter can be incorporated into the nanosystems and be tailored to contribute in different ways to the overall activity and safety. Secondly, the unique electromagnetic properties of inorganic materials at the nanoscale can be used in order to trigger some additional functionalities. Finally, nanoparticles have characteristic pathways and interactions inside the body that differ from those of molecules. Thus, nanoparticles can be used, for example, to differentiate pathological from normal tissues.

So, a careful design, fabrication, characterization and exploitation of activatable nanoparticle properties are going to be the main steps in order to create new functional nanosystems suitable for biological applications. The main advantages of *externally activatable nanoparticles* in nanomedicine rely on the high spatial and temporal control of the desired response, avoiding undesirable side effects and allowing for deep tissue penetration and real-time activation. To achieve this goal, the infrared and near-infrared wavelength range of the

electromagnetic spectrum becomes the best stimulus for biological applications due to different reasons: their highest power of penetration inside tissues (from several mm to cm), the relatively low heating associated effects after exposure, and the high spatiotemporal localization of its application. It is important to highlight that these wavelengths can induce a vibrational state in molecules, leading to unwanted tissue heating. Depending on this unspecific heating and the energy penetration depth some wavelengths are more suitable as external biological stimuli than others. For this, the so-called *biological windows* are going to be an important concept among this work. Different types of nanoparticles can absorb light within these windows to get activated. This work is focused on how nanomaterials can interact with this type of light or other external stimuli (in our case, catalytic-controlled systems), to control them without unwanted effects and the subsequent applications of their induced responses.

In the different chapters of this work, we are going to focus on the fabrication and different applications of the so-called externally activatable nanoparticles with different functionalities like plasmonic, photoluminescence or catalytic. Summarizing, *plasmonic nanoparticles* are capable of absorbing and scattering light from ranges within the biological windows. After activation, their localized surface plasmon resonance leads to a local heating on the nanoparticle surface. This response can be exploited to release different molecules from different plasmonic cavities or surfaces, or to perform therapies. In addition, *photoluminescence materials* can transform absorbed electromagnetic radiation into different energetic one. Organic dyes molecules or fluorophores are quite versatile because they can be designed with many different structures and properties. They can be attached to nanoparticles and cell components in order to track them using, for example, fluorescence techniques. These materials transform high energetic radiation into lower energetic one. On the contrary, other materials can transform low energetic photons into higher energetic. Due to this, activation inside the biological windows is possible. Upconversion materials (bulk and nanosized) show these unique properties. Both kinds of photoluminescent materials are going to be exploited and studied in this work. To conclude naming the activatable nanosystems used in this work, catalytic-controlled systems will be also developed. These systems respond to an external application of different substrates transforming or catalysing them into their products, which will change some of their initial properties like fluorescence emission, absorbance or cell toxicity, for example. The so-called catalysis can be performed in a concentration and temporal dependence manner.

In *chapter 2*, we present a project based on the unique upconversion properties of rare-earth-doped nanoparticles. They offer exciting opportunities for biomedical applications, in which near-infrared remote activation of biological processes is desired, including in vivo bioimaging, optogenetics, and

light-based therapies. Tuning of upconversion in purposely designed core-shell nanoparticles gives access to excitation within the biological windows in tissues. In recent years, there have been several reports on near-infrared-excitable upconverting nanoparticles capable of working in biological mixtures and cellular settings. Unfortunately, most of these nanosystems are based on ytterbium upconversion at 980 nm concurrent with water absorption within the first biological window. Thus, methods to produce robust upconverting nanoplatforms that can be efficiently excited with other than 980 nm near-infrared sources, such as 808 nm and 1064 nm, are required for biomedical applications.

Herein, we report a synthetic method to produce aqueous stable upconverting nanoparticles that can be activated with 808 nm excitation sources, thus avoiding unwanted heating processes due to water absorbance at 980 nm. Importantly, these nanoparticles, once transferred to an aqueous environment using an amphiphilic polymer, remain colloidally stable for long periods of time in relevant biological media, while keeping their photoluminescence properties. The selected functionalizing polymer was covalently modified with two FDA-approved photosensitizers (Rose Bengal and Chlorin e6), which can be efficiently and simultaneously excited by the different emission peaks of our upconverting nanoparticles. Thus, our polymer-functionalization strategy allows producing an 808 nm-activable photodynamic nanoplatform. These upconverting nanocomposites are preferentially stored in acidic lysosomal compartments, which do not negatively affect their performance as photodynamic agents. Upon 808 nm excitation, the production of reactive oxidative species and their effect in mitochondrial integrity are demonstrated. So, we are going to demonstrate the feasibility of using photosensitizer-polymer-modified upconverting nanoplatforms that can be activated by 808 nm light excitation sources for application in photodynamic therapy. Our nanoplatforms remain photoactive after internalization by living cells, allowing for 808 nm-activated reactive oxygen species generation. The versatility of our polymer-stabilization strategy promises a straightforward access to other derivatizations (for instance, by integrating other photosensitizers or homing ligands), which might synergistically operate as multifunctional photodynamic platforms nanoreactors for in vivo applications.

In *chapter 3*, metal-organic-frameworks are going to be presented. These solid coordination compounds are consisting in transition metal cation coordinated with multidentate organic ligands which present an extremely well-defined porosity. Hybrid nanomaterials composed of metal-organic-frameworks shells and inorganic nanoparticles as cores, have been exploited towards the generation of multifunctional nanomaterials for manifold applications. Apart from incorporating the nanoparticle characteristic properties to these

nanocomposites, the metal-organic-frameworks basic physicochemical properties (i.e., pore size, distribution and hydrophilicity/hydrophobicity) are key, for example, to get efficient different drug-delivery systems. In this context, nanocarriers based on the zeolitic imidazolate framework 8 (ZIF8) have been widely used for sustained delivery of wide variety of drugs, using the ZIF8 porosity to safely store the desired molecules. In addition to this, some carriers have been designed in order to carry out a stimulus-controlled drug-release (near-infrared-mediated in this chapter), which will allow the cargo to be delivered into the target with a spatiotemporal control. Unfortunately, the water instability of ZIF8 nanocomposites hinders the stimulus-controlled triggered release of the cargo.

Then, a plasmonic core-shell gold nanostars/ZIF8 nanocomposite was developed for thermoplasmonic-driven release of encapsulated active molecules inside living cells. Nanostars were selected as core due to their characteristic plasmonic band centred ~770 nm, which is suitable for excitation within the first biological window. These nanostars were used as seeds to grow the ZIF8 shell. As a proof of concept, nanocomposites were loaded with a cargo molecule taking advantage of the ZIF8 shell porosity. As bioactive cargo/reporter we chose a blue fluorescent dye typically used for cell nuclear DNA staining in molecular biology (Hoechst). Nanocomposites are wrapped with an amphiphilic polymer that prevents ZIF8 degradation in water-based solvents as well as to "trap" the cargo molecules and avoid Hoechst leakage in aqueous media or inside living cells. Finally, the demonstrated molecule-release mechanism relies on the use of near-infrared light coupled to the plasmonic absorption of the core gold nanostars, which creates local temperature gradients and, thus, favours molecules placed inside the ZIF8 pores to thermodiffuse out the particle. Confocal microscopy and surface-enhanced Raman spectroscopy are used to demonstrate the molecules loading/leakage and the near-infrared-triggered cargo release inside cells, thereby leading to nuclear DNA staining. We would like to remark that our approach in this chapter is an important step forward in the development of MOF-based intracellular vehicles for the controlled release of drugs. In summary, we developed an aqueous stable (even when stored in cells) ZIF8 based nanomaterial with combined thermoplasmonic and high drug-loading capabilities.

In *chapter 4*, we are going to focus on one of the current goals in chemical and cell biology. It consists in the development of intracellular reactions, usually catalysed by enzymes inside living cells. This allows for implementing non-native functions, thereby influencing the properties of cells in a predictable manner. During last decades, some advances in this field were achieved, even though important drawbacks should be still solved, as the lack of biocompatibility and efficiency of the metal-based reagents. Development of thermal-driven processes

could be an alternative, but it is obvious that cells cannot be heated above physiological temperatures. This problem can be solved using plasmonic nanoparticles as near-infrared-responsive thermal transducers, provided that the intended chemical reaction can be located near these heating generating units. The use of photothermal properties of plasmonic nanoparticles for photo-induced local heating is well precedented. These properties are particularly useful for biological applications because the heating can be triggered by near-infrared light sources, which are typically used to excite the corresponding plasmon band of anisotropic metal nanoparticles, nanostars in our case. However, the use of thermoplasmonic heating effects for achieving thermal-promoted chemical reactions inside living cells has not been yet well described. In this chapter, a microporous plasmonic nanoreactor was developed to carry out designed thermal-driven cyclizations inside living cells. As a proof of concept, we chose an intramolecular cyclization reaction that is based on the nucleophilic attack of a pyridine moiety over an electrophilic carbon, a process that requires high activation energies, typically achieved by bulk solution heating at ~ 90 °C, and that has never been performed using photothermal processes.

The core-shell nanoreactor has been designed in the same way that in the previous chapter: a gold nanostar core, which is embedded within a metal–organic framework nanoparticle based on a polymer-stabilized zeolitic-imidazole-framework-8. Once stored inside living cells, the metal–organic framework-based cloak allows an efficient diffusion of reactants into the plasmonic chamber, where they undergo the transformation upon near-infrared illumination. The reaction, in addition to generate a cyclized fluorogenic product, provides for the future photo-controlled uncaging of bioactive compounds with spatiotemporal resolution. The microporous nanoshell is critical to favour an effective concentration of the reactants near the heating source as well as to warrant the required thermal confinement. So, ours is the first example of a near-infrared-promoted nucleophilic substitution reaction. Overall, our plasmonic nanocomposites behave as excellent and biocompatible nanoreactors, which can work inside living cells to promote new-to-nature intracellular thermal-promoted transformations with spatiotemporal resolution.

To conclude, in *chapter 5* the concept and application of biological metal catalysis is introduced. Translating the potential of transition metal catalysis to biological environments, and eventually to living cells, is promising in order to have a profound impact in chemical and cell biology, as well as in biomedicine due to the innumerable types of transformations that can be achieved. While most of these reactions have been developed in organic solvents and under water-free conditions, recent years have witnessed an exponential increase in the development of metal-mediated reactions that can occur in complex aqueous environments, and even within living mammalian cells. Palladium based

catalysts are especially attractive owing to their well-established synthetic potential. However, the performance of homogeneous palladium complexes as well as palladium nanoparticles in biological media are usually compromised by their aqueous solubility, stability, passivation, palladium leaching and/or biocompatibility issues. In addition, obtaining robust, cell-permeable and biocompatible metal catalysts capable of performing designed intracellular reactions in a bioorthogonal manner is far to be obvious. Especially attractive is the possibility of obtaining intracellular reactors that remain active along time, as they could generate the products in a recurrent and dose-dependent way.

Herein, we report for the first time water compatible core-shell palladium-ZIF8 nanocomposites capable of working as efficient bioorthogonal heterogeneous nanoreactors. The nanocomposite features a single palladium nanocube core (the catalyst) and a porous nanometric ZIF8 shell (the filter) equipped with an amphiphilic polymer. In contrast to other metal-organic-framework-metal hybrids which display active metals on the surface, our core-shell architecture ensures that the reaction occurs in the core reaction chamber, which is critical for their biological application. In addition, the ZIF8-based shell plays a critical role to preserve the integrity of the catalytic chamber while providing for orthogonality (substrate selectivity) and biocompatibility. The polymer derivatization strategy renders the nanocomposite stable in water and biological environments. Apart from that, this architecture not only protects the palladium nanocatalyst from deactivation, leakage and aggregation, but its porosity allows a diffusion-controlled flow of reactants within the core reaction chamber. As a result, these nanoconstructs can be used as robust and efficient metallo-nanoreactors in complex aqueous media and, more importantly, inside living mammalian cells. These nanoplatforms tend to be stored in cytosolic compartments (endosomes and/or lysosomes), remaining stable, active and accessible to the reactants, and they can promote several consecutive reaction cycles using new batches of reactants, without losing efficiency, in 2D cell monolayers and 3D spheroids. Importantly, we also demonstrate that these nanoreactors can be readily incorporated into 3D tumour spheroids to produce tissue-like catalytic systems, which can also work in a recurrent, dose-dependent manner. This represents a pioneering demonstration of intracellular recurrent nanoreactors and set the basis for the development of *catalytic cellular* or *tissue nanoimplants*. These artificial nanoreactors featuring transition metal centres offer exotic possibilities for performing many other abiotic reactions in living environments, and therefore, promise to have important applications in chemical and cell biology, and in biomedicine.

So, along the different chapters of this PhD thesis we have demonstrated not only we can design, fabricate, characterize accurately and implement different operations of manifold nanosystems which can be external activatable (with

temporal and spatial resolution); but also we have controlled all their responses inside living cells in a safe and controllable manner without compromising biocompatibility.

RESUMO

O contexto deste traballo é o campo da *nanotecnoloxía,* o cal se pode definir como a creación de materiais funcionais, dispositivos e sistemas a través do control da materia nunha escala de lonxitude nanométrica. A explotación posterior dos novos fenómenos e propiedades derivadas (físicas, químicas e biolóxicas) nesta escala de lonxitude é o principal obxectivo deste campo de coñecemento. Os nanosistemas, deseñados dentro da escala nanométrica, poden mostrar novos fenómenos e propiedades que non presentan os seus correspondentes materiais a escala macroscópica. Isto ofrécelles unha multitude de novas propiedades que poden ser explotadas para producir dispositivos de nova xeración. Neste traballo deseñaranse, sintetizaranse e implementaranse diferentes tipos de nanosistemas, tratando de explotar as súas "nano-propiedades" exclusivas para diferentes obxectivos que se resumirán a continuación.

En xeral, os nanosistemas pódense clasificar considerando diferentes propiedades características. A primeira, e máis obvia, podería establecerse en termos da natureza dos materiais que compoñen o nanosistema. Nesta liña podemos falar de nanomateriais orgánicos e inorgánicos. Neste traballo imos explotar distintos tipos de *nanopartículas inorgánicas*: nanoestrelas de ouro, nanopartículas cerámicas sobreconversoras e nanopartículas de paladio. A segunda clasificación pode establecerse en termos da funcionalidade dos nanosistemas e/ou das súas propiedades características entre as que poderíamos destacar as plasmónicas (nanoestrelas de ouro), as fotoluminescentes (nanopartículas cerámicas sobreconversoras), a porosidade (materias metalo-orgánico estruturados, MOF) e o comportamento catalítico (nanopartículas de paladio) Para concluír dentro do contexto da miña tese doutoral, propoñemos unha clasificación baseada na posibilidade de controlar as propiedades do nanomaterial e as distintas formas de facelo. Deste xeito, os nanomateriais pódense clasificar como *nanomateriais inertes*, *activos* e *activables*. Os materiais inertes teñen propiedades inherentes que non se poden activar ou desactivar, como a porosidade, a súa biocompatibilidade ou propiedades eléctricas e térmicas. Poderíamos denominalos como sistemas que "non funcionan". Por outra banda, os sistemas presentados neste traballo teñen propiedades que poden ser activadas ou desactivadas mediante un estímulo endóxeno ou exóxeno específico. Os sistemas que poden ser activados por estímulos endóxenos cambiarán a súa conformación ou funcionalidade en resposta ás propiedades fisicoquímicas do seu ambiente, como variacións de pH e de temperatura, gradientes químicos, cambios na concentración molecular, etc. Finalmente, os nanosistemas activados de forma exóxena son aqueles que poden ser activados cun control espazo-temporal mediante estímulos externos. Algúns exemplos destes estímulos poden ser a radiación electromagnética, as ondas

sonoras, os campos magnéticos ou a presenza ou aplicación dunha molécula externa (como por exemplo os sistemas catalíticos controlados). Os nanomateriais activables serán o principal obxectivo deste traballo xa que a capacidade dun material para ser estimulado de xeito controlado é unha vantaxe evidente para mellorar as terapias clásicas e as técnicas de diagnóstico no campo biomédico.

O seguinte paso será referido ás distintas aplicacións dos nanosistemas nos diversos campos de coñecemento. Neste traballo, centrarémonos na aplicación dos nosos nanosistemas no campo da nanomedicina. O obxectivo principal é deseñar novos sistemas capaces de interactuar con entidades biolóxicas (como as células e con animais ou co mesmo corpo humano como obxectivo final) dun xeito máis seguro (biocompatibilidade) que outras propostas actuais. Unha vez introducidos os nanosistemas nos seres vivos, pódense obter respostas diversas. Hoxe, a nanomedicina céntrase no deseño de nanoplataformas teranósticas co obxectivo de combinar a terapia e as capacidades de diagnóstico nun único sistema.

Finalmente, para aplicar os nanosistemas que se propoñen no contexto da nanomedicina, é moi importante ter en conta que o deseño e a síntese das nanopartículas debe realizarse con coidado porque senón o rendemento dentro deste campo non seguirá as nosas expectativas, incluso podendo causar efectos adversos e perigosos. Para alcanzar este obxectivo, discutiremos o comportamento e a estabilidade dos nanosistemas sintetizados no contexto da bioloxía e a medicina. O obxectivo será controlar os factores máis importantes que inflúen nas interaccións das nanopartículas cando están inmersas en ambientes biolóxicos, incluída a súa integridade, a estabilidade coloidal e o rendemento obtido, entre outros. Para isto, estudaremos todos os factores e detalles importantes na fabricación dos nanosistemas deste traballo, así como proporcionaremos os resultados de caracterización detallados para cada un de eles.

Ademais das consideracións anteriores, os nanomateriais teñen algunhas vantaxes en comparación cos tratamentos e ferramentas de diagnóstico e terapia existentes causados polas súas propiedades nanométricas características. En primeiro lugar, xorde da diferenza de tamaño entre as nanopartículas e as moléculas. As plataformas nanoterapéuticas teñen un tamaño moito maior que a maioría das ferramentas moleculares utilizadas na medicina hoxe en día e, polo tanto, estas últimas pódense incorporar aos nanosistemas e adaptarse para contribuír de forma diferente á súa actividade e á súa seguridade. En segundo lugar, as propiedades electromagnéticas únicas dos materiais inorgánicos a escala nanométrica pódense empregar para activar algunhas funcionalidades adicionais. Finalmente, as nanopartículas teñen interaccións no corpo diferentes ás das moléculas.

Por iso, o deseño, a fabricación, a caracterización e a explotación das propiedades das nanopartículas activables debe realizarse dun xeito coidadoso e detallado, xa que estes serán os pasos principais para crear nanosistemas funcionais adecuados que serán utilizados en aplicacións biolóxicas. As principais vantaxes das nanopartículas activables externamente na nanomedicina baséanse na posibilidade dun alto control espacial e temporal da resposta desexada, evitando efectos secundarios non desexables e permitindo unha penetración máis profunda no tecido ademais da activación en tempo real. Para conseguilo, o rango de lonxitude de onda infravermella próxima do espectro electromagnético convértese na mellor opción para desenrolar aplicacións biolóxicas por diferentes razóns: a súa maior capacidade de penetración nos tecidos (de varios mm a cm), os efectos asociados ao quecemento nos tecidos son relativamente baixos e a alta localización espazo-temporal da aplicación de estímulo externo. É importante ter en conta que estas lonxitudes de onda poden inducir un estado vibracional nas moléculas, dando lugar a un quecemento non desexado do tecido. Dependendo desta subida da temperatura non específica e da profundidade de penetración da radiación, algunhas lonxitudes de onda son máis adecuadas que outras para o seu uso como estímulos biolóxicos compatibles. Polo tanto, un concepto a ter en conta ao longo deste traballo son as chamadas *fiestras biolóxicas*. Diferentes tipos de nanopartículas poden absorber radiación dentro destas fiestras para activarse. Este traballo céntrase en como os nanomateriais poden interactuar con esta luz ou outros estímulos externos (como no noso caso, sistemas controlados catalíticamente), que nos permitirán controlalos evitando efectos non desexados e poder desenrolar correctamente as respostas obtidas.

Nos distintos capítulos deste traballo, centrarémonos na fabricación e nas diferentes aplicacións das chamadas *nanopartículas activables externamente* con distintas funcionalidades como plasmónicas, fotoluminescentes ou catalíticas. En resumo, as *nanopartículas plasmónicas* son capaces de absorber e dispersar a luz nos intervalos correspondentes ás fiestras biolóxicas. Despois da activación, a resonancia plasmónica localizada conduce ao quecemento local na superficie das nanopartículas. Esta resposta pode usarse para liberar diferentes moléculas das cavidades ou superficies plasmónicas e incluso para realizar diversas terapias. Ademais, os *materiais fotoluminescentes* poden transformar a radiación electromagnética absorbida nunha diferente. As moléculas de colorantes orgánicos ou *fluoróforos* son bastante versátiles porque poden ser deseñadas con moitas estruturas e propiedades diferentes. Pódense unir a nanopartículas e aos compoñentes celulares permitíndonos seguilas mediante técnicas de fluorescencia. Estes materiais transforman a radiación de alta enerxía nunha menor. Pola contra, outros materiais poden transformar fotóns de baixa enerxía noutros de maior enerxía. Debido a isto, é posible levar a cabo a activación dentro do rango das fiestras biolóxicas. Os *materiais sobreconversores* (tanto

macroscópicos como na escala nano) teñen estas propiedades únicas. Ambos tipos de materiais fotoluminescentes serán implementados e estudados neste traballo. Para concluír cos distintos nanosistemas activables empregados nos seguintes capítulos, tamén se realizaron sistemas catalíticos controlados. Estes sistemas responden a unha aplicación externa de diferentes substratos transformándoos ou catalizándoos nos seus produtos, os cales cambiarán algunhas das propiedades iniciais do substrato como, por exemplo, a súa emisión fluorescente, a súa absorbancia ou a toxicidade celular. Polo tanto, poderase realizar a catálise cunha dependencia coa dose e co tempo.

No *capítulo 2*, presentamos un proxecto baseado nas propiedades exclusivas das nanopartículas sobreconversoras dopadas con terras raras. Ofrecen emocionantes oportunidades para as aplicacións biomédicas, onde se desexa a activación remota de procesos biolóxicos no infravermello próximo, incluíndo a bioimaxe *in vivo*, optoxenética e terapias baseadas na luz. As nanopartículas sobreconversoras presentadas neste traballo dan acceso ás fiestras biolóxicas. Nos últimos anos, houbo varios estudos sobre nanopartículas sobreconversoras excitables no infravermello capaces de traballar en tecidos biolóxicos e ambientes celulares. Por desgraza, a maioría destes nanosistemas baséanse na sobreconversión de yterbio a 980 nm, o que coincide coa absorción da auga dentro da primeira fiestra biolóxica. Polo tanto, as aplicacións biomédicas requiren métodos para producir nanoplataformas sobreconversoras máis robustas que poden ser excitadas de xeito eficiente por outras fontes de infravermello próximo que non sexan 980 nm, como 808 nm e 1064 nm.

Presentamos un método sintético para producir nanopartículas sobreconversoras estables en auga que poden ser activadas con fontes de excitación de 808 nm, evitando así procesos de quecemento non desexados debido á absorbancia de auga en 980 nm. É importante destacar que estas nanopartículas, que transferimos a un ambiente acuoso usando un polímero anfifílico, permanecen coloidalmente estables durante longos períodos de tempo nos medios biolóxicos relevantes mantendo as súas propiedades de fotoluminescencia. O polímero seleccionado modificouse de xeito covalente con dous fotosensibilizadores aprobados pola FDA (Rose Bengal e Chlorin e6), que poden ser excitados de forma eficiente e simultánea polos distintos picos de emisión das nosas nanopartículas sobreconversoras. Polo tanto, a nosa estratexia de funcionalización co polímero permítenos producir unha nanoplataforma fotodinámica que se pode activar a 808 nm. Estes nanocompostos sobreconversores almacénanse preferentemente nas células en compartimentos lisosómicos ácidos, o que non afecta negativamente ao seu rendemento como axentes fotodinámicos. Despois da excitación a 808 nm, demostrouse a produción de especies oxidativas reactivas e o seu efecto na integridade mitocondrial. Polo tanto, demostramos a viabilidade de usar nanoplataformas

sobreconversoras modificadas polo polímero fotosensibilizador que poden ser activadas por fontes de excitación de luz de 808 nm para aplicación en terapia fotodinámica. As nosas nanoplataformas permanecen fotoactivas despois da internalización nas células vivas, permitindo a xeración de especies reactivas de osíxeno activadas a 808 nm. A versatilidade da nosa estratexia de estabilización co polímero permítenos un acceso directo a outras derivatizacións (por exemplo a integrar outros fotosensibilizadores ou ligandos de referencia), que poderían operar sinerxicamente como nanoreactores de plataformas fotodinámicas multifuncionais para aplicacións *in vivo*.

No *capítulo 3* introduciremos os materiais metalo-orgánico estruturados (MOF). Estes compostos de coordinación sólidos consisten en catións de metais de transición coordinados con ligandos orgánicos multidentados os cales presentan unha porosidade moi ben definida. Os nanomateriais híbridos compostos por corazas de MOF e núcleos de nanopartículas inorgánicas, foron aproveitados para a xeración de nanomateriais multifuncionais para diversas aplicacións. Ademais da incorporación das propiedades características das nanopartículas a estes nanocompostos, as propiedades fisicoquímicas básicas dos MOF (é dicir, o tamaño do poro, a distribución e a hidrofilicidade / hidrofobicidade) son clave, por exemplo, para conseguir sistemas de administración de medicamentos eficientes. Neste contexto, os nanocompostos baseados no MOF imidazolato zeolítico-8 (ZIF8) foron moi empregados para a entrega sostida de ampla variedade de fármacos, usando a porosidade do ZIF8 para almacenar con seguridade as moléculas desexadas. Ademais, algúns nanotransportadores foron deseñados para levar a cabo unha liberación de fármacos controlada por un estímulo externo (infravermello neste capítulo), o que permitirá que a molécula cargada sexa entregada no destino cun control espazo-temporal. Por desgraza, a inestabilidade acuosa dos nanocompostos ZIF8 dificulta a liberación da carga especificamente mediante o estímulo.

A continuación, elaboráronse nanoestrelas plasmónicas de ouro como núcleo e o nanocomposto ZIF8 como coraza para a liberación de moléculas activas cargadas mediante propiedades termoplasmónicas dentro das células vivas. As nanoestrelas foron seleccionados como núcleo debido á súa característica banda plasmónica centrada en 770 nm, o que é adecuado para excitar dentro da primeira xanela biolóxica. Estas nanoestrelas usáronse como sementes para crecer a coraza de ZIF8. Como proba do concepto, os nanocompostos foron cargados cunha molécula aproveitando a porosidade da coraza ZIF8. Como molécula bioactiva eliximos un colorante fluorescente azul normalmente usado para a tinción de ADN nuclear celular en bioloxía molecular (Hoechst). Os nanocompostos están envoltos cun polímero anfifílico que impide a degradación do ZIF8 nos disolventes de base auga, así como para "atrapar" as moléculas cargadas e evitar as fugas de Hoechst en medios acuosos ou dentro das

células vivas. Finalmente, o mecanismo de liberación de moléculas demostrado depende do uso de luz infravermella que coincide coa absorción plasmónica das nanoestrelas de ouro do núcleo, creando gradientes de temperatura locais e, polo tanto, favorecendo que as moléculas colocadas dentro dos poros ZIF8 se termodifundas dende o interior da partícula. A microscopía confocal e espectroscopía Raman de superficie, son usadas para demostrar que as moléculas cargadas son liberadas e que o infravermello próximo libera a carga no interior das células, cambiando así a cor do ADN nuclear. Queremos destacar que o noso enfoque neste capítulo é un importante paso adiante no desenvolvemento de vehículos intracelulares baseados en MOF para a liberación controlada de fármacos. En resumo, deseñamos un nanomaterial baseado en ZIF8 estable (incluso almacenado nas células) con capacidades termoplasmónica combinadas e altas capacidades de carga de medicamentos.

No *capítulo 4* centrarémonos nun dos obxectivos actuais na química e bioloxía celular. Consiste no desenvolvemento de reaccións intracelulares, xeralmente catalizadas por enzimas dentro das células vivas. Isto permite que se poidan implementar funcións non nativas que influirán nas propiedades das células dun xeito previsible. Durante as últimas décadas avanzouse neste campo a pesar de importantes inconvenientes que aínda quedan por resolver, como a falta de biocompatibilidade e a eficiencia dos reactivos baseados en metais. O desenrolo deste obxectivo a través de procesos térmicos podería ser unha alternativa, pero é obvio que as células non se poden quentar por encima das temperaturas fisiolóxicas. Este problema pódese resolver empregando nanopartículas plasmónicas como transductores térmicos sensibles ao infravermello, sempre que a reacción química se poida situar preto destas unidades xeradoras de calor. Hoxe o uso das propiedades fototérmicas das nanopartículas plasmónicas para o quecemento local fotoinducido está ben definido. Estas propiedades son especialmente útiles para aplicacións biolóxicas porque o quecemento pode ser activado por fontes de luz próximas ao infravermello, que normalmente úsanse para excitar a correspondente banda plasmónica das nanopartículas metálicas anisotrópicas, como as nanoestrelas no noso caso. Non obstante, o uso de efectos de calefacción termoplasmónicos para promover termicamente reaccións químicas dentro das células vivas non foi aínda definido. Neste capítulo, deseñouse un nanoreactor plasmónico microporoso para realizar ciclizacións deseñadas por un impulso térmico dentro das células vivas. Como proba de concepto, escollemos unha ciclización intramolecular que se basea no ataque nucleófilo dunha piridina sobre un carbono electrófilo, un proceso que require altas enerxías de activación e que xeralmente se logra quentando a solución a 90 °C a cal nunca se describiu mediante procesos fototérmicos.

O nanoreactor de núcleo-coraza deseñouse do mesmo xeito que no capítulo anterior: un núcleo dunha nanoestrela de ouro, que está dentro dun MOF (ZIF8) estabilizado cun polímero. Unha vez almacenada dentro das células vivas, a coraza feita permite a difusión eficiente dos reactivos desde dentro da cámara plasmónica, onde sofren a devandita transformación despois da iluminación coa luz infravermella próxima. A reacción, ademais de xerar un produto fluoróxeno ciclado, proporciona compostos bioactivos con resolución espazo-temporal. A coraza microporosa é fundamental para promover unha concentración efectiva dos reactivos preto da fonte de calefacción, a nanoestrela, así como para garantir o confinamento térmico requirido. Por iso, neste capítulo demostramos por primeira vez a viabilidade de lograr reaccións químicas promovidas fototermicamente dentro das células vivas. En xeral, os nosos nanocompostos plasmónicos compórtanse como excelentes nanoreactores biocompatibles, que poden funcionar dentro das células vivas para promover transformacións intracelulares de nova xeración con resolución espazo-temporal.

Para finalizar, no *capítulo 5* introduce a catálise biolóxica con metais. Traducir o potencial da catálise con metais de transición a ambientes biolóxicos e finalmente a células vivas, promete ter un profundo impacto na bioloxía química e celular, así como na biomedicina, debido á infinidade de transformacións que se poden realizar. Aínda que a maioría destas reaccións leváronse a cabo en disolventes orgánicos e en condicións libres de auga, nos últimos anos observouse un aumento exponencial no desenvolvemento de reaccións mediadas por metais que poden producirse en ambientes complexos e incluso en células. de mamíferos vivos. Os catalizadores baseados no paladio son especialmente atractivos debido ao seu potencial sintético ben establecido. Non obstante, o rendemento de complexos homoxéneos de paladio, así como o das nanopartículas de paladio, en medios biolóxicos son xeralmente comprometidos por problemas de solubilidade acuosa, estabilidade, pasivación, fugas de paladio e/ou biocompatibilidade. Ademais, estamos aínda lonxe de obter catalizadores metálicos robustos, permeables ás células e biocompatibles, capaces de realizar reaccións intracelulares de forma bioortogonal. A posibilidade de obter reactores intracelulares que permanezan activos ao longo do tempo é especialmente atractiva, xa que poderían xerar ciclicamente os produtos ademais de depender directamente da dose administrada.

A continuación, presentamos por primeira vez un nanocomposto de paladio-ZIF8 compatible con auga, capaz de funcionar como nanoreactor heteroxéneos bioortogonal eficiente. O nanocomposto presenta un núcleo cun nanocubo de paladio (o catalizador) e unha coraza nanométrica porosa de ZIF8 (o filtro) equipada cun polímero anfifílico. Ao contrario doutros híbridos compostos por metais e MOF que teñen metais activos na superficie, a nosa arquitectura de núcleo-coraza asegura que a reacción se produza na cámara de reacción do

núcleo, fundamental para a aplicación biolóxica. Ademais, a coraza baseada no ZIF8 xoga un papel crítico na conservación da integridade da cámara catalítica ao tempo que proporciona ortogonalidade (selectividade do substrato) e biocompatibilidade. A estratexia de derivatización co polímeros fai que o nanocomposto sexa estable en auga e en ambientes biolóxicos. Aparte diso, esta arquitectura non só protexe o nanocatalizador de paladio da desactivación, das fugas e da agregación; senón que a súa porosidade permite un fluxo controlado da difusión dos reactivos cara a cámara de reacción no núcleo. Como resultado, estas construcións poden usarse como nanoreactores metálicos robustos e eficientes en medios acuosos complexos e o máis importante, dentro de células de mamíferos vivos. Estas nanoplataformas tenden a almacenarse en compartimentos citosólicos (endosomas e / ou lisosomas) onde permanecen estables, activos e accesibles para os reactivos, e poden promover varios ciclos de reacción consecutivos usando novos lotes de reactivos, sen perder a súa eficiencia. Isto pode realizarse en cultivos celulares en forma de monocapas 2D. Ademais estes nanoreactores poden incorporarse facilmente a esferoides tumorais 3D para producir sistemas catalizadores similares aos anteriores, que tamén poden funcionar repetidamente e dependendo da dose. Isto representa unha demostración pioneira de nanoreactores cíclicos intracelulares e senta as bases para o desenvolvemento de nanoimplantes catalíticos en tecidos celulares. Estes nanoreactores artificiais con núcleos de metais de transición ofrecen posibilidades exóticas para moitas outras reaccións abióticas en ambientes vivos e, polo tanto, prometen ter importantes aplicacións na bioloxía química e celular así como na biomedicina.

Polo tanto, ao longo dos diferentes capítulos desta tese doutoral, demostraremos que non só podemos deseñar, fabricar, caracterizar e implementar con precisión numerosas operacións empregando diversos nanosistemas que poden ser activados externamente (con resolución temporal e espacial); senón que tamén levamos a cabo todas estas respostas dentro de células vivas dun xeito seguro e controlable sen comprometer a biocompatibilidade.

1. INTRODUCTION

1.1. NANOWORLD. PROPERTIES, MATERIALS AND APPLICATIONS

1.1.1. What is nanoscale and nanotechnology?

In physics and chemistry, *nanoscale* refers to the length scale between quantum and classical physics. In other words, nanoscopic systems represent a bridge between macroscopic systems governed by classical physics and atomic ones such molecules that follow quantum chemistry/physics rules (Figure 1.1). In general, systems with any dimension lying in the size range of 1-100 nm may be considered as nanosystems. Importantly, these often present unexpected and novel physico-chemical properties compared with their bulk counterparts.

Nanotechnology may be defined as the fabrication of functional materials, devices and systems through the control of matter at the nanometre length scale and the subsequent exploitation of derived novel phenomena and properties (physical, chemical and biological) at that length scale.[1]

Colloids are among the most basic materials lying in the area of nanotechnology, which were not defined until late 19th century, but some colloidal phenomena were previously reported (Figure 1.1) as early as the 4th century such the Lycurgus cup, which exhibits characteristic colloidal colour changes (other natural examples will be further explained in section 1.3.2.1). The word *colloid* comes from Greek word *kolla* (glue), and was coined from the impression that colloidal substances were amorphous or glue-like materials rather than crystalline forms of matter.[2] Nowadays a *colloidal system* is considered as one or more dispersed phases, with some characteristic dimension(s) between 10 nm and 10 μm, in an external continuous phase (the dispersant). Stated in simple terms, a colloid is one substance finely dispersed in another. Depending on both phases, different colloidal systems can be defined; namely, bubbles in beer foam are an example of gas colloids in a liquid phase; liquid droplets in butter are liquid colloids in a solid matrix; and smoke are solid particles dispersed in air.

Historically, the earliest systematic definition and discussion of nanotechnology is considered to be the speech given by Richard Feynman in 1959.[3] In that moment, the talk entitled *There is plenty of room at the bottom* and the statements Feynman exposed could be perfectly considered as pure science fiction. He talked about scientific knowledge referring to micro and nanoscale and discussed, for instance, about the possibility of writing all the information from the British encyclopaedia in a pin head. Another "insane" idea that he manifested was the creation of tiny autonomous robots with the ability of

performing a heart surgery. These statements were completely unrealistic for the 60's scientific community. As Jules Verne's science fiction novels like *From the Earth to the Moon* (1865), almost all of them were achieved years later thanks to scientific advances (in 1969, 100 years later, humans landed on the Moon). Could Feynman "science fiction ideas" from that may be a premonition of future nanotechnology advances too? Tiny robots for non-invasive surgeries are still impossible today, only 50 years later, but the storage of huge amounts of information in very small volumes, smaller even than that pin head, is a daily reality. Feynman also stated: "multidisciplinary science is needed for further relevant advances". Then, physics, chemistry or biology cannot go further alone. My PhD work is an example in this direction.

Figure 1.1. Nanosystems lye between the macroscopic and the atomic worlds.
The Lycurgus cup is made of glass containing gold and silver nanoparticles (NPs). Depending on how light shine through the glass, the NPs interact with it with subsequent colour change. Photo from British Museum archive.

Herein, I will briefly discuss the state of the art of nanotechnology, with strong emphasis on properties and advances for life science purposes. In the context of those science fiction ideas proposed by Feynman, the so-called bionanotechnology field is focused on getting us closer to that autonomous nanorobot with biomedical performance, even though we are still far away. Here, different nanosystems that can be activated by different stimuli in order to obtain controlled responses in living environments such as cells and animals will be analysed. The examples discussed herein could be considered among the initial steps towards making possible the concept of autonomous nanorobots given by Feynman.

1.1.2. Physics at the nanoscale

Nanosystems may show new phenomena and properties with respect to their counterpats at the macroscopic scale. In this section, we are going to discuss selected phenomena related to the size reduction in some materials, in comparison with the corresponding bulk materials. This provides nanosystems with a new variety of properties that can be exploited to produce next generation devices.

1.1.2.1. Surface to volume ratio

Reducing the size of bulk materials has an obvious and direct consequence regarding the volume and the surface area of a material (Figure 1.2a). Interestingly, nature tends to increase accessible surfaces in order to avoid inactivated material from the bulk. Good examples of this could be the highly sticky geckos' feet or the high storage efficiency of a honeycomb (Figure 1.2b).

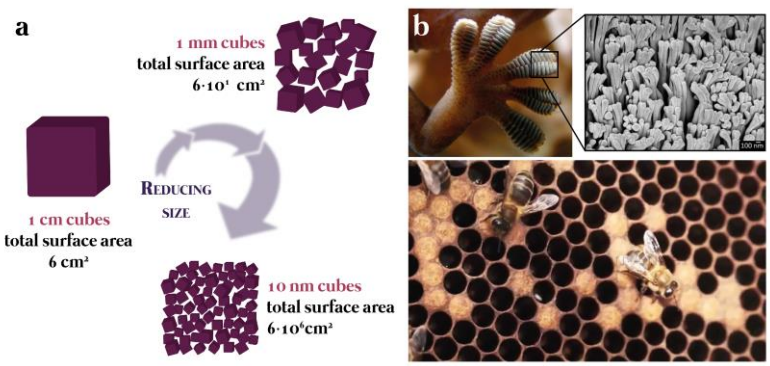

Figure 1.2. Surface area and storage efficiency of nanostructures.
a) Illustration showing the increased surface area when the size of bulk materials is reduced. b) Nanostructures in gecko lizards' feet present a high surface area, which allows them to stick the walls. Honeycombs are a good example of natural structures with high storage efficiencies.

Coming back to nanosystems, we will consider a spherical nanoparticle (NP) in order to illustrate this effect; we can define the ratio between the surface area and the volume, where *r* is the NP radius, as in equation 1 (Eq. 1):

$$\frac{A}{V} = \frac{4\pi r^2}{\frac{4}{3}\pi r^3} = \frac{3}{r} \qquad \textbf{Eq. 1}$$

Representing the *A/V* ratio as a function of the NPs radius, we can observe the following trend (Figure 1.3.): for NPs radii below 100 nm, the amount of atoms in the NP's surface starts to be relevant in comparison with their total number (total volume). Atoms on a solid surface have an environment that differs

significantly from that of bulk ones. In other words, they have fewer neighbours and a higher free space around them, therefore they can interact easily with another atoms/molecules/entities. This effect has different consequences, such as enhanced reactivity and catalytic properties as, for example, in the case of palladium NPs that we will further discuss later (see chapter 5).

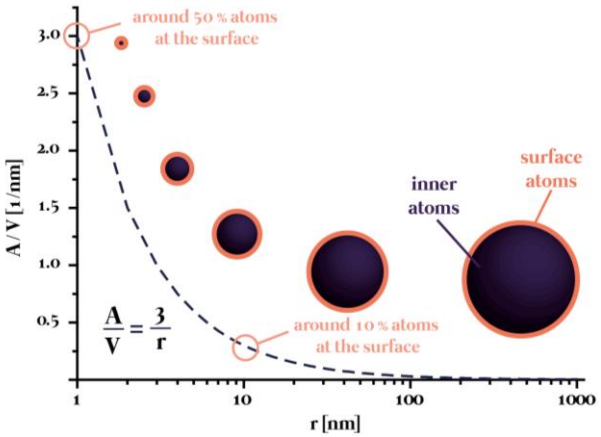

Figure 1.3. Surface to volume ratio as a function of NP radius.
The number of surface atoms can be estimated easily using Eq. 1.

1.1.2.2. Confinement effect

Another consequence of reducing the systems size is based on the Heisenberg's uncertainty principle. This states that the position and the velocity of an object cannot be measured exactly at the same time (Eq. 2). So, the main consequence of size reduction of materials and restricting space for electrons to move (confinement) is an increase in electrons momentum moving around the atomic nucleus and, thus, an energy enhancement.

$$\Delta x \Delta p \geq \frac{\hbar}{2} \qquad \textbf{Eq. 2}$$

When the particle size starts to be reduced, the spatial extension of the electronic wave function is comparable to the particle size. This "geometrical" constraint makes the electrons "feel" the presence of the particle boundaries and, then, it responds to changes in particle size by adjusting their energy. When the particle dimension is near or below the bulk Bohr exciton radius, this effect becomes more relevant. This radius is related to the distance between an electron-hole pair; that is, the energy needed for electron excitation. Thus, when the particle's size approaches the Bohr exciton radius, the quantum confinement causes an increase in the transition energy and, then, a blue shift in the absorption and luminescence band gap energy (

Figure 1.4).[4] This effect leads to discrete, atomic-like energy levels and a discrete absorption spectrum, which contrasts with the continuous absorption one of a bulk material. NP structure (core-shell configurations) and shape are also important variables which modulate this quantum effect.

Amazing examples of this effect are, for example, the photoluminescence properties of semiconductor quantum dots (QD), and the localized surface plasmon resonance in metallic NPs (see section 1.3.2.1 for further explanation).

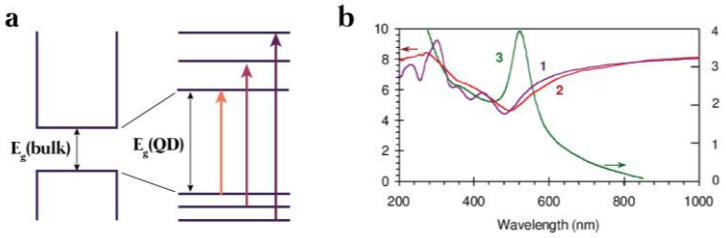

Figure 1.4. Quantum confinement effect.
a) Band gap in bulk and nanosized (QD) semiconductor materials. b) Absorption spectra of gold materials of different sizes: 1 (bulk gold, theoretical), 2 (bulk gold, experimental) and 3 (gold NP suspension).[5]

1.1.2.3. Finite size effects

In bulk materials, characteristic lengths governing the physical properties of the solid are much smaller than the size of the system. When these sizes are reduced in any dimension, these lengths become of the same order of magnitude. Manifold phenomena are related just to finite size effects and, therefore, nanosystems can be implemented in order to take advantage of them. Some of those properties in different fields of research are summarized in Table 1.1. Although any of these effects is interesting per se, we are not going to discuss them in detail. This table is focused only on giving a very brief state of the art of how materials´ properties can depend on size to the reader.

Field	**Characteristic length/Property**	**Scale length [nm]**
Electronics	Electronic wavelength	10-100
Magnetism	Superparamagnetic critical diameter	1-30
Optics	Evanescent wave decay length	10-100
Superconductivity	Meissner penetration depth	1-100
Mechanics	Grain boundaries	1-10
Catalysis	Surface topology	1-10
Polymers	Kuhn length	1-100
Immunology	Molecular recognition	1-10

Table 1.1. Different characteristic lengths that affect physico-chemical properties at the nanoscale.[6]

1.1.3. Materials in the nanoscale

In order to talk about all nanomaterials that have been discovered in the last years, we must note that different classifications can be used.

The first classification, and the most obvious one, could be established in terms of the nature of the materials that compose the nanosystem (Figure 1.5). In this line, we can talk about organic and inorganic nanomaterials. In particular, in this work we are going to work with different types of inorganic NPs. Metallic NPs made of gold, silver, palladium or copper, for example, are widely studied.[7] Owing to the wide range of metal NP-based applications, manifold fabrication protocols have been reported in order to adjust their size, shape, morphology, structure, surface functionality(ies) and so forth.[8] Other types of inorganic NPs are semiconductor NPs, nanocrystals with a characteristic, size-dependent band gap in their electronic structures. Fluorescent QDs[9] are the most usual examples. Ceramic NPs are non-metallic crystal structures with a huge variety of compositions.[10-11] Depending on these, different properties can be tuned, including dielectric,[12] piezoelectric,[12], superconductive,[13] and electro-optical,[10] among others.

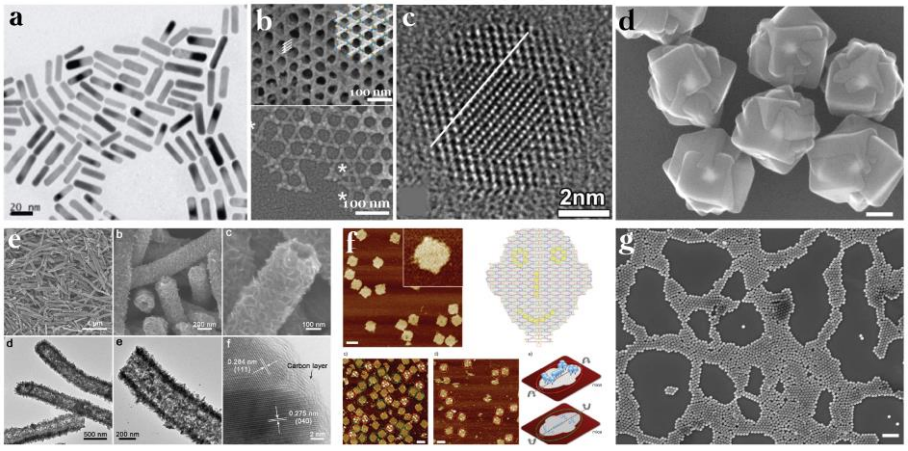

Figure 1.5. Different examples of inorganic and organic nanomaterials.
a) Metallic Au nanorods, reproduced from ref. [14] with permission from Elsevier; b) 3D DNA origami crystals with and without AuNPs, reprinted from ref. [15] with permission from John Wiley and Sons; c) HR-TEM of PbTe/CdTe core-shell QD, reprinted from ref. [16] with permission from American Chemical Society; d) NS-MOF (scale bar 100 nm),[17]; e) carbon coated SnS nanotube for sodium storage: FESEM images, TEM and HR-TEM, reprinted from ref. [18] with permission from John Wiley and Sons; f) orthogonal protein decoration of DNA-Origami from ref [19] with permission from John Wiley and Sons (scale bars 100 nm); g) ceramic UCNP (scale bar 300 nm).

Between organic nanoparticles, carbon nanostructures rely on the unique nature of the carbon bond to form several interesting structures. Graphene, fullerenes and carbon nanotubes[18] are some examples. Other organic

nanomaterials are made of other organic molecules, which though self-assembly processes can form bigger and more organized synthetic supra-structures (dendrimers, nanoparticles, micelles, vesicles, lamellas, etc); or in the case of biological entities such as lipids or DNA, to obtain liposomes[20] and DNA-origami structures,[19] respectively. Also, the membranes of cells can be extracted and self-assembled to form artificial cell membrane-derived nanosystems.[21] In between organic and inorganic nanomaterials, there are different hybrid nanomaterials. For instance, metal-organic frameworks (MOFs) are highly porous materials formed by metallic ions (or metallic clusters) coordinated with organic ligands to form highly crystallinity structures.[22]

Another type of classification can be given in terms of the nanosystems functionality and/or their characteristic properties, such as plasmonic, luminescent, magnetic, sono-sensitive, porosity, catalytic behaviour and electronic and superconducting materials. In section 1.3.2 we are going to talk more in detail about selected examples of NP functionalities.

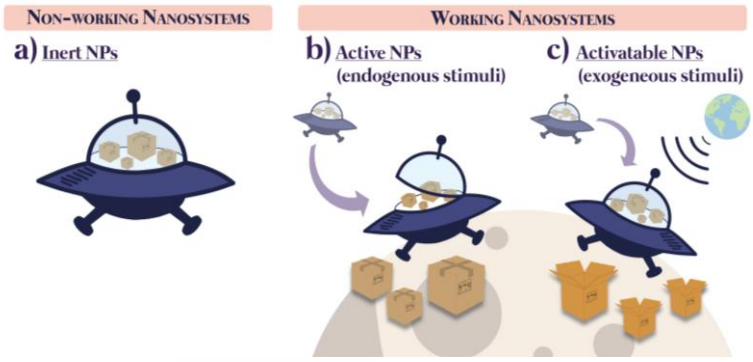

Figure 1.6. Schematic representation of inert, active and activatable nanomaterials.
a) Inert NPs do not change their properties; b) active NPs can perform some simple responses under different changes of the environment properties (endogenous stimuli); c) activatable NPs can be switched on/off with spatiotemporal control under different external stimuli.

To conclude within the context of my PhD work, an interesting classification may be proposed in terms of whether and how to control the nanomaterials properties; in this manner, nanomaterials can be classified as inert, active and activatable nanomaterials (Figure 1.6). *Inert materials* have inherent properties that cannot be switched on or off like, for example, porosity, biocompatibility or electrical and thermal properties. They are referred as *non-working systems*. On the other hand, *working systems* have properties that may be activated, switched on/off or vice versa, by an endogenous or exogenous specific stimulus. Active systems by endogenous stimuli will change their conformation or functionality as a response to the physico-chemical properties of their surrounding environment such as pH and temperature variations, chemical gradients, molecular crowdedness and so forth. Lastly, exogenously activated nanosystems

are those than can be activated with spatiotemporal control by external stimuli. Examples are electromagnetic radiation, sound waves, magnetic fields (see section 1.3.2 for further information) or the presence/application of an external molecule (catalytic controlled systems). Activatable nanomaterials have been the focus of this work, since the ability of a material to be stimulated in a controlled manner is an obvious advantage in order to improve classical therapies and diagnosis techniques in the biomedical arena.

1.1.4. Applications of nanoscale materials

Taking profit of all these nanomaterials with new properties, a huge variety of applications have been designed/elucidated over roughly the past three decades (Figure 1.7).

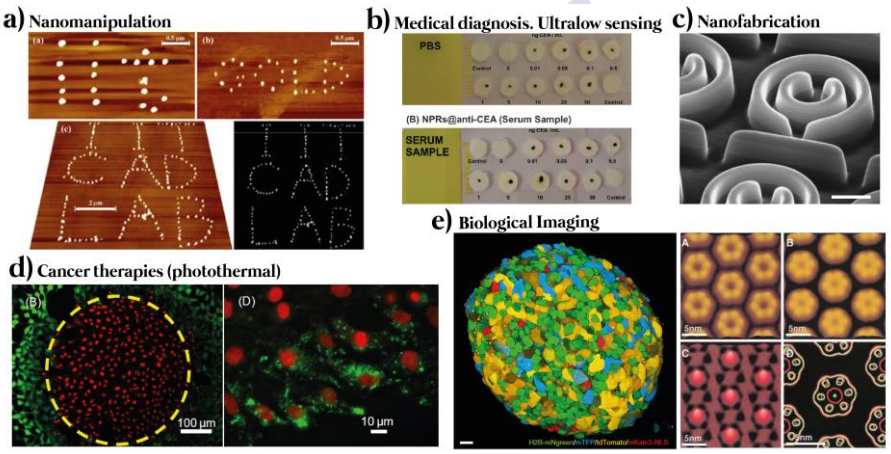

Figure 1.7. Different examples of nanomaterials applications.
a) AFM-based AuNP manipulation from ref [23], ©2011 IEEE, top scale bars represent 0.5 µm and down scale bars represent 2 µm; b) ultralow detection plasmonic-drive., reproduced from ref. [24] with permission from The Royal Society of Chemistry; c) focused Ion Beam Lithography. SEM image from [25] reprinted with permission from IOP Science (scale bar 500 nm); d) photothermal nanonachos, from ref. [26] with permission from American Chemical Society; e) biological imaging: left, ultra-high resolution 3D fluorescence imaging of human breast cancer organoid and human colonic organoid from [27] with permission from Springer Nature, and right, AFM imaging of cellular membrane proteins connexin from [28] with permission from European Molecular Biology Organization.

In this work, we will focus on the application of our nanosystems in the *nanomedicine field*. The main aim of this work is to design new nanosystems capable of interacting with biological entities (cells and ultimately, with animals and the human body) in a safer way (biocompatibility) than other state of the art approaches (check section 1.4). Once nanosystems are immersed in living environments, different responses can be obtained. Nowadays, one of the fields

of nanomedicine is focused on designing platforms with the aim of both combining therapy and diagnosis capabilities, that is, theranostic nanosystems. A variety of therapeutic and diagnostic techniques can be benefited from properties derived from the nanoscale: new biosensors with better sensitivity, earlier detection of cancer, efficient drug delivery with reduced side effects, gene delivery, neuro-modulation and optogenetics, among others, are impressive applications that are starting to be a reality.

In contrast to this, other fields of knowledge are being updated with nanotechnology. For example, information technologies are focused on creating systems for data storage with high density and processing at high speeds. Nanoelectronics, spintronics or quantum computing have also advanced quite fast in recent years thanks to nanoscale systems.[29]

More examples of "nanoproperties" applications are energy production and storage (photovoltaic cells and batteries), nanofabrication and nanomanipulation (as AFM tip functionalization or some bottom-up NPs nanofabrication techniques) and creating new materials with completely new properties (like perovskites, graphene or superconductors).[30]

1.2. INORGANIC NANOPARTICLES PREPARATION FOR BIOLOGICAL APPLICATIONS

The general context of this work is within the framework of biomedical applications based on inorganic NPs. Since the late 1990s, a large variability of NP-based options, or nanobiotools, has been developed, either as therapeutic and/or diagnostic tools.[31-32] However, only a few nanobiotools such as nanomedicines, NP-based biosensors or bioimaging agents, have been successfully reached the market.[33] The main reason for this lack of real applicability is the inherent complexity of biological environments, including fluids, biomolecules, cells, tissues or whole animals.[34-35] Therefore, studying how the individual physicochemical properties of NPs such their size,[36] shape,[37] charge,[38] colloidal stability,[39] corrosion,[17] stiffness,[40] and so forth, become affected by such bionanointerfacing is paramount. The research focused on bionano-interactions has two main purposes: firstly, to take advantage of the great expectations for health that have raised from the intended use of new nanomaterials and nanostructures; and secondly, as materials may be also released unintentionally, for instance, through mechanical weal or chemical powder waste, to avoid possible health concerns.

In this section, we are going to discuss the NPs behaviour and stability in the context of biology and medicine. The focus will be put on the most important factors influencing NPs' interactions when they are immersed in biological environments: NP integrity, protein corona and colloidal stability. Towards this end, first, we will provide the most important concepts and considerations to the

fabrication and characterization of NPs for this purpose; secondly, we will briefly expose and discuss several case examples of relevance in the field of bionanotechnology. For the sake of brevity, we will exclusively restrict to engineered NPs obtained by bottom-up fabrication methods. We consider such NPs the most adequate models to deal with the topic in question, owing to their homogeneity.

1.2.1. Nanoparticle fabrication, general considerations

In the following, we briefly introduce some general concepts and approaches which may be useful to design different NPs with robust biostability.

1.2.1.1. Synthesis of inorganic nanoparticles

During the last two decades, synthetic methods to produce NPs have been greatly developed. Most of the synthetic techniques to produce NPs are based on wet-chemical routes. Thanks to them, a fine control over the NP size, shape, structure and composition can be achieved. In addition, these methods are highly reproducible in any advanced chemistry laboratory.[41] They are based on some common aspects:

i. Metal or metal oxide precursors (same for non-metallic elements like rare earths) are dispersed in a solvent (polar, non-polar or mixtures).

ii. Temperature of the solvent and/or the addition of reducing agents dictates when nuclei (NPs' precursors) start to grow.

iii. The addition of surfactants, linkers or capping molecules influences NP shape and size.

iv. The absolute and relative concentration of reactants, as well as heating ramps during the NP growth, influences the final NP size and shape.

v. A purification step is usually needed after synthesis. Centrifugal precipitation is the most common technique to obtain a final colloidal dispersion of NPs coated by a shell (*e.g*. purely organic like oleic acid, silica or MOF). Not performing this last step can lead to aggregation into the corresponding bulk materials.

These steps allow us to control the NP size, shape, composition, structure (core-shell/multi-shells and element doping, for example) and monodispersity, which will determine their physicochemical properties.[42] For plasmonic NPs (*e.g*. gold, silver, copper and /or aluminium; gold nanostars (NS) in this work in chapters 3 and 1), these properties define the localized surface plasmon resonance (LSPR) that governs the photothermal capabilities and other plasmonic-derived processes (section 1.3.2.1).[43] The morphology dependent quantity in the case of magnetic NPs (*e.g.* magnetite, maghemite, doped-ferrites and iron) is the hysteresis loop, which affects directly their biological performance (section 1.3.2.2).[44] Photoemissive NPs (*e.g*. QDs, up- or down-

conversion NPs or nano-perovskites, section 1.3.2.1) have multiple optical properties that depend on the above mentioned factors. Photoemission intensity and wavelength as well as *quantum yield* (QY) can be tuned in terms of such morpho/structural properties.[45] Lastly, the performance of heterogeneous nanocatalysts (*e.g*. palladium, copper, gold, ruthenium or platinum, chapter 5) is influenced by crystal structure, valence state, porosity, and coating of the NP surfaces.[46]

1.2.1.2. Surface modification (functionalization)

Independently of whether NPs are produced in aqueous media or in organic solvents, the stabilizing capping shell after their synthesis is, in most cases, insufficient to stabilize the NP in biological media; specially, for organic synthesis whose final products are, in general, non-polar. Biologically relevant media have high ionic strengths, polarity, pH values which, in addition to the coexistence of polyelectrolytes, biomolecules and biomacromolecules in high concentration giving rise to a highly crowded medium, may trigger NP precipitation, aggregation and even reshaping. To increase the control and performance of nanosystems and warrant their colloidal stability under these demanding conditions, a further chemical surface engineering (or functionalization) step is needed.[47]

After the synthesis and purification of NPs, they do not present "naked" surfaces so they should be considered as core-shell inorganic-organic nanostructures. Changing or modifying the original surface-coating surfactants may be done by two types of stabilization.[48] On one hand, *electrostatic repulsion* by charged species (*e.g.* compounds containing amine and carboxylic groups or different types of polymers) and, on the other hand, *steric hindrance* (*e.g.* proteins, gelatin, silica shells and MOF-based shells). As a result, colloidal stability in biological environments is improved. It is important to keep in mind that biological relevant pH values range from the extracellular neutral environment (pH ~ 7) to the acidic lysosome milieu (pH ~ 4.5). To avoid a loss in particle stability, charged groups from NPs should remain electrically charged at those biological pH values.

In this work, a polymer coating process based on the amphiphilic polymer poly(isobutylene–alt–maleic anhydride)–graft–dodecyl (PMA) was performed for NP aqueous water transfer of our synthesized non-polar nanosystems.[49] In this work, as synthesized oleic acid capped upconverting NPs were successfully transferred to water using this strategy (section 2.3). Also, MOF shells were used to stabilize, protect and act as filter of NS and palladium nanocubes (sections 3.3, 4.3 and 5.3), followed by an additional functionalization step involving a PMA-coating step to avoid the characteristic MOF-shell degradation in aqueous media.[50]

1.2.2. NP characterization

1.2.2.1. Size and zeta (electrokinetic) potential characterization

Dynamic Light Scattering (DLS) and *Nanoparticle Tracking Analysis* (NTA) allow for determining the *hydrodynamic diameter* of NPs dispersed in solution. Both techniques are based on the measurement of particles/molecules Brownian motion as well as light scattering by colloids.

Brownian motion was discovered in 1827 by the botanist Robert Brown after some microscopically observations of the movement of particles contained in the pollen of plants. He reported an irregular and jittery motion of the particles (1.8). Even earlier, the Roman philosopher Lucretius' scientific poem *On the Nature of Things* (*c.* 60 BC) showed a remarkable description of the motion of dust particles. NPs' Brownian motion depends directly on the particle size, temperature and solvent.

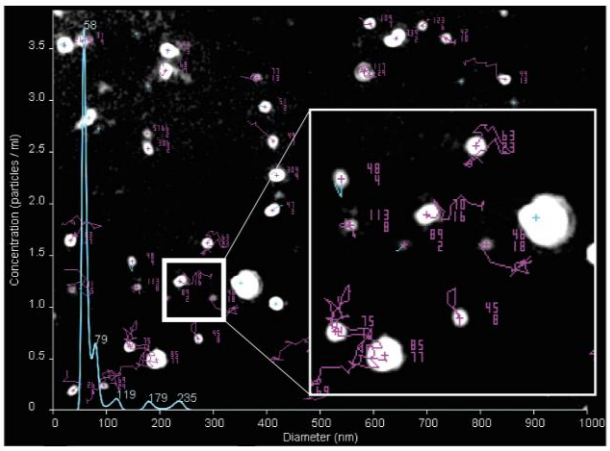

Figure 1.8. Brownian motion measurements by NTA.
Figure shows raw data in pink. Size histogram from water-dispersed NPs around 50-55 nm in diameter is shown in cyan.

When light impinges on a NP, different amounts of light will be absorbed and scattered. The most famous exact solution to Maxwell's equation, for the case of small particles or colloids, was developed by Gustav Mie (1908) with the aim of explaining the different colours exhibited by small colloidal particles of gold suspended in water. This effect can be observed in many situations in nature when particles in a continuous medium are in the same size range than the incident light wavelength (Figure 1.9).

DLS and NTA are used to determine the hydrodynamic diameter, d_h, of NPs in solution. Raw data obtained by NTA provide number-weighted d_h distributions due to individual particle counting, whereas DLS experimentally provides intensity-weighted distributions coming from overall sample scattering, which

after deconvolution can be also expressed in number-weighted size distributions. This value typically exceeds the size observed by electron microscopy because of NP surface dehydration process in the latter technique.

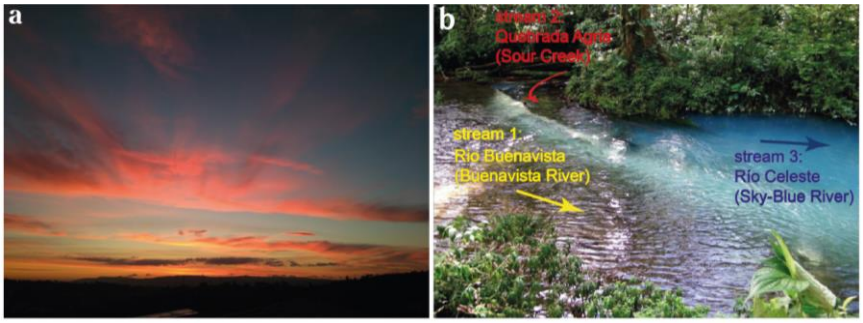

Figure 1.9. Mie scattering examples due to colloidal NPs in nature.
a) Sky colours are a consequence of light scattering due to colloidal particles suspended in the atmosphere; b) recently, the colour change of Rio Celeste was demonstrated as a result of the aggregation of aluminosilicate NPs when the acidic waters from a lateral water stream are mixed (Copyright © 2013 Castellón et al).[51]

The *zeta potential* or *ξ-potential* is another important magnitude to be determined in order to obtain biological stable colloids. At the surface of any colloid (see colloid definition in section 1.1.1) a separation of charged components is always present. The origin of the surface charge is consequence of different effects like lattice imperfections, ionizable groups at the surface (as carboxyl or amino groups, which also depends on the solution pH) and a preferable adsorption of specific ions. The formation of an *electrical double layer* (EDL) occurs via attraction of oppositely charged counterions by the primary surface charge followed by a diffusion of the counterions away from the surface. The potential energy of this layer highly depends on the distance from the surface (*d*). If we assume a highly negative colloid, positively charged species will be attached to the surface within the Stern layer. The potential within this layer decays linearly with *d*, the distance to the colloid surface. Once this increases, counterions start to diffuse in the so-called diffuse layer. Here, the potential decays exponentially with *d* (Figure 1.10). The total potential of the EDL is a sum of the Stern layer and the diffuse layer potentials. We can define now the slipping plane as the last stationary layer of counterions attached to the dispersed particle. This plane moves at the same time than the particle, and the ξ-potential can be defined as the potential difference between the dispersion medium and the slipping plane.

Measurement of the ξ-potential, a derived magnitude from electrophoretic measurements, is quite important in order to obtain colloidally stable solutions, and it can be experimentally obtained by Laser Doppler Anemometry (LDA). LDA is performed in aqueous solutions at a known pH. It consists on applying an

electric field to measure how a particle moves under its influence. Therefore, ξ-potential is also referred to as electrokinetic potential.

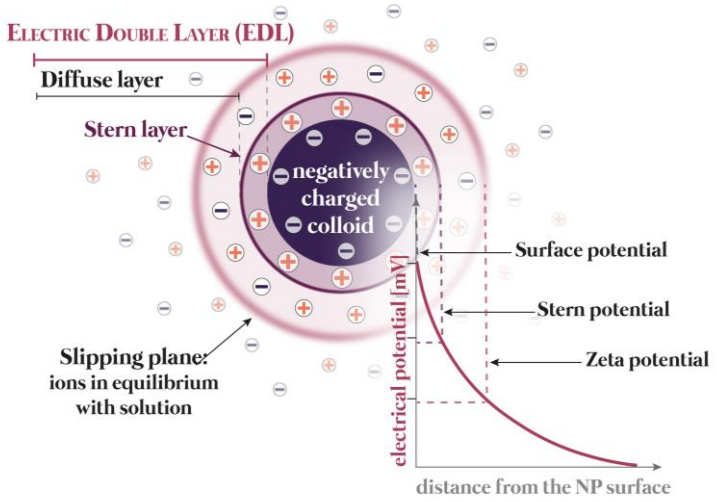

Figure 1.10. EDL scheme.
Once distance to the colloid starts to increase, counterions start to diffuse in the diffuse layer. Here, the potential decays exponentially with *d*.

The combination of DLS (or NTA) and LDA provides valuable information in order to obtain biologically stable NPs. Studying the evolution of d_h and ξ-potential of NPs over time in relevant biological media such as phosphate buffer saline (PBS), cell culture medium (Dulbecco's modified Eagle's medium or DMEM) or artificial lysosomal fluid (ALF) is becoming more and more usual.

1.2.2.2. Ultraviolet-Visible (UV-Vis) Spectroscopy

The *absorbance spectrum* of NP solutions provides insightful information about their colloidal state. This technique, typically used to characterize plasmonic NPs, is fast, ultrasensitive, affordable and reliable. Changes in LSPR are directly related to changes in the dispersion media (*e.g*. polarity), size, shape, and specially, to the NPs aggregation state induced, for instance, by ionic screening (*e.g.* salts present in the medium) or by the presence of proteins, charged polymers or other biomolecules.[52] Moreover, as in solutions of nucleic acids, dyes, or in general, any UV-Vis active molecule, absorbance at NP-type specific wavelengths can be used to determine the NP concentration in solution (using the corresponding calibration curves).[40] Moreover, this technique can be used with non-plasmonic NPs since aggregation induces an absorbance broad peak in the near infra-red (NIR) region of the electromagnetic spectrum due to scattering produced by the NP aggregates.[53]

1.2.2.3. Photoemission techniques

Photoemission processes are going to be explained in detail in section 1.3.2.1. Here, we are going to discuss how photoemissive materials may be characterized by different techniques.

When a material absorbs a photon, an energetically excited state is formed, which is later deactivated with the corresponding loss of energy, returning to its ground state. The QY of any photoemission process is the ratio of absorbed photons to the emitted ones. In other words, it describes how efficient materials will transform the absorbed photons into the desired emitted ones. Different ways of QY quantification can be used as, for example, fluorescent materials whose QYs can be obtained by representing the absorbance of the material against the integrated fluorescence intensity (the area under the fluorescence peak).[54] Other case can be upconverting materials, where photon absorption and emission are nonlinear; it will depend on many factors such as NP surface defects, concentration or solvents. A specific protocol based on the relationship between the total amount of photons reaching the sample and the total amount of emitted ones has been designed for that QY estimation.[55]

In addition, photoemissive materials have an important role in biological imaging. Fluorescent probes, not only nanomaterials but also a huge variety of molecules, enables researchers to detect components of complex biomolecular assemblies, such as living cells, with impressive sensitivity and selectivity. For biological imaging with fixed biological samples as well as living ones, the combination of fluorescent probes with different types of nanomaterials increases the applicability of many fluorescent techniques. For example, in chapter 2, the fluorescent probes attached to the NPs not only allows us to achieve the desired objective (as for example killing cells by photodynamic therapy), but also NPs can be tracked and localized inside cells.

Fluorescence microscopes resolve fluorescence as a function of spatial coordinates in two or three dimensions for microscopic objects. Manifold techniques have been discovered along the last years (confocal microscopy, two-photon excitation microscopy or Stimulated Emission Depletion, STED, microscopy)[56] for the excitation of photoemissive probes and light collection. Year by year, the spatial resolution as well as the sample damage are being reduced meaningfully.

Another interesting and quite relevant technique in biological sciences is flow cytometry. This technique measures fluorescence per cell or particles making use of microfluidic systems, which allows the suspended cells or particles to pass one by one in front of an excitation laser and suitable fluorescent detectors. It can be used to quantify individual fluorescent events inside a whole population, providing us with useful statistical information. It is an interesting technique to quantify fluorescent properties from large biological populations.

1.2.2.4. Microscopy techniques

Among all the analytical methods that are typically used for evaluating the physicochemical characteristics of manufactured nanomaterials, techniques based on electron microscopy can provide us in-depth structural information.

Transmission Electron Microscopy (TEM) is one of the most efficient tools for nanomaterials characterization. It relies on how electrons go through the materials, obtaining bright contrast from thinner and non-electron interacting parts, and dark contrast for parts where electrons are interrupted. As electrons can be diffracted by a crystal structure, it provides high resolution of structural details like crystallinity and granularity (*e.g.* Kukuchi lines are diffraction patterns of electrons). Inorganic materials are perfect to use this technique because of their inherent high contrast. To be suitable for observation by TEM, biological samples and organic materials usually need to be dehydrated and contrast improved with heavy metal staining, but a freezing option (*cryo-TEM*)[57-58] can be also performed (Figure 1.11). *Scanning electron microscopy* (SEM) uses electrons reflected from the sample and collects their structural superficial information.

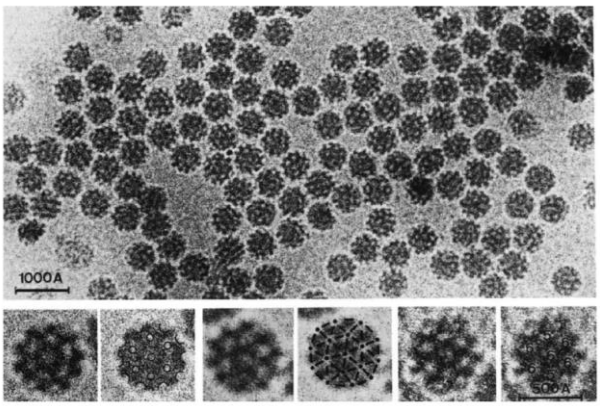

Figure 1.11. Semliki Forest viruses under *cryo*-TEM.
The Nobel Prize in Chemistry 2017 was awarded jointly to Jacques Dubochet, Joachim Frank and Richard Henderson for developing cryo-electron microscopy for the high-resolution structure determination of biomolecules in solution (1984). Scale bars correspond to 100 nm (top) and 50 nm (bottom)(Copyright © 1984, Springer Nature).[57]

Scanning Probe Microscopy (SPM) is one of the most versatile microscopy techniques. It relies on the sample being scanned by a tip and measuring a property at the sample surface. A feedback mechanism is used to maintain the tip at a constant height above the sample. *Atomic Force Microscopy* (AFM) is one of the most widely SPMs techniques used for nanosystems and biological characterization. When the AFM tip and the material are placed very close together (typically closer than 5 nm), attractive short-range forces, called Van

deer Waals, appear between them. When the materials are placed even closer until they "touch" the tip, then, a strong repulsion appears due to the impossibility of two electrons to occupy the same state (Pauli principle). All these are the forces "feel" by an AFM, and measuring these interactions allows the microscope to obtain topographical information from a huge variety of samples, including living cells.

The SPM probe can be designed in multiple ways (size, shape and functionalization) as well as different detectors can be used (*e.g*. force, shear or current sensors). Other different modes of SPM, apart from the widely used AFM, are Scanning Near-Field Optic Microscopy (SNOM), Scanning Capacitance Microscopy (SCM), Scanning Electrochemical Microscopy (SECM), Electrostatic Force Microscopy (EFM), Current-Sensing AFM (CS-AFM) or Magnetic Force Microscopy (MFM). Specially, AFM is also adaptative to living organisms imaging, like cells or bacteria. Different AFM modes have been also designed over the years (Figure 1.12).[59]

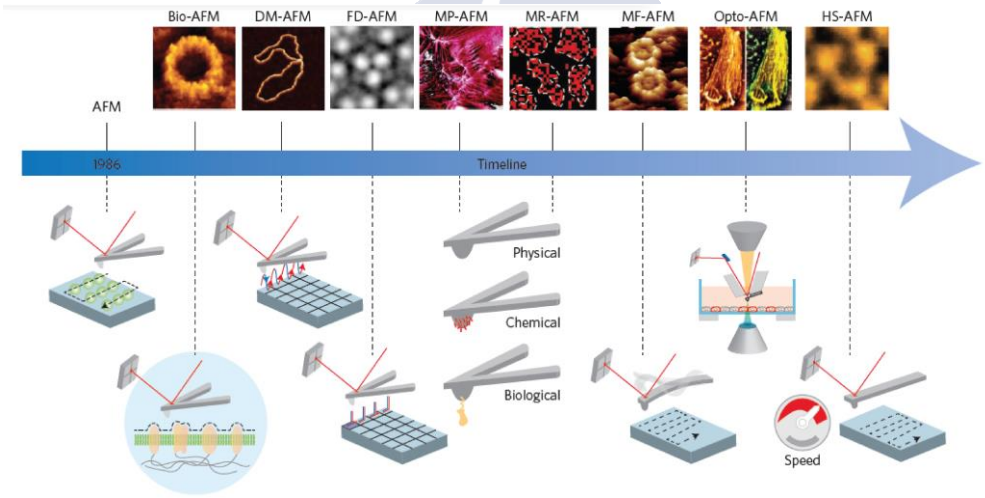

Figure 1.12. Timeline of AFM key inventions.
Starting from the birth of AFM in 1986 to the latest AFM imaging modes in molecular and cell biology. From left to right: Bio-AFM (contact mode AFM which enables to operate in aqueous solution); DM-AFM (dynamic mode AFM, which oscillates the AFM tip to reduce friction); FD-AFM (force-distance curve-based AFM); MP-AFM (multiparametric AFM); MR-AFM (molecular recognition AFM); MF-AFM (multifrequency AFM); Opto-AFM (correlating advanced optical imaging and AFM); HS-AFM (high-speed AFM which speeds up the image acquisition time by a factor of ~1000, providing access to dynamic processes in biology), copyright © 2017, Springer Nature.[59]

1.2.3. Concentration determination

The concentration determination (*i.e.* atomic species and/or NPs as individual species) is a quite relevant factor when interfacing NPs and biological media. Dose always matters and for that, this step on NPs characterization is key for nanomedical applications.

NTA (see section 1.2.2.1 for further explanation) can be performed in order to obtain the concentration of a dispersion of NPs in solution, as Inductively Coupled Plasma Mass Spectrometry (ICP-MS).

As we already explained, NTA measures the Brownian motion of individual particles. The sample flux through the instrument's microfluidic system can be controlled with a peristaltic pump. A microscope and a camera allow for recording videos from particles in solution and how they scatter light through the microfluidic channel. It can count the number of particles that scatter certain amount of light, relating it to their size. As the flux can be controlled and so the volume of solvent measured, with a simple calculation NTA can gives us also an estimation of the NPs concentration.

One of the most extended ways of expressing NP dosage is milligrams or material per millilitre of solution (mg/mL). However, the conversion of the mg/mL to molarities (mol of NPs per L) provides a more easily comparable metric, allowing for a more rationale comparison of the results. In this way, NPs may be considered as molecules.

With the aim of doing this change, ICP-MS measurements of samples can be performed. After sample ionization with inductively coupled plasma, atomized samples can be analysed by the instrument in order to quantify the different elements in terms of their atomic mass. Although this technique is very accurate by measuring the concentrations of elements in a sample, many considerations about NPs size, shape and other are needed to provide molarity metrics. Firstly, the composition of the material should be precisely defined. For gold NPs, for example, Au density is well known but it is not so obvious for another type of doped crystals. Secondly, NPs shape and size are also quite important since we need to know theoretically the NP volume and how many atoms of the measured element are inside one NP. NP size and shape are normally defined by other characterization techniques. For more complex structures (as, for example, core-multishells with different shell dopants), these calculations are a challenge. Finally, NPs are not only formed by the inorganic core, but the organic shell is also important in order to obtain the specific composition of each NP, and the number of organic ligands on the NP surface is difficult to characterize. This parameter, frequently omitted, is of vital importance to interpret colloidal stability results since NP corrosion (or leakage of atoms and/or surfactants) directly induces biological effects, including cytotoxicity, oxidative stress, genotoxicity, immunotoxicity, etc.[60]

1.2.4. Protein corona and NPs physicochemical properties if biological media

When NPs interact with a protein containing media, a layer of adsorbed proteins is formed onto their surface. This is the so-called protein corona and it is one of the most crucial factors influencing the interaction of NPs with living matter. Consequently, the protein corona may determine the biological fate of NPs as well as their colloidal properties.

The protein corona was a subject of intense studies during the last decade.[61] When the complexity of the biological media is higher than just proteins, as usual complex biological fluids, other molecules like sugars or lipids can also be adsorbed onto the NPs. In those cases, the protein corona can be named more precisely as biomolecular corona.[62]

In order to understand how NPs are recognized by cells both *in vivo* and *in vitro*, a deeper knowledge about the identity, the abundance and orientation of the adsorbed proteins might be quite useful.[63] The affinity constant determines the capability of the proteins to interact with a particular NP. However, the complexity of the medium leads to a dynamic behaviour of the corona, whose composition is a result of the competition equilibrium between the affinities of the medium components (the so-called Vroman effect).[64] Of course, this dynamic nature makes more complicated to characterize this particle corona.

It is important to note that *in vitro* studies about protein corona formation have failed to minimally reproduce commonly observed *in vivo* phenomena.[65] Therefore, research is moving to focus towards *in vivo* protein corona formation. After circulation for varying time periods in living animals, NPs are extracted for protein corona analysis.[66]

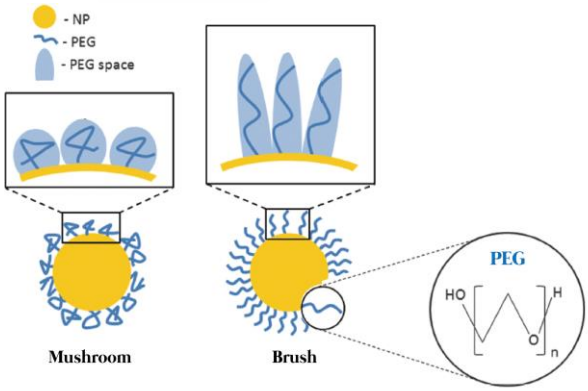

Figure 1.13. PEGylated NPs and PEG structure.
Mushroom (left) and brush (right) conformations of PEG on spherical NPs.[67]

In any case, evading the formation of the corona provides the nanocarriers with longer circulation times and, as a direct consequence, with enhanced success to achieve an efficient targeting[68]. To achieve this goal, the most common strategy is PEGylation of the NP surface (Figure 1.13). *In vitro* and *in vivo* studies have shown that PEG (poly-ethylene glycol) polymeric chains may avoid protein adsorption onto NP surfaces as well as can prevent the opsonization of NPs.[69] However, PEGylation of NPs modifies more than one physico-chemical property: the hydrodynamic size is increased, the surface charge is reduced, and usually, the colloidal stability is enhanced.[70]

1.2.5. Stability and degradation in biologically relevant media

Although NPs stability in water is the first step to create biological stable and functional nanosystems, characterizing their stability in another biologically relevant media is quite useful. Some examples might be various buffers with different ionic strength, protein-supplemented and cell culture media or blood plasma. In order to achieve the desired stability, different protocols have designed to decorate and functionalize NPs. However, not every of them are suitable for every NP. For example, using ligands that contain reactive groups that will preferentially react with a specific material, for example, gold and thiolated molecules, ensure a strong ligand-NP interaction that will enhance the NP stability. Yet, this strong interaction might not be enough if the ligand length is too short compared with the NP size, or if the ligand hydrophilicity is low. So, a rational selection of the elements that compose our nanomaterial and their surface functionalizing layer is required.

Furthermore, perfectly stable NPs in water or in low salt-content aqueous solutions can suffer from an impaired stability once they are in a harsher, more complex environment, as the biological media are. The electrical charge losses induced by screening processes[71-72] and unspecific protein adsorption, as discussed above, are two of the major inducers of NP aggregation. Nevertheless, we should also acknowledge that protein adsorption (*i.e.*, protein corona) may also help to stabilize NPs in biological media. That said, NP aggregation is not the only process that affect the NP stability in these media; for instance, leakage of metal ions due to redox reactions, the production of reactive oxidative species, and processes of ligand replacement can also occur, among others.

Regarding the NP aggregation state, obviously, to have completely aggregated NPs that are not colloidally stable and rapidly precipitate, differs from partial aggregation. The first aggregation type will produce big NP groups/clusters that might even be visible with the naked eye. Those aggregates will quickly sediment, and if large enough, they might not be even internalized by cells. Needless to say, such aggregation will dramatically affect the properties of the NPs that are related to their size and shape. The fact that the NPs are

dramatically, irreversibly aggregated can lead to wrong conclusions and, therefore, to misinterpret their cell regulation capabilities; specially, if the aggregation of the NP is not considered. More important than the aggregation of NPs that can be detected just at a glance is the partial aggregation, which produces aggregates that can only be observed using techniques such as DLS or NTA. For plasmonic NPs, the formation of such aggregates as discussed above can be detected easily by visualizing a change in the solution colour (see section 1.2.2.1); however, many other NPs do not exhibit this property. Partial aggregation in solutions of TiO_2, ZnO, silica, or iron oxide NPs will not be visible without a proper analysis, for instance, by DLS.

Then, the routine characterization of the aggregation state in media such as PBS, HEPES, or other biological relevant buffers at the biological pH range, protein containing media such PBS with BSA (bovine serum albumin) or FBS (fetal bovine serum), and cell media with and without supplements (*i.e.*, antibiotics, and essential amino acids), among others, should be considered as a fundamental physico-chemical characterization of nanomaterials.

We should also acknowledge, in any case, that some NP-based applications benefit of biomolecule-driven aggregation and/or self-assembly processes, mostly in the biosensing area, including colorimetric sensors, surface-enhanced Raman scattering (SERS), and magnetic relaxation switching.[43]

In addition, NP degradation (as breaking down NPs to smaller building blocks such as atoms, clusters and molecules) must be taken also into account. The components of biological media include dissolved oxygen and other potential oxidative agents that can affect the integrity of the NP core, leading to ion leakage and, thus, NP corrosion. Many articles have reported on the induced toxicity of NPs due to these processes as, for example, Cd-containing QDs.[73] In addition, after cell internalization by endocytic processes, NPs will end up within the endo/lysosomal system of cells and, therefore, they will be subjected to an acidic environment and enzyme digestion processes. It is important to note that enzymes are also present in cell and, in general, in living media. The abundance of these enzymes will vary within the cellular type and tissue localization. Then, understanding how enzymatic NP degradation processes work has allowed for the development of more efficient nanocarriers.[74]

We must also acknowledge that NP degradation may become useful for drug release applications and/or to avoid long-term accumulation inside living entities such as cells or animals, thereby, positively impacting on the NP biocompatibility.[75]

1.3. NANOMEDICINE AND SMART MATERIALS

1.3.1. Application of nanosystems in medicine

Nanomaterials present some advantages in comparison to current treatments and diagnosis tools due to their characteristic nano-properties. Shortly, the first advantage arises from the size-difference ratios between NPs and molecules. Nanotherapeutic platforms are much bigger in size than most of the molecular tools used in medicine (drugs, pro-drugs, targeting agents, antibodies, contrast agents, and so forth), and therefore, the latter can be incorporated into the nanosystems and be tailored to contribute in different ways to the overall activity and safety. Secondly, the unique electromagnetic properties of inorganic materials at the nanoscale can be used in order to trigger some extra-functionalities. Finally, NPs have characteristic pathways and interactions inside the body that differ from those of molecules. Thus, NPs can be used to differentiate pathological from normal tissues.[76]

Figure 1.14. NP functionalities in nanomedicine.

1.3.1.1. Manipulating their functionality

Compared to small molecules, NPs are big enough to include different functional components. Depending on the nature of these molecules, the purpose or effectiveness of NPs can be tuned. Here, we discuss some different functions that can be implemented into the nanosystems using different kinds of molecules (Figure 1.14), and which can have application in the nanomedicine field.

a) Drug solubilization and sustained release. The simplest way to take advantage of the NPs properties in nanomedicine is incorporating drugs within/attached to NPs. Most of the clinical used chemotherapeutic drugs are poorly water-soluble; thus, toxic solvents are administered to patients to increase free drug solubility. When drugs are encapsulated/attached to nanosystems, side effects derived from the inherent toxicity of these solvents can be evaded.[77] Another important consideration is the high drug loading capacity of NPs that allows reducing the exposure to free drugs in excess, thus decreasing potential side cytotoxicities .[78]

In addition, some NPs enable a sustained drug release. In comparison with concentrations of small molecules in the body that fluctuate between the toxic and sub-therapeutic levels, nanosystems may maintain more sustained drug blood concentrations.[79] However it is important to note that even if nanosystems may reduce drug toxicity, some kind of unexpected side effects can arise derived from, for example, nanoparticle accumulation, unspecific biodistribution, undesired bio-interactions, etc.[80]

b) Protection from degradation. Another interesting advantage from the use of nanomaterials is drug protection from enzymatic and mechanical degradation. Some gene-silencing agents such as small interfering RNA (siRNA) or microRNA (miRNA) provide new ways to modulate disease-associated signalling pathways. Although these applications seem to be promising, such molecules are sensitive to ribonucleases that are present in really high concentrations in blood, extracellular space and lysosomes, and which cause a restriction in their therapeutic effectiveness. Also, the negative charge of gene-silencing agents as well as their size difficult a good cellular uptake. Protection of oligonucleotides from enzyme degradation, improvement of their cellular uptake as well as the achievement of lysosomal escape can be possible with some kind of nanosystems´ formulations.[81]

c) Immuno-evasion. Some strategies to avoid the immunological recognition as well as the clearance of NPs from the body are, for example, surface modifications with anti-fouling polymers, self-peptides[82] or cell-derived coatings. A relevant example of this is the stealth PEG polymer, which is clinically approved. NP PEGylation creates a steric barrier that reduces significantly the binding of proteins to NP surfaces and prevents interaction with cells.[83]

d) Combination therapy. One of the most important advantages of nanomedicine is the ability of one unique system to deliver different drugs at the same target cell/tissue. In fact, it is easier to control the intracellular drug concentration when both drugs are delivered using the same nanosystem than

controlling the pharmacokinetics of both individual therapeutic agents separately.[84]

e) Active targeting. This strategy consists of the surface conjugation of molecular targeting ligands onto the NP surfaces, leading to NPs that bind specifically to molecules overexpressed on the surface of the tumour vasculature or cancerous cells. Using active-targeting, NPs can be accumulated in the desired tissue reducing subsequently side, undesired effects in healthy tissues. Despite this, the vast majority of studied targeted NPs have shown some undesired responses. For example, in the presence of these surface ligands, immunological recognition and clearance are usually increased. Also, these targeting molecules increase NPs hydrodynamic radius, causing less extravasation and intratumoral penetration.[85] Finally, when ligands bind strongly to target molecules, the so called biding-site-barrier can avoid NPs diffusion inside tumoral cells.[85]

f) Triggered activation. Some nanomaterials can react to some stimuli in order to change their physical or chemical properties. Consequently, different responses can be triggered as, for example, drug release, imaging, catalysis or some other kinds of therapies. These stimuli may come from the own biological target where the nanosystems must exert their action (endogenous stimuli), but also electromagnetic irradiation (light, magnetic fields) or ultrasounds can be used as exogenous stimuli (further explained in detail in section 1.3.2). Endogenous stimuli are based in some characteristic properties from the tumour environment as, for example, temperature increases, lower pH values, higher levels of glutathione[86] (an antioxidant peptide that prevents damage of cellular components caused by reactive oxygen species), redox reactions[87] or an elevated number of enzymes[74]. These triggers generate some desired changes in the nanosystems, as for example, a controlled degradation via different ways (*e.g.*, pH or enzymatic), heat production/light emission from NPs or drug release from the NP cavities.

1.3.1.2. Exploiting mass transport characteristics inside the body

In contrast to small molecules, NP transport within the body is more dependent on vasculature properties than in the case of free drugs. Characteristics of the vascular system will vary depending on the development stage, organ type and disease condition. Vessel diameter, blood flow velocity and vascular permeability vary depending on the physiological function of the tissue.[76] Apart from organ-specific vasculature, drugs are small enough (less than 1 nm in size) to overcome all these barriers and widespread all over the body easily and, importantly, they can be finally eliminated by the renal or hepatic system. Patient side effects and low efficiencies of some therapies are the main consequence of the latter. When using NPs, much larger in size than free drugs,

transport is more dependent on vasculature properties, making barriers more critical. A huge amount of NPs are retained in the liver due to vascular fenestrations and macrophages,[88] since the cutoff size for renal clearance is ca. 5.5 nm.[89] So, smaller NPs are efficiently cleared and do not widespread all over the body, while bigger ones can be retained by other organs like the liver, spleen or lungs.

Oncophysics transport refers to new designs of drug delivery nanocarriers that take advantage of the unique transport properties of tumors.[90-92] Understanding the movement of NPs within different vasculature systems inside the body is a key factor. Once a tumour has grown beyond 2-3 mm in diameter, a new vasculature network is formed really fast (compared to healthy tissues) to maintain tumoral cells needs satisfied as gas, nutrients and waste exchange.[93] These blood vessels have relevant differences compared to healthy ones. Due to the high ratio of growth, they are usually arranged as disorganized networks with immature structured such endothelial porous fenestrations. These pores, known as *fenestrae* ("windows" in Latin), up to 500 nm in diameter,[94] can be exploited to increase drug accumulation in tumours. The enhanced permeability and retention effect (EPR) as well as hemodynamics, are the most well-known phenomena used to take advantage of abnormal tumour vasculature structure for drug delivery-based NP therapeutics.

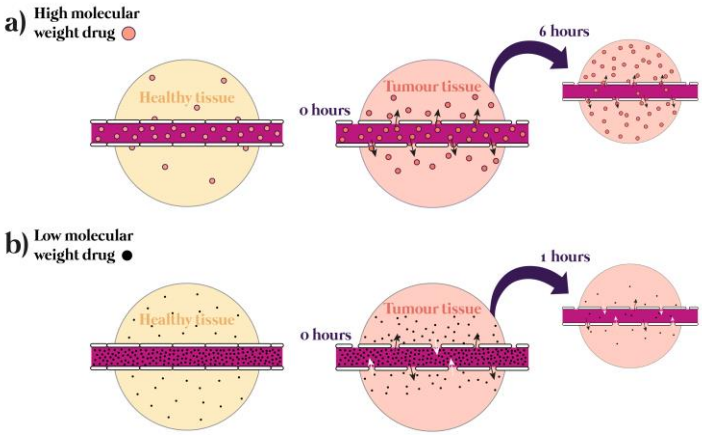

Figure 1.15. Illustration of the EPR effect.
It relies on the molecular weight of molecules.[95]

Enhanced Permeability and Retention effect. The EPR effect was first described in 1986[96-97] and, nowadays it is a controversial issue. In general, molecules are supposed to accumulate to larger extents in tumour tissues than in normal ones in a size-dependent fashion (Figure 1.15). This effect is thought to be a consequence of vascular fenestrations (structural gaps in the vessel walls)

as well as poor lymphatic drainage of the tumoral vasculature due to the lack of lymphatic vessels. Outstanding bioaccumulation data from clinical approved nanoformulations (as liposomes[98] or polymeric NPs[99]) are thought to being promoted by this effect. However, a notable heterogeneity of results reporting the amount of accumulated nanomaterial by tumour weight among individuals is noted.[100] One important factor that can lead to this variability relies on tumour size:[101] the bigger the tumoral tissue is, the larger necrotic areas lacking vascular functionality are. Consequently, a lower NP accumulation by weight is found. As commented previously, another relevant factor is the vasculature density. The higher this density is, better extents for nanomaterials accumulation are found.[102] Despite this, the EPR effect is still not fully confirmed with NPs due to the high complexity of biological tissues. Many other different factors consequence of the complexity biological complex may also contribute to NP accumulation in tumours.[103]

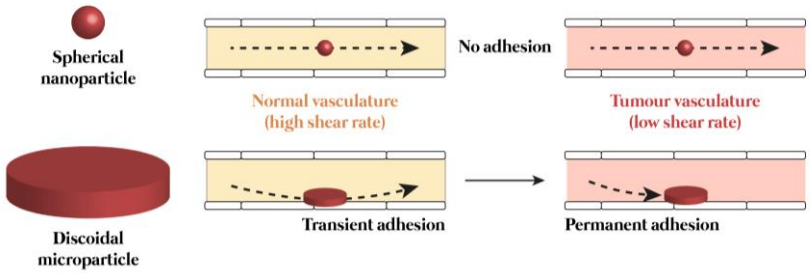

Figure 1.16. Hemodynamic-based tumour targeting.[76]

Hemodynamic-based tumour targeting. Tumoral vasculature is much more disorganized than that of healthy tissues. This leads then to blood flow abnormalities. The fluid flow through a tube can be expressed as the *shear rate*, which is calculated based on the tube diameter and fluid velocity. It is demonstrated that shear rates of tumoral vessels are lower (less than 100 s^{-1}) than those in normal ones (higher than 100 s^{-1}).[104-105] Taking this into account, NPs can be designed in order to promote better adhesions to the vessel walls. With normal shear rates, spherical NPs tend to follow the streamline while discoidal ones flow closer to the walls.[106] When this rate is decreased, no significantly changes are expected for spherical NPs, whilst disc shaped ones can tune their pattern of adhesion due to their much larger parallel surface area (Figure 1.16).[104, 107] As an example of this, platelets have a discoidal morphology.

1.3.1.3. Taking advantage of electromagnetic properties

Some types of inorganic NPs can interact with different wavelengths of the electromagnetic spectrum and other different stimuli (as sound waves or electric and magnetic fields). Different physical and chemical mechanisms of

interaction can occur between photons and electrons from these materials, providing the nanosystems with a library of controlled responses. This new "activatable properties" can rely on the characteristic nano-size (*e.g.* LSPR) or from the own bulk inorganic material properties (*e.g.* upconversion luminescence). Obtained responses will depend on nanosystems properties (*e.g.* material, crystallinity, size or shape), the nature of the stimulus and its interaction with the nanosystems and the surrounding medium.

1.3.2. Exogenous stimuli for nanomaterials activation

A huge amount of nanomedicine applications for activatable nanomaterials are nowadays an object of study. A range of different kinds of therapies such as chemo-, gene-, photothermal or photodynamic-based therapies, and a variety of imaging diagnosis techniques have been improved or designed using activatable nanosystems. It is important to note that new advances are focused on designing multifunctional nanomaterials that combine properties for simultaneous therapy and diagnosis (*theranostics*).

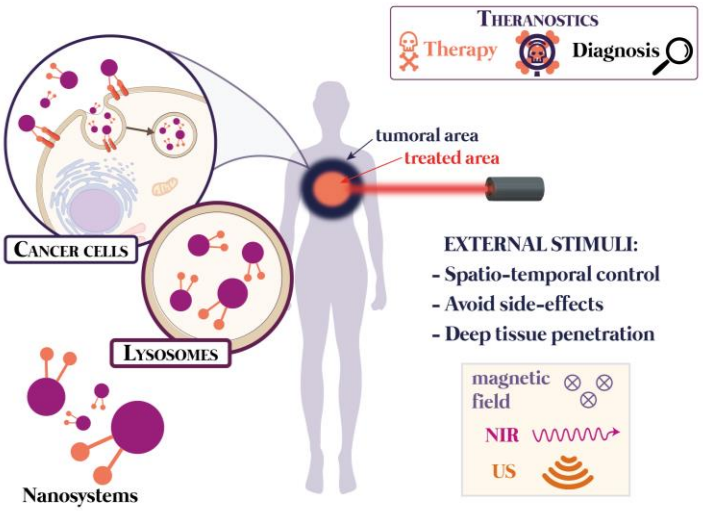

Figure 1.17. Different external stimuli to activate nanosystems for therapeutic and diagnostic purposes in nanomedicine.

The main advantages of externally activatable NPs in nanomedicine rely on the high spatial and temporal control of the desired response, avoiding undesirable side effects, and allowing for deep tissue penetration and real-time activation (Figure 1.17).

As a general concept, radiation is the emission or transmission of energy in form of waves or particles through the vacuum or a material medium. The nature

of waves (*e.g.* electromagnetic, acoustic) and their energy will define the interactions between the body, which acts as a "filter", and the nanosystem, the main target of this radiation. For nanomedicine purposes, the interaction between the addressed stimuli and the biological tissues should be minimized as much as possible, choosing the best properties and energies for these waves to avoid unwanted effects (*e.g.* heating or ionization). Of course, not all external sources can generate responses in all kind of nanomaterials so both interactions, radiation-body and radiation-NPs, should be taken carefully into account. Radiation must have the ability to specifically initiate and control the NP therapeutic or diagnostic effects in the target region (*e.g*. tumour) with as low as possible side effects to adjacent healthy cells, tissues or organs. In the following, we are going to discuss how electromagnetic and acoustic waves as well as alternating magnetic fields interact with the body, and their huge and promising applicability in biological purposes.

In this section, we are going to discuss electromagnetic radiations (focusing on visible and near infrared wavelengths), magnetic fields and ultrasounds as biocompatible external stimuli. In addition, different activatable nanosystems and their applications in nanomedicine will be further explained, as examples.

1.3.2.1. Electromagnetic waves: photoactive and plasmonic nanomaterials

Electromagnetic (EM) waves are emitted by electrically charged particles undergoing acceleration. These charged particles could be, for example, photons or electrons that will interact with materials. They are transversal waves (wave propagation and oscillations are perpendicular among them) and classically, they consist of synchronized oscillations of electric and magnetic fields (Figure 1.18).

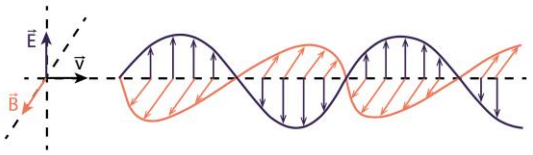

Figure 1.18. Electromagnetic transversal wave.
Propagation velocity, electromagnetic and magnetic field are perpendicular one each other.

We are going to consider the penetration depth of the waves (that is, how much of these waves can travel through a material maintaining its energy) and the possible unwanted effects on biological tissues. Due to this, only some wavelengths from the complete electromagnetic spectra (Figure 1.19) are suitable as external stimuli in nanomedicine.

The body is completely transparent (do not absorb or scatter light) for *radio wave*s (> 10^{-1} m) due to the low energetic photons and enormous wavelengths

compared to body size. *Microwaves* (10^{-1} m to 10^{-3} m) almost are invisible to the body too. Only a tiny amount of radiation is absorbed, which rotates molecules and contributes to heating. Nevertheless, they have quite low spatial specificity (too big wavelengths) for extended nanomedicine performance.

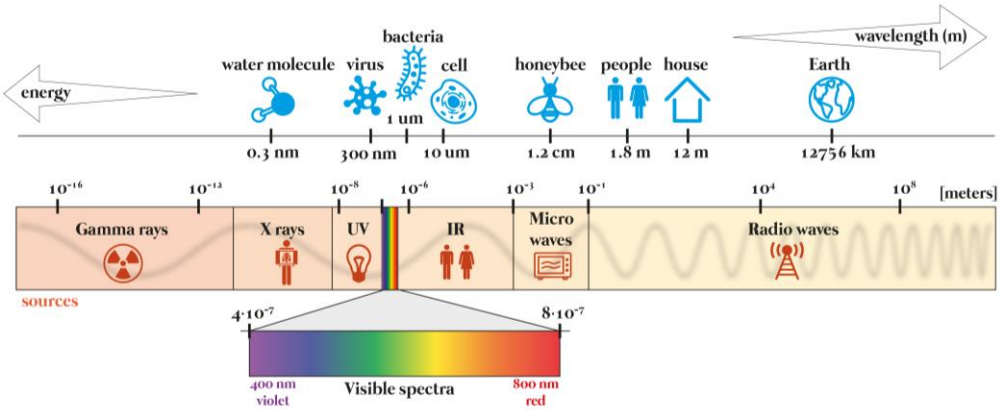

Figure 1.19. Complete electromagnetic spectrum classified in terms of wavelengths. In blue, size comparison between EM waves and common things; in red, sources of different types of radiation.

At the other end of the EM spectra, we found *X-rays* (10^{-8} m to 10^{-12} m) and *gamma radiation* (< 10^{-11} m). On the contrary to radio or microwaves, this kind of radiation has quite short wavelengths and really high energies. The body is relatively transparent for these waves because atoms cannot absorb so much high quantum energies. Consequently, they remain intact and no heating effects are found in biological materials. Nevertheless, their small wavelengths can be compared in size to atoms and molecules, causing a direct damage in, for example, nuclear DNA avoiding cell proliferation and inducing potential mutations. This disadvantage can be controlled in order to perform *radiotherapy*, which is nowadays one of the most widely used therapies for cancer treatment. X-ray and gamma radiation are also widely used in a variety of diagnosis techniques, such as *X-ray imaging* (imaging technique based on difference in X-ray absorption by different tissues) or *Positron Emission Tomography* (PET, based on the detection of emitted gamma rays from special radioactive materials/molecules inside the body). Other techniques based on all the possible effects that occur when highly energetic radiation interacts with matter (photoelectric and Compton effects, pairs production, etc.) are commonly used in the clinic. All these possibilities and their implementation in the medical field, in therapy as well as in diagnosis, are the main object of study of *medical physics*.

The *ultraviolet* and *visible* middle part of the electromagnetic spectrum ($4{\cdot}10^{-7}$ m to 10^{-8} m for UV and $8{\cdot}10^{-7}$m to $4{\cdot}10^{-7}$m for visible) could be amazingly

used for the activation of a huge amount of organic molecules (*e.g*. fluorophores) and NPs. UV-Vis is, however, strongly absorbed by body tissues because it causes electron jumps in higher electronic levels, leading to strong tissue autofluorescence and avoiding deep light penetration. As a consequence, penetration depth of this light in biological tissues is limited by only a few micrometres to 1 millimetre.[108]

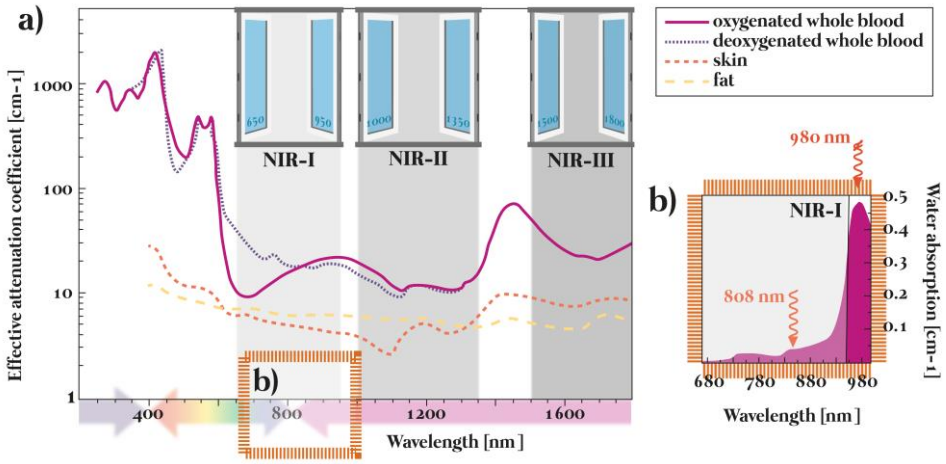

Figure 1.20. Absorption spectrum of human skin.
Image shows the first (NIR-I), second (NIR-II) and third (NIR-III) biological windows; b) zoom-in of the two first optical windows in most relevant biological tissues and fluids. Plots represent the effective attenuation coefficient (on a log scale) *versus* wavelength (in nm).[108-109]

Due to this, the *InfraRed* and *Near-InfraRed* (IR and NIR, from 10^{-3} m to 10^{-6} m) wavelength range becomes the best option for biological applications due to their highest power of penetration inside tissues (from several mm to cm), the relatively low heating-associated effects, and high spatiotemporal localization of the external stimulus application. It is important to note that these wavelengths can induce a vibrational state in molecules, leading to unwanted tissue heating too. Depending on this unspecific heating (for example, promote by water NIR absorption) and the energy penetration depth, that will be defined by the absorption of the material, some NIR-IR wavelengths are more suitable as external biological stimuli than others. For this, the so-called *biological windows* were defined. In Figure 1.20 the absorbance spectra of blood elements and water are shown as a function of IR and NIR wavelengths. The first, second and third biological windows lie in the ranges [650-950] nm, [1000-1350] nm and [1500-1800] nm, respectively.

Plasmonic nanomaterials. In the framework of Drude's model, metals are made of heavy, static, positively charged ions immersed in a cloud of light,

negatively charged and easily mobile electrons, which form an electron gas (plasma) that follows the Maxwell-Boltzmann statistics. The natural frequency of a free oscillation of this plasma is called the plasma frequency. *Plasmons* (or volume plasmons macroscopically) are the quanta associated to these charge oscillations.

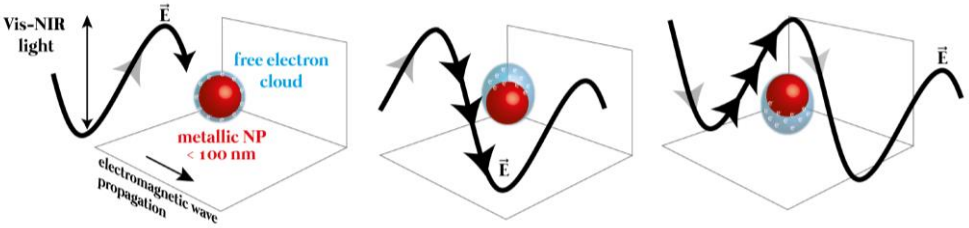

Figure 1.21. Localized Surface Plasmon Resonance in plasmonics nanomaterials. Produced when the electrical field of an electromagnetic wave interacts with its electronic free cloud.

Following the so-called Drude's model, how EM waves interact with metals can be defined considering effects only from electrons that are in the metal conduction band. Here, we are not going to discuss this model in detail, but stated in simple terms, it treats this electronic gas from metals in the framework of the kinetic theory of gases taking only into account electron-ion collisions. Considering the properties of the material and media, the characteristics of incident EM waves and the properties of the electronic cloud, some metallic phenomena can be explained.[110] In the context of this work, we are going to focus on the LSPR, as the characteristic phenomenon that take places when EM waves interact with metallic materials at the nanoscale.

When a light beam impinges on a plasmonic NP much smaller in size than the incident wavelength, the incoming electric field can make free electrons to collectively move away from the metal particle in one direction, creating a dipole than can switch its direction with a change in the direction of the electric field. Therefore, this electronic cloud will start to oscillate in resonance with the incident wave (Figure 1.21). The frequency and amplitude of this resonance is sensitive to the particle's composition, size and shape, which determine how the free electrons are distributed and subsequently polarized on the particle surface. Also, since the penetration depth of an EM wave in a metal surface is limited (less than 50 nm for Ag and Au), only plasmons caused by surface electrons are significant, and they are referred to as localized surface plasmons.[43]

Plasmonic NPs are capable of absorbing and scattering light at highly specific regions of the EM spectrum. Optical properties of plasmonic NPs (LSPR, absorbance and scattering) are determined by the particle's extinction cross-sections, which can be obtained by summing the particle absorption and scattering cross-sections. When particles interact with each other (interparticle

collisions), their scattering cross-sections are only related to their geometric size. On the contrary, when particles interact with radiation composed by quanta (*e.g*. light), their scattering cross-sections, or the probability of light and NP interaction to occur, will depend on the particle size, geometry and relative positions. Taking this into account, LSPR are responsible of different physical phenomena related to light-particle interactions. They possess a strong and well defined absorption peak of light at the LSPRs maximum,[111] the colour of colloidal solutions of noble metals NPs can change due to far-field scattering (scattering of light at distances larger than NPs dimensions),[112] and the near-field scattering is the responsible of an increase of light concentrations in the close surroundings of the NPs.[113]

An extensive library of different plasmonic NPs of several sizes, shapes and materials (mostly noble metals like gold, silver, platinum, palladium, titanium or copper) have been developed for many bioapplications (the so-called *bioplasmonics* field), including different light-activated therapies and diagnostic techniques. They can be used as nanoantennas or nanotrasducers, which can be remotely (wirelessly) activated using light from outside the body. The variety of responses like nanoheating, reporting reactions (binding, aggregation, etc.) or surface-enhanced signals (surface-enhanced Raman, fluorescence and IR absorption spectroscopies) will depend on the excitation wavelength and NPs properties. The nanoplatform characteristics (material, NPs size and shape, coatings and functionalizations, excitation wavelength, etc.) should be chosen taking into account the final objective.[43]

Plasmonic nanomaterials in theranostics. Controlled localization of the electric field in plasmonic NPs has favoured the development of *biosensing* platforms capable of detection in biological complex scenarios. When analytes attach to the NPs surfaces, some NPs properties change like size and shape, leading to scattering, absorption and LSPR variations. Measuring such alterations allows for the quantitative detection of analytes.

Moreover, in the therapeutic field, plasmonic NPs can be remotely activated for heating-triggered drug delivery and *photothermal therapy* (PTT). Both techniques are based on the local heating produced around NPs when light impinges the NP and is used to excite their LSPR, which decays both radioactively and non-radioactively. In brief, the first radioactive decay radiates the electromagnetic energy at the same frequency as surface plasmon oscillations, it constitutes the elastic/Rayleigh scattering by the NP and it has a key role in NP emissions and plasmonic enhancements. The second one constitutes the light absorption by the NP and, as a consequence, it is the one responsible for generating electrons (photoelectric effect) with very high kinetic energies, *hot electrons*, which eventually contribute to a local heating.

This local heating can be used to *release drugs* from different plasmonic cavities or surfaces[17] or to perform *hyperthermia*.[114]

Hyperthermia is the elevation of temperature above the physiological level with the objective to achieve a therapeutic gain. Tumour cells can be weakened by a mild increment of the temperature prior to other cancer treatment (< 45 °C, the so-called thermo-sensitization process), or they can be simply thermos-ablated (temperature > 45 °C) giving rise to cell necrosis and death. As the main advantage, local heating produced by NPs is a promising possibility to avoid systemic heating. This local heating can be used for various purposes in the context of bioapplications; in this work we are going to discuss two different ones.[43] (chapters 3 and 1).

Photoactive nanomaterials. Luminescence is a process by which susceptible molecules emit light from electronically excited states created by a physical (light absorption), mechanical (friction) or chemical mechanism. When luminescence is generated through excitation of a molecule by any kind of light, the phenomenon is termed *photoluminescence* (PL). Different effects of PL can occur depending on the electronic configuration and vibrational states of the excited molecule/NP and the emission pathway.

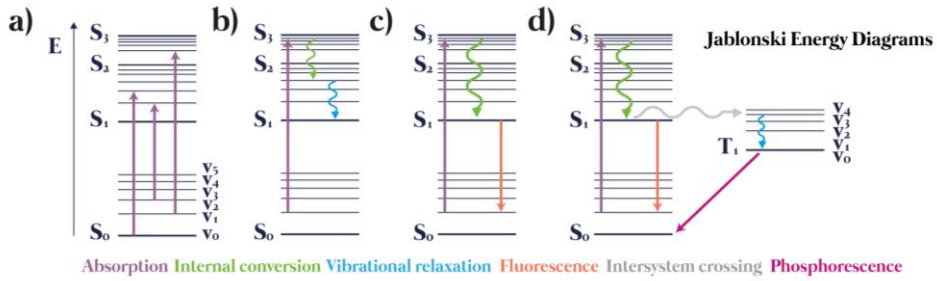

Figure 1.22. Jablonski diagrams.
They represent energetically and schematically a molecule energy levels. Different decay processes which occur when the systems absorb photons are represented, from right to left: absorption, internal conversion and vibrational relaxation, fluorescence, intersystem crossing and phosphorescence, respectively.

The electronic levels of a system are defined in the *Jablonsky energy diagram*, showed in Figure 1.22. When atoms start to bond each other, each electronic state is further subdivided into several *vibrational energy levels* associated to bonding orbitals and nuclei. Here, atoms vibrate in a standing wave manner with different frequencies. Once the system absorbs energy from a photon, several decay processes will occur with varying probabilities and velocities or, in other words, relaxation times (Table 1.2). The most likely will be the relaxation to a lower vibrational energy state. These processes can be *internal conversion* or *vibrational relaxation* (Figure 1.22), both laying in the loss of energy in the

absence of light emission, and occurring much faster than photon emissions.[115] Vibrational relaxation occurs between vibrational levels so electrons will not change their initial electronic level. On the contrary, if vibrational energy levels strongly overlap electronic energy levels, a possibility exists that the excited electron can transition from a vibration level in one electronic state to another vibration level in a lower electronic state. This is called the internal conversion but mechanistically is identical to vibration relaxation.

Taking this into account, the Franck-Condon principle states that when a change in the electronic state of some molecule is caused by the absorption of a photon, the extra energy goes into an increase in the energy of the vibrational modes of the molecule. Stated in simple terms, the photon energy transforms into molecule's kinetic energy before a PL process. Also, it is interesting to note when the absorbed photon contains more energy than the necessary for a simple electronic transition, the excess is usually converted into vibrational energy. When a material displays the so-called *Stokes shift* between the absorption and emission maximum spectral peak, it means the emitted radiation has lower energies than the absorbed one due to the former effect, as expected.

Transition	**Time scale [s]**
Absorption	10^{-15}
Internal conversion	10^{-14} - 10^{-11}
Vibrational relaxation	10^{-14} - 10^{-11}
Intersystem crossing	10^{-10} - 10^{-8}
Fluorescence	10^{-9} - 10^{-7}
Phosphorescence	10^{-4} - 10^{-1}

Table 1.2. Average timescales for radiative and non-radiative processes.[116]
The faster the transition, the more likely it happens.

A slower relaxation process is *fluorescence* (Figure 1.22). It occurs more often between the first excited electronic state and the ground state. This happens because when relaxation occurs between other energetic levels, it is more likely that energy will be dissipated through internal conversion and vibrational relaxation.

Finally, another process by which systems can dissipate their absorbed energy is *intersystem crossing processes*, the slowest and the less probable one (Figure 1.22). Selection rules make this transition forbidden, but considering in addition the vibrational factor, it becomes weakly allowed and able to compete with the time scale of fluorescence. Different interesting routes back to the ground electronic state appear at this moment. One example is *phosphorescence* (when a radiative transition from an excited triplet state to a singlet ground state occurs), a very slow and forbidden transition.

A huge variety of photoluminescence materials with Stokes shifts have been designed. The most used ones are organic dye molecules or fluorophores, that is, organic molecules with fluorescent properties. They are quite versatile because they can be designed with many different structures and properties, and can be attached to NPs, antibodies, drugs, and cell components. The main problem for their bioactivation is their lack of absorption into the biological windows because, typically, they can be activated only by UV and visible radiation. Going to nano, QD made of semiconductor crystals are the kings of fluorescent nanomaterials. They possess extremely high quantum yields. This quantity gives us an understanding of how efficient the material is to transform absorbed photons into emitted ones. Also, their tunability,[117] their sharp emissions bands[118] and possible emissions in the IR[119], are others of their main advantages. Nevertheless, their high toxic profiles due to the presence of heavy metals, such as cadmium or lead, restrict their biological/medical applicability in living organisms.

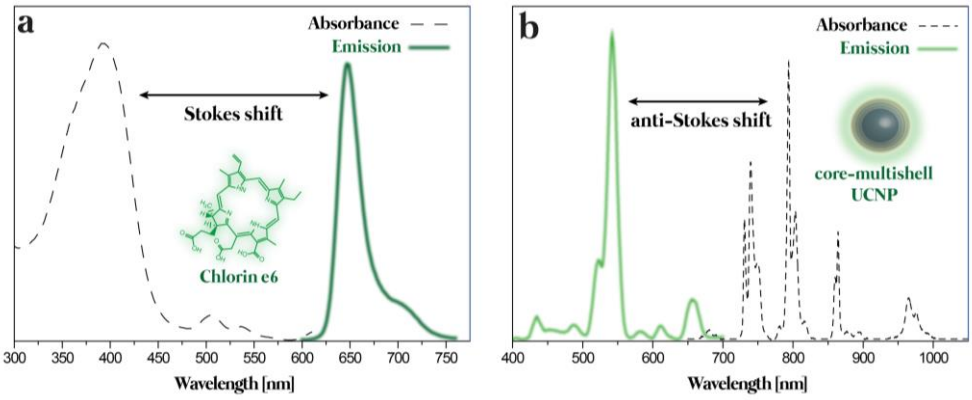

Figure 1.23. Stokes and anti-Stokes shift in photoactive materials.
a) Chlorin e6, organic molecule that can be used as photosensitizer, and b) core-multishell UCNPs doped with neodymium. Data obtained experimentally.

In contrast, other materials can transform low energetic photons into higher energetic ones, presenting a peculiar *anti-stokes* shift (Figure 1.23). *Upconversion (UC) materials* (bulk and nanosized) present these unique properties that lead to completely different processes of radioactive and non-radioactive decays.[120] Some of the extra-energy needed for this upconversion effect happens, comes from dissipation of thermal phonons in a crystal lattice, cooling the crystal in the process.[121] Apart from the NIR activation possibility and quite large anti-Stokes shifts, other advantages of *upconverting nanoparticles* (UCNPs) are their really low photobleaching, narrow band emissions, absence of autofluorescence, high photostability, or no citotoxicity caused by the materials they are made of.

Photoactive nanomaterials in theranostics. Most of the nanomaterials show Stokes shifts (QDs and common fluorophores). Despite all the other fluorescent properties like photobleaching, photostability, and quantum yield, anti-stokes shifts make activation through the biological windows possible with a subsequent emission in the UV-Vis region. In addition, avoiding excitation in the UV-Vis range precludes the huge problem of tissue autofluorescence. Lots of proteins from the biological media have fluorescent properties when being excited with these wavelengths, causing a relevant background noise (Figure 1.20). In spite of a huge amount of useful applications for fluorophores and QDs have been successfully developed -as excellent imaging probes for bio labelling-, these kinds of limitations are still present.[9]

In this section, we are going to focus on UC activatable materials designed for being activated within the biological windows and with emissions in the UV-Vis range. An anti-Stokes shift is needed to obtain this desired response. This is the most characteristic property of UCNPs. They have allowed the scientific community to take profit of all the advances along last years about UV-Vis emitting materials at higher tissue depths using the characteristic activation-emission properties of UCNPs. These nanomaterials may produce ultraviolet and visible light inside the body, which has been impossible to be reached with another non-invasive way.

For example, *photodynamic therapy* (PDT) is a widely studied and highly efficient therapy which can be benefited from upconversion processes. PDT consists on ROS generation (*reactive oxygen species* which cause irreversible intracellular damage) inside the tumour. *Photosensitizers* (PS) are molecules or nanomaterials which can absorb the energy from radiation in a specific wavelength range. Consequently, they turn into a high unstable state and, then, transfer energy to surrounding oxygen molecules. The most significant effect is ROS generation to damage nearby biomolecules, although they also can convert absorbed energy into heat, raising local temperature, and can emit photons forcing the activated material turn back to the ground state. The main drawback of PDT is that PS agents get activated in the same way that normal fluorophores. To solve such drawback, UCNPs are being combined with PS to perform PDT with spatial-temporal controlled activation.[122]

Another kind of applications of UCNP in theranostics are being implemented. For example, they are used like "nanotorches" inside the organism.[123] This opens a new world of possibilities. Visible light can initiate many kinds of reactions like photo-isomerization, photo-crosslinking/decrosslinking, photosensitized oxidation, light-triggered polarity switching, photodegradations and photocatalysis that can be used for designing more specific nanoplatforms.[124]

As an example of an interesting brand-new field using UCNPs optical properties is *optogenetics*. Membrane ion channels are ultimately responsible for the propagation and integration of electrical signals in the nervous, muscular and

other systems. Their activation or malfunctioning plays a significant role in physiological processes. These channels may be genetically modified to be regulated by light-sensitive proteins. The functionality of these proteins can be triggered with light, so UCNPs can be tuned and designed with this aim.[125]

Finally, emissions from photoactive materials are quite useful tool to record information of biological entities ranging from individual cells to tissues and organs as *imaging probes*.[126] QDs and fluorophores are widely used in many types of bioimaging techniques collecting their characteristic emission peaks to detect the desired target. UCNPs photoluminescence have low quantum yields in comparison with their stokes-shifted neighbours so, understanding emission processes are still a challenge to improve their performance in these applications.[127] Even that, their possible activation inside the biological windows opens the field to deep tissue fluorescence imaging. Different UCNPs have been manufactured for application in UC luminescence optical image-guided cancer therapy.[128] In addition, another interesting property of UCNPs is that their photoluminescence is temperature-dependent; thus, several studies have been focused on using these nanosystems as thermometers inside living cells.[129]

1.3.2.2. Alternating magnetic fields: magnetic nanomaterials

The *magnetic field* is a region around a magnetic material or a moving electric charge within magnetic force acts. It is generated by electric charges in relative motion as well as by magnetic materials (*e.g.* permanent magnets or the Earth by itself). Depending on the current used to generate the magnetic field (direct, DC, or alternating, AC), *static* or *alternating magnetic fields* (AMF) can be obtained.

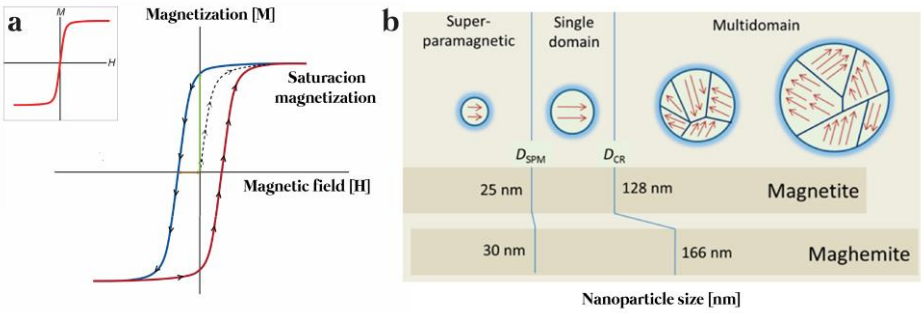

Figure 1.24. Magnetization effects in magnetic nanomaterials.
a) Magnetization as a function of the applied magnetic field: hysteresis curve for ferromagnetic materials (red line in the upper-right zoom-in represents the superparamagnetic case); b) superparamagnetic domains (schematically) when reducing the size of bulk magnetic materials, magnetite and maghemite are represented.

The outcome of this stimulus is based on the response of materials to the presence of magnetic fields. All the materials are magnetic to some extent

depending on their atomic structure and temperature. Electrons circulating around atomic nuclei or rotating positively charged atomic nuclei have magnetic dipoles, also called *magnetons*. Nevertheless, depending on the arrangement of these dipoles, they may cancel each other and as a result the material will not have magnetic dipole. In other case, the atom will have a permanent magnetic dipole (iron atoms are a good example) with a strength given by the magnetic dipole moment[130].When an external magnetic field is applied to the sample, magnetic moments of the protons tend to align and a total magnetization of the material occurs. The relation between the magnetization (M) and the magnetic field (H) is related through a proportional constant called susceptibility (χ) following $M = \chi \cdot H$. Magnetic materials can be classified in terms of their susceptibility or, in other words, how their magnetization changes with and without application of an AMF.[131] *Diamagnetic* and *paramagnetic* materials remain their magnetic properties stable with and without magnetic field. *Ferromagnetic* materials change their magnetization when field is applied. After that, magnetization does not disappear and a characteristic hysteresis loop (in the H vs M curve) appears (Figure 1.24).

Magnetic nanomaterials. Application of these types of materials in nanomedicine is focused on how the previously mentioned material magnetic moments align and misalign with the applied magnetic field. On one hand, when an AMF with a resonant frequency capable to transfer energy to protons, is applied, it will rotate the magnetic dipoles to be aligned in resonance with the stimuli. Once the *radiofrequency* pulse (RF) is removed, the protons will recover their initial states after a relaxation time depending on the surrounding tissues.

After the application of RF pulses, relaxation times can be measured. In this regard, there are two types of relaxation times. The first one is the longitudinal or spin-lattice relaxation time (T_1) and it is related to how fast the magnetization parallel to the static magnetic field recovers after a perturbation applied to the system. Protons with shorts T_1 recover full magnetization along the longitudinal axis quickly and produce high signal intensities. In contrast, high T_1 impede to recover the full magnetization before another RF pulse and, for that, a lower contrast intensity is obtained. The other relaxation time (T_2) is the spin-spin relaxation and it is related to the transverse relaxation. This means how fast the magnetization in the perpendicular plane to the static magnetic field loses coherence. This coherence has its origin during the RF pulse when proton nuclei are in phase each other. After the pulse, the magnetic fields of all nuclei interact each other, energy is exchanged between them. As a consequence, the nuclei loose their phase coherence and tend to spin in a random fashion: T_2 is a measure of this loss of coherence after removing the RF pulse.[132]

For instance, relaxation times are the key factor in *magnetic resonance imaging* (MRI). Soft tissues have endogenous contrast by itself (Figure 1.25) due

to the differences in proton densities, which cause different values of T_1 and T_2. However, in some cases this contrast is not enough and to enhance it by increasing the applied magnetic field, data acquisition for longer times or the use of contrast agents are needed. In this regard, the use of magnetic NPs (MNPs) as contrast probes is a promising option.[131]

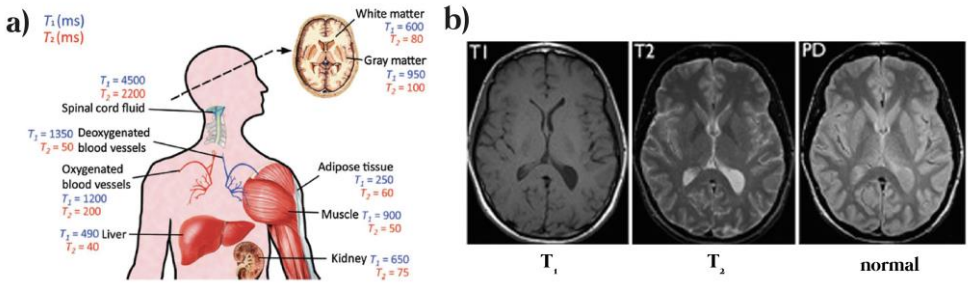

Figure 1.25. Biological differences between T_1 and T_2 contrast agents.
a) Relaxation time values for different organs and parts of the body (Copyright © 2011, American Chemical Society).[133] b) Examples of T_1-weighted, and T_2-weigthed and normal weighted-MRI imaging of a human brain (adapted from ref. 121).[134]

Finally, the size of a bulk ferromagnetic material can be reduced below the superparamagnetic diameter D_{SPM} (few tens of nanometres, Figure 1.24), to obtain a *superparamagnetic nanomaterial*. When the external magnetic field is applied, these materials become magnetic, but they return to a non-magnetic state when the external magnetic field is removed. Two ferromagnetic materials, magnetite and maghemite, can be reduced to the nanometre scale in order to obtain superparamagnetic NPs: 25 nm for magnetite and 30 nm for maghemite. Because of this, magnetic nanomaterials have different values of T_1 and T_2 than biological tissues, and they can be used promisingly in nanomedicine applications.[135]

Magnetic nanomaterials in theranostics. Thanks to afore mentioned these characteristic properties of magnetic nanomaterials in comparison with biological tissues, magnetic NPs (MNP) can be used in many biological applications.[131]

Magnetic fields, static and alternating ones, are not readily absorbed by tissues, and their influence in cell viability was already reported in different studies.[137] Due to its high performance window, remote monitoring or manipulation without physical contact can be performed. Anyway, established limits for biological safety are still controversial, but magnetic fields up to about 10 T are currently used for research in several institutions worldwide (Figure 1.26).[138] In terms of AMF compatibility, high frequencies are considered to be > 100 kHz.[139]

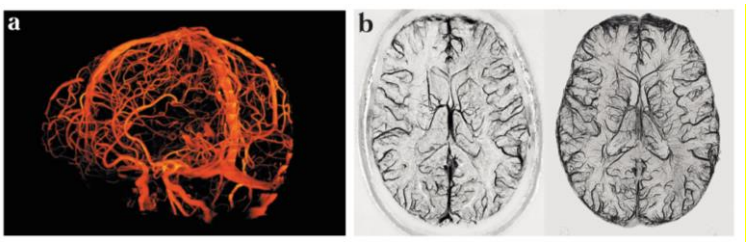

Figure 1.26. Brain images obtained by magnetic imaging techniques.
a) Cerebral blood vessels glow orange. Image generated by a 7-Tesla magnetic resonance imaging scanner at the University of Queensland, Australia; b) the brain of a volunteer is imaged using a 3-Tesla (left) and 9.4-Tesla (right) magnetic resonance imaging machine (Copyright © 2013 Elsevier Inc).[136]

In terms of diagnosis and bioimaging, MRI is an indispensable medical tool due to their real-time spatial resolution and offers a non-invasive option due to endogenous contrast of tissues. As said, MNPs can increase the sensitivity of magnetic resonance signals from tissues background. They can be performed as T_1 or T_2 weighted contrast agents. For example, NPs made of Fe, Gd and Mn are T_1 weighted and superparamagnetic iron oxide NPs (SPIONs) are the most used T_2 weighted. Different images with higher resolutions can be obtained when using these contrast agents due to the different relaxation times values between NPs and tissues (Figure 1.25).

MNPs can also be implemented in some therapeutic techniques. As we already explained, thermal ablation is an interesting technique for cancer treatment which consists on rising tumour local temperature to cause smooth or severe damage in both cells and tissues, and consequently cell sensitization or death. *Magnetic hyperthermia* can be performed with this aim, where the area enclosed by the hysteresis loop is related to dissipated thermal energy.[140] SPIONs are being extensively researched in this field because of their produced heating after AMF application.[131]

Also, in order to overcome the low efficiency of EPR and increase MNPs accumulation in the target tissue, NPs can be magnetically guided to the place of interest (*magnetic accumulation* and *magnetofection*).[141] Apart from that, some nanoplatforms can be activated once they are accumulated in order to produce heat generation for drug release, for example.[142]

1.3.2.3. Acoustic waves. Ultrasonic responsive nanomaterials.

Sound travels as a mechanical longitudinal wave in which displacement of the medium is parallel to the direction of wave travel. *Mechanical waves* need an elastic medium to travel through. Their velocity will depend highly on the material's nature. For example, the sound velocity in air is 343 m/s, in water around 1500 m/s, and over 5000 m/s in iron, respectively. Moreover, waves will

suffer different effects when they arrive to a new medium: reflection, absorption and diffusion are the most significant ones (Figure 1.27).

Ultrasounds (US) are a high frequency part from the sound spectrum (Figure 1.27) above 20 kHz. In nature, human ears can hear sound frequencies between 20 Hz and 20 kHz; elephants can generate and detect sound with frequencies less than 20 Hz for long distance communication; and bats and belugas produce sounds in the range of 20 to 100 kHz for precise navigation.

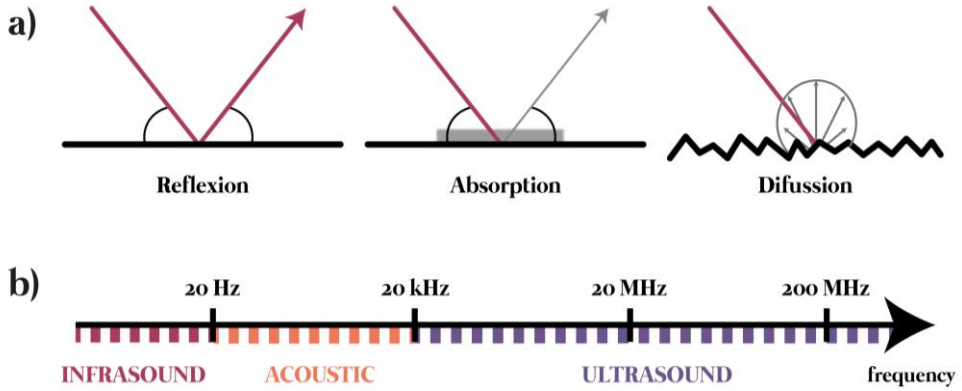

Figure 1.27. Longitudinal waves.
a) Waves suffer different effects when the medium of propagation changes; b) sound spectrum in terms of waves frequencies.

Ultrasounds waves can be generated artificially using the *piezoelectric effect.* Many crystalline materials exhibit piezoelectric behaviour. Normally, the charges on a piezoelectric crystal are exactly balanced, even if they are not symmetrically arranged and electric dipole moments exactly cancel each other. When such a crystal is mechanically deformed (squeezed, twisted or bent), the positive and negative centres are shifted one to each other, breaking this balance.[143] Therefore, total positive and negative charges appear on opposite faces generating an electric current (Figure 1.28); the greater the pressure, the greater the electric current generated. If the crystal is suddenly stretched rather being compressed, the direction of the current will reverse itself. Alternately compressing and stretching the crystal generates an alternating current. When the alternating current matches the natural frequency of the crystal, this will expand and contract at the same time than the alternating current, and sonic waves are generated. The frequency of the waves will be given by the material's piezoelectric nature, and ultrasonic waves can be tuned. This piezoelectric effect will be then the transducer, which transforms electrical energy to mechanical energy (sound waves). These sound waves will be reflected and return to the transducer as echoes, and they will be converted back to electric signals.

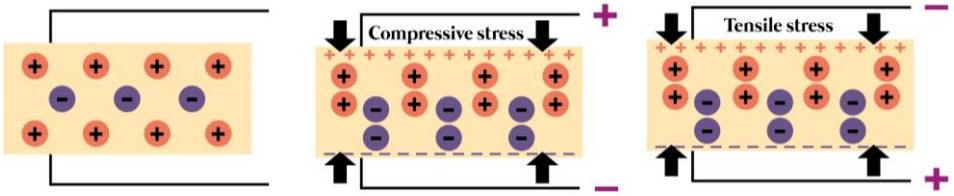

Figure 1.28. Direct piezoelectric effect.

Sonosensitive nanomaterials in theranostics. US application in nanomedicine is an amazing example of multidisciplinary science. In 1942, Karl Dussik, a neuropsychiatrist, and his brother, Friederich Dussik, a physicist, described ultrasound as a medical diagnostic tool to visualize brain structures. Nowadays, US are used in medicine as a non-invasive tool, which allows spatiotemporal control with millimetre precision. The basis of ultrasonic-responsive nanomaterials relies on the velocity of the sound inside the body and the tissue-reflected waves. This magnitude depends directly on the medium properties and how it affects the wave propagation, as already explained. The average propagation speed in soft tissues is 1540 m/s and the penetration depth depends directly on the wave frequency (*e.g.* 20 cm in tissue for a 1 MHz ultrasound waves). However, ultrasound cannot penetrate lung or bone tissues. Measuring echoes from emitted waves (like belugas do with fishes in the sea, Figure 1.29) allows us to make body tissues maps.

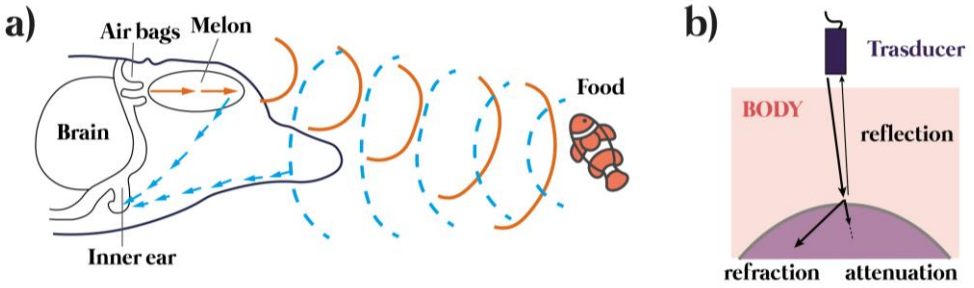

Figure 1.29. Schematic representation of ultrasound interacting with body.
a) Beluga's geo-localization, and comparison with a real ultrasound system for biological applications in b).

These ultrasonic waves are biocompatible due to the absence of ionizing radiations. They have quite high wavelengths, low frequencies and low energies corresponding to the micro and radio waves parts of the electromagnetic spectra (see section 1.3.2.1). The facile regulation of tissue penetration depth by tuning frequency, duty cycles and exposure time makes it highly adaptive for medical purposes. Despite this, it is a non-invasive imaging mode which allows spatial-temporal control with millimetre precision, and US-contrast agents can improve

considerably imaging resolution. Solid inorganic NPs and aggregates have larger acoustic impedance (opposition of a material to the acoustic flow) than soft tissues, being an interesting option for this purpose.[144] Apart from imaging, a focused US beam can induce drug release via localized heating due to accumulation of acoustic energy at the focused region.[78]

1.4. MAIN OBJECTIVES

In the previous sections, the state-of-the-art of nanotechnology with focus on its interaction with the biomedical field was discussed. Characteristic physico-chemical properties consequence of materials size reduction was summarized in section 1.1 as well as the requirements for nanomaterials engineering for biological/biomedical purposes (section 1.2). Finally, the emerging field of activatable nanomaterials and the different external stimuli that can be applied with that aim were detailed in section 1.3.

Nanobiotechnology has been the context along all this work, but we still need to present our main characters: the selected nanosystems. In the following, we are going to introduce the different nanosystems developed in this work. Detailed information about their properties, characterization, final purposes and objectives as well as obtained results will be further explained in the forthcoming chapters.

1.4.1. Upconverting nanoparticles (UCNPs)

UCNPs are inorganic crystalline nanomaterials that convert NIR excitation light into visible and ultraviolet emission one. As previously explained, they show appreciable anti-Stokes shifts (Figure 1.23). The main advantage of using NIR light as external stimuli to activate them is to minimize the autofluorescence background and to enable deeper penetration into biological samples due to reduced light scattering (see Figure 1.20 and section 1.3.2). UCNPs optical properties (absorbance and emissions) can be tuned by choosing their crystal matrix and dopants carefully. Typically, a matrix (*e.g*. $NaYF_4$ or $NaGdF_4$) can be doped with different lanthanide ions (mostly rare earth elements like Yb^{3+}, Er^{3+}, Tm^{3+}, Nd^{3+}, Ho^{3+}…). The *matrix* and *dopants* choice, as well as dopants percentages, will define the UCNP performance. For example, Yb^{3+} is widely used as ~ 980 nm light *sensitizer*, which will transfer photons to the *emitters* (*e.g.* Er^{3+} or Tm^{3+}) by different electronic processes (further explained in Chapter 2). Emitters choice and percentages will define NP emissions or, in other words, the NPs colour (Figure 1.30).[145]

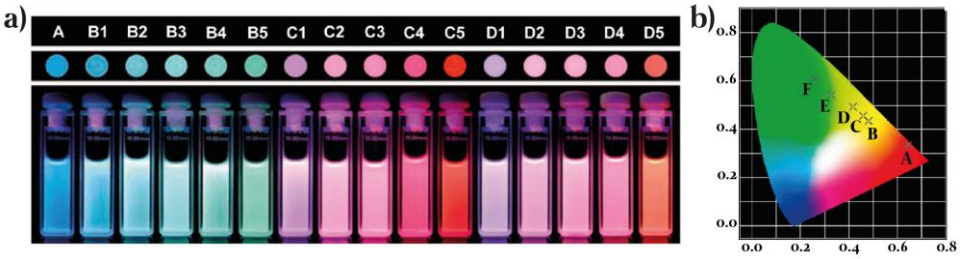

Figure 1.30. Multicolor emission UCNPs.
a) Photographs showing UCNPs luminescence under UV light excitation; b) CIE chromaticity diagram for corresponding UCNPs from a). Reproduced from [146] with permission from John Wiley and Sons.

Nowadays, the vast majority of reported UCNPs are activated by ~ 980 nm light (using Yb^{3+} as sensitizer), which has low deep penetration depth and higher absorbance coefficient with regards to biomolecules and water when compared to ~ 800 nm light.[147] Thus, many new platforms which use Nd^{3+} as sensitizer for ~ 800 nm excitation light are being designed.[148]

Moreover, the UCNPs low performance is still a key factor for improvement because of their low optical brightness or, in other words, their poor quantum yields. Research in this field is focused on strategies to boost upconversion luminescence brightness and efficiencies.[11]

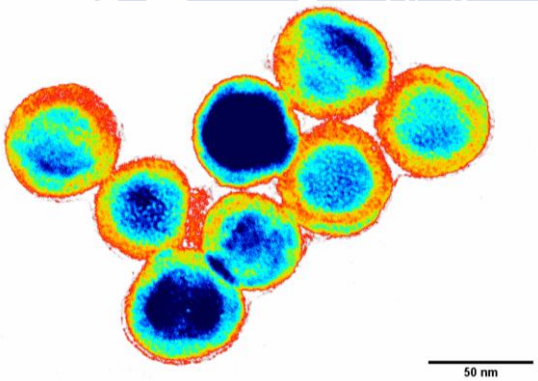

Figure 1.31. Core-multishell UCNP TEM image
The image was treated with ImageJ software.

To overcome those two main drawbacks, in this work we report a synthetic method to produce aqueous stable upconverting nanoparticles that can be activated with 808 nm excitation sources,[149-150] thus, avoiding unwanted heating processes derived from water absorbance at 980 nm. A core-$shell_1$-$shell_2$-$shell_3$ structure made by a layer-by-layer strategy was chosen in order to maintain the monodispersity[151] (Figure 1.31) as well as to improve its efficiency. Importantly, these nanoparticles, once transferred to an aqueous environment using an amphiphilic polymer, remain colloidally stable for long periods of time in

relevant biological media,[49] while keeping their photoluminescence properties. The selected polymer was covalently modified with two FDA (Food and Drug Administration)-approved photosensitizers (Rose Bengal and Chlorin e6), which can be efficiently and simultaneously excited by the light emission of our upconverting nanoparticles.[122, 152-153] Thus, our polymer-functionalization strategy allows producing an 808 nm-activable photodynamic nanoplatform. These upconverting nanocomposites are preferentially stored in acidic lysosomal compartments, which do not negatively affect their performance as PDT agents. Upon 808 nm excitation, the production of ROS [154] and their effect in mitochondrial integrity were demonstrated.

1.4.2. Inorganic NP-MOFs nanocomposites (NC)

MOFs are coordination and crystalline compounds consisting in transition metal cations coordinated with multidentate organic ligands.[155] Due to the cross-linking between the different ions and the ligands, these solids present an extremely well-defined porosity. This is a consequence of the ligand length and coordination sites, as well as coordination number and geometry of the ligands. MOF's basic physicochemical properties (*i.e.*, pore size, distribution and hydrophilicity/hydrophobicity) are key parameters to fabricate efficient drug-delivery systems. Firstly, the pore size determines the upper size limit of the cargo. Secondly, the pore distribution determines the amount of drug that can be loaded. Finally, the chemical nature of the cavity defines the affinity with the cargo and, all the three parameters, the diffusivity of the payload.[155] In this work, we are going to work with nano-MOF, or in other words, MOF that can be considered colloids maintaining their crystal and porous properties but in the nanoscale range size.[22]

Zeolitic imidazolate framework-8 (ZIF8) represents the successful combination of MOF and colloidal science. ZIFs are a subfamily of MOFs with a crystalline topology with large cavities connected through small windows.[22] Along the last years, many synthetic tools have been discovered for ZIF8 production with uniform sizes and morphologies at the nanometre scale.[22]

Even though all ZIF8 advantages, it breakdowns quickly in many water-based solvents, making it incompatible with biological milieus.[156] In order to avoid this fact, we have performed for the first time a polymer-coating protection step in a similar way as it has been widely applied with other inorganic NPs.[17, 49] This provides our nano-MOF with the biocompatibility that it is needed for our final purposes.

Finally, combination of ZIF8 (as a shell) and inorganic NPs (as a core) have been exploited towards the generation of functional nanomaterials with different applications.[157] These kind of nanocomposites (NC) seem a good strategy to promote different types of responses under a given stimulus.[17] In the following

sections, we are going to introduce the two types of NCs that have been developed in this work in order to reach different objectives: *plasmonic NP-MOF composites* for thermo-related responses (chapter 3 and chapter 1), and *catalytic NP-MOF* (chapter 5). We have developed in a reproducible and biocompatible way how to synthesize these NCs and, how after the polymer protection strategy, our NCs are stable in biological media. In addition, we have demonstrated that this approach allows ZIF8 to act as a filter or a sieve for the NP core, allowing some molecules to diffuse in and out through the MOF pores, reaching the active core NP.

1.4.3. Plasmonic NC: gold nanostars (NS)-ZIF8

Plasmonic nanomaterials were carefully discussed in section 1.3.2.1. NS were selected as the plasmonic core (Figure 1.32a) due to their characteristic LSPR, and suitability for excitation with NIR light around 800 nm. This characteristic is quite useful to obtain a good thermal response or, in other words, a high efficient heating using wavelengths within the first biological window. In addition, NS are quite useful to perform SERS, a surface sensitive detection technique, which allows us to detect or "see" molecules on the NS surface with very high sensitivity. Some of the main advantages of this nanocomposites compared to bare NS are the avoidance of NS surface passivation as well as NS aggregation, a more controlled and localized heating thanks to ZIF8 thermal insulation, and the use of the composite the shell as a filter, which not only allows specific molecules to flow till the core (Figure 1.32) but also allow them to go out. In addition, ZIF8 provides the composite with a high encapsulation efficiency.

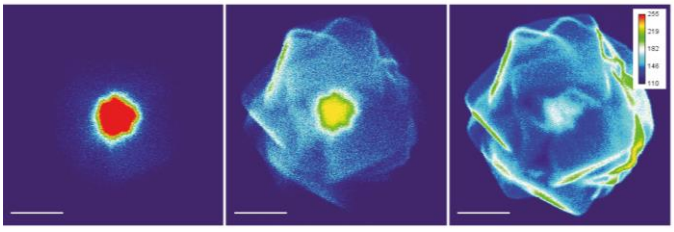

Figure 1.32. Plasmonic core-shell NS/ZIF8 nanocomposite.
SEM images taken with different detectors at different voltages: a) AsB detector (backscattered electrons) at 20 Kv; b) Everhart-Thornley detector (SE2, secondary electrons) at 20 kV; c) InLens detector (SE1, secondary electrons) at 20 kV. Scale bars represent 100 nm. Images were treated with ImageJ in order to appreciate clearly differences between images.

In chapter 3, a plasmonic core-shell NS-ZIF8 nanocomposite was developed for thermoplasmonic-driven release of encapsulated active molecules inside living cells. The NC were loaded, as a proof of concept, with bisbenzimide molecules as functional cargo, and wrapped with an amphiphilic polymer that

prevents ZIF8 degradation and bisbenzimide leakage in aqueous media or inside living cells. The demonstrated molecule-release mechanism relies on the use of NIR light coupled to the plasmonic absorption of the core NS, which creates local temperature gradients and, thus, bisbenzimide thermodiffusion. Confocal microscopy and SERS were used to demonstrate bisbenzimide loading/leakage and NIR-triggered cargo release inside cells, thereby, leading to DNA staining.

In chapter 4, the previous plasmonic NC was used to carry out designed thermal-driven cyclizations inside living cells. As a proof of concept, we chose an intramolecular cyclization reaction that is based on the nucleophilic attack of a pyridine moiety on an electrophilic carbon, a process that requires high activation energies, typically achieved by bulk solution heating at ~ 90 °C, and that has never been performed using photothermal processes. The core-shell nanoreactor (NR) has been designed to include a NS core, which is embedded within a MOF based on a polymer-stabilized ZIF8. Once stored inside living cells, the MOF-based cloak allows an efficient diffusion of reactants into the plasmonic chamber, where they undergo the transformation upon NIR illumination. The reaction, in addition to generate a cyclized fluorogenic product, provides for the future photo-controlled uncaging of bioactive compounds with spatiotemporal resolution.

1.4.4. Catalytic NR: palladium nanocube (Pd-NP)-ZIF8

Many catalytic transformations can be achieved through *transition metal catalysts,* which are especially interesting in the catalysis field. These reactions are usually performed in water-free conditions even though, in recent years, metal-mediated reactions that can take place in complex aqueous environments were exponentially increased.[158-164] Nowadays, *palladium (Pd) homogeneous catalysts* are quite promising in terms of their wide applicability; however, their performance is still compromised by Pd solubility, stability and/or biocompatibility issues.[165-168] Pd-NPs have been studied as *heterogeneous catalysts;*[166] however, two main issues exists. Firstly, in the absence of surface functionalization, NPs tend to aggregate, get passivated by biological components, and suffer from Pd leakage, which leads to toxic effects.[166, 169] Secondly, after NP surface functionalization to avoid these drawbacks, their catalytic activity can dramatically decrease.[46] Due to all these reasons, the achievement of efficient, robust and bioorthogonal Pd-catalyzed reactions in complex aqueous media, and especially inside living cells, represents a major challenge in research at the interface between metal catalysis and cell biology.

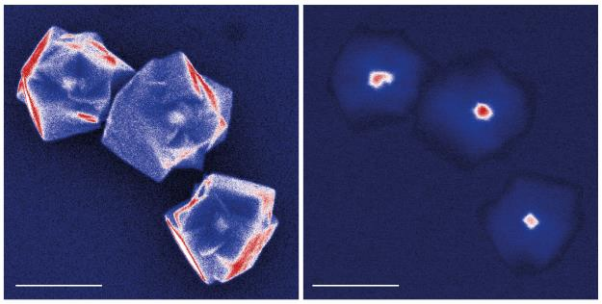

Figure 1.33. Plasmonic core-shell Pd-NP/ZIF8 NC.
SEM images taken with different detectors at different voltages: a) InLens detector (SE1, secondary electrons) at 20 kV and b) AsB detector (backscattered electrons) at 20 kV. Scale bars represent 200 nm. Images were treated with ImageJ in order to appreciate clearly differences between images.

In chapter 5, we report the fabrication of a water-compatible, highly robust NR composed of a Pd nanocube core and a nanometric porous metal-organic shell based on ZIF8. The nanoplatforms are engineered with an amphiphilic polymer, which further warrants their stability in water and biological milieu. The ZIF8-based cloak protects the Pd core from passivation and deactivation, while allowing a suitable diffusion of designed reactants into the catalytic Pd chamber. As a proof of concept, we demonstrated that these catalytic NRs can be used for removing propargylic groups from phenol-derived pro-fluorophores in the biological milieu and inside living mammalian cells. Importantly, the intracellular reactivity of the heterogeneous NRs drastically outperforms that of other heterogeneous systems like pristine Pd NPs, and state-of-the-art homogeneous Pd catalysts. Moreover, they are robust enough to be reused within the same cells, promoting the chemical transformation of recurrent batches of reactants. Finally, we also reported the assembly of tissue-like 3D spheroids containing the Pd NRs and demonstrated that they can also carry out the designed reactions in a sequential, dose-dependent manner. These results set the principles for the development of future "implantable catalytic tissues".

2. UPCONVERTING NPS MEDIATED PHOTODYNAMIC THERAPY

808 NM-ACTIVABLE CORE@MULTISHELL UPCONVERTING NANOPARTICLES WITH ENHANCED STABILITY FOR EFFICIENT PHOTODYNAMIC THERAPY

2.1. INTRODUCTION

The potential of rare-earth (RE) upconverting nanoparticles (UCNPs) as the next generation luminophores is unique.[170] This potential relies on their distinctive optical properties, including the absence of blinking, low excitation rate compared with organic dyes or semiconductor nanocrystals,[171] excitability by wavelengths within biological windows, and high signal-to-noise ratio, among others.[172] However, some challenges related to their translatability for diagnosis and therapy remain troublesome, such as the NIR wavelength required for upconversion activation. Many approaches have been recently developed to shift this NIR excitation wavelength from the commonly used 980 nm to 808 nm,[122, 129, 173] where the water absorbance is *ca.* 5% compared with the absorbance at 980 nm,[174] avoiding thereby undesired heating processes and losses of the excitation efficiency due to water absorption. One of the most successful solutions relies on the inclusion of Nd^{3+} ions as sensitizers, taking advantage of their 800 nm characteristic excitation band. It has been demonstrated that Nd^{3+} is able to transfer energy successfully to Yb^{3+} and this one to Er^{3+}.[175] However, the limitation of this approach is the presence of deleterious energy transfer processes that happen when all the lanthanide ions are located inside the same matrix. This issue has been overcome by the introduction of core@shell structures that enable the use of higher doping percentages.[149, 176]

Another open challenge is related to the stability and upconversion efficiency in water and biologically relevant media of this type of NP.[11, 177] In this direction, manifold surface coatings have been explored in order to not only properly stabilize UCNPs in these media, but also to preserve their luminescent properties.[129, 177-181] Note that the synthesis of high-quality colloidal UCNPs is typically carried out in organic solvents with relatively high boiling points (*e.g.*, mixtures of 1-octadecene and oleic acid) by using thermal decomposition methods.[11] These synthetic processes allows the obtaining of UCNPs capped with aliphatic ligands, which provide colloidal stability in organic solvents; it is thus mandatory to carry out a water transfer process if the UCNPs are going to be used in biological fluids. To perform this step, two main strategies can be: i) a ligand exchange process consisting in the replacement of the hydrophobic ligands attached to the NP surface;[182] and ii) the growth of a hydrophilic outer shell on top of the primary capping ligands.[183] The first approach deals with modifications

directly performed onto the UCNPs surface, in which the generation of defects and the existence of efficiency losses are more likely to occur compared with the second approach. One of the most versatile strategies for the UCNPs stabilization, as well as many other inorganic NPs, entails the use of amphiphilic polymers such as PMA.[172, 184]

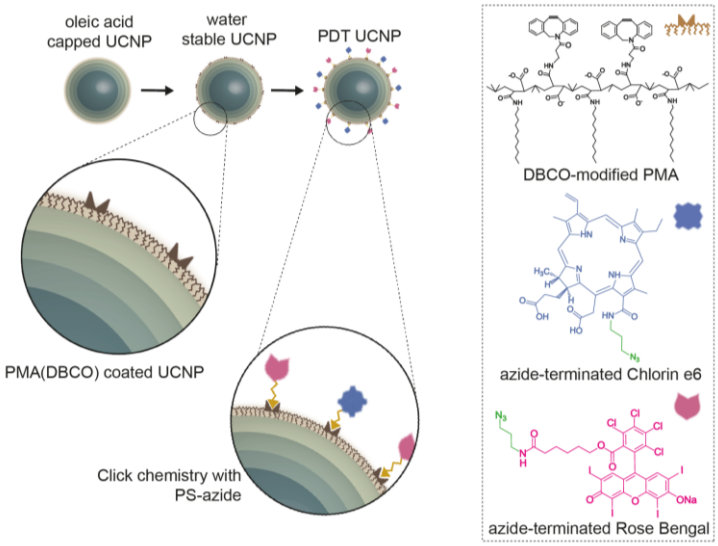

Figure 2.1. UCNP based nanoplatform.
Illustration of the synthetic steps to produce UCNPs, water transfer, and functionalization with two PSs (Rose Bengal and Chlorin e6)

As mentioned above, the potential of UCNPs as therapeutic agents is promising, particularly, as photodynamic therapy (PDT) agents. Moreover, their use for other purposes such as optogenetics has been also evaluated.[185] Nevertheless, most of the literature precedents involved the use of 980 nm-excitable UCNPs. The use of photosensitizers (PS) covalently linked to the UCNPs allow for the design of more efficient multifunctional PDT agents, which combined with 808 nm-photoactivable UCNPs, provides for new opportunities to develop more effective, translational therapeutic approaches. The use of 808 nm-gated PDT agents based on UCNPs has been previously explored by using both PS-filled porous shells,[186-187] and PS-modified polymer-based coatings.[149, 153, 188-190] We chose to modify our PMA with dibenzocyclooctyne (DBCO) groups, thereby, providing for a versatile platform to attach azide-containing molecules by copper-free click chemistry.

In the present chapter, the synthesis of 808 nm-activable UCNPs using a layer-by-layer methodology without the use of trifluoroacetate precursors is proposed. These UCNPs were water-transferred using a polymer coating strategy based on the amphiphilic DBCO-modified polymer PMA. Taking advantage of the

PMA's tailorability, two different FDA-approved photosensitizers, Rose Bengal (RB) and Chlorin e6 (Ce6), were covalently attached to the UCNPs by click chemistry (Figure 2.1) to produce PDT nanoprobes for 808 nm-gated intracellular generation of reactive oxidative species (ROS) with spatiotemporal resolution (Figure 2.2).

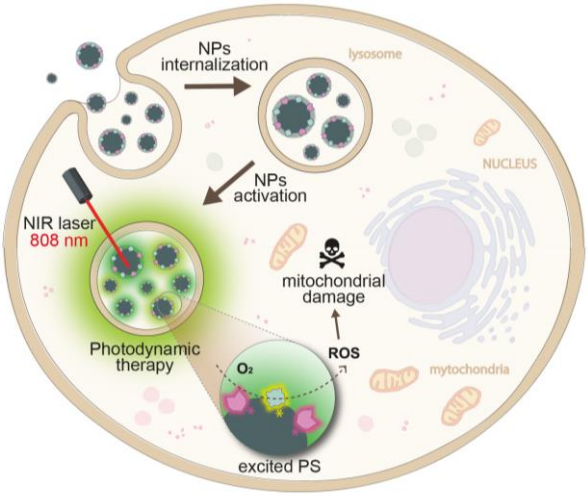

Figure 2.2. Photodynamic therapy activation using UCNPs.
Intracellular location of UCNPs in endocytic compartments and PDT therapy induced by 808 nm laser irradiation, leading to the impairment of mitochondria.

2.2. RESULTS AND DISCUSSION

Lanthanide-doped core@multishell UCNPs with inorganic diameters of ~ 60 nm were synthesized in organic solvents, aiming to specifically obtain $NaYF_4$:$Yb_{18\%}Er_{2\%}$ @$NaYF_4$:$Yb_{10\%}$ @$NaNdF_4$:$Yb_{10\%}$ @$NaYF_4$:$Yb_{10\%}$ lumiprobes, and featuring a highly effective 808 nm to visible upconversion, as previously reported;[149] such structure entails (see Table S2.1): (i) an upconversion luminescence core; (ii) an energy transfer layer ($shell_1$); (iii) an energy absorption layer ($shell_2$); (iv) an energy transfer and luminescence reduction layer ($shell_3$). We followed the thermal decomposition route (see experimental setup in Figure S2.1), adapting previously reported layer-by-layer protocols,[151] in which the commonly used trifluoroacetate precursors were replaced by chloride precursors. The replacement of trifluoroacetate reactants avoids the potential decomposition of the precursors into HF gas or fluorinated species during the reaction at high temperature.[145]

Firstly, nanocores with diameter ~ 24 nm were produced (Figure S2.2 and Figure S2.3); their X-ray diffraction pattern confirmed the expected hexagonal

crystalline structure (Table S2.2 and Figure S2.4)[191] The shell growth was characterized by TEM and SEM, see Figure 2.3, Figure S2.2 and Figure S2.3.

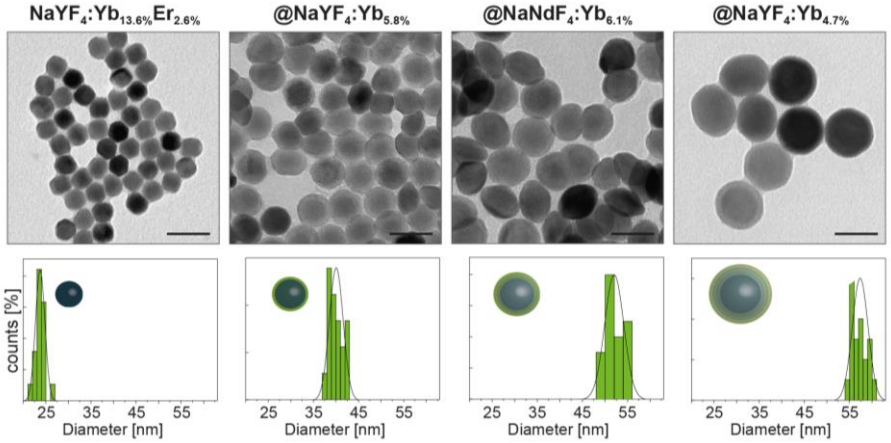

Figure 2.3.TEM micrographs of the UC layer by layer process.
From cores (left) to the multishell particles (right). Scale bars correspond to 50 nm. The corresponding histograms for the synthetic steps are depicted in green bars below each image.

We combined TEM and SEM data and compositional analysis by ICP-MS to determine the composition of each shell and the core (Table S2.3, Table S2.4, Table S2.5, Table S2.6 and Table S2.7). The diameters and the individual shell compositions are summarized in Figure 2.4a (for additional details, see Table S2.6 and Table S2.7). The obtained composition corresponds to $NaYF_4:Yb_{13.6\%}Er_{2.6\%}$ @$NaYF_4:Yb_{5.8\%}$ @$NaNdF_4:Yb_{6.15\%}$ @$NaYF_4:Yb_{4.67\%}$. Based on this, and the size previously determined, the UCNPs molecular weight was estimated (MW ~ $30 \cdot 10^7$ g·mol^{-1}), allowing for an accurate determination of the UCNPs concentration. The MW value experimentally obtained (see Table S2.8) here is in good agreement with the theoretical value recently calculated by Mackenzie *et* al.,[192] which have developed a theoretical method to determine the UCNPs MW. They described that UCNPs ($NaYF_4$:RE) with diameters between 10 to 45 nm show MWs ranging from 10^6-10^8 g·mol^{-1}. The experimental determination of NPs MW is critical for their biomedical application.[193] In our case, it allows for controlling the dose of UCNPs used in the experiments involving living cells.

As expected, our nanocores ($NaYF_4:Yb_{13.6\%}Er_{2.6\%}$) were excitable at 980 nm but showed residual emission when they were excited with an 808 nm laser, as it can be qualitatively observed in photographs of cores solutions under the two light sources (Figure 2.4 b), as well as in the corresponding emission spectra (Figure 2.4 c). On the other hand, the final core@multishell UCNPs were activable under the excitation of both wavelengths (Figure 2.4 b,c). The emission spectra of the core@multishell UCNPs showed that the emission peaks and intensity

ratios remained unaltered for both laser sources (using ~ 5 nM UCNP solution and an irradiance of 1 W·cm^{-2}). In all these cases, the most intense peaks were centered at 522, 542 and 657 nm. These values and intensities are in good agreement with reported samples with a matrix of $NaYF_4$ doped with Er^{3+} as activator and Yb^{3+} as sensitizer.[145]

a

	CORE	SHELL$_1$	SHELL$_2$	SHELL$_3$
Y%	(83.8 ± 0.1)	(94.2 ± 0.6)	–	(95.3 ± 1.6)
Yb%	(13.6 ± 0.1)	(5.8 ± 0.1)	(6.1 ± 0.2)	(4.7 ± 0.2)
Er%	(2.6 ± 0.1)	–	–	–
Nd%	–	–	(93.8 ± 0.2)	–
d [nm]	(24.0 ± 1.1)	(42.1 ± 6.5)	(52.3 ± 2.1)	(59.3 ± 9.4)

b

c

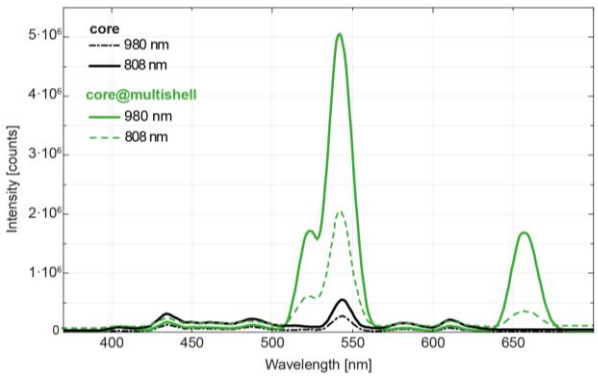

Figure 2.4. Core@multishell UCNP compositions and emission.
a) Table reflecting UCNPs composition, including the diameter/thickness of the particle core and layers based on TEM images, and the individual core and shell composition as determined by ICP-MS. b) Photographs of solutions of cores (left) and core@multishell UCNPs (right) under excitation with 980 nm- and 808 nm-excitation lasers, respectively. c) Emission spectra of cores (black lines) and core@multishell UCNPs (green lines) in chloroform (~ 5 nM particles) under 808 nm and 980 nm excitation (1 W·cm^{-2}), respectively.

The synthesized UCNPs were hydrophobically capped (oleic acid); therefore, a step to water-transfer them was required. The stabilization of UCNPs in relevant biological media while keeping their photoluminescence properties is still an open challenge.[11] Manifold strategies have been explored including ligand exchange processes,[177, 194] and the use of amphiphilic polymers.[172, 181]. Considering this, the use of an amphiphilic polymer (PMA) was selected. The polymer coating technique has been employed to successfully water transfer most types of inorganic nanoparticles.[183] This approach has been recently proven to be also valid for the water transference of NPs with diameters larger than 20 nm,[195] and extremely water-sensitive photoluminescence NPs such halide nanoperovskites.[196] The selection of this polymer was based on the following points: i) this technique has been widely used to stabilize quantum dots,

minimally affecting their optoelectronic properties, and recently, for the stabilization of 980-activable UCNPs;[172] ii) a high yield of NPs with robust colloidal stability, even in complex biological media, can be obtained;[197] and iii) it offers a very versatile platform to perform the covalent bioconjugation of different ligands of interest.[198] The PMA used here was modified with DBCO pendant groups before the coating of the UCNPs (see Materials and Methods for details and Figure 2.14). Thus, resulting polymer-coated NPs could be easily modified with azide-containing ligands using a copper-free click chemistry reaction.

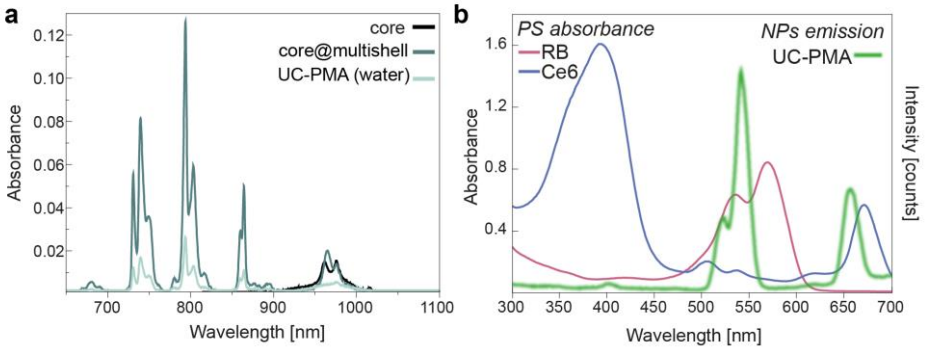

Figure 2.5. Absorbances of UCNP and PS.
a) Absorbance of core, core@multishell, and UC-PMA NPs in chloroform and water. b) Overlay of Rose Bengal and Chlorin e6 absorbance and UC-PMA emission in water.

After the PMA-coating of the UCNPs (UC-PMA), the absorbance and the emission spectra were recorded (Figure 2.5a). For a solution with the same concentration, the absorbance after UCNPs water transfer dropped to ~ 25% of the initial absorbance of uncoated NPs in chloroform. Interestingly, the relative peak intensity, the ratio of the main three emission peaks, remains unaltered after the coating in agreement with other water-transferred UCNPs.[194] Emission peak position remained unaltered after the water transfer, but as it occurs with absorbance, the emission rate decreased (see Figure S2.5).

To maximize the efficiency of the PDT potential of UCNPs two PSs, RB and Ce6, were selected as they match the most intense emission peaks of the designed UCNPs upon NIR excitation (see Figure 2.5 b and SI). Both PSs were modified to include an azide group in their structure (Figure 2.13) for their covalent binding to PMA. Three different probes containing one or both PS were prepared: UC-RB, UC-Ce6 and UC-RB,Ce6 (see Figure S2.6). During the conjugation process and due to its high efficiency compared with other bioconjugation techniques,[198] it is important to have a good control over the following parameters: i) the NP:PS ratio, since ratios above 1:750 will decrease dramatically the hydrophilicity of the NPs, thereby, impairing their colloidal stability and leading to their partial

aggregation;[198] ii) the final NP concentration during the reaction (not higher than 16 nM); and iii) to keep the H_2O:DMSO ratio during the reaction below than 4:1. A quantitative determination of the number of PS attached in each probe was determined, using appropriate calibration curves (Figure S2.7). When modifying the NPs with one PS type (RB or Ce6), approximately 100 molecules were linked per NPs. This number is in good agreement with the size and the loading efficiency compared with other modified-PMA coated NPs.[198-199] Interestingly, when both PS were used together to modify the UCNPs, the efficiency for the Ce6 binding remained constant, ~ 100 Ce6·NP^{-1}, but the number of RB molecules per NP dropped to 50 (Figure 2.6 a). This might indicate some priority in Ce6 binding over RB during the bioconjugation that is not present when the UCNPs are modified just with one PS type.

a

	UC-PMA-RB	UC-PMA-Ce6	UC-PMA-RB,Ce6
RB per NP	(135 ± 4)	–	(59 ± 2)
Ce6 per NP	–	(120 ± 5)	(115 ± 5)

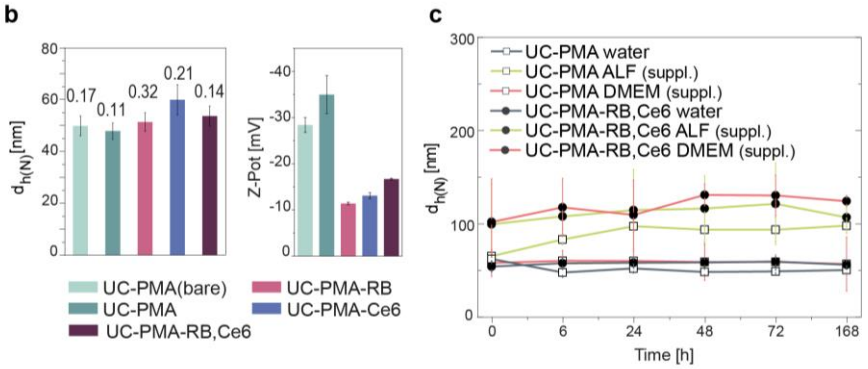

Figure 2.6. UC-PMA water characterization.
a) Summary of the PSs attached per UCNP. b) DLS and LDA values of the different ligands combinations attached to the UCNPs; each bar labelled with the corresponding polydispersity index (PDI). c) Hydrodynamic diameter values (number-weighted) overtime in different media (water, blue; supplemented ALF, green; supplemented DMEM, orange) of UC-PMA (white dots) and UC-PMA-RB,Ce6 (black dots) (raw data showed in Table S2.9).

After the PS conjugation, colloidal characterization using SEM (Figure S2.8), DLS and LDA was performed in water. Changes in the bare and functionalized UCNPs hydrodynamic diameter (d_h) were not significant, but in the functionalized NPs a decrease in the ξ-potential value was observed in all cases from ~ -30 mV to -15 mV (see Figure 2.6 b, Figure S2.9 and Table S2.9 for the obtained values), consistent with PS attachment.

Finally, the colloidal stability of the UC-PMA and UC-PMA-RB,Ce6 over time, for at least one week, was studied (Figure 2.6 c). To do so, four different aqueous-

based media were selected; that is, water, DMEM supplemented with FBS (10% v/v), and ALF with and without FBS (10% v/v). Both types of NPs remained stable along incubation in water. However, as reported previously, the PMA-coated NPs were unstable in medium without FBS (see Figure S2.10).[195] Both samples remained stable in the complete media, both DMEM and ALF. As expected, an increase in size was observed in both cases likely due to the unspecific adsorption of proteins,[200] but the size variation remained constant along the observation time, confirming the nanoplatforms stability.

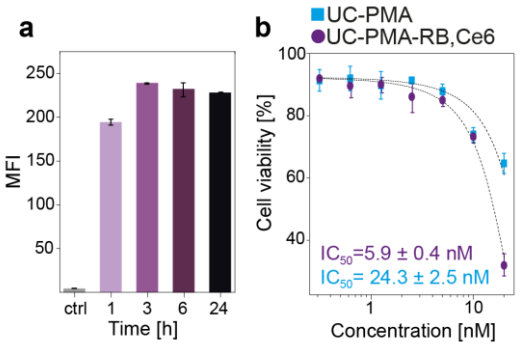

Figure 2.7. *In vitro* behavior of the UCNPs.
a) Uptake of UC-PMA-RB,Ce6 (2 nM) by HeLa cells at different incubation times. b) Viability studies of UC-PMA and UC-PMA-RB,Ce6 after 24 h of NPs incubation in dark conditions, and IC50 values.

The *in vitro* behaviour of the UCNPs was studied using different methodologies. First, the internalization rate of UC-PMA-RB,Ce6 NPs by HeLa cells was followed up from 1 h to 24 h incubation (Figure 2.7 a). Interestingly, the internalization rate, as determined by the fluorescence of the RB attached to the NPs, remained constant since the first measured time point (3 h). In parallel, the internalization rate of UC-PMA NPs was also determined by ICP-MS after 3 h of incubation. The number of internalized NPs was ~ $13.4 \cdot 10^3$ NP·cell^{-1}; this represent an internalization rate of ~ 0.05% of the total added UCNPs (see Table S2.10). The order of magnitude of internalized cells is in good agreement with previous uptake experiments using PMA-coated NPs.[201]

The viability under dark conditions in HeLa cells was studied after 24 h of exposure to the UCNPs (from 0.3 to 20 nM). Using a fitting function, the half maximal inhibitory concentration (IC50) value was determined, resulting in values in the range of previously reported IC50 data for other PMA-coated NPs.[39, 197] As expected, the obtained IC50 value for the UC-PMA-RB,Ce6 NPs was lower than that of their UC-PMA counterparts (Figure 2.7 b). This evidence supports the fact that the UCNPs are not degraded *in vitro*, which would allow for releasing toxic ions; hence, the observed cytotoxicity is likely due to a combination of factors (*e.g.*, size, organic shell, presence of dyes and their potential leakage, and

the number of particles per cell). Based on these results, the dose for cell-treatment with the UCNPs was fixed to 2.5 nM.

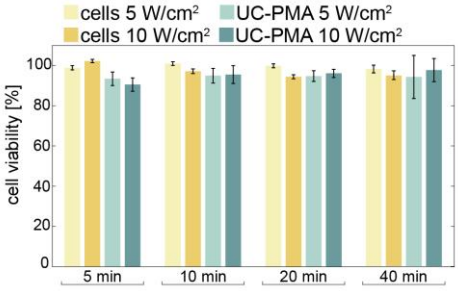

Figure 2.8. Cell irradiation controls.
"Empty" cells (only cells and laser), and cells loaded with UC-PMA (2.5 nM) after 3 h of incubation and different irradiation times using an irradiance of 5 or 10 W·cm^{-2}.

For all irradiation experiments, a collimated laser beam with a controlled spot size was used, and therefore, each sample was homogeneously irradiated (Figure 2.16). To establish the experimental conditions to perform PDT therapy, irradiation experiments varying the irradiance (5 or 10 W·cm^{-2}) and the exposure time (from 5 to 40 min of irradiation) were performed with "empty" HeLa cells and HeLa cells treated with UC-PMA NPs (2.5 nM) (Figure 2.8). In all the cases, the viability remained above 90%, showing that both the irradiances and exposure times with the 808 nm laser were harmless to cells, and that the UCNPs without PS do not impair cell viability, even under NIR irradiation.

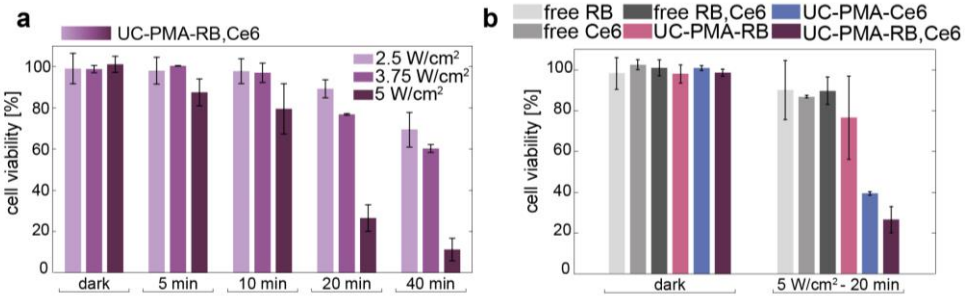

Figure 2.9. Photodynamic therapy efficiency studies.
a) Impact on cell viability of UC-PMA-PS (2.5 nM, 3 h of incubation) under different laser irradiances and different irradiation times. b) Comparison in the viability impact of free PS and its combinations at a concentration of 250 nM, and the PS linked to the UCNPs incubated at 2.5 nM, under dark conditions and after 20 minutes of irradiation with an 808 nm laser at a irradiance of 5 W·cm^{-2}.

Finally, PDT experiments were performed under strict dark conditions using UC-PMA-RB,Ce6 NPs at different laser irradiances (2.5, 3.75 and 5 W·cm^{-2}) and different irradiation times 5, 10, 20 and 40 min) using a constant NP concentration of 2.5 nM (Figure 2.9 a). Interestingly, the impact of PDT in cell viability was noticeable even at just 5 min of irradiation at the highest irradiance selected (5 W·cm^{-2}). Using that irradiance, viabilities below the 25% were reached following 20 min of irradiation. Viabilities close to the 50% were also obtained after 40 minutes of irradiation at 3.75 W·cm^{-2}; moreover, the lowest irradiance (2.5 W·cm^{-2}) had also an important effect in the viability at the longest irradiation time. To confirm that the induced cell death was caused by an effective PDT effect, adequate controls were performed. These controls included the incubation of the cells with i) the free PS, alone or combined, in a comparable dose to that attached to 2.5 nM UCNPs, *i.e.*, 250 nM of PS(s); and ii) UCNPs with only one attached PS. The results summarized in Figure 3e proved that none of the probes, including UC-PMA-RB,Ce6 NPs, had any impact in the cellular viability if NIR light was not used. Also, after PDT experiments, viabilities of ~ 90% were found for all the cells treated only with free PS, alone or combined. The present results proved that the most efficient PDT probe was, as expected, the UCNPs containing both PS (UC-PMA-RB,Ce6), followed by the UC-PMA-Ce6 (viability lower than 40%) (see Figure 2.9 b).

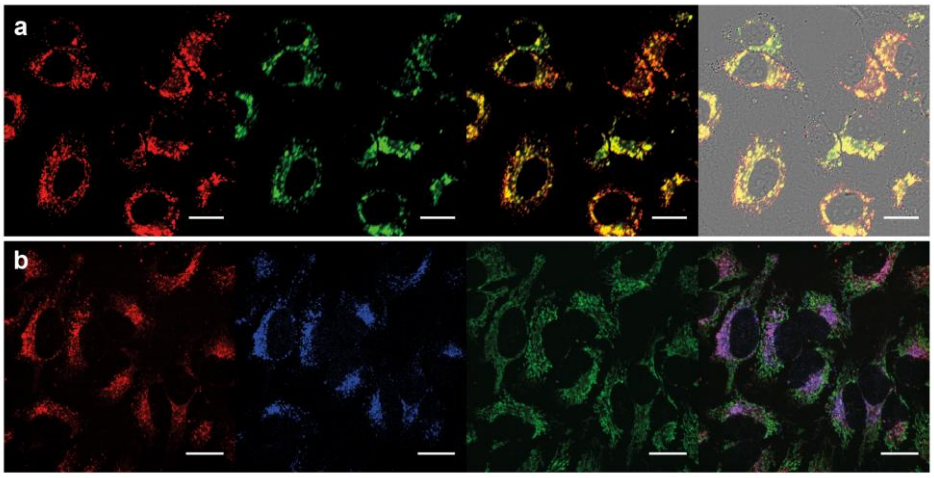

Figure 2.10. Intracellular location of UCNPs platforms.
a) Intracellular localization of UC-PMA-RB,Ce6 in HeLa cells after 3 h of incubation (2.5 nM of NPs). From left to right: red (RB, Ex. 561, Em 620/60), green (Ce6, Ex. 405, Em. 725/40), red + green (yellow colour indicated colocalization of RB and Ce6), merged image of bright field (BF) + red + green. b) Intracellular colocation of UC-PMA-RB and lysosomes and mitochondria in HeLa cells after 3 h of incubation. From left to right: red (RB, Ex. 561, Em 620/60), blue (Lysotracker Blue, Ex. 405, Em. 450/50), green (Mitotracker Green, Ex. 488, Em. 525/50), merged image of blue + red + green. Purple indicates lysosomes and UCNPs colocalization. Scale bars represent 20 μm.

After proving the efficiency of the developed UCNPs as 808 nm-PDT agents, the next step was to evaluate their intracellular location and to study the mechanism by which PDT occurs. Therefore, the internalization of UC-PMA NPs was studied. Confocal microscopy images of HeLa cells incubated for 3 h with UC-PMA-RB,Ce6 NPs (2.5 nM) showed that both PSs were colocalized intracellularly (100X magnification images are shown in Figure 2.10 a, and 60X in Figure S2.11). As expected, the NPs were distributed in the perinuclear region indicating they are likely to be storaged in lysosomal compartments (see z-scan slices in Figure S2.12). This intracellular location has been reported previously for similar systems involving PMA-coated NPs.[202] Colocalization experiments were performed to confirm this evidence. To do so, lysosomes and mitochondria of HeLa cells treated with UC-PMA-RB NPs were stained with Lysotracker and Mitotracker dyes, respectively. As expected, the intracellular location of the UCNPs was colocalized with the lysosome staining but not with the mitochondria one (Figure 2.10 b and Figure S2.13).

To conclude, the production of ROS was studied both in test tube and *in vitro*. First, the degradation rate of 1,3-diphenylisobenzofuran (DPBF) was followed over time (2 min) under a constant irradiation of 5 W·cm^{-2} with the 808 nm laser irradiation setup (Figure 2.11 and Figure 2.15 for raw data). The degradation of this probe is due to ROS production in solution, which leads to a loss of absorbance at 407 nm. Free PSs, and all types of UCNPs were tested under the same conditions. Results are summarized in Figure 2.11, which clearly shows a high degradation rate of DPBF in the presence of UC-PMA-RB,Ce6 NPs. This trend was followed by the UCNPs modified with Ce6. Lower degradation rates were observed for UC-PMA-RB NPs and UC-PMA NPs mixed with free PS or alone, respectively. The irradiation of the PS alone does not induce any significant DPBF degradation. The trend observed in the test tube experiment correlates perfectly with the observed trend in the induced cell toxicity assay, which supports that the cell death is induced by ROS production.

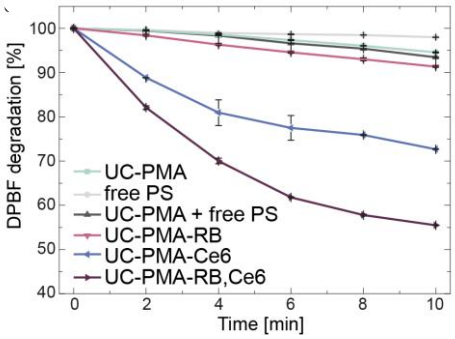

Figure 2.11. Photodynamic therapy test tubes.
Degradation rate of DPBF at 407 nm upon 5 W·cm^{-2} irradiation with an 808 nm laser at 2.5 nM concentration of UCNPs or 250 nM of free PS.

Finally, the intracellular ROS production was determined using a mitochondrial membrane potential assay based on the use of a tetramethylrhodamine ethyl ester (TMRE). This probe can label active mitochondria but cannot label depolarized or inactive mitochondria. Therefore, if upon PDT mitochondria are impaired, the labelling with TMRE will be reduced. Figure 2.12 shows the differences in TMRE labelling of mitochondria in cells incubated with UC-PMA-RB,Ce6 NPs before and after NIR exposure (for additional images check Figure S2.14). A clear decrease of fluorescence is observed (Figure 2.12 a) after the exposure to the 808 nm light indicating that the mitochondria potential is affected by the ROS produced by the UC-PMA-RB,Ce6 NPs. This decrease in fluorescence was quantified using a fluorescence readout, that is, the corrected total cell fluorescence (CTCF) per cell before and after irradiation; the differences are clear, dropping from a CTCF per cell ~ 40000 before irradiation to a CTCF close to 1000 after irradiation (Figure 2.12 b).

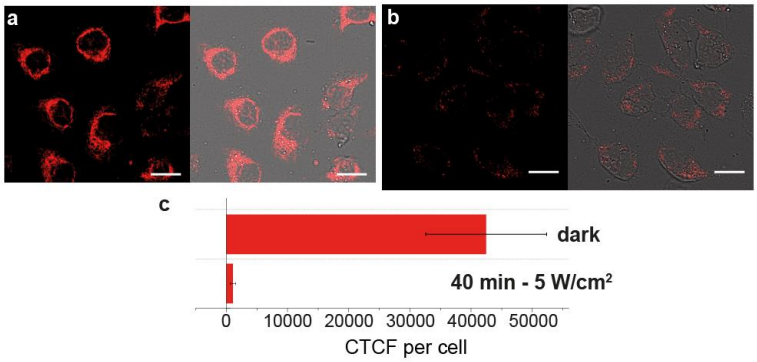

Figure 2.12. PDT evaluation by confocal microscopy.
a) Cells treated with UC-PMA-Rb,Ce6; 2.5 nM for 3 hours under dark conditions after TMRE exposure and b) after 40 minutes of 5 $W \cdot cm^{-2}$ irradiation. c) Corrected-total cell fluorescence (CTCF) of cells incubated for 3h with 2.5 nM UC-PMA-RB,Ce6 and TMRE with and without PDT.

2.3. MATERIALS AND METHODS

For detailed experimental methods and additional results see section *Chapter 2 Appendix.*

General considerations. All the reagents including 1-octadecene (ODE, 90%), oleic acid (OA, 90%), ethanol (EtOH) and methanol (MeOH), dimethylformamide (DMF), chloroform, milli-Q water, tetrahydrofuran (THF), yttrium(III) chloride anhydrous (YCl_3, 99.9%), ytterbium(III) chloride anhydrous ($YbCl_3$, 99.9%), erbium(III) chloride anhydrous ($ErCl_3$, 99.9%), ammonium fluoride (NH_4F, 96%), Sodium hydroxide (NaOH, 96%), Sodium trifluoroacetate

(Na-TFA, 98%), neodymium(III) chloride ($NdCl_3$ 99.9%), 1-ethyl-3-(3-dimethylaminopropyl)carbodiimide (EDC), N-hydroxysuccinimide (sulfo-NHS), Rose Bengal (RB), 6-bromohexanoic acid (Br-HA), poly(isobutylene-alt-maleic anhydride), dodecylamine (DDA), dibenzocyclooctine-amine (DBCO-NH_2), 1,3-Diphenylisobenzofuran (DPBF, 97%) were purchased from Sigma-Aldrich. Chlorin e6 (Ce6) were purchased from Santa Cruz Biotechnology. 3-azido-propylamine (NH_2-N_3) were purchased from Fluorochem Ltd.

Synthesis of 980 nm activable cores. The synthesis of highly monodisperse β-$NaYF_4$:$Yb_{18\%}Er_{2\%}$ was carried out by modification of previously reported methods.[203-204] Typically, 2 mmol of dry precursors at the desired proportions (80% of YCl_3 or 485.34 mg; 18% of $YbCl_3$ or 139.50 mg and 2% $ErCl_3$ or 15.27 mg) were mixed into a 250 mL three-neck round bottom flask with 30 mL of ODE and 12 mL of OA. The solution was heated slowly (3 °C/min) to 150 °C under vacuum to eliminate oxygen and water traces. After 1 hour, the solution was cooled down to RT and subsequently, 296.5 mg of NH_4F and 200 mg of NaOH dissolved in 10 mL of methanol were added to the flask and kept under stirring during 30 minutes at 50 °C. A translucent yellow-white solution was formed. Then, methanol was evaporated under vacuum and by increasing the temperature to 80 °C. After 20 minutes, the solution became transparent. Finally, the reaction was heated at 7 °C/min up to 300 °C under N_2 atmosphere for 1 h since the final reaction temperature is reached. The cores were precipitated with methanol (20 mL) and isolated by centrifugation (2000 RCF, relative centrifugal force, 10 min). The purified cores were dispersed in 30 mL of chloroform, ca. 500-600 mg of material per synthesis were obtained. The cores were characterized by electron microscopy techniques and ICP-MS. The final concentration of the solution was determined by combining the results from TEM and ICP-MS.

Preparation of shell precursors. The solutions needed for shell growing onto the previously synthesized cores were prepared before starting with the final reaction. [149 151] First, Na-TFA-OA was prepared by mixing 10 mL of OA and 4 mmol of Na-TFA under vacuum at room temperature (RT) to obtain a final solution of 0.4 M. Secondly, Ln-OA solutions were prepared with the lanthanide elements in the desired proportions. Two different Ln-OA were prepared ($Y_{90\%}$,$Yb_{10\%}$-OA and $Nd_{90\%}$,$Yb_{10\%}$-OA) by mixing 10 mL of OA, 15 mL of ODE and 2.5 mmol of precursors mixture and heating the solution to 150 °C under vacuum. In this way, for Y,Yb-OA, we added 2.25 mmol (682.56 mg) of YCl_3 and 0.25 mmol (96.87 mg) of $YbCl_3$ and for Nd,Yb-OA we mixed 2.25 mmol (563.85 mg) of $NdCl_3$ and 0.25 mmol (96.87 mg) of $YbCl_3$.

Synthesis of 808 nm switchable core @shell$_1$ @shell$_2$ @shell$_3$ upconverting nanoparticles (UCNPs). The selected structure was

$NaYF_4:Yb_{18\%}Er_{2\%}$@$NaYF_4:Yb_{10\%}$@$NaNdF_4:Yb_{10\%}$@$NaYF_4:Yb_{10\%}$. 2 mL of a 600 nM solution of the previously purified cores in chloroform (1.2 nmol of cores) were mixed with 4 mL of OA and 6 mL of ODE into a 100 mL three-neck round bottom flask. Solution was heated to 50 °C , kept under vacuum and magnetically stirred to evaporate the chloroform. After this, the reaction was heated quickly (10 °C/min) to 300 °C and kept under N_2 flux. Once the temperature was stabilized, precursor solutions were added to the reaction flask. The reaction time after each injection was 15 minutes. Finally, reaction was cooled down to RT and NPs were collected by centrifugation (2000 RCF, 5 min) after adding 10 mL of ethanol. The supernatant was discarded and a solution at 600 nM NPs was obtained by adding 2 mL of chloroform to the pellet. This process was repeated to grow the desired shell number following the steps.

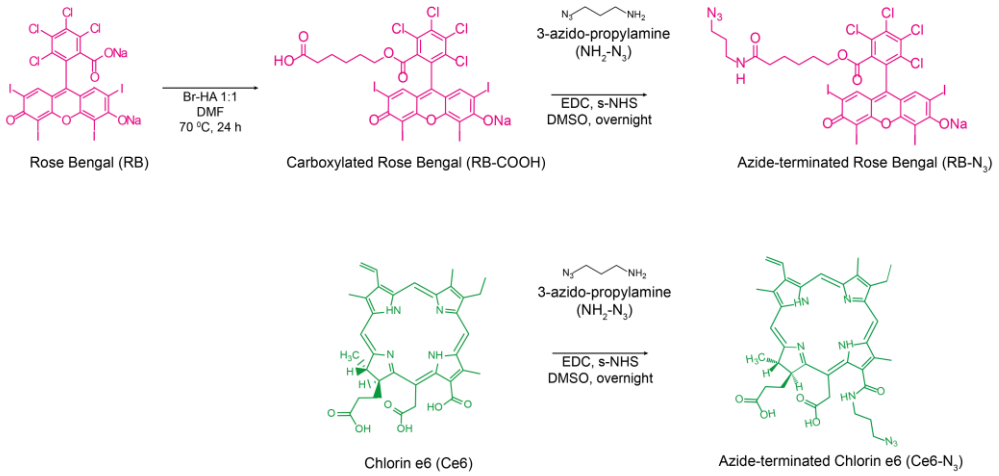

Figure 2.13. Scheme of the synthetic process for the PS.
Modification to produce azide-modified PSs (RB and Ce6).

Carboxylate rose Bengal (RB-COOH). The modification of the commercial rose Bengal was done following a previous protocol.[180] RB and Br-HA were mixed in a 1:1 molar ratio. For that, two solutions in DMF were prepared, one containing 101.8 mg of RB dissolved in 2 mL of DMF and a second one containing 19.5 mg of Br-HA dissolved in 2 mL of DMF at 70 °C until both solutions are completely dissolved. Then, the RB solution was added onto the Br-HA solution and stirred at 70 °C for 24 hours. Final product was dried and stored under dark conditions.

N_3-modification of photosensitizers. The two carboxylated-PS (RB-COOH and commercial Ce6) were activated with carbodiimide (Figure 2.13). In general, 400 µL of RB-COOH or Ce6 (1.8 mM in MeOH) were added to 2 mL of DMSO. 800

µL of EDC (3 mg/mL in DMSO) and 400 µL of sulfo-NHS (5 mg/mL in DMSO) freshly prepared were added to activate the carboxylic groups of the PSs. After 30 minutes of stirring at RT and dark conditions, 144 µL of the ligand NH_2-N_3 were added (10.2 mM in DMSO). The reaction was left overnight, and final solutions were kept at 4 °C and dark conditions for further use, considering the final concentration of both PS-N_3 as 192 µM in DMSO. The PS concentration was determined using the corresponding calibration curves (Figure S2.7).

DBCO-modified polymer preparation. The amphiphilic polymer PMA was synthesized as described previously [49] with some modifications (Figure 2.14). Briefly, 1.85 mmol of poly-isobutylene-alt-maleic-anhydride (285 mg, MW ≃ 6000 g/mol), 1.39 mmol of DDA (265.8 mg, 75% of the monomers) and 0.04 mmol of DBCO-NH_2 (2% of the monomers) (10.2 mg) were mixed together in 50 mL of THF. The solution was kept under magnetic stirring and reflux overnight. THF was evaporated and the dried polymer was dispersed with 3.7 mL of chloroform to obtain a final monomer concentration of 0.5 M.

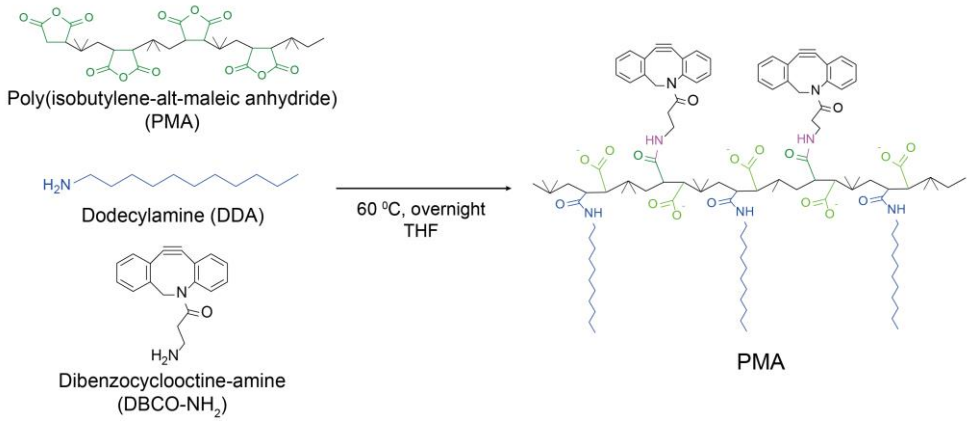

Figure 2.14. PMA(DBCO) preparation.
Polymer modification for further NPs functionalization and click chemistry onto their surface.

PMA coating. The procedure was performed by mixing 100 µL of UCNPs in chloroform at ~ 300 nM with 150 µL of PMA(bare) or PMA (with DBCO) in chloroform at 0.25 M (monomer concentration) and 1 mL of chloroform. After this, the solvent was evaporated under vacuum in a round bottom flask with rotavapor system. Then, 2 mL of sodium borate buffer (SBB, 0.1M, pH 12) were added. Samples were sonicated until a transparent and colourless solution was obtained. NPs were centrifugated at 30000 RCF during 30 minutes at 10 °C. Final solutions of UCNP@PMA were kept in milli-Q water and characterized.

PS-N_3 and UC-PMA NPs conjugation by click chemistry. The modification with one or two PS of UC-PMA NPs was performed using a copper-free click chemistry reaction. Typically, 500 µL of UC-PMA at 60 nM (particles concentration) in water were mixed with RB-N_3 and Ce6-N_3 vigorously for 30 minutes. The ratio of dyes per UCNP was fixed to 750 (for each PS). Three different PDT platforms were prepared, i) RB only (NP:RB 1:750), ii) Ce6 only (NP:Ce6 1:750) and iii) with RB and Ce6 (NP:RB 1:750 and NP:Ce6 1:750). When reaction was finished, samples were dialyzed overnight through a membrane of MWCO 14000 kDa to remove all non-covalently bond molecules. Finally, samples were precipitated (7000 RCF, 10 min, 10 °C) and dispersed in water to yield solutions of 300 nM. The PS number and concentration was used using independent fluorescence calibration curves (Figure S2.7).

Stability studies in biological media. The stability of the polymer-coated nanoparticles with and without PS in different media overtime was studied. Samples were incubated in water, ALF, ALF supplemented with 10% v/v of FBS and complete cell culture medium (DMEM supplemented with 10% v/v of FBS) under stirring up to a week.

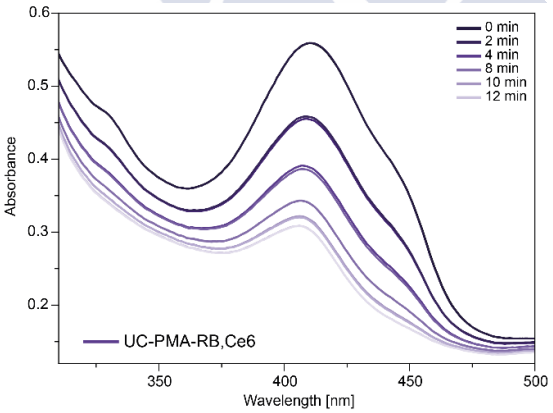

Figure 2.15. Degradation of DPBF, raw data.
DPBF degrades due to the ROS production under 808 nm laser excitation of UC-PMA-RB,Ce6 NPs.

DPBF degradation. In order to perform the experiment, 1 mL of a freshly prepared solution of the sample of interest was mixed with 10 µL of a freshly prepared DPBF solution (10 mM ethanol). Samples were maintained in dark conditions, in 1 cm path length Hellma quartz cells inside an UV-Vis spectrophotometer (Biochrom Libra S60-UV) equipped with an 808 nm laser properly aligned with the sample on the top of the instrument. Samples were irradiated at periods of 2 minutes at 5 $W \cdot cm^{-2}$ from the top and the absorption value at 407 nm was recorded. UC-PMA-RB, UC-PMA-Ce6, UC-PMA-RB,Ce6 at a concentration of 2.5 nM in water. As controls, UC-PMA (2.5 nM), free dyes RB and

Ce6 (250 nM) and 2.5 nM of UC-PMA mixed with free dyes RB-N_3 and Ce6-N_3 at 250 nM. Figure 2.15 shows the variation of the absorbance spectra of DPBF in solution containing 2.5 nM UC-PMA-RB,Ce6 versus time upon 808-laser irradiation.

Cell culture. HeLa (human cervical cancer cell line) were cultured in DMEM with phenol red, 4.5 g/L D-glucose, L-glutamine and pyruvate (DMEM, 1X, Gibco) supplemented with 10% v/v FBS (Gibco) and 1% v/v Penicillin-Streptomycin (P/S, Corning, 100X). Cells were maintained under humid conditions at 37 °C and 5% of CO_2. Cells were passaged after cleaning (PBS, 1X, Gibco) with 0.25% Trypsin-EDTA (1X, Gibco) when the culture reached confluency.

Figure 2.16. Laser irradiation setup.
Image of spot diameter using a NIR detector card (left) and the collimation/zoom system (right).

Laser irradiation experiments. Cells were seeded in multi-well plates and an 808 nm laser (Lasing, #FC-W-808A) connected to a zoom fiber collimator (Thorlabs, #ZC618SMA) was used to perform all irradiations. To obtain the spot size an infrared viewing card (Thorlabs, #VRC4) was used to see the spot and ImageJ to measure it. As the beam is collimated (see fabricant details for laser collimation conditions), a homogeneous spot is produced and, thus, the irradiance can be easy calculated just dividing the power by the spot surface (in cm^2). Different time and irradiance conditions (as well as spot sizes) were performed as it is indicated in each experiment procedures. Figure 2.16 shows the homogeneous spot and its size produced by an 808 nm collimated laser used for cell irradiations.

Nanoparticles internalization studies.

- *ICP-MS.* Typically, 250000 cell/well were seeded in 2 mL of cell culture medium in 6-well plates. After 24 hours, medium was removed and 2 mL of 5 nM of UC-PMA dispersed in medium, were added. After 3 hours of cell exposure to the UCNPs, medium was removed, and cells were washed with PBS (x3). 200 µL of trypsin were added and cells were collected with 1 mL of DMEM

and counted after that. After cell centrifugation (5000 RPM, revolutions per minute, 6 min), they were digested overnight in aqua regia (200 µL). Then, they were diluted with 2 mL of HCl 2% v/v for ICP-MS analysis. The ICP-MS analysis was performed in an Agilent 7700x inductively coupled plasma mass spectrometer.

- *Cytometry studies*. 15000 cell/well were seeded in 48-well plates in 200 µL of complete cell medium. 24h later, 2 nM of previously diluted UC-PMA-RB,Ce6 in medium were added to the cells and kept 1, 3, 6, 12 and 24 hours under incubation. After washing the cells three times with PBS, these were treated with 50 µL of trypsin and diluted with 150 µL of PBS (supplemented with 10% FBS) and analysed by cytometry in a Guava® easyCyte BG HT flow cytometer (Millipore®). Cell fluorescence was collected in the Yel-G channel (Ex. 532 nm, Em. 583/26 nm) counting always at least 5000 events. Controls were also performed with cells without NP treatment.

- *Confocal imaging of living cells.* Typically, 20000 HeLa cells in 200 µL were seeded on µ-Slide 8 well-ibiTreat chambers (1 cm^2 *per* well, Ibidi, Germany) at least 12 hours before particle exposure. UCNPs were diluted to a concentration of 2.5 nM in cell medium. After three hours, cells were cleaned with PBS (3x) in order to remove non-associated particles. 200 µL of supplemented DMEM supplemented with HEPES without phenol red were added to the cells before imaging on an Andor Dragonfly spinning disk confocal system mounted on a Nikon TiE microscope equipped with a Zyla 4.2 PLUS camera (Andor, Oxford Instruments) and an OKO-lab incubator to keep cells at 37 °C during experiment time. RB channel was obtained with an excitation of a 561 nm laser and a 620(60) nm filter. Ce6 emission was collected exciting with a 405 nm laser and using a 725(40) nm filter. All the images were processed with the free software ImageJ. For colocalization experiments, lysosomes were labeled with Lysotracker Blue (Ex. 405, Em. 450/50, Thermofisher) and Mitotracker Green FM (Ex. 488, Em. 525/50, Thermofisher) following the manufacturer's instructions.

Cell Viability. Resazurin assay was performed on HeLa cells seeded in 96-well plates (NEST Scientific). In general, 7500 cells per well in 100 µL of cell medium were seeded 24 hours before the UCNPs exposition. Then, medium was removed and 100 µL of new cell medium with the desired concentration of UCNPs were added and incubated at 37 °C and 5% CO_2. After the desired time, each well was washed with PBS (3x) and 100 µL of freshly prepared solution with 90% of medium and 10% of resazurin (resazurin sodium salt in water 0.2 mg/mL filtered; Resazurin Sodium Salt, Sigma Aldrich) was added per well. After 3 hours, plates were measured with a plate reader (Infinite® 200 PRO, Tecan, Switzerland) under 560/20 nm excitation and collecting fluorescence with a

610/20 nm filter. The value for control cells ($I_C = I_+ - I_-$), untreated cells, is an average of at least nine independent well values. Sample values (I_S) are a mean of three independent well values. Cell viability values are calculated as Eq. 3.

$$\text{cell viability (\%)} = \frac{I_S}{I_C} \cdot 100 \qquad \textbf{Eq. 3}$$

Photodynamic therapy. 7500 cell/well in 100 µL were seeded in 96-well plates. After one day, cells were exposed to a fresh solution of 2.5 nM of UCNPs in complete cell medium. After 3 hours, the medium was removed, and cells were washed with PBS three times. Then, 100 µL of clean medium supplemented with HEPES and without phenol red were added. Laser irradiations were performed at different times and powers with a spot size of 0.33 cm^2. Cells were kept in dark conditions, humidity and 37 °C during the irradiation time using an incubator. Then, cells were incubated overnight. Afterwards, cell viability was read using the resazurin viability test. The four platforms were tested at a concentration of 2.5 nM: UC-PMA (as control), UC-PMA-RB, UC-PMA-Ce6 and UC-PMA-RB,Ce6.

ROS production measurements.

- *Confocal microscopy TMRE studies.* Confocal imaging experiments were done comparing cells without laser treatment and after 40 min of exposure to 5 $W \cdot cm^{-2}$ using a protocol similar to the one performed for confocal internalization studies. After nanoparticles cleaning and subsequent irradiation, cells were treated with a 100 nM TMRE solution for 30 minutes. Cells were maintained under dark, temperature and humidity conditions in all the steps of the experiment, even during data acquisition.

2.4. CONCLUSIONS

In this work, we have prepared a modification of the methanol-assisted high temperature UCNP synthetic process and subsequent layer-by-layer functionalization methodology to produce highly monodisperse 808-activable UCNPs. These particles have been water transferred using a DBCO-modified amphiphilic polymer that allows the efficient linkage of two different PSs by click chemistry. The PS selection was done in order to maximize the absorbance of the emitted light from the UCNPs. The UC-PMA-PS(s) nanoplatforms have been tested as PDT agents *in vitro* showing a good performance and a great colloidal stability even in complex biological media. The ability of these UCNPs to produce ROS in test tube and *in vitro* has been demonstrated. Once intracellularly stored in lysosomal compartments, the produced ROS are able to act in the mitochondria.

USC
UNIVERSIDADE
DE SANTIAGO
DE COMPOSTELA

3. PLASMONIC NCS FOR NIR TRIGGERED RELEASE

AQUEOUS STABLE NS/ZIF8 NCS FOR LIGHT TRIGGERED RELEASE OF ACTIVE CARGO INSIDE LIVING CELLS

3.1. INTRODUCTION

Metal-organic-frameworks (MOFs), consisting in cations coordinated with multidentate organic ligands,[155] have recently emerged as the latest class of promising drug nanocarriers.[205] The MOF most basic physicochemical properties (that is, porosity, hydrophilicity/hydrophobicity, biostability) are key parameters to fabricate efficient drug-delivery systems, combining high drug loadings with a controlled release. Despite their associated exceptional cargoes, the often limited aqueous (bio)stability of MOFs limits their preclinical application. As a representative example, the biocompatible microporous zeolitic imidazolate framework 8 (ZIF8)[206] have been widely proposed for sustained delivery of wide variety of challenging drugs.[75, 207-209] Although with progressive release, most previous reports refer to that 80-90% of the encapsulated cargo is released within the first ~10 h after exposure to physiological environments. These properties are derived from the chemical instability of ZIF8 in water,[210] which degrades depending on the ZIF8 mass to water ratio and medium pH,[208, 211] thus releasing its cargo.

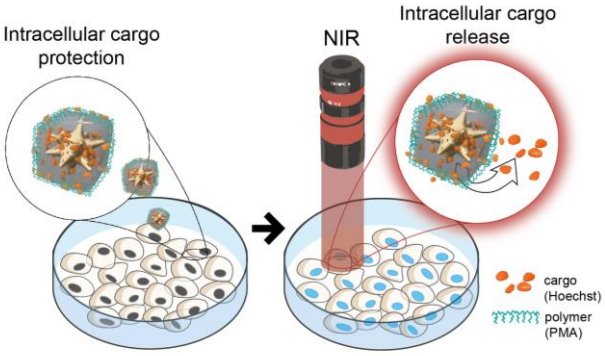

Figure 3.1. Intracellular cargo protection and release using NS-ZIF8-PMA nanocomposites.

In this context, once water stability of NCs based on MOF and inorganic NPs is achieved, they seem a good strategy to promote drug delivery under a given stimulus (e.g., light, magnetic fields, ultrasounds), as already demonstrated for other materials.[212] These type of NCs have been recently explored for optical sensing,[213] therapeutics,[214] theragnostic,[215] and heterogeneous catalysis with

encouraging results.[216] Nevertheless, the precise (temporal and spatial) controlled delivery of the cargo inside cells upon stimuli has not been achieved, since the challenging inherent aqueous instability of MOFs has not yet been addressed.

In this chapter, we designed a thermoresponsive carrier comprising gold nanostars (NSs) coated with ZIF8 stabilized with PMA. The newly developed NC has high drug loading (like the conventional ZIF8), is stable in aqueous solution and can be activated to release the cargo upon illumination with NIR light (Figure 3.1). This concept is demonstrated both in aqueous solution and inside living cells.

3.2. RESULTS AND DISCUSSION

NSs were selected as core due to their characteristic plasmonic band centered at ~770 nm (Figure S3.1),[50] which is suitable for excitation within the first biological window.[43] These NSs were used as seeds to grow the ZIF8 shell around.[213, 217] The number of seeds was optimized to minimize by-products such as non-coated NSs and/or pristine ZIF8 NPs. The resulting NCs showed polyhedral morphology with average size of 218 ± 24 nm (Figure 3.2 and Figure S3.2). As bioactive cargo/reporter we choose the bisbenzimide compound Hoechst H 33258 (HOE), a blue fluorescent dye typically used for DNA staining in molecular biology.[218] The properties of HOE are particularly interesting for our purposes because: DNA-unbound HOE is less fluorescent (ca. 1:30) and emits at a longer wavelength (520 *vs.* 461 nm) than the DNA-bound one; and the dye free or released from the carrier HOE will stain cell nuclei.[218] NCs were loaded with HOE (NC-HOE) by immersion of the former in a HOE solution (methanol). After purification, an average of ~$2.9 \cdot 10^5$ HOE/NC was estimated by fluorescence measurements (Figure S3.3).

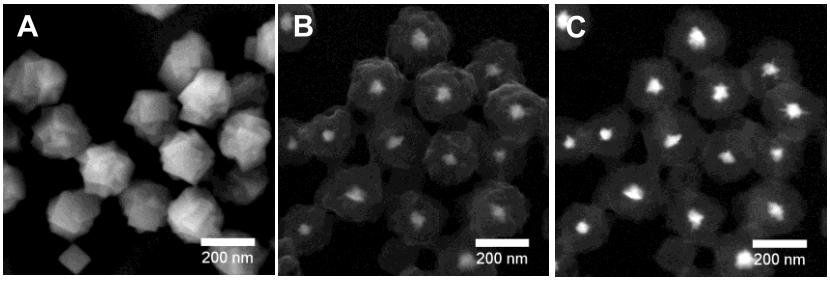

Figure 3.2. SEM micrographs of NCs; images acquired at different voltages and different detectors.

A) Everhart-Thornley detector (SE2, secondary electrons) at 3 kV; B) InLens detector (SE1, secondary electrons) at 20 kV and C) AsB detector (backscattered electrons) at 20 kV. Scale bars represent 200 nm.

Next, a polymer grafting strategy was developed to "trap" the HOE inside the ZIF8 voids. To that aim, we employed a post-functionalization strategy based on PMA (Figure S3.4), which has been extensively used for polymer coating of inorganic NPs.[50] After PMA functionalization and redispersion in water, the purified NCs (NC-HOE-PMA) retained the polyhedral morphology and size (Figure S3.5, Figure S3.6 and Figure S3.7), bluish aspect (colour and turbidity, Figure S3.8) and the hydrodynamic diameter (d_h = 235 ± 85 nm by DLS, Figure S3.9and Table S3.1) of the original NCs, with a ξ-potential of −27.5 mV, consistent with that obtained from other PMA-coated NPs.[50] After PMA-functionalization, the HOE loading dropped to ~40% of the original content (~$1.2 \cdot 10^5$ HOE/NC), suggesting that some dye-leaking occurred during PMA-functionalization and/or PMA partially replaced the dye within the porosity. PMA and non-PMA samples exhibit the characteristic Bragg peaks of ZIF8 and Au^0, confirming that PMA-functionalization does not affect the ZIF8 shell crystallinity (see powder X-ray diffraction (PXRD) in Figure S3.10 and Table S3.2, Table S3.3 and Table S3.4).

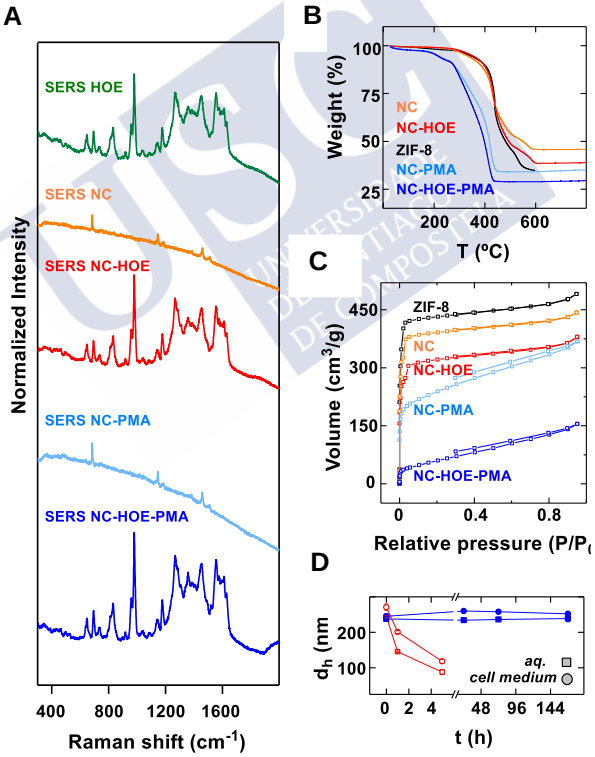

Figure 3.3. NCs characterization: SERS, TGA, N_2 absorption isotherms and colloidal stability in aqueous medium.

A) SERS spectra of free HOE and NCs with or without HOE entrapped: HOE, NC and NC-HOE in methanol, and NC-PMA and NC-HOE-PMA in water. B) TGA of the different NCs. C) N_2 sorption isotherms at 77K of the different NCs. D) Mean d_h during one week for the NC (red) and NC-PMA (blue) systems in water (squares) and cell medium (circles).

To test the encapsulation of HOE into the MOF composites, we studied the SERS spectra of the different NCs (with and without PMA and/or HOE) and free HOE (Figure 3.3). The plasmonic NCs without HOE were dominated by the characteristic vibrational modes of ZIF8 (the imidazole ring puckering, 685 cm^{-1}; the CN stretching, 1146 cm^{-1} and the CH waging, 1460 cm^{-1}).[219] Notably, when the NCs were loaded with HOE, none of these vibrational features can be observed as a consequence of the strong signal promoted by the dye in close contact with the plasmonic surface (ring breathing, 980 cm^{-1}; CH deformation 1270 and 1455 $cm^{-1}$and CC and CN stretching, 1554 and 1575 cm^{-1}).

To investigate the thermal behaviour of the prepared NCs and pristine ZIF8, thermogravimetric analysis (TGA) was performed under air atmosphere (Figure 3.3E). The samples without PMA showed a sharp weight loss (50–60 wt%) at around 400 °C, associated with the total combustion of 2-methylimidazole and the formation of different inorganic residues: ZnO in case of ZIF8, or ZnO and Au^0 in case of NC and NC-HOE, as identified by XRPD of the residues (Table S3.5and Figure S3.11). In contrast, the presence of PMA is evidenced by the more abrupt weight loss before 400 °C on PMA-modified samples. They showed an initial mass loss (~10 wt%) associated with the PMA glass transition (150–250 °C) and final departure (~20 wt%) at around 250–350 °C.[50] Finally, weight loss is followed by the combustion of the 2-methylimidazole as in non-PMA samples (~400 °C). The different inorganic residues served us to estimate the relative content of Au, PMA, ZIF8 and HOE among samples (Table S3.5).

N_2 sorption measurements at 77K of ZIF8, NC, NC-HOE, NC-PMA and NC-HOE-PMA show type I isotherms (Figure 3.3F), characteristic of microporous materials, with a Brunauer-Emmett-Teller specific surface areas (S_{BET}) of 1800, 1570, 1260, 850 and 220 $m^2 \cdot g^{-1}$, respectively. The normalization of the S_{BET} by the porous ZIF8 weight shows no significant difference between the ZIF8 and NCs, indicating that the ZIF8 shell shares the same textural properties as the pristine ZIF8 (Table S3.6). Counter like, the important reduction of the microporousity (normalized S_{BET} before and after HOE encapsulation ~1800 versus 1500 $m^2 \cdot g^{-1}$) confirms that the HOE is allocated within the ZIF8 shell. Importantly, corrected surfaces indicate that PMA, besides providing an outer coating for the NPs, partially fills NC-PMA ($S_{BET} \approx 1440$ $m^2 \cdot g^{-1}$), which is concordance with the results found by fluorescence (~60% HOE loss after PMA, final corrected $S_{BET} \approx 470$ $m^2 \cdot g^{-1}$). Furthermore, the additional and progressive N_2 sorption at higher pressures (P/P_0 = 0.3- 0.9) in the PMA associated samples suggests the gas adsorption on the superficial polymer branches (0.25 $cm^3 \cdot g^{-1}$ in NC-PMA versus 0.06 $cm^3 \cdot g^{-1}$ in the pristine ZIF8). Of note, the volume occupied by HOE in NC (estimated from the total HOE content and N_2 sorption measurements: V~0.13 $cm^3 \cdot g^{-1}$, see Table S3.6 and Figure S3.12, and from fluorescence data: V~0.15 $cm^3 \cdot g^{-1}$, see SI) is within the range of its theoretical volume (V~0.24 $cm^3 \cdot g^{-1}$, estimated by taking into account the volume of a HOE

molecule under vacuum and its loading in the solid, see Appendix). In fact, although the estimated HOE dimensions (18.5×4.1×4.1 Å) are slightly larger than the accessible windows of ZIF8 (~3.6 Å),[220] the potential HOE rearrangement and the flexibility of ZIF8,[221] support the HOE location within the porosity, being consistent with SERS results.

Colloidal stability of the PMA- and non-PMA functionalized systems was evaluated in water and cell medium during one week by DLS (Figure 3.3D, Figure S3.13 and Table S3.7). The integrity of non-PMA samples was compromised in both media as reflected by the rapid decrease of d_h (< 5 h). SEM inspection of NCs redispersed in water illustrates their "disintegration" (Figure 3.4). By simple visual inspection, one could also see how the characteristic turbidity of the NC gradually disappears within few hours (Figure 3.4). In contrast, d_h of PMA samples remained stable, indicating that water or cell medium did not affect their integrity, which was also corroborated by SEM inspection of NC-PMA after dispersion for over one week in water (Figure S3.5).

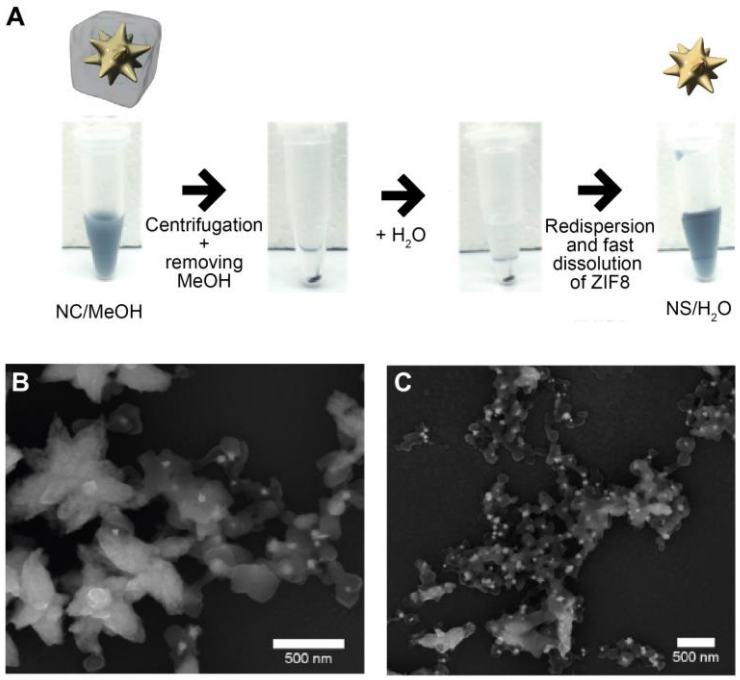

Figure 3.4. NC degradation on water.
A) Assay to check the lack of stability of NC particles in aqueous solution. NC particles initially stable in MeOH were centrifuged, MeOH (supernatant) was removed, and the NC particles (precipitate) were redispersed in water, resulting in the dissolution of the ZIF8 shell around the NSs. B-C) SEM micrographs of NCs (after exposure to aqueous solution, without centrifugation/purification) after drop casting on Si substrates.

To investigate the thermoplasmonic behaviour of the samples, non-PMA (in methanol, see Figure S3.14A) and and PMA-functionalized (in water, see Figure 3.5A) systems, solutions at different concentration were irradiated during 1 min (7 W·cm^{-2}) with a NIR optical system (Figure 2.16 in the previous chapter). The bulk temperature of the solutions after NIR excitation was measured, showing the expected thermoplasmonic behaviour: the greater the concentration, the higher temperatures were achieved (~46°C – 56°C). After irradiation, samples were precipitated and the HOE content (released) was quantified by fluorescence (Figure 3.5A). In both non-PMA and PMA systems, the same trend was observed: irradiated samples showed a much higher HOE release than the control ones, that is, samples heated in a thermostatic batch (1 min, 50 °C), or non-treated ones (RT). To investigate the encapsulation efficiency of the NC-HOE-PMA system, HOE release was quantified in the irradiated (1 min, 7 W·cm^{-2}) and non-irradiated (RT) control samples, at different time points: 0, 8 and 24 h after irradiation. In the non-irradiated samples (RT), either in water (Figure 3.5B) or in phosphate buffered saline (PBS, Figure S3.14), HOE release were maintained negligible (≤ 1%) over time, in contrast to the NC-HOE system in methanol in which HOE's sustained release occurred, reaching ~ 20% HOE's release after 24 h (Figure S3.14). In the irradiated NC-HOE-PMA system in water or PBS, the initial HOE release (t=0, ~30% of the maximum HOE loading) remained nearly constant over time. On the other hand, the NC-HOE system in methanol showed a 10% HOE release after irradiation, which was progressively increased due to the inherent sustained release of the non-PMA system in methanol (Figure S3.14). After irradiation, NCs maintain their morphologies as it is shown in Figure S3.15.

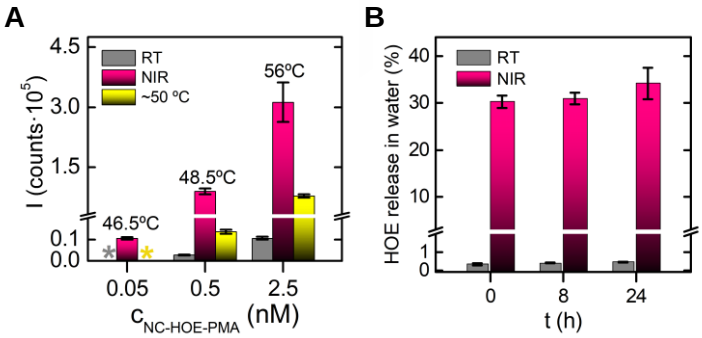

Figure 3.5. HOE release after NIR illumination.

A) HOE release in water by fluorescence (I) after NIR illumination (1 min, 7 W·cm^{-2}) of the NC-HOE-PMA system (pink) at different concentrations (*c*); as controls, NC-HOE-PMA was heated in a thermostatic bath (50 °C, 1 min, yellow) or non-heated (grey, RT); control samples at c = 0.05 nM did not show any significant HOE release (* bellow the detection limit). B) HOE release (% of maximum HOE loading) in water for the NC-HOE-PMA system (pink, c = 0.5 nM) immediately (0 h), 8 h and 24 h after NIR illumination; as controls, non-treated equivalent samples (grey, RT) are shown (HOE release < 0.5 %).

HOE loaded, non-PMA and PMA NC systems were added to adherent cells (see section 3.3). The viability of cells was similarly affected by both systems, showing the expected characteristic dose-response behaviour (2–300 nM NCs, Figure 3.6).

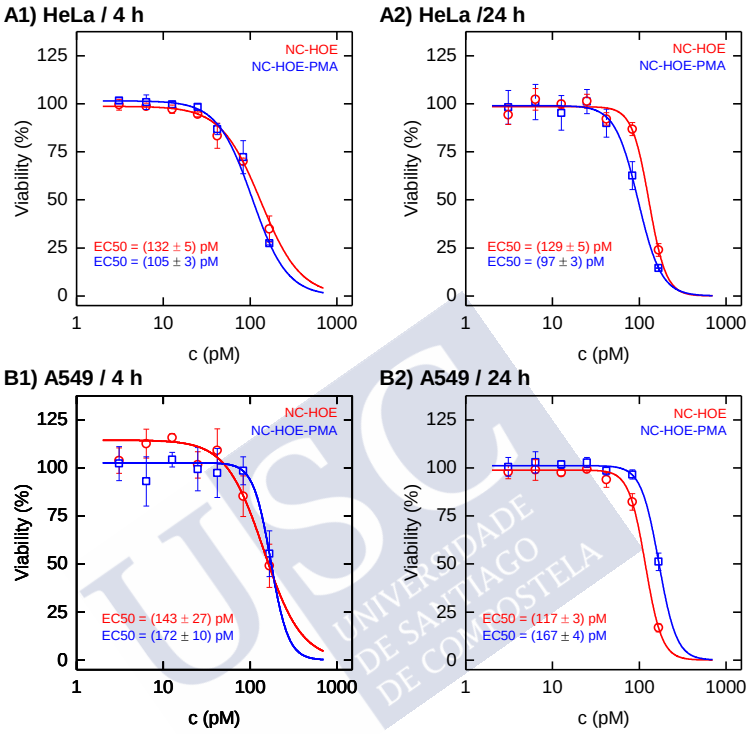

Figure 3.6. Cell viability using the resazurin assay

HeLa cells (A) and A549 cells (B) under exposure to increasing concentrations of the particles before (NC-HOE) and after PMA-functionalization (NC-HOE-PMA), evaluated at two incubation times: 4 h (1) and 24 h (2). Half-maximal responses (EC50 values) were calculated by fitting (logistic function in OriginLab, fixing minimum viability to 0 %).

The intracellular monitoring of cargo delivery upon illumination with a NIR light (785 nm, 3 mW) was carried out by using SERS imaging with a confocal microscope. Figure 3.7A shows the SERS spectra and Figure 3.7B the HOE intensity (ring breathing, 980 cm^{-1}) registered in the mapping of cells (Figure 3.7C) for both NCs loaded with HOE in the presence and absence of light irradiation. No signal belonging to HOE was detected for NC-HOE. This is consistent with degradation of the ZIF8 in water previously to cell uptake. Conversely, in the case of NC-HOE-PMA, a clear HOE signal was observed in certain regions of the cell (likely in lysosomes)[222] previously to light illumination. In fact, after 8 h of irradiation, no HOE signal could be discerned. However, the release kinetics clearly show that ~75% of the HOE is released during the first 2

h of illumination. These results contrast with those obtained for the same material but without continuous illumination. At time 0 and after 8 h SERS spectra show clear HOE signals indicating that the integrity of the drug carrier was not compromised.

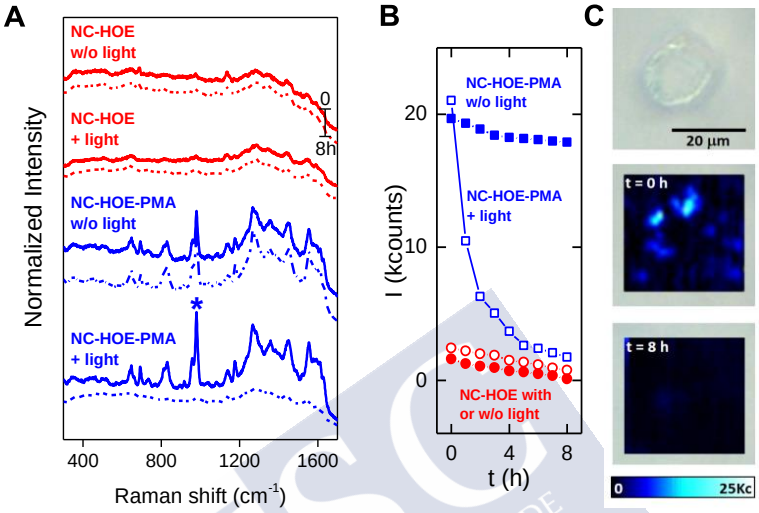

Figure 3.7. SERS cell studies.

A) SERS spectra of the NCs after incubation with cells. Spectral kinetics data were acquired with and without NIR illumination (785 nm); solid and dashed lines represent the time points 0 h and 8 h, respectively. B) SERS intensity of the ring breathing of HOE (980 cm^{-1}) with time for both materials, with and without NIR light. C) Representative SERS imaging of a single cell incubated with NC-HOE-PMA. Optical image (top) and SERS images at time 0 (middle) and after 8 h of irradiation (down).

SERS data fully agree with equivalent studies by confocal microscopy. Firstly, cell uptake of NC-HOE-PMA system in which PMA was fluorescently labelled with a rhodamine (see section 3.3) was confirmed by confocal microscopy (Figure 3.8 and Figure S3.16). Then, NC-HOE-PMA showed accumulation (blue coloured dots) in the vicinity of the nuclei, which did not present blue-staining due to the lack of HOE leakage(Figure 3.9B, Figure S3.17); in contrast, as expected from the stability studies and SERS imaging, the non-PMA system showed bright nucleus staining as consequence of the HOE leakage (that is, lack of integrity of the non-PMA system in cell medium, Figure 3.9A, Figure S3.18). Finally, NIR-induced HOE-release from the PMA system inside living cells was attempted. Cells containing NC-HOE-PMA were irradiated with the NIR illumination setup (5 min, 7 $W \cdot cm^{-2}$, beam diameter ~1 cm^2) and samples were immediately inspected in the confocal microscope, which showed the HOE release, as can be concluded from the nuclei staining (Figure 3.9C, Figure S3.19).

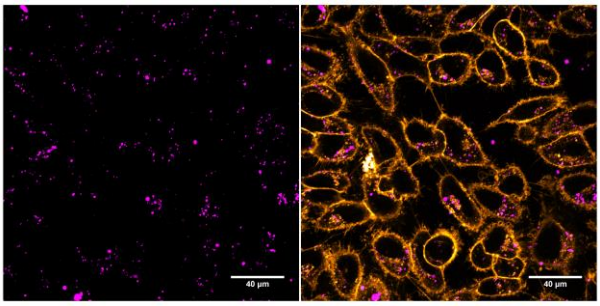

Figure 3.8. Collage confocal microscopy images for NC-HOE-PMA(rhodamine) system. Pink channel (left) and merged orange + pink channels (right); at 60X magnifications. Pink and orange colours represent rhodamine and cell membrane staining respectively (CellMaskTM Deep Red). Scale bar is 40 μm.

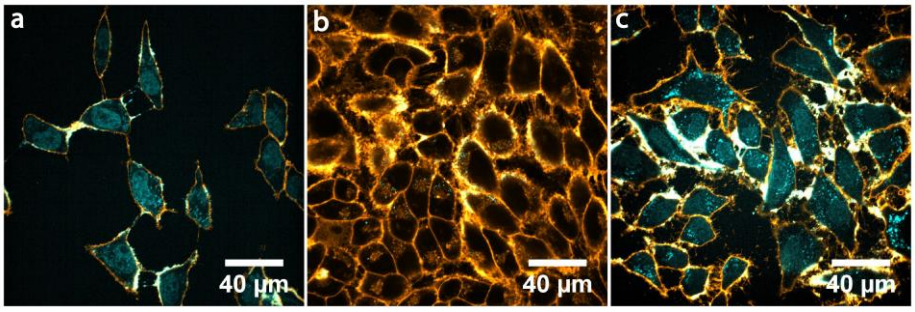

Figure 3.9.NIR irradiation confocal cells studies with NC-HOE-PMA.
a) Cells incubated with NC-HOE; b) NC-HOE-PMA and c) NC-HOE-PMA after NIR treatment. Cyan and orange colours represent HOE and cell membrane staining (CellMask™ Deep Red), respectively. Scale bars represent 40 μm).

3.3. MATERIALS AND METHODS

For detailed experimental methods and additional results see section *Chapter 3 Appendix*.

Preparation of PMA-modified NS/ZIF8 NCs. The here designed and studied NCs consisted of a NS core and a ZIF8 shell, which was further functionalized with a polymer (PMA). The synthetic method involved four main steps: i) CTAB-coated NS were first synthesized with previously prepared Au NPs seeds and with CTAB as capping agent and stabilizer; ii) these NS were then used as seeds (NS at a concentration of 2 nM in $5 \cdot 10^{-4}$ M CTAB aqueous solution) onto which a shell of ZIF8 was grown by following an aqueous procedure in which the surfactant CTAB works as size-controlling and structural-directing agent; iii) NCs loading with HOE (NC dispersed in MeOH at 0.67 nM, 1 mL, incubated overnight at RT with a

solution of HOE in MeOH at 1.87 mM, 100 µl); iv) finally, in order to provide colloidal stability in diverse complex aqueous media, these NS-ZIF8 core-shell particles were wrapped with the amphiphilic polymer PMA before last washing steps.

Characterization techniques. SEM and TEM were used to study the size and morphology of the nanomaterials. SEM images were acquired with a FESEM Zeiss Ultra Plus operated at 3 kV and 20 kV. TEM images were acquired with a JEOL JEM-2010 microscope operated between 80 and 200 kV accelerating voltage. ImageJ free software and Origin software were used for the size measurements and distribution analysis, respectively. UV-Vis absorption spectra and fluorescence spectra were acquired using Jasco V-670 spectrometer and Varian Cary Eclipse fluorescence spectrofluorometer, respectively. An X-ray diffractometer Philips was used to study the crystallinity of the samples, operating in the range of 2θ between 2° and 75° with a passage of 0.02° and a time by step of 2s. A Malvern Zetasizer (Nano ZSP) instrument, equipped with a 10 mW He–Ne laser operating at a wavelength of 633 nm and fixed scattering angle of 173˚, was used to measure the hydrodynamic diameters (by DLS) and the ξ-potentials (by LDA). ICP-MS measurements were performed using an Agilent 7700x ICP-MS after acidic digestion of the samples with aqua regia. Thermogravimetric analysis (TGA) of powder samples (freeze-dried) was performed using a TA Instruments Inc, SDT Q-600 thermobalance with a general heating profile from 30 to 600 °C with a heating rate of 5 °C·min^{-1} under air using a flux of 100 mL min^{-1}. SERS imaging was performed using a Renishaw Invia system with a high-resolution grating of 1200 g cm-1 and a NIR laser (785 nm).

Laser irradiation experiments. An 808 nm laser (Lasing, #FC-W-808A) connected to a zoom fiber collimator (Thorlabs, #ZC618SMA) was used to perform all irradiations. To obtain the spot size an infrared viewing card (Thorlabs, #VRC4) was used to see the spot and ImageJ to measure it. As the beam is collimated (see fabricant details for laser collimation conditions), a homogeneous spot is produced and, thus, the irradiance can be easy calculated just dividing the power by the spot surface (in cm^2) (see Figure 2.16). Different time and irradiance conditions (as well as spot sizes) were performed as it is indicated in each experiment procedures.

Cell studies. Hela (cervical cancer cell line) and A549 cells (adenocarcinomic human alveolar basal epithelial cell line) were cultured in DMEM with phenol red, 4.5 g/L D-glucose, L-glutamine and pyruvate (DMEM, 1X, Gibco, #41966-029) supplemented with 10 % FBS (Gibco, #10270-106) and 1% P/S (Corning, 100X, #30-002-CI). Cells were maintained under humid conditions at 37 °C and 5 % of

CO_2. Cells were passaged after cleaning (PBS, 1X, Gibco, #14190-094) with 0.25 % Trypsin-EDTA (1X, Gibco, 25200-056) when the culture reached confluency.

- *Cell viability.* In order to study the number of viable cells after NPs exposure, we carried out resazurin assays, *cf.*Figure 3.6. HeLa and A549 cells were seeded in 96-well plates (NEST Scientific, #701001), 7500 cells per well in 100 µL of cell growth medium (0.3 cm^2 *per* well) 24 h before NPs exposure. Then, cell medium was removed and 100 µL of fresh one with the desired concentration of NPs were added. We incubated the cells with the NCs along the time of interest (4 and 24 h) at 37 °C and 5 % CO_2. After that, we rinsed each well three times with PBS and added 100 µL of freshly prepared solution with 90 % of medium and 10 % of resazurin (resazurin sodium salt in water 0.2 mg/mL filtered, Sigma Aldrich, #199303-1G). Cells were incubated during 3 h at 37 °C and 5 % CO_2 under dark conditions before being measured with a plate reader (Infinite® 200 PRO, Tecan, Switzerland) under 560/20 nm excitation and collecting fluorescence with a 610/20 nm filter. Final values were calculated using Eq. 3 (Figure 3.6).

- *Confocal imaging.* Typically, 20000 HeLa cells in 200 µL were seeded on µ-Slide 8 well-ibiTreat chambers (1 cm^2 *per* well, Ibidi, Germany, #80826) at least 12 h before the particle exposure. Our NCs were diluted to a concentration of 50 pM in culture media. After 4 hours, cells were cleaned three times with fresh PBS in order to remove particles non-associated with cells. Confocal images of living cells were captured on an Andor Dragonfly spinning disk confocal system mounted on a Nikon TiE microscope equipped with a Zyla 4.2 PLUS camera (Andor, Oxford Instruments) and an OKO-lab incubator to keep cells at 37 °C during all the experiment. Images were taken with different magnification objectives (20X, 60X, 100X). HOE fluorescence was measured with an excitation of a 405 nm laser and a 450(50) nm filter. For cell membrane staining, we made a CellMask™ Deep Red (ThermoFisher, #C10046) dilution with 1 µL in 1000 µL of DMEM. We added 100 µL of this staining solution to the cells and we incubated them during 3 minutes at 37 °C in dark conditions. After this, we cleaned again three times with PBS. CellMask™ Deep Red channel was obtained under the excitation with a 637 nm laser and using the 725(40) nm filter (Figure S3.18, Figure S3.17 and Figure S3.19).

Additional confocal microscopy images of the NC-PMA system in which PMA was fluorescently labelled with a rhodamine, are shown in Figure S3.16, aiming to illustrate the efficient cell internalization (HeLa cells) of the NC-PMA system proposed (50 pM, equivalent conditions to Figure S3.17). All the images were processed with ImageJ.

- *Laser irradiations.* After checking the cells with the NC-HOE-PMA nanosystems to the microscope without treatment, we performed an irradiation

protocol as follows: we used an 808 nm laser (Lasing, #FC-W-808A) with a zoom fibre collimator (Thorlabs, #ZC618SMA-B) to control the spot size as well as irradiate cells homogeneously, cf. Figure 2.16. In order to calculate the intensity in W·cm-2 that cells received, we used a power energy meter (Thorlabs, #PM100D) with a thermal power head (10 W, 25 mm, Thorlabs, #S425C) to measure the output power. To obtain the spot size we used a viewing card (Thorlabs, #VRC4) to see the spot and ImageJ to measure it. Since the beam is collimated, we consider a homogeneous spot and thus, we can obtain the intensity just dividing the power by the surface (in cm2) of the spot. We performed different time and power conditions and chose 5 min at 7 W·cm-2.

- *SERS imaging.* To perform SERS imaging with living cells, A549 cells were seeded at a density of 60000 cells/cm^2 onto a Nunc™ Δ-Petri Dishes (Thermo Fisher Scientific). After 16 h of culture, A549 cells. NC-HOE and NC-HOE-PMA systems were redispersed in MeOH or in sterile Milli-Q water, respectively, at a concentration of 0.5 nM. NCs were added to A549 cells to a final concentration of 50 pM and kept in the incubator for 4 h. At the end of the experiment, culture media with non-internalized NCs was discarded, and cells were inspected in the SERS confocal microscope. The laser was focused onto the samples with a 5x objective, providing an optical resolution of 1 µm. The inelastic radiation was collected with a Renishaw Invia system by using a high-resolution grating of 1200 g cm^{-1} and a NIR laser (785 nm). Samples were studied in single points or by mapping extended areas with the Renishaw StreaLine accessory. Experiments with and without light were carried out as follows. For NIR illumination, cells were placed under the microscope and illuminated continuously with 3 mW of power at the sample. Spectra were collected every hour at 0.3 mW with acquisition times of 10 s. This difference of power was set to minimize the effect of the laser on the composites during the collection

3.4. CONCLUSIONS

In conclusion, our approach is an important step forward in the development of MOF-based intracellular vehicles for drug vectorization. A plasmonic core-shell nanostar/ZIF8 nanocomposite was developed for thermoplasmonic-driven release of encapsulated molecules inside living cells. The nanocomposites were loaded, as a proof of concept, with HOE molecules as functional cargo (DNA staining) and wrapped with an amphiphilic branched polymer (PMA) that prevents ZIF8 degradation and HOE leaking in aqueous media and inside living cells. The molecule-release mechanism relies on the use of NIR light coupled to the plasmonic absorption of the core AuNS, which creates local temperature gradients, thereby leading to increased cargo diffusivity. The

molecule-release mechanism was demonstrated in aqueous solution. Confocal microscopy and SERS were used to demonstrate bisbenzimide loading/leaking and NIR -triggered cargo-release inside cells, thereby leading to DNA staining.

USC
UNIVERSIDADE
DE SANTIAGO
DE COMPOSTELA

4. PLASMONIC NCS FOR NIR TRIGGERED REACTIONS

PLASMONIC-ASSISTED THERMOCYCLIZATION USING MOF-BASED NANOREACTORS IN LIVING CELLS

4.1. INTRODUCTION

Living cells respond to external signals through cascades of connected chemical reactions that take place at physiological temperatures. Most of these reactions are catalysed by enzymes and have been selected by evolution to ensure an appropriate functioning of living organisms.[223] A major current goal in chemical and cell biology consists of the development of new-to-nature, intracellular reactions that allow to implement non-native functions, thereby influencing the properties of cells in a predictable manner.[224] The last two decades have witnessed a sustained progress in the development of a variety of bioorthogonal and biocompatible reactions, most of which are based on the use of strained reactants, or on metal-mediated transformations.[225-226] While these processes have led to impressive advances and applications,[227] they are not devoid of important drawbacks, such as the intrinsic reactivity of the strained reactants, or the problems of biocompatibility and efficiency of the metal-based reagents.[224]

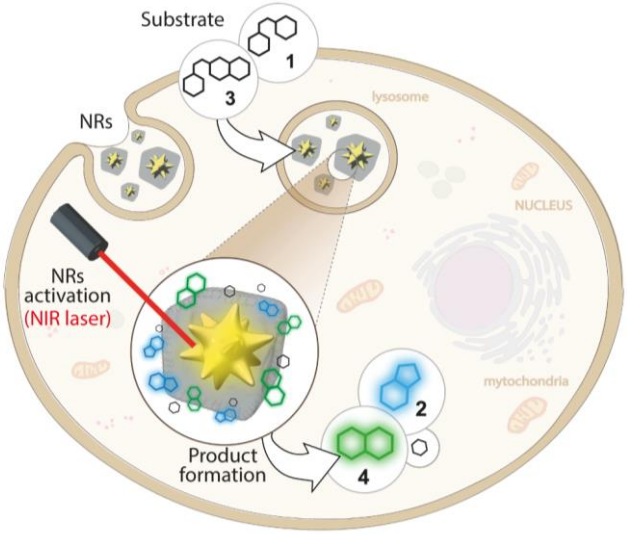

Figure 4.1. Core-shell MOF-based plasmonic NR for intracellular photothermal reactions. NRs comprising a NS coated by a porous polymer-modified ZIF8 cloak are colloidally and structurally stable in aqueous media and work as heterogeneous photo-gated nanoreactors capable of transforming (thermocyclization) thermolabile substrates inside living cells.

An alternative to these reactions could be based on the development of thermal-driven processes, as this would allow for using stable reactants and control their reactivity using a thermal stimulus; however, it is obvious that cells cannot be heated above physiological temperatures. We envisioned that this problem may be solved by using plasmonic NPs as NIR-responsive thermal transducers, provided that the chemical reaction can be located near these heating generating units. This requires the accumulation of the reactants near the heated NPs, which is not obvious, and by avoiding the passivation of the NP surfaces that is expected when they are exposed to biological media crowded with manifold "sticky" biomolecules.[228]

Herein we demonstrate the viability of this approach by reporting the first thermal-promoted chemical reaction, in this case a nucleophilic substitution (thermocyclization), that takes place inside living mammalian cells (Figure 4.1). We show that locating gold nanostars (NS) inside appropriately designed ZIF8 NPs enables for very efficient NIR-induced intramolecular nucleophilic substitutions (Figure 4.2). Key for the success of the approach is the microporous structure of the ZIF8 based nanoshell, which allows an efficient internal flow of reactants near the heating source, that is, the NS core under NIR excitation.

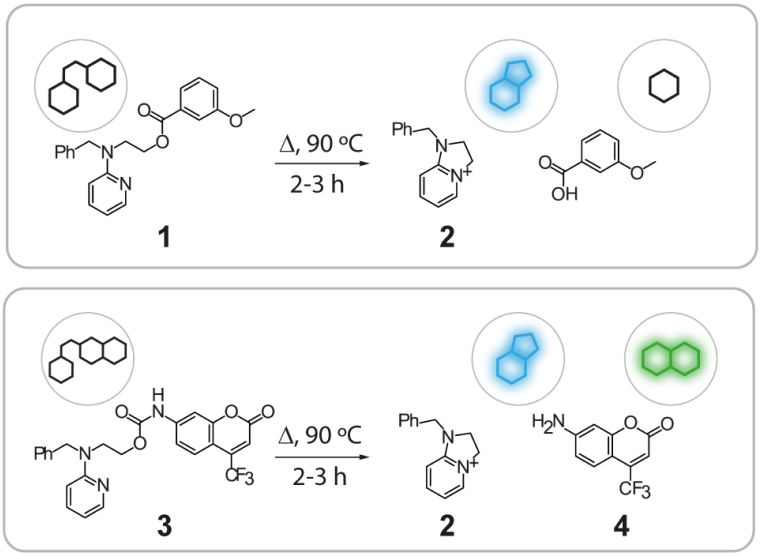

Figure 4.2. Reacting probes used in this study (substrates 1 and 3), and fluorescent products (2 and 4).

Products are resulting from a thermoplasmonic-promoted reaction (Figure S4.1), see section 6.3.1). Thermocyclization of substrate **1** releases an aromatic carboxylic acid upon nucleophilic intramolecular displacement by the pyridine group (product **2**); in addition to product **2**, thermocyclization of substrate **3**, which holds a carbamate as leaving group, undergoes a concomitant decarboxylation reaction delivering an amine moiety, in this case a fluorogenic coumarine **4**.

The use of photothermal properties of plasmonic NPs for photo-induced local heating is well precedented.[43] These properties are particularly useful for biological applications because the heating can be triggered by NIR light sources,[109] which are typically used to excite the corresponding plasmon band of anisotropic metal NPs, usually gold NPs[229-230] such as nanorods,[14] nanostars[231] and nanoprisms.[232] The thermoplasmonic approach has been used in biomedically relevant applications such as photothermal therapy (analogous to magnetic-induced hyperthermia for treatment of solid tumours) and NIR-gated delivery of payload in tissues and cells.[43]

Plasmonic photocatalysis, both hot carrier and thermal-based contributions, has also been demonstrated for various reactions such as ammonia decomposition,[233] oxygen dissociation[234] and carbon dioxide hydrogenation,[235] among others.[236] In these reactions, pulsed illumination is required, which in a irradiance-dependent manner can lead to NP reshaping and vapor nanobubbles.[237-238] However, the use of thermoplasmonic heating effects for achieving thermal-promoted chemical reactions inside living cells, either with pulsed or continuous wave (CW) light sources, has not been described. A recent report on the intracellular removal of propargyloxycarbonyl groups using silica-plasmonic constructs are based on the action of catalytic gold nanocrystals, in which NIR irradiation is proposed to accelerate the uncaging reaction, rather than on simple heating.[239] Moreover, it deals with typical uncaging reactions that might be alternatively performed using palladium catalysts[240] as well as NP-based gold catalysts without light stimulation.[241]

4.2. RESULTS AND DISCUSSION

Our initial work herein was prompted by our recent discovery that the modification of ZIF8 structures with the amphiphilic polymer PMA (Figure 4.3), renders the nanocomposites stable in aqueous media and even inside living cells.[231] We thus hypothesized that placing a plasmonic core (NS) in the interior of the microporous ZIF8 based shell might allow to install light-responsive nanoreactors (NRs) in the interior of cells. Although in non-biological contexts, related composites of plasmonic NPs immobilized in mesoporous materials such as alumina[234] and silica, have been described.[242] More recently, different MOF based combinations have been proposed for thermoplasmonic catalysis in solar energy conversion.[243] Moreover, plasmonic nanocomposites comprising silica-supported plasmonic NPs have been also used for encapsulation of drugs, which can then be intracellularly released upon resonant plasmonic excitation.[244]

We designed nearly monodisperse NRs with diameter ~ 220 nm (Figure S4.2), which remain colloidally stable in water and cell medium as confirmed by DLS (hydrodynamic diameter, d_h ~ 240 nm; Figure S4.3, Table S4.1). The core-

shell nanocomposite contains a single NS per particle that provides NIR plasmonic absorption (Figure S4.3) and thereby, can be used for repeated photothermal heating using a homogeneous NIR 808 nm irradiation set up (Figure 4.4a, Figure 4.12).

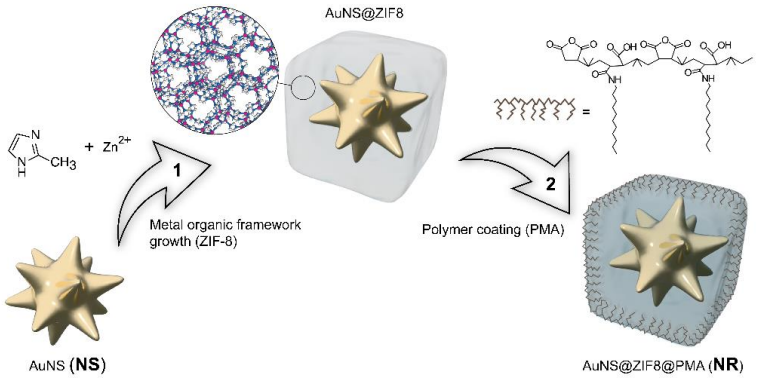

Figure 4.3. Schematic illustration of the synthetic procedure of PMA-modified NS/ZIF8 nanoreactors (NRs).

To investigate their photothermal behaviour, aqueous solutions of our NRs (200 µl of 1 nM NRs solution or 0.2 pmol in total) were irradiated for different irradiation doses (Figure S4.4, Table S4.2), varying both irradiance (2, 4 or 8 $W \cdot cm^{-2}$) and exposure time (2, 5 or 10 min). In contrast to our engineered NRs, surfactant-stabilized NSs do not sustain repeated illumination cycles and gradually lose their heating capability (Figure S4.5a), likely due to heating-induced aggregation; this can be prevented by pre-stabilizing NSs with FBS (FBS-stabilized NSs, Figure S4.5b). Importantly, distinct heating profiles for our NRs compared with those for both surfactant- and FBS-stabilized NSs, were observed (Table S4.1 and Table S4.2). Although using equivalent experimental parameters (200 pmol of particles, NRs or NSs in water, 8 $W \cdot cm^{-2}$ applied for 5 min), the maximum bulk solution temperature is very similar among the samples (T_{max} ~76 °C, ΔT ~ 54 °C); however, the heating rate for the NRs (~ 0.5 min^{-1}) is significantly damped compared with that for the NSs (~ 0.8 - 1.0 min^{-1}, Table S4.3). This is in agreement with previous work indicating that differences in thermal dissipation upon resonant illumination of core-shell gold-silica nanoparticles with varying silica thickness are ascribed to the varying thermal conductivity of the silica shells.[245] In the case of our NR particles, the intrinsically low thermal conductivity of the ZIF8 shell compared to that of water,[246] leads to a higher thermal confinement (of most importance for the foreseen application) and thus a lower heating rate than in the case of surfactant- or FBS-stabilized NSs. Notice, for instance, that while in the case of NSs three irradiation cycles require less than 35 min (Figure S4.5), an analogous experiment with NRs requires ~ 45

min (Figure 4.4a). Cooling to RT (~ 22 °C), either for NRs or NSs, presented similar rates (~ 0.5 min^{-1}). Electron microscopy confirmed that the NR's integrity remains intact after NIR treatment (Figure S4.6).

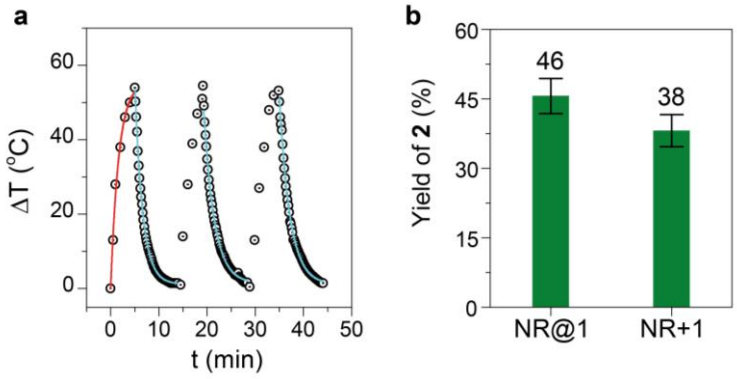

Figure 4.4. Heating/cooling cycles and reaction yields with/without substrates encapsulation.

a) Heating/cooling cycles ΔT versus irradiation (NIR, 808 nm) exposure (t) for 8 W·cm^{-2} applied during 5 min; NRs dispersed in water (0.2 pmol in 200 µl); solid lines represent simulation curves for heating (Box-Lucas function) and cooling (exponential) using the fitting parameters shown in Table S4.3. b) Yield of **2** after NIR treatment (8 W·cm^{-2}, 5 min); NRs dispersed in water (0.2 pmol in 200 µl) with 27 mmol substrate **1**, either encapsulated in the NR (NR@**1**) or "free" in solution (NR+**1**); ratio NR:**1** = 7.7·10^{-4} mol% NR.

With the NRs at hand we decided to test its potential performance as photothermal catalysts in the thermocyclization reactions indicated in Figure 4.4b. We chose this type of transformation for several reasons: i) the lack of precedents on abiotic nucleophilic substitutions in biological media; ii) the requirement of heating; iii) the formation of a cyclic fluorogenic product that allows a straightforward quantification (calibration curves in Figure S4.7) and eventually fluorescence readout inside cells; iv) and the associated release of leaving groups, which might be useful to produce bioactive products.

First, we tested the loading capacity of our NRs, for which substrate **1** was encapsulated into the core-shell NS-ZIF8 particles before the PMA stabilization step (NR@**1**). The process generated the expected particles, containing ~ 1.33·10^5 substrates **1** per particle (*i.e.*, 7.7·10^{-4} mol% NR; see details about the quantification of substrate loaded in section 6.3.5). After transfer to water with the PMA strategy,[231] NR@**1** particles (1 nM particles) were irradiated with our NIR setup (5 min, 8 W·cm^{-2}), leading to bulk heating of the mixture (T_{max} ~ 76 °C) that prompted the formation of **2** (46% yield, Figure 1b, calculated using fluorescence calibration curves, Figure S4.7).

We also tested the NR performance as photoreactors by externally adding substrate **1** to a solution of our NRs (*i.e.*, NR + **1**) using the same NR:**1** mol ratio (*i.e.*, 7.7·10^{-4} mol% NR) and irradiation conditions (5 min, 8 W·cm^{-2}). Gratifyingly,

we confirmed the formation of **2** in a quite similar reaction yield (38%, Figure 4.4b). The slightly lower value with respect to the use of NR@**1** is not surprising since in the case of NR + **1**, substrates must access the plasmonic core NS, being transformed and leaving thereafter the particles.

One demonstrated that our NR particles could work as NIR-gated reactors for promoting nucleophilic substitutions, we tested different substrate **1**-to-NR molar ratios (note that NR's concentration was kept constant ~ 1 nM) and confirmed that, as expected, the reaction proceeds in a ratio dependent manner; that is, increasing the mol% of NR positively affects the yields of **2**, so that using equivalent irradiation conditions (5 min, 8 W·cm^{-2}) and 1·10^{-4}, 2·10^{-4} and 7.7·10^{-4} %mol NR leads to 22%, 33% and 38% yield of **2**, respectively (Figure S4.8a). Importantly, control experiments irradiating either ZIF8 particles lacking the NSs (equivalent to our NRs but without the plasmonic core) or just the "free" substrate, showed virtually no conversion of **1**. Of note, using FBS-stabilized NSs, we observed very poor conversions (Table S4.5), likely due to the combination of two facts:

i. the limited access of substrates to the heated FBS-stabilized NSs

ii. poorer thermal confinement in FBS-stabilized NSs than in our NRs.

This result confirms the relevance of the microporous shell to allow a suitable accumulation of the reactants near the NIR-heated active site. Also relevant, controls using bulk solution heating by immersing the samples in a thermostatic bath (5 min, 80 °C) revealed no reaction (Figure S4.8b, Table S4.5). Notice that in all these controls, equivalent experimental conditions (irradiation, particle concentration and %mol particle) were used, as summarized in Table S4.5.

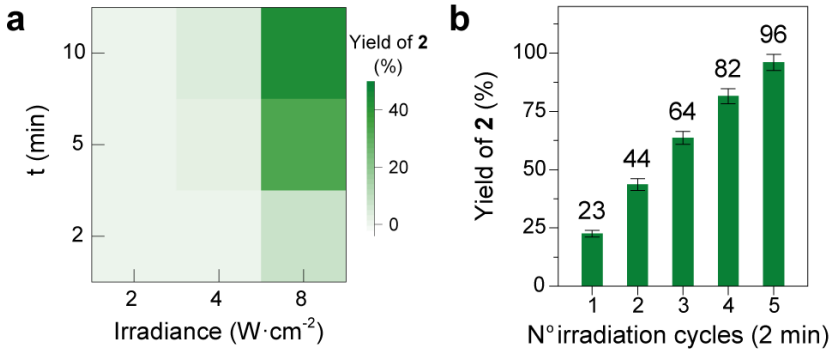

Figure 4.5. Yield of 2 after irradiations: heatmap and cumulative yield.

a) Heatmap of yield of **2** after different NIR irradiations (2, 4 and 8 W·cm^{-2}) applied for 2, 5 and 10 min; NRs dispersed in water (0.2 pmol in 200 µl) with 100 nmol substrate **1**; ratio NR:**1** = 2·10^{-4} mol% NR. b) Cumulative yield of **2** after different NIR cycles (8 W·cm^{-2}, 2 min NIR and 5 min cooling to RT); NRs dispersed in water (0.2 pmol in 200 µl) with 20 nmol substrate **1**; ratio NR:**1** = 1·10^{-3} mol% NR.

The thermal reaction was further tested using different exposure-irradiance combinations, confirming that increasing the exposure and/or irradiance translates into a more efficient production of **2** (Figure 4.5). The reaction can also be extended to other interesting precursors like **3**, which in addition to the cyclized product **2**, generates a fluorescent coumarin **4** (Figure S4.8b, Table S4.5).

Taking advantage of the photostability of our NRs, we inspected their reusability to produce **2**, using two different approaches (Table S4.4). Firstly, we confirmed that the NRs can be recycled, washed by precipitation and reused in up to five independent reactions (1 nM NR, $2 \cdot 10^{-4}$ mol% NR, 8 $W \cdot cm^{-2}$ applied for 5 min) leading to virtually equal yields in all the assays (~ 30% of **2**; Figure S4.9). Secondly, we observed that performing five consecutive irradiations (2 min)/cooling cycles, the conversion of substrate **1** is almost complete (> 96 % of **2**; Figure 4.5b). Equivalently, three consecutive irradiations (5 min)/cooling cycles allowed to reach very high yields (> 85% of **2**; Figure S4.9).

Overall, these results confirm that the observed much-improved performance of our NRs compared with NS must be related to their core-shell nanoarchitecture, in which the MOF-based shell shields the heated NS (thermal confinement) and plays a critical role to provide the substrates with access to the heated core, while allowing an appropriate flow of reactants and products.

Having demonstrated and quantified the photoconversion capability of our NR particles in water, our next aim consisted of demonstrating that the photothermal-responsive reactivity can be performed in the complex milieu of a mammalian living cell. To this end, we first carried out cell viability assays using HeLa cells supplemented with different concentrations of either NRs, FBS-stabilized NSs, substrates (**1** or **3**) and their thermally converted products (**2** or **4**, respectively). This allowed us to set the concentration of reagents and NIR irradiation conditions compatible with cell viability (24 h incubation, Figure 4.6). Accordingly, cells were incubated with particles (NRs or FBS-stabilized NSs, 50 pM) overnight (~18 h); and non-internalized particles were removed by washing with PBS before adding fresh medium, in which the probes of interest (**1**, **2**, **3** or **4**, 10 μM) were previously dissolved, and incubated for 30 min. Before NIR treatment and/or inspection by microscopy or flow cytometry, extracellular probes were removed by washing with PBS.

Cell uptake of fluorescently labelled NRs was confirmed by flow cytometry (Figure 4.7) and confocal microscopy (Figure S4.10); after 12 h of incubation of cells with the NRs we observed saturation of the NR uptake (Figure 4.7). We quantified the average gold content per cell by ICP-MS, which thereby allowed us to estimate the average number of NRs per cell (~ 335). We also quantified the amount of internalized gold when using FBS-stabilized NSs instead of the NRs, observing a decrease in the intracellular gold content per cell (~ 166 NSs). This is likely consequence of the pre-formed protein corona, which in general leads to decreased particle uptake by cells.[247]

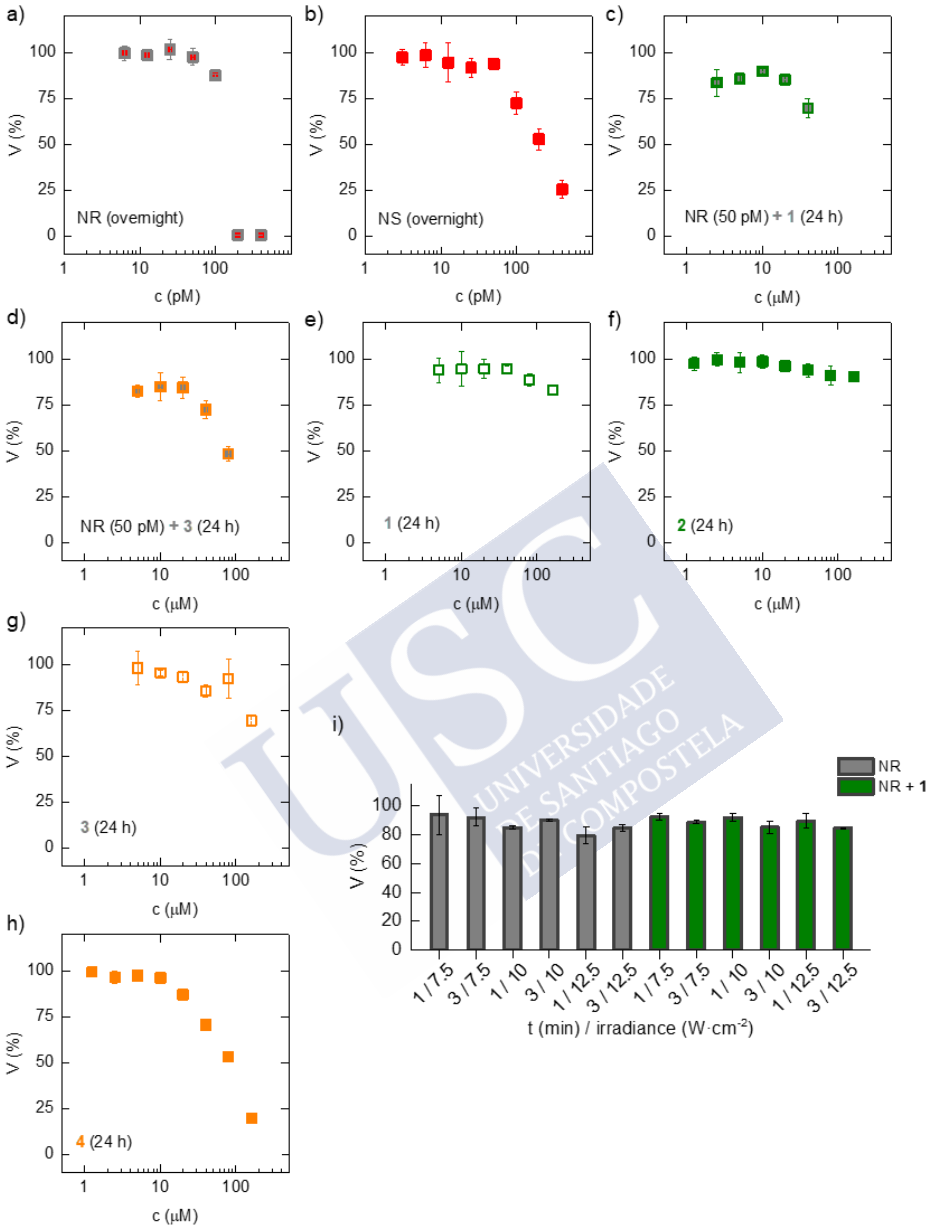

Figure 4.6. Cell viability of cells exposed to increasing concentrations of reactant(s), NRs and/or FBS-stabilized NSs.

a) NRs (50 pM) at 24 h incubation; b) NSs (50 pM) at 24 h incubation; c) **1** at 24 h incubation with NR (50 pM)-preloaded cells; d) **3** at 24 h incubation with NR (50 pM)-preloaded cells; e) **1** at 24 h incubation; f) **2** at 24 h incubation; g) **3** at 24 h incubation; h) **4** at 24 h incubation. i) NIR treatments, varying exposure time *t* (**1** or **3** min) and irradiance (7.5, 10 and 12.5 W·cm^{-2}), of NR (50 pM)-preloaded cells, either after 24 h incubation with **1** (10 mM, green bars) or in the absence of substrate (grey bars). Data expressed as mean ± SD, n=3.

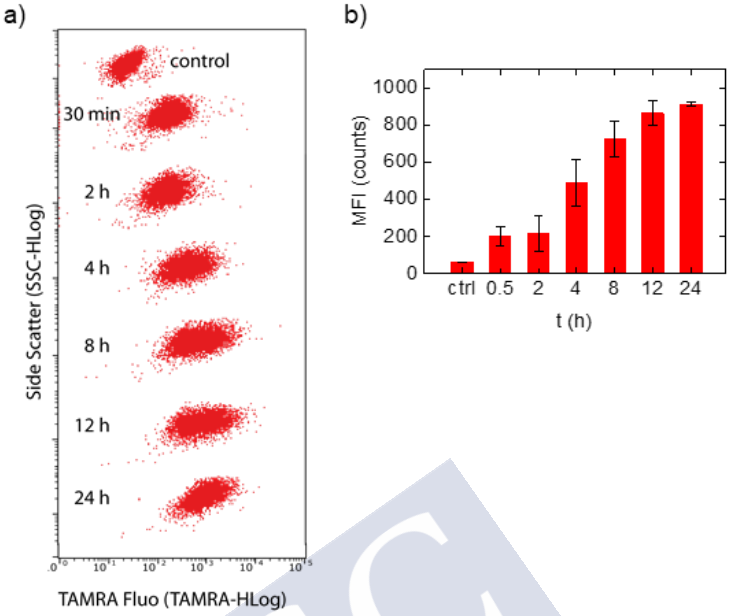

Figure 4.7. Cytometry NRs internalization studies.
a) Scatter density plots of SSC signal versus fluorescence signal (channel Orange-G, Ex. 532 nm, Em. 620/52 nm) for TAMRA-labelled NRs; b). quantification of the MFI of the cellular uptake of TAMRA-labelled NRs in HeLa cells after different incubation times. Data expressed as mean ± SD, n=3.

The intracellular thermolytic deprotections, with both probes **1** and **3**, were performed by incubating the cells with NRs (50 pM, overnight) to obtain NR-loaded cells. The addition of the reaction probes was carried out either pre-encapsulated within the NRs (*approach A*), or posteriori (*approach B*) to NR-loaded cells.

Approach A. Substrates were pre-encapsulated within the NRs (NR@**1** or NR@**3**) before their addition to the cells and overnight incubation. Then, after removing non-internalized particles, fresh cell medium was added and NR(probe)-loaded cells were irradiated using a 785 nm-NIR pointer (diameter ~ 5 µm, circular spot with ~ $5 \cdot 10^5$ W·cm^{-2}), which allows us to irradiate specific regions of single cells, one after another. We tested our hypothesis in cells preloaded with NR@**1** or NR@**3**. Excitingly, we confirmed that the thermolytic reaction proceeds; that is, short irradiations (~ 5 - 10 s) immediately trigger the production of corresponding product **2** (Figure 4.8a, Figure S4.11), as deduced from the clear build-up of fluorescence. In the case of probe **3**, we also observed the characteristic fluorescence of the coumarin **4** released in the process (Figure 4.8b, Figure S4.12).

Approach B. Cells loaded with "empty" NRs were incubated 30 min with probes **1** or **3** (10 µM) and then washed with PBS before adding fresh medium. The NIR pointer (785 nm, ~ $5 \cdot 10^5$ W·cm^{-2}, ~ 5 - 10 s) was used to release product

2 or **4** (Figure 4.8c, Figure S4.13), which illustrate the potential of our NR to function as a NIR-controlled reactor for drug uncaging with spatiotemporal resolution, as illustrated here with the release of **2** and **4** in each case.

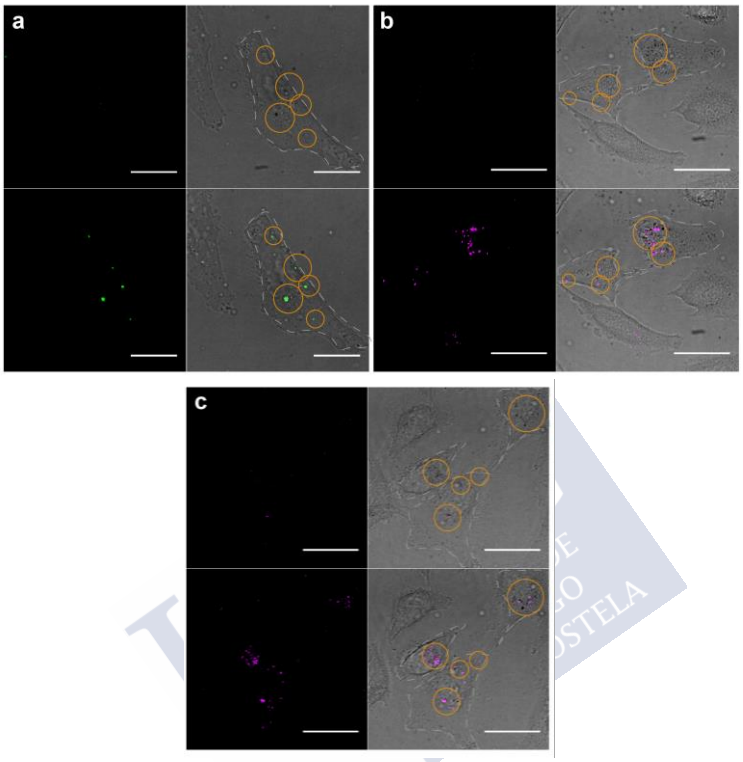

Figure 4.8. NR-preloaded cells before and after NIR pointer irradiation.
Confocal microscopy images after NIR-pointer irradiation (~ 5-10 s) of NR-preloaded cells, for which the probes were pre-encapsulated in NRs (a) NR@**1**; b,)NR@**3**), or substrate **3** was incubated (30 min, 10 μM) and washed before NIR (c). Green represents **2** formation and **4** is represented by pink.

To further address the true potential of our NIR-controlled reactivity, we carried out equivalent intracellular reactions using a collimated NIR beam system (10 W·cm^{-2}, 1 min), which allows for irradiation of thousands of cells simultaneously. We were glad to observe that probe **1** could be efficiently converted into the corresponding thermocyclization product **2** (Figure 4.9b-c). In the case of probe **3**, we observed the typical fluorescence of product **4** (Figure 4.9d). As negative controls experiments shown in Figure S4.14 and Figure S4.16 were carried out. Of note, analogous experiments using cells loaded with FBS-stabilized NS instead of our NRs were done (Figure S4.15, Figure S4.17), in which we did not observe any fluorescence build-up (Table S4.5), as expected from the previous experiments carried out in water.

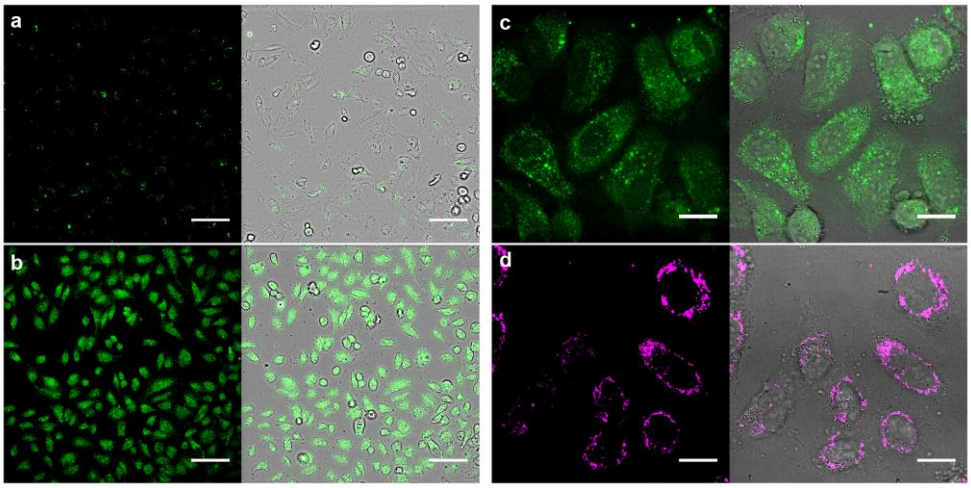

Figure 4.9. Intracellular thermocyclation performance in NR-preloaded cells .
a) Confocal microscopy image of NR-preloaded cells incubated with probe **1**, without NIR treatment (control). b-d) Confocal microscopy images of NR-loaded cells with probe **1** (b,c) or **3** (d), after NIR irradiation using the collimated beam system (10 W·cm^{-2}, 1 min). Green represents **2** formation and **4** is represented by pink. Scale bars correspond to 100 μm (left column, 20X) or 20 μm (right column, 100X).

A comparative analysis using a fluorescence readout (CTCF per cell) confirmed that our NRs drastically outperform FBS-stabilized NSs (Figure 4.10), leaving no doubts about their greater outcome. The reasons for the excellent performance of our NRs inside living cells must be related to the core-shell nanoarchitecture in which the MOF-based shell plays a critical role to produce thermal confinement, while providing the accumulation of reactants near the NIR-responsive heated cores and an efficient efflux of compounds.

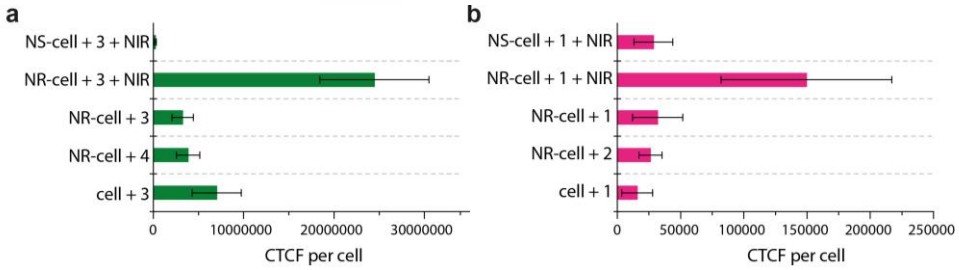

Figure 4.10. CTCF per cell intracellularly generated after 1 **or** 3 **application.**
Comparison of the intracellular fluorescence (CTCF) generated in the NIR-triggered thermocyclization of substrate **1** (a) or **3** (b) achieved by our NR, or by FBS-stabilized NSs; for comparison, controls without NIR treatment and the different probes are included.

4.3. MATERIALS AND METHODS

For detailed experimental methods and additional results see section *Chapter 4 Appendix.*

Synthesis and characterization of the probes. The compounds **1** and **3** were synthesized and characterized in the group of Mascareñas at CIQUS in Santiago de Compostela by adapting previously reported procedures aimed to derivatize carboxylic acids with thermolabile protecting groups.[248] The fluorogenic products **2** and **4** (Figure S4.1), resulting from the thermocyclization reactions depicted in Figure 4.2, were used herein to assess the efficiency of the thermal reactions (yield of the cyclized product **2** and/or release of **4**) in water and inside living cells. Figure 4.11 shows the general synthetic route followed to produce both substrates **1** and **3.**

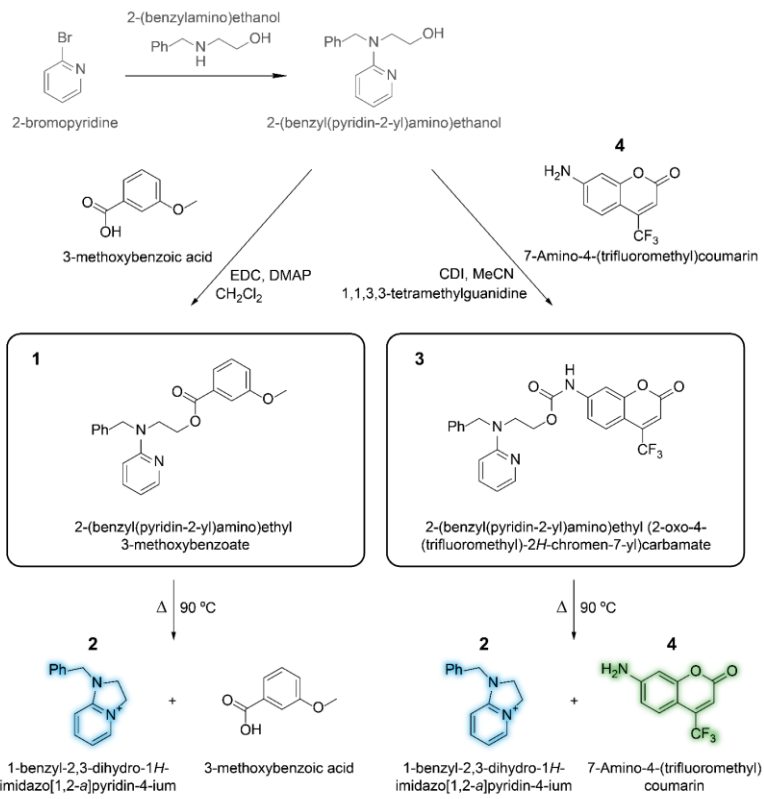

Figure 4.11. Diagram of the synthetic method to produce substrates 1 **and** 3**, and the corresponding thermal-promoted thermocyclization reactions.**
EDC stands for N-(3-Dimethylaminopropyl)-N′-ethylcarbodiimide; CDI stands for 1,1-carbonildiimidazol; DMAP stands for 4-Dimethylaminopyridine.

Preparation of PMA-modified NS/ZIF8 NCs (NRs). The here designed and studied NRs consisted of a NS core and a ZIF8 shell, which was further functionalized with a polymer (PMA). The synthetic method involved four main steps: i) CTAB-coated NS were first synthesized with previously prepared Au NPs seeds and with CTAB as capping agent and stabilizer; ii) these NS were then used as seeds (NS at a concentration of 2 nM in $5 \cdot 10^{-4}$ M CTAB aqueous solution) onto which a shell of ZIF8 was grown by following an aqueous procedure in which the surfactant CTAB works as size-controlling and structural-directing agent; iii)(optional step for 'Approach A', further explained in section 3.2) pre-encapsulation overnight of substrates within the NRs (NR@**1** or NR@**3**); iv) finally, in order to provide colloidal stability in diverse complex aqueous media, these NS-ZIF8 core-shell particles were wrapped with the amphiphilic polymer PMA before last washing steps.

Characterization techniques. TEM and SEM was used to study the size and morphology of the nanomaterials. SEM images were acquired with a FESEM Zeiss Ultra Plus operated at 3 kV and 20 kV (Figure S4.2). TEM images were acquired with a JEOL JEM-2010 microscope operated between 80 and 200 kV accelerating voltage. ImageJ free software and Origin software were used for the size measurements and distribution analysis, respectively. A Biochrom Libra S60 UV–Vis spectrophotometer was used to record UV-Vis absorption spectrum of the NRs in water. A Malvern Zetasizer (Nano ZSP) instrument, equipped with a 10 mW He–Ne laser operating at a wavelength of 633 nm and fixed scattering angle of 173°, was used to measure the hydrodynamic diameters (by DLS) and the ξ-potentials (by LDA). ICP-MS measurements were performed using an Agilent 7700x ICP-MS after acidic digestion of the samples with aqua regia.

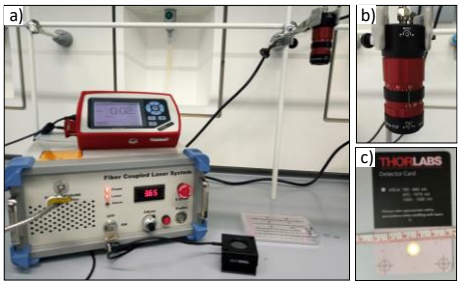

Figure 4.12. NIR irradiation set-up (a), collimation/zoom system (b) and beam diameter (c).

NIR irradiation set-up. For laser irradiation experiments, the samples (without or with cells depending on the experiment type as described in each section) were placed in wells of a 96-well plate and were irradiated by using an 808 nm laser (Lasing, #FC-W-808A) coupled to a zoom fibre collimator (Thorlabs, #ZC618SMA-B) to control the spot size as well as irradiate cells

homogeneously, *cf*. Figure 4.12. To calculate the intensity in $W \cdot cm^{-2}$ that cells receive, a power energy meter (Thorlabs, #PM100D) with a thermal power head (10 W, 25 mm, Thorlabs, #S425C) was used to measure the output power. To obtain the spot size a viewing card (Thorlabs, #VRC4) was used to see the spot and ImageJ to measure it. As the beam is collimated, a homogeneous spot was assumed, and thus, the intensity could be calculated just dividing the power by the surface (in cm^2) of the spot. Different time and power densities conditions were investigated as indicated in each experiment.

Thermoplasmonic properties of NRs. To evaluate the thermoplasmonic properties of the NR particles, solutions containing NRs in water (200 µL, 1 nM, placed in the wells of a 96-well plate) were irradiated with a 808 nm laser at different power densities (2, 4, and 8 $W \cdot cm^{-2}$) and for different irradiation times (from 0 to 10 min). The temperature of the solution after each irradiation condition was measured obtaining the ΔT versus-irradiation time curves presented in Figure S4.4.

Thermal-promoted nucleophilic substitutions by NRs. The thermoplasmonic properties of NRs were used to promote the thermal reaction (nucleophilic substitution) depicted in Figure 4.11, leading to the transformation the non-fluorescent substrates (**1** and **3**) into the corresponding fluorescent products (**2** and **4**). An aqueous solution of NRs (200 µL, 1 nM) was mixed with the solution of the substrate (10 µL, 10 mM) in a well of a 96-well plate, and the mixture was irradiated with our 808 nm NIR set up (Figure 4.12). Different power densities (2, 4, and 8 $W \cdot cm^{-2}$) and irradiation times (from 0 to 10 min) were studied. After irradiation, the temperature of the solution was measured (T_{max}), the NRs were then precipitated by centrifugation, and the generated product in the supernatant was quantified by fluorescence using the corresponding calibration curves (Figure S4.7).

Photostability and reusability of the NRs. *P*erformance of NRs for promoting the thermal reaction in successive steps was studied as follows: for 1 cycle, a solution of NRs (200 µL, 1 nM) was mixed with the solution of the substrate (10 µL, 10 mM) in a well of a 96-well plate, and the mixture was irradiated with a 808 nm laser at 8 $W \cdot cm^{-2}$ for 5 min (2 min cycles are represented in Figure 4.5, Table S4.4); then, the NRs were precipitated by centrifugation and the generated product in the supernatant was quantified by fluorescence. The same was repeated up to a total of 3 cycles. Yields are presented in Figure S4.9a and Table S4.4. Finally, the reusability was also tested by performing the reaction using the same NRs (200 µL, 1 nM) mixed with the substrate **1** (10 µL, 10 mM) in five repetitive cycles at 8 $W \cdot cm^{-2}$ for 5 min.

Cell studies. HeLa (human cervical cancer cell line) were cultured in DMEM with phenol red, 4.5 g/L D-glucose, L-glutamine and pyruvate (DMEM, 1X, Gibco) supplemented with 10% v/v FBS (Gibco) and 1% v/v P/S, (Corning, 100X). Cells were maintained under humid conditions at 37 °C and 5% of CO_2. Cells were passaged after cleaning (PBS, 1X, Gibco) with 0.25% Trypsin-EDTA (1X, Gibco) when the culture reached confluency.

- *Cell viability.* In order to study number of viable cells after the exposure to the substrates or particles (NS or NR), resazurin assays were performed (Figure 4.6). HeLa were seeded in 96-well plates (NEST Scientific, #701001), $7.5 \cdot 10^3$cells per well in 100 µL of cell growth medium (0.3 cm^2 *per* well) for 24 h before treatments. Then, medium was removed and 100 µL of cell culture growth medium with the desired concentration of the substrates or the particles were added. The cells were incubated with the samples the time of interest at 37 °C and 5% CO_2. Then, each well was rinsed three times with PBS and 100 µL of a freshly prepared solution with 90% of media and 10% of resazurin (resazurin sodium salt in water 0.2 mg/mL filtered; Sigma Aldrich, #199303-1G) was added. Cells were incubated during 3 h at 37 °C and 5 % CO_2 under dark conditions before being measured with a plate reader (Infinite® 200 PRO, Tecan, Switzerland) under 560/20 nm excitation and collecting fluorescence with a 610/20 nm filter. Final values were calculated using Eq. 3 (Figure 4.6).

- *Au content per cell.* ICP-MS was used to quantify the average gold content per cell, which we used to estimate the number of FBS-stabilized NSs or NRs per cell. Hela cells ($\sim 5 \cdot 10^6$ cell per experiment seeded in 6-well plates) were cultured as previously discussed, supplemented with FBS-stabilized NSs or NRs (50 pM), and incubated overnight. Extracellular gold (either free or particles) were rinsed with PBS (3x), and the particle-loaded cells were digested with aqua regia after counting them. Digested samples were diluted with HCl 2% before quantifying gold content by ICP-MS.

For comparison of particle uptake (NR or NS) among samples, we assumed that the gold mass of one NS is $\sim 8 \cdot 10^{-16}$ g (*i.e.*, $4.1 \cdot 10^4$ nm^3),[303] which allowed us to make an estimation about the average particle uptake per cell: (335 ± 12) NRs/cell and (166 ± 61) NSs/cell.

- *Cytometry.* Internalization of NRs over time was qualitatively monitored by cytometry studies using TAMRA-labelled NRs (see also section 6.4.2). $15 \cdot 10^3$ HeLa cells (300 ul) were seeded on 48-well plates and allow 24 hours to attach. After NRs administration in complete DMEM during different times (50 pM, 0.5 - 24 h), cells were washed three times with PBS to remove non-internalized NRs. Then, 50 µl of trypsin were added to each well. After 5 minutes, 150 mL of PBS was added before measuring cells in the cytometer (Guava®

easyCyte BG HT flow cytometer, Millipore®). Mean fluorescence intensity (MFI, Orange-G channel: Ex. 532/Em. 620(52) nm) of gated cell populations (5000 counts) was analysed to compare the number of NRs internalized by cells at different times after incubation (Figure 4.7).

- *Laser irradiations*. After checking that NR-preloaded cells with the added substrate (**1** or **3**, 10 mM, 30 min incubation) appear morphologically normal under the microscope, we chose one of the following irradiation protocols:

  i. Single-cell experiments. Highly focused NIR spot (high power densities of a 785 nm laser "pointer" with diameter ~ 5 μm, *i.e*. optical setup equivalent to optical tweezers.[304]

  ii. Multi-cell experiments. Illumination of thousands of cells with a large diameter (~ 0.65 cm; low power density) collimated NIR beam, for which we used a 808 nm laser (see section 3.3). Since the beam is collimated, we consider a homogeneous spot and, thus, we can obtain the intensity just dividing the power by the surface (in cm^2) of the spot. We explored different irradiation conditions (exposure time and irradiance). For multi-cell irradiation aimed to achieve intracellular conversion of substrates (**1** or **3**, 10 μM, 30 min incubation) into products (**2** and **4**), we used 10 $W \cdot cm^{-2}$, 1 min. For single cell experiments using the NIR pointer, we used exposure times ~5-10 s.

Ex./Em. [nm]	Dye/staining	Experiment
561/620(60)	TAMRA-labelled NRs	Figure S4.10
637/725(40)	CellMask™ Deep Red: cell plasma membrane	Figure S4.10
405/450(50)	product **2** (single cell)	Figure 4.8 and Figure S4.11
405/525(50)	product **4** (single cell)	Figure 4.8, Figure S4.12 and Figure S4.13
488/525(50)	product **2** (multi cell)	Figure 4.9, Figure S4.14 and Figure S4.15
540/620(60)	product **4** (multi cell)	Figure 4.9 and Figure S4.17

Table 4.1. Ex./Em. wavelengths used for confocal imaging.

- *Confocal imaging.* In order to perform all the confocal imaging experiments with living cells, $20 \cdot 10^3$ HeLa cells (200 μL) were seeded on μ-Slide 8 well-ibiTreat chambers (1 cm^2 *per* well, Ibidi, Germany, #80826) at least 12 h before particle/substrate incubation. Confocal images of living cells were captured on an Andor Dragonfly spinning disk confocal system mounted on a Nikon TiE microscope equipped with a Zyla 4.2 PLUS camera (Andor, Oxford

Instruments) and an OKO-lab incubator to keep cells at 37 °C during all the experiment. Images were acquired with different magnification objectives (20X, 60X, 100X). All the images were processed with ImageJ (Figure 4.8, Figure 4.9 and from Figure S4.10 to Figure S4.17). Ex./Em. wavelengths used for the experiments of this work are all collected in Table 4.1.

4.4. CONCLUSIONS

We have demonstrated for the first time the feasibility of achieving photothermal-promoted chemical reactions in the interior of living cells. The transformation, consisting of an intramolecular nucleophilic substitution (thermocyclization), is possible thanks to the use of purposely designed ZIF8 based nanocomposites with a plasmonic core (NS), which generate heat upon NIR irradiation. The microporous nanoshell is critical to favour an effective concentration of the reactants near the heating source as well as to warrant the required thermal confinement. Ours is also the first example of a NIR-promoted nucleophilic substitution reaction. Overall, our plasmonic nanocomposites behave as excellent and biocompatible nanoreactors, which can work inside living cells to promote new-to-nature intracellular thermal-promoted transformations with spatiotemporal resolution.

USC
UNIVERSIDADE
DE SANTIAGO
DE COMPOSTELA

5. PALLADIUM NCS FOR CONTROLLED CATALYTIC REACTIONS

CORE-SHELL PD/ZIF8 PLATFORMS AS DIFFUSION-CONTROLLED NANOREACTORS FOR BIOORTHOGONAL UNCAGING CHEMISTRY IN LIVING CELLS AND TISSUE MODELS

5.1. INTRODUCTION

Intracellular enzymes play an essential role in maintaining and controlling the cell metabolism and function and have evolved to catalyse life-sustaining reactions. Scientists are not limited by the constraints of life and evolution and can therefore aspire to develop non-natural catalytic reactors capable of working inside living environments. These systems could provide unprecedented opportunities for cellular intervention, and eventually lead to the discovery of innovative biomedical tools.[227]

Within the catalysis field, transition metal catalysis is especially appealing, owing to the innumerable type of transformations that can be achieved. While most of these reactions have been developed in organic solvents, and under water-free conditions, recent years have witnessed an exponential increase in the development of metal-mediated reactions that can occur in complex aqueous environments, and even within living mammalian cells.[164, 224, 249-253] Initial progress in the field has been focused on homogeneous copper-promoted azide-alkyne annulations,[254-259] and ruthenium-mediated uncaging reactions;[260-265] however, more recently, other metals like gold,[241, 264, 266] iridium,[267] osmium,[268] and palladium,[269] have also demonstrated potential to induce specific transformations in biological settings.

Pd-based catalysts are especially attractive owing to their well-established synthetic potential. However, the performance of homogeneous Pd complexes in biological media is usually compromised by aqueous solubility, stability, and/or biocompatibility issues.[165-168] As an alternative, Pd NPs have also been studied as heterogeneous catalysts;[166, 270] however, in absence of a suitable surface functionalization,[34, 271] the NPs tend to aggregate, suffer from Pd leaching, and are easily passivated by biological components of the milieu.[166, 169] Alternatively, the functionalization of NPs with organic coatings, typically required to fabricate colloidally stable systems, can dramatically decrease the catalytic capability of metal NPs surfaces.[272]

Bradley and Unciti-Broceta approached some of these issues by embedding "pristine" Pd NPs within polystyrene microspheres.[240, 273] This heterogenous formulation allowed to carry out designed uncaging reactions in biological media, and even in the presence of mammalian cells; however, as the own

authors noted, the solvent exposed NPs are deactivated over time because of fouling.[274]

In an effort to avoid the passivation of Pd by the biological components, hollow silica microcapsules containing Pd NPs in the internal cavity have been previously engineered, and their potential used for removing propargylic groups from phenol derivatives in PBS and in the presence of added proteins demonstrated. Unfortunately, these microcapsules were not effective in intracellular settings.[275]

Overall, achieving efficient, robust and bioorthogonal Pd-catalysed reactions in complex aqueous media, and especially inside living cells, represents a major challenge in research at the interface between metal catalysis and cell biology.

Metal-organic frameworks (MOFs), porous materials self-assembled from metal ions and organic ligands, have attracted attention for gas storage and biomedical applications such as drug delivery, imaging and biosensing.[276] In recent years they have also demonstrated great potential in metal-promoted heterogeneous catalysis.[277-278] In this context, a number of Pd-containing MOF structures have been used as catalysts to promote hydrogenations,[279] oxidations,[280] and even C-C bond-forming processes.[281] Not surprisingly, most of these MOF-promoted reactions have been carried out in organic solvents, and under water-free conditions, due to the well-known sensitivity of most MOF architectures to the presence of bulk water.[211, 282-286]

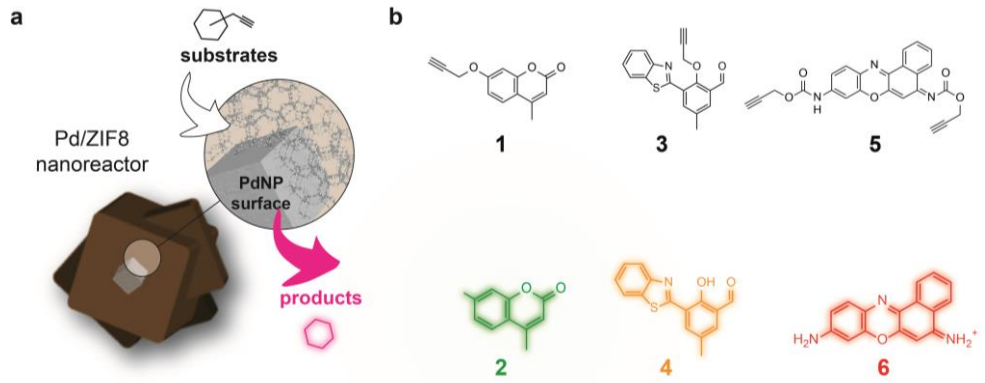

Figure 5.1. Core-Shell Pd/ZIF8 nanoreactor for intracellular uncaging chemistry and caged probes.

a) Pd nanocubes coated by a porous ZIF8/PMA shell are colloidally and structurally stable in water. b) Caged probes (substrates **1**, **3** and **5**) used in our study and their corresponding fluorescent products (**2**, **4** and **6**) resulting from a Pd-promoted removal of their propargylic protecting groups (see Figure S5.1 to Figure S5.4 and Section 6.4.1).

While several MOF-based composites (NC) compatible with aqueous media have been made, for instance, for removal of pollutants from waste water,[287] their use for transition metal catalysis in aqueous milieu remains largely

unexplored.[288-289] Needless to say, they have never been used in living settings, except for a very recent report involving MOF-supported copper NCs for achieving azide–alkyne cycloadditions in the presence of cells.[290] However, in these constructs, the distribution of copper nanoparticles in their MOF-based NC (including solvent-exposed catalytic centres) does not allow to discern whether the reaction occurs on the surface and/or throughout the NC.

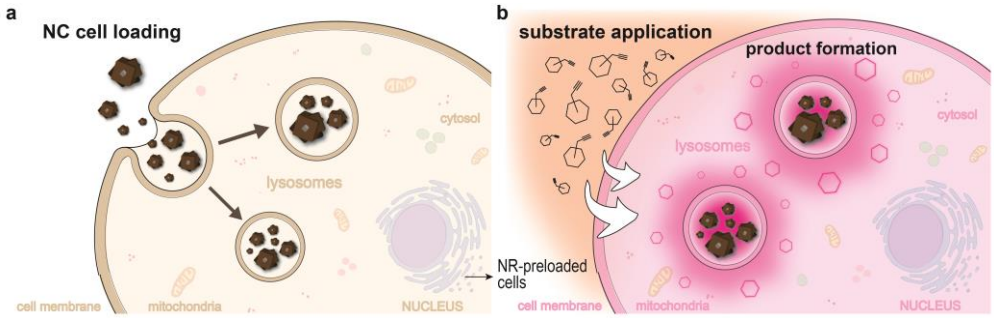

Figure 5.2.Intracellular uncaging reactions scheme.
a) NRs tend to accumulate in cytosolic compartments (endosomes/lysosomes) and work as heterogeneous palladium-based nanoreactors by first incubating the cells with the NRs to obtain NR-preloaded cells; b) then cells are capable of processing substrates into different fluorescent products with a dose and temporal dependency and even in a recurrent manner.

Herein, we report water compatible core-shell Pd/ZIF8 NCs capable of working as efficient bioorthogonal heterogeneous nanoreactors. The NC features a single Pd nanocube core (the catalyst) and a porous nanometric ZIF8 shell (the filter) surface-coated with an amphiphilic polymer (PMA). The PMA derivatization strategy renders the NC stable in water and biological settings, as we have recently demonstrated with a structurally related plasmonic NC (see chapters 3 and 4).[231] Importantly, we demonstrated that the ZIF8/PMA architecture not only protects the Pd nanocatalyst from deactivation, leakage and aggregation, but its porosity allows a diffusion-controlled flow of reactants within the core reaction chamber (Figure 5.1). As a result, these nanoconstructs can be used as robust and efficient metallo-nanoreactors (NRs) in complex aqueous media and, more importantly, inside living mammalian cells. These nanoplatforms tend to be stored in cytosolic compartments (endosomes and/or lysosomes), remaining stable, active and accessible to the reactants, and they can promote several consecutive reaction runs using new batches of reactants, without losing efficiency (Figure 5.2). Importantly, we also demonstrated that these NRs can be readily incorporated into 3D tumour spheroids to produce tissue-like catalytic systems, which can also work in a recurrent, dose-dependent manner.

5.2. RESULTS AND DISCUSSION

Design and synthesis of Pd/ZIF8 NCs. Pd nanocubes (Pd-NP) were selected as catalytic cores owing to their shape-enhanced catalytic performance.[291] The selected nanocubes with side length ~ 24 nm (Figure S5.5) were synthesized in aqueous solution at RT (~23 °C), in the presence of the cationic surfactant cetyltrimethylammonium bromide (CTAB), using K_2PdCl_4 as Pd source and L-ascorbic acid (AA) as reducing agent.[292] These CTAB-coated Pd-NP cores were added during the synthesis of the ZIF8, enabling the formation of core-shell Pd/ZIF8 particles with average size ~ 250 nm (Figure 5.3a-b, Figure S5.6). This synthetic approach allows for fabricating one Pd/ZIF8 particle per Pd-NP seed, as shown by electron microscopy. Pd/ZIF8 particles exhibit the characteristic Bragg peaks of ZIF8 and Pd^0, as shown by powder X-ray diffraction (PXRD, Figure S5.7 and Table S5.1). Importantly, the resulting nanosystems were post-functionalized with the amphiphilic polymer PMA in order to provide aqueous stability.

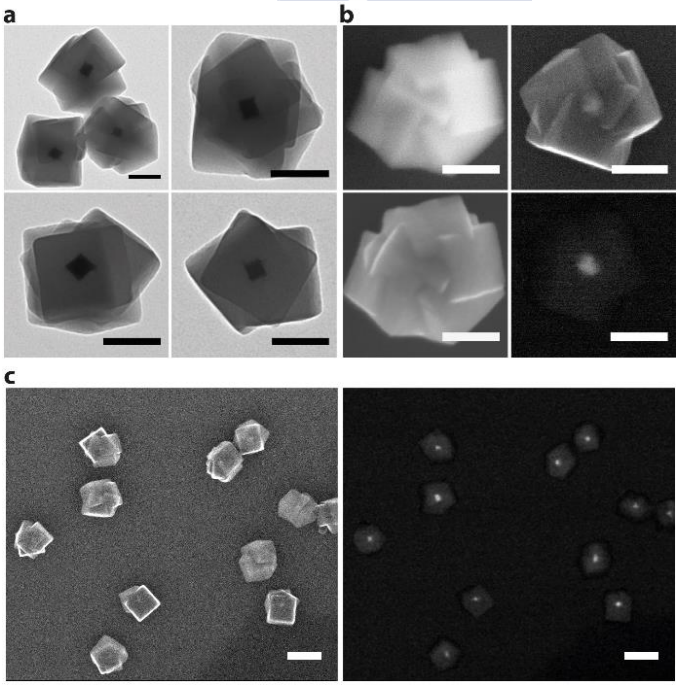

Figure 5.3. Electron microscopy characterization of core-shell Pd/ZIF8 NRs.
a) TEM micrographs confirm the core-shell Pd/ZIF8 structure (without PMA); b) SEM micrographs of the same core-shell Pd/ZIF8 particle using different detectors, at different voltages, provide depth-dependent structural and textural information; c) SEM micrographs of PMA-derivatized Pd/ZIF8 NCs (NRs) using two detectors at 20 kV (left: InLens detector, secondary electrons; right: AsB detector, backscattered electrons).

Albeit related core-shell metal NP/ZIF8 composites have been previously reported using other surfactants[293] or different nanoparticle cores,[294] none of them were demonstrated to be water stable over extended periods of time. Indeed, the inherent aqueous instability of ZIF8 has been used for the progressive release of encapsulated drugs inside cells.[207, 284, 295-296] Notice that when such composites are internalized into cells they tend to accumulate in lysosomes (pH ~ 4.8), where the acidic pH accelerates the ZIF8 degradation and, hence, the drug release. Such aqueous instability is incompatible with the potential use of these nanostructures as biocompatible catalysts.

Our PMA-modified Pd/ZIF8 NCs (in the following referred to as NRs, Figure 5.3c) with ξ-potential ~ -30 mV are colloidally stable in aqueous solution, as well as in supplemented (10% FBS) cell medium and in artificial lysosomal fluid (ALF, plain or supplemented). Dynamic light scattering (DLS) demonstrates that they remain stable for at least one week (hydrodynamic diameter d_h ~ 250 nm, see Figure 5.4 and Table S5.2, Figure S5.8). In contrast to our NRs, Pd-NPs (equivalent to the Pd cores of NRs) rapidly aggregate and precipitate in water or ALF buffer, albeit they remain colloidally stable in supplemented cell medium or supplemented ALF (Figure 5.4), likely due to the adsorption of serum proteins.

Inductively coupled plasma mass spectrometry (ICP-MS) was used to corroborate the Pd content before and after the ZIF8 coating (Table S3), as well as to quantify the amount of Pd per Pd/ZIF8 particle (3.8 wt%). Taking geometrical and structural considerations regarding the Pd-NPs used herein,[291, 297] we estimate that ~5% of the Pd content of one Pd-NP are surface atoms (surface Pd), and thereby potentially available for the catalytic processes (Table S5.4). Importantly, although the specific surface area of the NRs decreases after PMA-modification,[231] likely because the PMA partially fills voids in the nanostructure, the ZIF8 shell remains porous and accessible for small molecule loading by diffusion, as demonstrated with model fluorescent probes (Table S5.5, Figure S5.9).

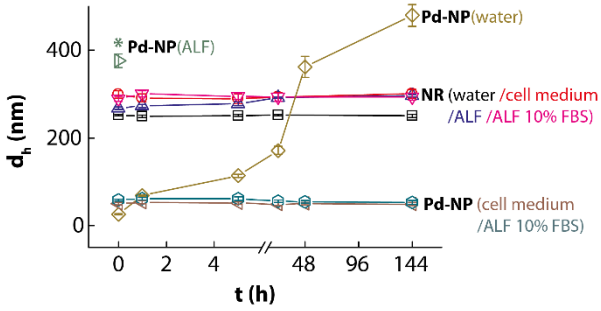

Figure 5.4. NR stability over time in different aqueous-based media.
Mean d_h of NRs and Pd-NPs in different media: water, 10% FBS supplemented cell medium, artificial lysosomal fluid (ALF) and 10% FBS supplemented ALF. Scale bars are 200 nm. * indicates immediate, irreversible aggregation and precipitation.

NR-promoted removal of propargylic groups in aqueous solution. With the water compatible Pd/MOF structures (NRs) at hand, we tested their catalytic performance in the depropargylation of the coumarin derivative **1** (Figure 5.1b). This is a reaction that it has been already studied with discrete Pd complexes[168] and with hollow nanocapsules,[275] and therefore, represents an excellent model to assess the transformative potential of our system. The reaction allows for releasing a fluorescent probe, and therefore, it can be readily monitored even in biological settings.

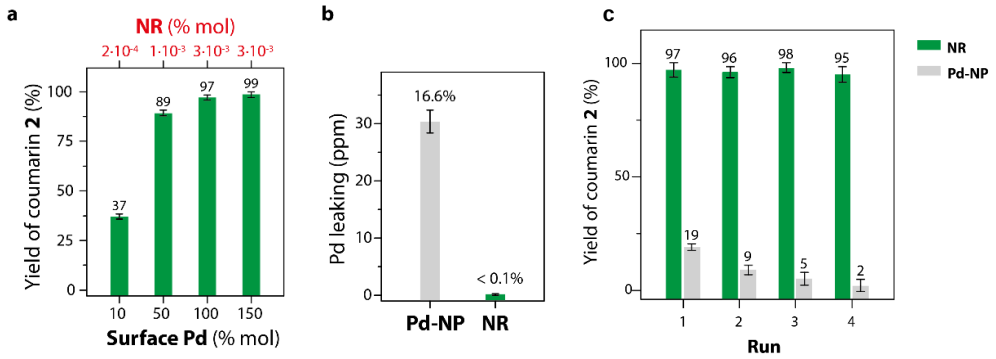

Figure 5.5. Characterization of the Pd-promoted (NR or Pd-NP) uncaging of coumarin 1 in aqueous solution.

a) Yield (%) of **2** using increasing concentrations of NRs, and therefore, of surface Pd; reaction conditions: 10 μM of **1**, H_2O:MeOH 9:1, 37 °C, 15 h. b) Pd leakage after one run. c) Reusability comparison between NRs and Pd-NPs; reaction conditions: 100 % mol surface Pd, 10 μM of **1**, H_2O:MeOH 9:1, 37 °C, 15 h.

Gratifyingly, when the propargyl-protected coumarin **1** (10 μM) was mixed with the NRs (0.23 nM NR ≈ 100 mol % surface Pd, Table S5.6) in water/methanol (9:1) at 37 °C, we observed a formation of the fluorescent coumarin **2** (15 h, Figure 5.5a). After centrifugation (7000 RCF, 10 min) and washing of NRs, quantification of the product by fluorescence, using calibration curves, allowed to calculate a 97% reaction yield (see the effect of washing in Table S5.7). Remarkably, using "pristine" Pd-NPs, under identical conditions, led to a much more modest yield (19%, Figure 5.5c), likely because of their poor colloidal stability (Table S5.6, Figure 5.6). Indeed, the Pd content of the NRs remained virtually unaltered, whereas in the case of the Pd-NPs, their integrity was significantly disrupted after just one cycle (> 16 % Pd leakage, Figure 5.5b, Table S5.8).

The NR-promoted deprotection of **1** can be carried out in PBS instead of water/methanol (9:1), leading to similar results (92% yield, Table S5.6). Moreover, using lower amounts of the NRs and, therefore, of Pd at the surface (10 mol%), the reaction is slower, but also effective (37% or 99% yield after 15 h or 7 days, respectively); confirming that the Pd/MOF composite behaves as a true

heterogeneous catalyst (Table S5.9). The need of the Pd to promote the depropargylation reaction was confirmed with a control experiment using equivalent ZIF8 particles lacking the Pd core (Table S5.6).

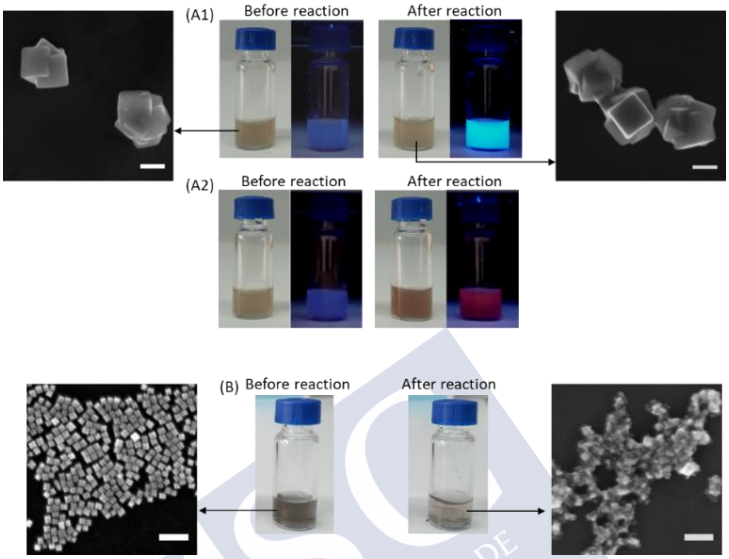

Figure 5.6. Photographs of NRs (or Pd-NPs) solutions before and after incubation with 5. A) Photographs under visible and UV light of the reaction mixture for the depropargylation reaction of **1** (A1) or **5** (A2) promoted by NRs taken before and after the reaction; B) Photographs under visible light of the reaction mixture for the depropargylation reaction of **1** promoted by Pd NPs taken before and after the reaction, where aggregation of Pd-NPs is observed. Scale bars correspond to 100 nm.

We also attempted the uncaging of the propargyl derivative of 2-(2'-hydroxyphenyl)benzothiazole (**3**, Figure 5.1b), a probe that emits light at longer wavelengths. Surprisingly, in this case the reaction did not proceed; however, it can be achieved with pristine Pd-NPs (15% yield after 15 h, Table S5.6). While this result could be considered unsatisfactory, it is rather valuable from a mechanistic perspective. DLS data resulting from exposing the NRs to **1** and/or **3** suggest that the lack of reaction in the case of substrate **3** is likely due to the coordination of the thiazole nitrogen atom to the unsaturated Zn^{2+} ions of the ZIF8 surface, an interaction that prevents the penetration of the substrate into the reaction chamber (Table S5.10). In consonance, adding one equivalent of the benzothiazole **3** to the reaction of pro-coumarine **1** with the NRs, compromises the reaction rate, albeit still allows the formation of product **2** in 54% yield (after 15 h), and in quantitative yield after 72 h (Table S5.6, Figure S5.10). These observations confirm the filtering role of the ZIF8 shell; that is, only substrates that can permeate through the porous structure will be able to reach the nanoreactor's core. Therefore, the MOF structure not only protects the reactive

Pd core, but also allows for discriminating among reactants, which can be especially relevant in terms of orthogonality.

Importantly, the NRs can be recycled without compromising their catalytic activity, as corresponds to a true heterogeneous nanocatalyst. Indeed, as shown in Figure 5.5c, after four runs of overnight reaction with **1**, the NRs were just as effective as in the first round. In contrast, Pd-NPs gradually lost efficacy after each use, which is in consonance with their poor colloidal stability under the reaction conditions (Figure 5.5c, Table S5.11).

As expected, the NRs can efficiently promote the depropargylation of other precursors that do not feature zinc coordinating moieties, even when the substrate contains two propargyl caging groups, as in the case of the bis-protected cresyl violet **5** (Figure 5.1b), which showed a similar reaction trend than the coumarin derivative **1** in terms of yield, reusability and turnover number (TON, Table S5.9). In this case, we also tested consecutive runs using the same NRs (10 μM surface Pd) and adding the substrate **5** (10 μM) up to three times separated by ~18 h. The cumulative yield of the product **6** (> 250%, Table S5.12) demonstrates the feasibility of the NRs to work as true heterogeneous flow nanoreactors.

Bioorthogonality. The shell-based architecture of the microporous ZIF8 structure allows not only for protecting the Pd core from colloidal degradation and/or Pd leakage, but also filters large components of biological mixtures, thereby partially preventing Pd inactivation by biomolecule adsorption. As shown in Figure 5.7a, the reaction of the propargylated coumarin **1** tolerates the presence of excess amounts of BSA. Even using very high BSA concentration (150 μM; *i.e.*, ~ $75 \cdot 10^3$ molecules of BSA per NR particle), four times more than typically contained in supplemented cell media, the reaction yield was over 30% (after 15 h). Using pristine Pd-NPs instead of our NRs, the yields are rather low (less than 10%).

The NRs are also effective in media of higher complexity, such as DMEM supplemented with 10% FBS, or HeLa cell lysates, albeit the reaction yields after 15 h were modest (Figure 5.7b). However, leaving the reaction in DMEM supplemented with 10% FBS for a longer time (72 h), the yield increases up to 47%, which confirms the ability of the NR to remain active for longer periods, even in a crowded molecular environment. Analogous bioorthogonality experiments using the cresyl violet precursor **5** led to similar results (Figure 5.7c, Table S5.13).

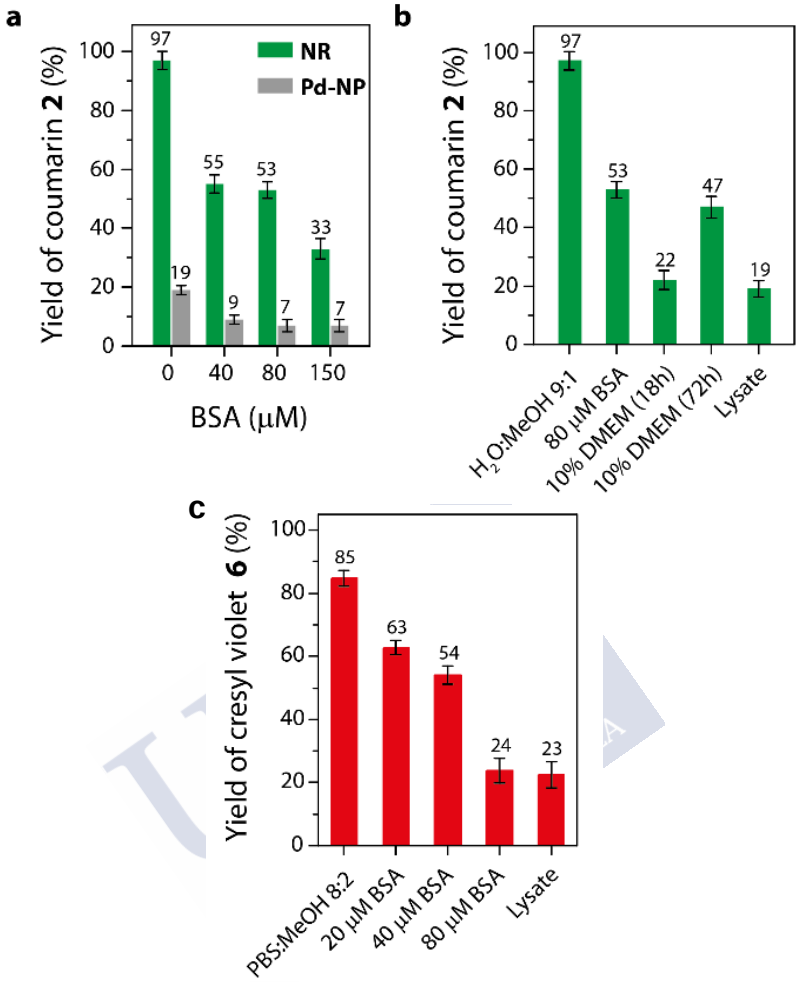

Figure 5.7. Characterization of the Pd-promoted (NR or Pd-NP) generation of fluorophores 2 or 6 in biological media.

a) Yield of coumarin **2** in the presence of increasing concentrations of BSA (10 μM of 1, 37 °C, 15 h). b) Yield of **2** in the presence of media of increasing biocomplexity (10 μM of 1, 37 °C, 15 h unless otherwise noted). c) NRs performance as catalyst for the uncaging of cresyl violet **6** in the presence of media of increasing biocomplexity (10 μM of 5, 37 °C, 15 h). In all cases, the concentration of NR or Pd-NP was kept constant at 0.23 nM ≈ 100 mol % surface Pd.

Intracellular reactions. Having demonstrated and quantified the catalytic performance of our Pd/MOF particles in aqueous media with increasing biocomplexity, our next aim consisted of demonstrating that the uncaging chemistry can be achieved inside living mammalian cells. Toward this end, we first carried out viability studies using HeLa cells supplemented with different concentrations of either the NRs, Pd-NPs and/or the bispropargyl carbamate-protected cresyl violet **5** (Figure 5.8). This allowed us to set the range of

concentrations for substrates and catalysts compatible with > 90% cell viability (24 h incubation): ≤ 2 μM in surface Pd (equivalent to ≤ 50 pM NRs considering particles); and ≤ 45 μM bispropargyl carbamate-protected cresyl violet **5**. The "pristine" Pd-NPs did not impair viability in the concentration range studied here (0.3 μM – 167 μM in surface Pd content, equivalent to 7 pM – 4 nM Pd-NPs). In addition, control experiments were performed to test the viability of cells against varying concentrations of the cresyl violet **6** (Figure 5.8). The cresyl violet **6** was significantly more toxic (0.6 μM, ~ 25% viability after 24 h incubation) than any other of the tested compounds (Figure 5.8).

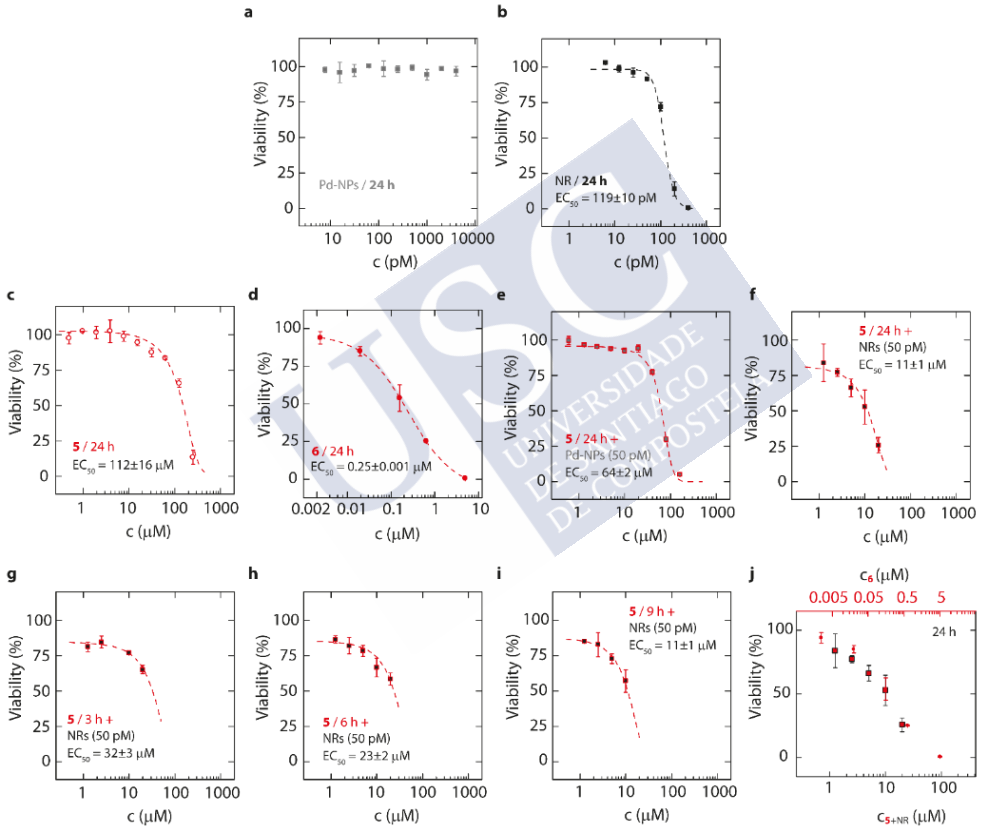

Figure 5.8. Cell viability of HeLa cells exposed to increasing concentrations of reactant(s) and/or NRs and/or Pd-NPs.

Half-maximal responses (EC_{50} values) were estimated by fitting (Dose Response function in OriginLab). a) Pd-NPs and b) NRs, 24 h incubation; c) **5**, 24 h incubation; d) **6**, 24 h incubation; e) **5**, 24 h incubation with Pd-NPs (50 pM)-preloaded cells; f) **5**, 24 h incubation with NR (50 pM)-preloaded cells; g) **5**, 3 h incubation with NR (50 pM)-preloaded cells; h) **5**, 6 h incubation with NR (50 pM)-preloaded cells; i) **5**, 9 h incubation with NR (50 pM)-preloaded cells; j) comparison between the incubation (24 h) of **6** with Pd-free cells and **5** with NR (50pM)-preloaded cells.

Cell uptake experiments with fluorescently labelled NRs (50 pM) confirmed an efficient internalization and the accumulation in the endocytic compartments (endosomes or lysosomes) after 12 h (Figure 5.9). ICP-MS was used to quantify the average Pd content per cell (Table S5.14), which thereby allowed us to estimate the average number of NRs per cell (~120). We also quantified the amount of internalized Pd when using Pd-NPs instead of the NRs, resulting in a decreased intracellular Pd content (~71 Pd-NPs) per cell, which is not surprising owing to the poor colloidal stability of the "pristine" Pd-NPs.

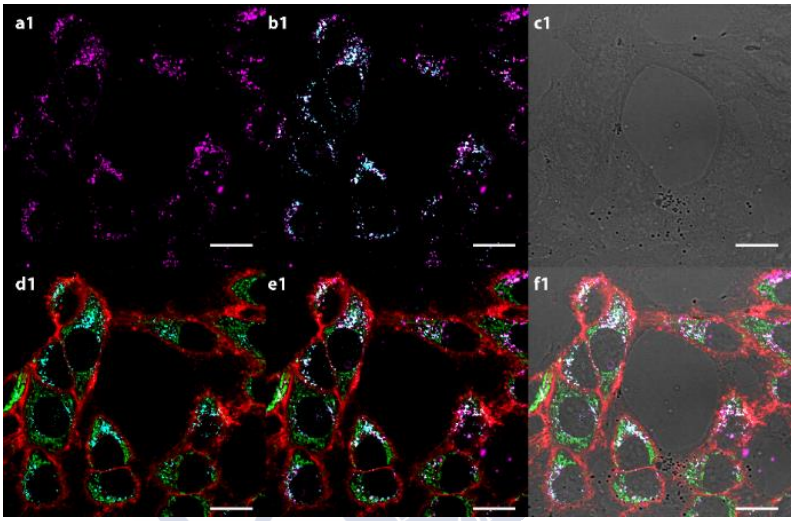

Figure 5.9. NR intracellular localization evaluation using confocal microscopy.
Collage of confocal microscopy images. a1) Rhodamine-labelled NRs (pink); b1) Rhodamine-labelled NRs (pink) + LysoTracker® Blue (cyan); c1) bright field; d1) LysoTracker® Blue + MytoTracker® green + CellMaskTM Deep red; e1) d1 + rhodamine-labelled NRs (pink); f1) e1 + bright field. Scale bars correspond to 40 μm.

The uncaging reactions were performed by first incubating the cells with the NRs (50 pM ≈ 2 μM in surface Pd, overnight) to obtain NR-preloaded cells. Before adding the substrate **5**, cells were extensively washed with PBS to ensure that non-internalized or membrane-bound particles were removed (see Section 6.4.8).

Due to the toxic profile of the cresyl violet **6**, in the reaction of its precursor **5** we tested several experimental conditions, including different concentrations and incubation times (Figure 5.8 and Figure S5.11 to Figure S5.15). Thus, we were glad to see that, after incubating NR-preloaded cells for 6 h with 2.5 and 10 μM of **5**, a clear dose dependent increase in cellular fluorescence was observed (Figure 5.10a). Using these latter conditions, we observed a decrease of ~25% in cell viability (see Figure 5.8).

Interestingly, when the reaction of **5** (10 μM) was analysed at different incubation times (1, 3, 6, and 24 h), we observed a fluorescence maximum intensity between 3 and 6 h, whereas, after 24 h there is a significant decrease in emission (Figure 5.10b). This result suggests that after its intracellular generation, the product **6** is slowly expelled out of the cell. Control experiments of cells treated with the substrate (Figure S5.11 to Figure S5.15) or the product (Figure S5.16), in the absence of Pd NRs, are included in the Section 6.4.8.

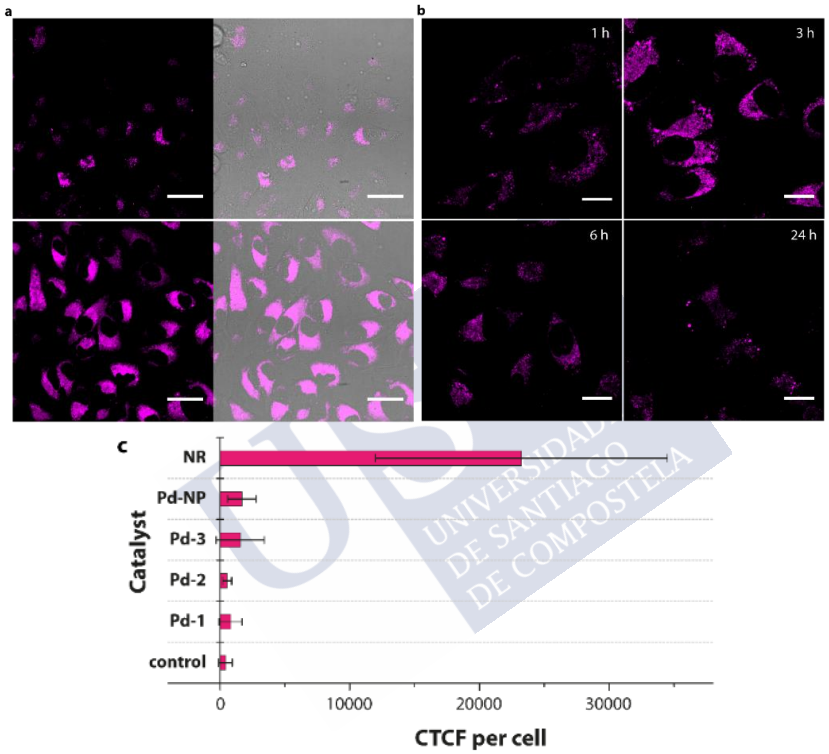

Figure 5.10. NR-promoted intracellular uncaging chemistry.
a) Confocal microscopy images after incubation of substrate **5** at different concentrations (top: 2.5 μM, down: 10 μM; 60X) with NR-preloaded cells during 6 h, for the intracellular production of cresyl violet **6**. b) Incubation of **5** (10 μM) with NR-preloaded cells and confocal images at different incubation times (1-24 h, 100X). c) Comparison of the intracellular fluorescence generated in the reactions of substrate **5** (CTCF per cell) achieved by our NR, or other palladium reagents (Pd-NPs, Pd-1, Pd-2 or Pd-3), using equivalent incubation conditions (2 μM of Pd overnight) and cell treatment (PBS washings and incubation with 10 μM of substrate **5** during 6 h); at least 35 cells per catalyst were analysed (see Figure S26). In a), fluorescence images are also shown as merged images (bright-field plus fluorescence channels). In all cases, cells pre-treated with the palladium reagents were washed with PBS (three times) before adding fresh medium and the substrates. Scale bars correspond to 20 μm (100X) or 40 μm (60X).

In consonance with the toxicity of **6**, we observed that longer incubations, and/or using higher concentrations of the substrate **5** with the NR-preloaded

cells correlates with increased loss of cell viability (Figure 5.8). For instance, cell viability (24 h) was equally impaired (~ 50%) by either exposure of cells (without NRs) to 0.15 μM of the cresyl violet **6** (the product) or by addition of 10 μM of the bisprotected precursor **5** to NR-preloaded cells. We should acknowledge at this point that Pd-NPs (50 pM ≈ 2 μM in surface Pd, overnight) without the MOF shell also promoted the intracellular generation of the cresyl violet **6**. However, as expected from the test tube experiments, the efficiency was considerably lower than with the NRs (Figure S5.17). This is also reflected from the less impaired viability (that is, less cresyl violet production from **5**) in cells pretreated with Pd-NPs than with our NRs (Figure 5.8).

To illustrate the real potential of our palladium nanoreactors, we carried out equivalent in vitro reactivity studies using three state-of-the-art Pd homogeneous catalysts: **Pd-1** ([Pd(allyl)Cl]$_2$),[165] **Pd-2** ([PPh_3)Pd(allyl)Cl]),[168] and **Pd-3** ([($PdCl_2$($TFP)_2$])[270]. In consonance with these previous reports on related uncaging reactions, these homogeneous catalysts showed only marginal activity in the intracellular depropargylation of **5** (2 μM Pd, overnight incubation, Figure S5.17). A comparative analysis using a fluorescence readout (CTCF per cell) confirmed that our NR drastically outperform any of these catalysts, leading to CTCF per cell ~15 times higher than those obtained with Pd-2, which was the best of these complexes (Figure 5.10c, Figure S5.17). The comparison with the reactivity of Pd-NPs (included also in Figure 5.10) provides also no doubts about the superiority of the NRs. The reasons for this much-improved performance of our metallo-nanoreactors inside living cells must be related to the core-shell nanoarchitecture in which the MOF-based shell plays a critical role to protect the metal reactive chamber from deactivation, while providing for a controlled flow of reactants.

Diffusion-controlled core-shell Pd/ZIF8 as recurrent intracellular nanoreactors. The above studies confirm that the designed Pd/MOF NCs are readily internalized into mammalian cells, and capable of promoting intracellular depropargylation reactions. We then envisioned that the core-shell, microporous structure of our constructs might allow an efficient flow of reagents and products without damage to the core catalytic Pd, and therefore, the Pd/ZIF8 platforms could work as recyclable NRs. Accordingly, we examined the feasibility of reusing the nanocatalyst-loaded cells, which can be especially relevant in terms of accomplishing the long-term goal of developing catalytic cellular implants.

Given that product **6** can be readily washed out of the cells, we explored the viability of using our Pd/MOF platforms as recurrent (flow) intracellular nanoreactors. Therefore, the NR-preloaded cells were incubated during 3 h with the substrate **5** (20 μM = run-1) as previously discussed; and the intracellular formation of cresyl violet **6** was confirmed by confocal microscopy (Figure 5.11a, left). Cells were washed with PBS twice to remove extracellular

substrates/products and fresh cell medium was added, which further facilitated the self-cleansing of **6**. Indeed, after 3 h there is almost no intracellular fluorescence (Figure 5.11a, right). Next, cells were incubated with a second dose of substrate **5** (20 μM = run-2) during 3 h. We observed again a rise up of fluorescence associated to the production of **6** (Figure 5.11b, left), which again, as previously discussed, was cleared by the cells after 3 h (run-2 / self-cleansing; Figure 5.11b, right). We repeated this protocol up to 4 cycles (Figure 5.11; additional images in Figure S5.18), with similar outcomes, which demonstrates the robustness of our heterogeneous NRs to perform dose-dependent, sustained intracellular transformations. For completeness, we also attempted equivalent experiments with either the pristine **Pd-NPs** or the homogeneous catalysts (**Pd-1**, **Pd-2** and **Pd-3**). Not surprisingly, these reagents, which already performed poorly in a first cycle, were unable to sustain a second reaction cycle (Figure S5.17). These results further corroborate the unique performance of our NRs in this type of recurrent reactivity and represent a first approach to the development of reusable "catalytic cells".

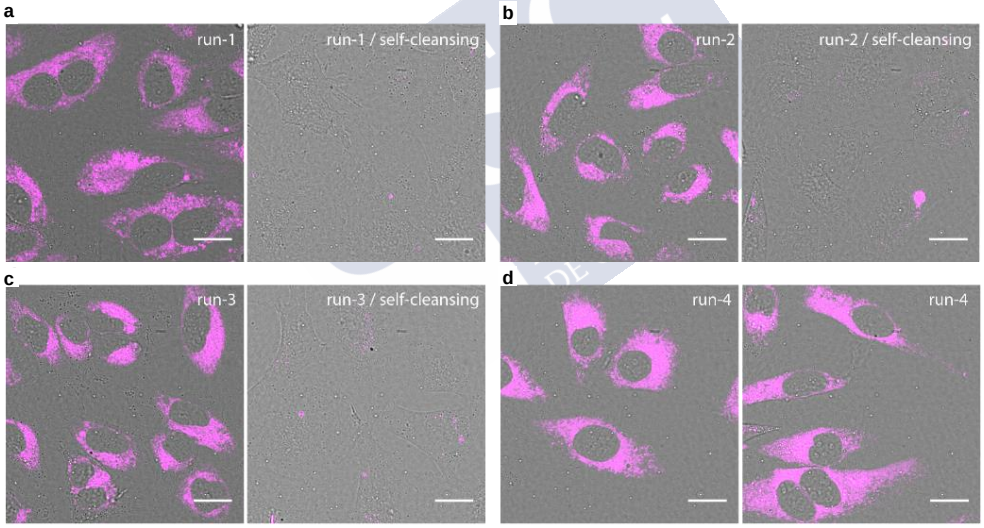

Figure 5.11. NR-preloaded cells working as recurrent "flow" nanoreactors.
a-c) First, second and third uncaging runs using the same NR-preloaded cells and recorded by confocal microscopy; left: after 3 h incubation of **5**; right: after 3 h of self-cleansing. d) Two images of the fourth deprotection run of precursor **5** with the same NR-preloaded cells. In a-d), confocal images (100X) correspond to merged channels: bright-field plus fluorescence. Scale bars correspond to 20 μm.

3D spheroid catalytic model. Having demonstrated the potential of our NRs to carry out intracellular depropargylation reactions in adherent 2D cultured cells, and the viability of using these NR-containing cells in a recurrent manner, we questioned whether the reactivity could be exported to tissue-like models.

This would be an important step to further narrowing the frontier between transition metal catalysis, and cellular biology and biomedicine. In particular, we wondered whether it would be possible to build 3D tissue-like systems containing our NRs, and if these cellular networks could be capable of performing the designed metal-promoted reactions. We chose 3D tumour spheroids as models of avascular tissues, as they are widely used in cancer research as intermediate models between in vitro cancer cell line cultures and in vivo tumors.[298]

To test the viability of building these spheroids we first used NRs in which the PMA contains a rhodamine tag, in order to facilitate the analysis by confocal microscopy. Therefore, Hela cells were loaded with these NRs as previously discussed, and grown in agarose templates for 24 h (see Section 6.4.8, Figure S5.19). Microscope inspection of the cell cultures confirmed the presence of the desired 3D structures (developed from an initial density of $\sim 1 \cdot 10^4 - 3 \cdot 10^4$ cells per spheroid, which presented a diameter ~0.4 – 1 μm). Importantly, we observed a homogeneous distribution of the NRs inside the cells of the spheroids (Figure 5.12a).

Following the same procedure, we synthesized homologous spheroids using NRs without the fluorescent label, and their reactive potential was analysed in the uncaging of bis-propargylated probe **5** (Figure S5.20). Excitingly, when the NR-loaded spheroids were incubated with **5** (20 μM) for 24 h, we observed a clear build-up of fluorescence corresponding to product **6** (Figure 5.12b). Curiously, and in contrast to the homogeneous distribution of the rhodamine-labelled NRs Figure 5.12a), the fluorescence arising from **6** is non-homogeneous, but mostly concentrating as a thick "crust" in the spheroid. This result is not surprising, and it is very likely due to the diffusion-limited distribution of the substrate **5**, which prefers to enter the cells located in the more external layer of the tissue model. It is important to note that tumour spheroids are in fact suitable models to reproduce the heterogeneity of environments within solid tumours: decreasing chemical gradients of nutrients from the outermost cells to the hypoxic core of the spheroid.

After one run, as previously discussed for the 2D cell experiments, NR-loaded spheroids were washed with PBS (three times) to remove extracellular substrates/products, and fresh cell media was added, which facilitated the self-cleansing of **6** (for 24 h, Figure 5.12c). The resulting NR-loaded spheroids were again incubated with **5** (20 μM) during 24 h. Gratifyingly, we observed a new rise up of fluorescence associated to the production of **6** (Figure 5.12d), which is again mainly concentrated in the crust.

These results represent the first demonstration of a transition-metal promoted reaction carried out in a living tissue model. More importantly, the spheroids can be considered as recyclable "catalytic tissues", a concept without

precedent, which might have profound implications in the future development of "catalytic cellular or tissue implants".

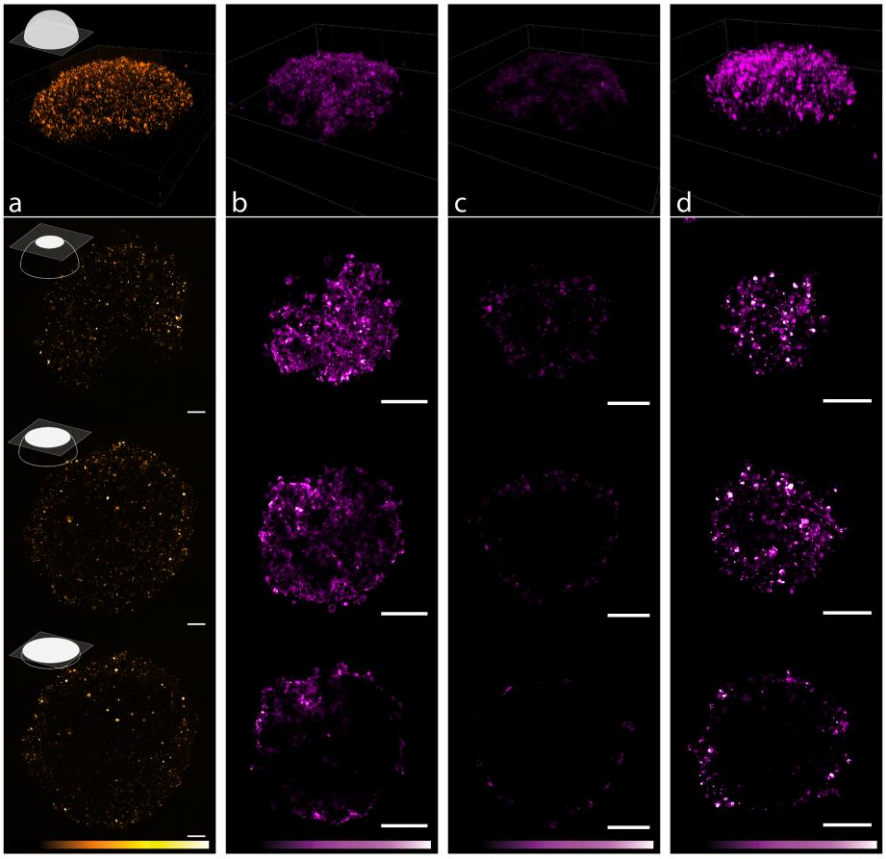

Figure 5.12. NR-preloaded 3D spheroids working as recurrent flow tissue-like reactor. a) Top: 3D reconstruction of confocal microscopy z-scans of a NR-preloaded spheroid; NRs were fluorescently labelled (i.e., PMA was covalently modified with a rhodamine tag). Bottom: Three individual scans at different depths are shown, illustrating the homogeneous distribution of the NRs throughout the spheroid volume. b) Top: 3D reconstruction of confocal microscopy z-scans of a NR-preloaded spheroid 24 h after incubation with substrate 5 (20 μM), showing the fluorescence resulting from the generation of 6. Bottom: Three individual scans at different depths are shown, illustrating the non-homogeneous "crust-like" distribution of 6 throughout the spheroid volume. c) Top: 3D reconstruction of confocal microscopy z-scans of a NR-preloaded spheroid, which after one reaction run with **5**, was washed with PBS (three times) and incubated for 24 h in fresh cell media, which led to self-cleansing of the spheroid. Bottom: Three individual scans at different depths are shown to illustrate the self-cleansing process at different depths. d) Top: 3D reconstruction of confocal microscopy z-scans of a NR-preloaded spheroid, which after one reaction run with **5** (24 h), and the self-cleansing step (24 h), was gain incubated with more substrate (5, 20 μM). Bottom: Three individual scans at different depths are shown, illustrating the non-homogeneous "crust-like" distribution of fluorescence (from **6**) throughout the spheroid volume. 3D reconstructions were done with ~ 300 stack images (total thickness ~ 150 μm; step thickness ~ 0.5 μm). Scale bars correspond to 100 μm (20X).

5.3. MATERIALS AND METHODS

For detailed experimental methods and additional results see section *Chapter 5 Appendix.*

***Synthesis of probes*.** The compounds propargyl-protected coumarin **1**, propargyl-protected **2**-(2'-hydroxyphenyl) benzothiazole **3**, and bis-propargyl carbamate-protected cresyl violet **5** were synthesized and characterized by the Mascareñas group at CIQUS, Santiago de Compostela.[167, 299-300]

Preparation of PMA-modified Pd/ZIF8 NCs (NRs). The here designed and studied NRs consisted of a Pd-NP core and a ZIF8 shell, which was further functionalized with a polymer (PMA). The synthetic method involved three main steps: i) CTAB-coated Pd nanocubes enclosed by {100} facets were first synthesized using K_2PdCl_4 as precursor, AA as reducing agent, CTAB as capping agent and stabilizer. ii) These Pd-NPs were then used as seeds onto which a shell of ZIF8 was grown by following an aqueous procedure in which the surfactant CTAB works as size-controlling and structural-directing agent. iii) Finally, in order to provide colloidal stability in diverse complex aqueous media, these Pd/ZIF8 core-shell particles were wrapped with the amphiphilic polymer PMA by following a recently described protocol;[231] alternatively, PMA was covalently modified with a rhodamine (specifically, we used TAMRA: tetramethylrhodamine 5 - (and - 6) - carboxamide cadaverine) for fluorescence labeling of our NRs, as previously reported for analogous plasmonic NCs.[231]

Characterization techniques. SEM and TEM were used to study the size and morphology of the nanomaterials. SEM images were acquired with a FESEM Zeiss Ultra Plus operated at 3 kV and 20 kV. TEM images were acquired with a JEOL JEM-2010 microscope operated between 80 and 200 kV accelerating voltage. ImageJ free software and Origin software were used for the size measurements and distribution analysis, respectively. Mass spectra were acquired using IT-MS Bruker AmaZon SL and using electrospray ionization (ESI). UV-Vis absorption spectra and fluorescence spectra were acquired using Jasco V-670 spectrometer and Varian Cary Eclipse fluorescence spectrofluorometer, respectively. An X-ray diffractometer Philips was used to study the crystallinity of the samples, operating in the range of 2θ between 2° and 75° with a passage of 0.02° and a time by step of 2s. A Malvern Zetasizer (Nano ZSP) instrument, equipped with a 10 mW He–Ne laser operating at a wavelength of 633 nm and fixed scattering angle of 173˚, was used to measure the hydrodynamic diameters (by DLS) and the ξ-potentials (by LDA). ICP-MS measurements were performed using an Agilent 7700x ICP-MS after acidic digestion of the samples with aqua regia. Reverse phase high-performance liquid chromatography-diode array

detector/mass spectrometry (RP-HPLC-DAD/MS) analysis was done by using Thermo Dionex Ultimate 3000 coupled with a MSD Bruker AmaZon SL.

General procedures for the uncaging reactions. The reaction with NRs or with Pd-NPs in aqueous solution was performed as follows: **1**, **3** or **5** (8 µL, 0.5 mM stock solution in MeOH) was added to a H_2O:MeOH 9:1 solution (342 µL of the reaction medium; H_2O:MeOH 8:2 solution for substrate **5**) in a 1.5 mL small vial (containing a stirring bar), followed by addition of an aqueous solution of Pd-NPs or NRs (50 µL, 2 nM, unless otherwise specified; this corresponds to 10 µM of surface Pd). Reactions were carried out overnight under continuous stirring (400 RPM) at 37 ºC. Afterwards, the particles were collected by centrifugation (7000 RCF, 10 min) and washed with 400 µL of reaction medium, and the generated product (supernatant) was quantified by fluorescence.

Parameters such as the catalyst concentration, the influence of washing steps, the presence of bio-additives in the reaction medium were studied and evaluated. Potential leakage of Pd during the reaction was determined by ICP-MS of the supernatants. Procedures for obtaining kinetic curves and TONs, and testing the reusability of the particles (Pd-NPs or NRs) are described in the Appendix (Section 6.4.6). Each experiment was performed at least in duplicate, and the values given correspond to the mean value ± standard deviation (SD) of $n \geq 2$. Each measurement was taken from distinct samples. R^2 is the coefficient of determination, used as statistical parameter of goodness-of-fit in the calibration curves. Data analysis was performed using OriginPro 8 statistical software.

2D and 3D cell studies. HeLa (cervical cancer cell line are readily available from ATCC) were cultured in DMEM with phenol red, 4.5 g/L D-glucose, L-glutamine and pyruvate (1X, Gibco, #41966-029) supplemented with 10% FBS (Gibco, #10270-106) and 1% P/S (Corning, 100X, #30-002-CI). Cells were maintained under humid conditions at 37 °C and 5% of CO_2. Cells were passaged after cleaning (PBS 1X, Gibco, #14190-094) with 0.25% Trypsin-EDTA (1X, Gibco, 25200-056) when the culture reached confluency.

- *Cell Viability.* In order to study number of viable cells after the exposure to the substrates, Pd-NPs and/or NRs, we carried out resazurin assays (Figure 5.8). HeLa cells were seeded in 96-well plates (NEST Scientific, #701001), $7.5 \cdot 10^3$ cells per well in 100 µL of cell growth medium (0.3 cm^2 per well) for 24 h before particle exposure. Then, medium was removed and 100 µL of cell culture growth medium with the desired concentration of the substrates, Pd-NPs and/or NRs, were added. Cells were incubated with the samples the time of interest at 37 °C and 5% CO_2. After that, we rinsed each well three times with PBS and added 100 µL of freshly prepared solution with 90% of medium and 10% of resazurin (resazurin sodium salt in water 0.2 mg/mL filtered, Sigma Aldrich, #199303-1G).

Cells were incubated during 3 h at 37 °C and 5 % CO_2 under dark conditions before being measured with a plate reader (Infinite® 200 PRO, Tecan, Switzerland) under 560/20 nm excitation and collecting fluorescence with a 610/20 nm filter. Final values were calculated using Eq. 3 (Figure 5.8).

- *Pd content per cell.* ICP-MS was used to quantify the average Pd content per cell, which we used to estimate the number of Pd-NPs or NRs per cell (Table S5.14); see calculations in section 6.4.4. Note that to estimate the number of particles per cell, we assume that the particles (Pd-NPs or NRs) retain their original Pd content; however, in contrast to Pd-NPs, such assumption seems valid for NRs according to the stability data (Table S5.2). HeLa cells (~ $6.4 \cdot 10^6$ cell per experiment) was cultured as previously discussed, supplemented with Pd-NPs or NRs (50 pM ≈ 2 μM in surface Pd, equivalent to ~ $5.7 \cdot 10^3$ particles per cell), and incubated overnight. Extracellular Pd (either free, Pd-NP or NRs) were washed out, and the Pd-loaded cells were digested with aqua regia (see detailed procedures in previous work[305]).

- *Confocal imaging.* To perform all the confocal imaging experiments with living cells, $20 \cdot 10^3$ HeLa cells (200 μL) were seeded on μ-Slide 8 well-ibiTreat chambers (1 cm^2 *per* well, Ibidi, Germany, #80826) at least 12 h before NR/substrate exposure. Organelle staining with LysoTracker Blue (#L7525), Mitotracker Green (#M7514) and CellMask Deep Red (#H32721) was performed following provider (Thermo Fisher Scientific) instructions. Confocal images of living cells were captured on an Andor Dragonfly spinning disk confocal system mounted on a Nikon TiE microscope equipped with a Zyla 4.2 PLUS camera (Andor, Oxford Instruments) and an OKO-lab incubator to keep cells at 37 °C during all the experiment. Images were taken with different magnification objectives (60X, 100X). All the images were processed with ImageJ. Confocal microscopy images of the NR system in which PMA was fluorescently labelled (covalently) with a rhodamine (tetramethylrhodamine 5-(and-6)-carboxamide cadaverine),[231] are shown in Figure 5.9, aiming to illustrate the efficient cell internalization (HeLa cells) of the proposed NRs (50 pM) and colocalization with lysosomes. Note that we used equivalent particle (NR or Pd-NP) incubation conditions in all the cell studies.

  Excitation/Emission wavelengths used for confocal imaging of the rhodamine-labelled NRs/product **6** are 561/620(60) nm.

- *Uncaging reactions*. A standard *in vitro* experiment consists of incubation of HeLa cells with NRs or Pd-NPs (50 pM ≈ 2 μM in surface Pd) overnight (~ 12 h). In all cell studies, before adding the substrates (**5**) or resazurin (for cell viability studies; Figure 5.8), non-internalized nanostructures were washed out from the cell culture. In the case of the intracellular uncaging of

5, before confocal inspections, washing of extracellular probes (substrates and/or products) were not required.

Different concentrations of substrate **5** (Figure S5.11 and Figure S5.12) were added to cells pre-treated with NRs or Pd-NPs (50 pM, overnight). The production of **6** was inspected after the time of interest (1 - 24 h).

For the analysis of the uncaging of **5** over time (Figure S5.12, Figure S5.13, Figure S5.14 and Figure S5.15), we preload the cells with NR (50 pM) overnight and, after three washing steps with PBS to remove the excess of NR non-associated with cells, substrate **5** (10 μM) was added. We incubated substrate **5** for 1, 3, 6 and 24 h. Washing steps to remove extracellular excess of **5** and or **6** were not required before confocal inspection.

Controls for all the experiments were carried with non-toxic concentrations of **6** but with Pd-free cells (Figure S5.16). We also confirmed that Pd-NPs (50 pM ≈ 2 μM in surface Pd, overnight) without the MOF shell, or a series of discrete Pd complexes (**Pd-1**, **Pd-2** and **Pd-3**; 2 μM Pd, overnight), promote the intracellular uncaging of the cresyl violet **6** (Figure S5.17), although with much less efficiency than NRs.

- *Intracellular recycling*. To study the reusability of our cell-nanoreactor for the uncaging of **5**, we stopped the incubation of the substrates with NR-preloaded cells after the time of interest (substrate **5**: 20 μM, 3 h). Then, the intracellular production of **6** was inspected under the microscope; it is worth noticing that washing to remove extracellular substrates/products step was not required for visualizing the uncaging of **5**. Next, before adding a second shot of **5** (10 μM, 3 h), we cleaned with PBS, added fresh complete DMEM and waited for the cells to "wash away" **6** (~ 3 h, self-cleansing). We repeated these steps to complete up to four cycles (Figure 5.13, Figure S5.18).

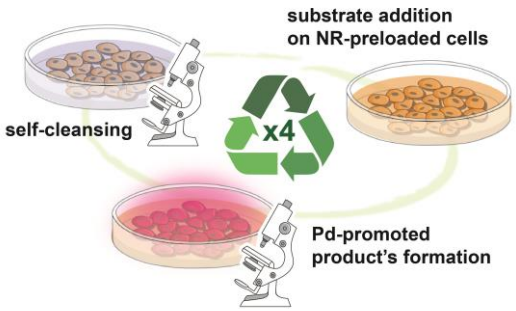

Figure 5.13. Intracellular recycling with NRs preloaded cells methodology.
Reusability scheme (4 cycles) demonstrated for the deprotection of precursor 5 (see Figure 5.11 and Figure S5.18).

As controls for the recycling experiments, we also performed similar studies for the uncaging of **5** (two runs) but using Pd-NPs (50 pM ≈ 2 μM in surface Pd, overnight) or the discrete Pd complexes (**Pd-1**, **Pd-2** or **Pd-3**; 2 μM Pd, overnight). However, such alternative Pd catalysts were unable to achieve a second uncaging cycle, at least to any degree observable by the intracellular fluorescence of **6** (Figure S5.17).

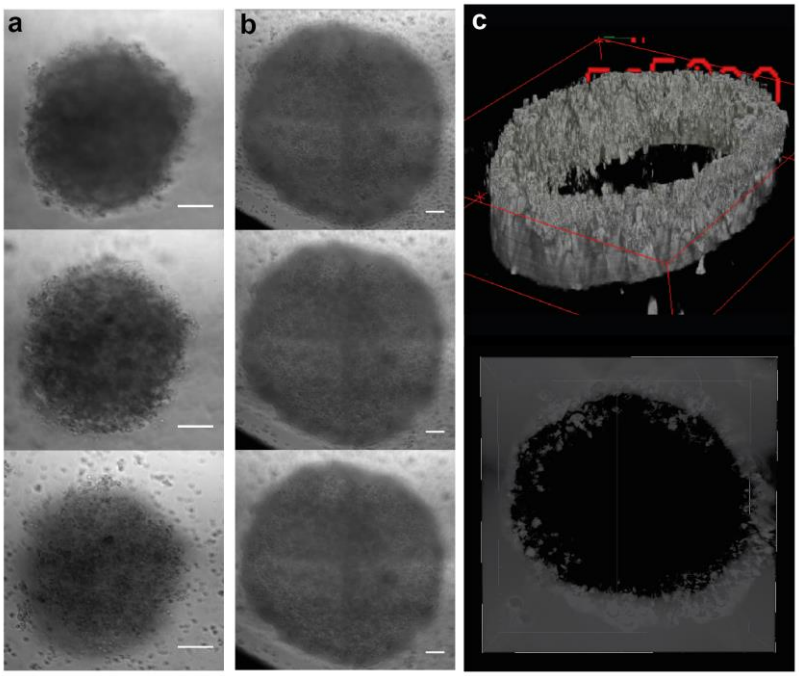

Figure 5.14. Brightfield images of 3D HeLa spheroids.
Collage of brightfield images of 3D HeLa (Pd "free" spheroids). a) HeLa spheroid with diameter ~ 0.4 μm (1 image per stack), three different stacks of the spheroid; b) HeLa spheroid with diameter ~ 1 μm (4 images in each plane), three different stacks of the spheroid; c) 3D reconstructions of a spheroid with diameter ~ 0.4 μm. Scale bars correspond to 100 μm.

- *Uncaging and recycling in 3D NR-preloaded HeLa spheroids.*

Spheroids of HeLa cells were cultured in a flat bottom 96-well plates previously treated with agarose as follows:[298] a 1% agarose solution in filtered PBS was heated until 100 °C; the tips and the 96-well plate was pre-warmed in the incubator for ~ 1 h, and 40 μL of the agarose solution were added to each well; the agarose filled wells were led to cool down during, at least, 30 minutes in sterile conditions. Then, we confirmed a homogeneous agarose gelation without bubbles by inspection under the microscope. Once agarose was solidified, 100 μL of cells (NR-preloaded or "empty") solution at different cell concentrations ($1 \cdot 10^5$ cells/mL for final spheroid diameter ~ 0.4 μm, $2 \cdot 10^5$ cells/mL for ~ 0.8 μm and $4 \cdot 10^5$ cells/mL for ~ 1 μm) were added slowly. Cells were led to attach to each

other during 24 hours before checking the spheroids formation. After 24 h, the sizes of spheroids were between 0.4 and 1 μm when varying total cells amounts from ~ $1 \cdot 10^4$ to $3 \cdot 10^4$ cells per spheroid (Figure 5.14). Media of the wells containing the spheroids were changed daily.

For spheroids imaging, spheroids formed as previously discussed were placed onto a μ-plate angiogenesis 96-well (0.125 cm^2 per well, Ibidi, Germany #89646) using a pipette with a sterile cut tip to facilitate the spheroid's manipulation. Using an Andor Dragonfly spinning disk confocal system with the 20X objective, spheroids were observed in the brightfield channel (Figure 5.14) and in the Cy3 channel (Ex./Em, 561/620(60) nm) where the fluorescence from TAMRA (Figure S5.19) or from the uncaging of **6** (Figure S5.20) were collected. For the bigger ones (~ 1 μm in diameter), 4 different images in the XY plane were required. Z-scans were made with ~ 300 different stack images in the Z-axis. 3D reconstructions were done with ~ 300 stack images (total thickness ~ 150 μm; step thickness ~ 0.5 μm). Scale bars correspond to 100 μm (20X). To treat the 2D images as well as to crop or stitch 4x4 images, ImageJ was used. Deconvolution of the z-scans were done with Fusion software and finally, for 3D reconstructions, Imaris software (Oxford Instruments) was used.

To form spheroids with catalytic properties, $2 \cdot 10^4$ cells per well were seeded on 6-well plates. After 24 hours of cell attachment, cells were treated with NRs (50 pM, overnight) as previously discussed. Notice that non-treated cells were always seeded and maintained as control to form control non-catalytic spheroids. Once the NR were internalized, extracellular NRs were washed three times with fresh PBS. Cells were trypsinized with 200 μL of trypsin and neutralized with 2 mL of supplemented DMEM. After that, dilutions were made to obtain the desired number of cells in 100 μL. After one day of spheroids formation, the medium was removed and fresh medium containing **5** (20 μM) was added to both NR-loaded spheroids and control spheroids without NRs (Figure S5.20). After 24 hours, spheroids were checked under the confocal microscope. Media was removed and the spheroids were thoroughly washed (3x) with PBS to remove extracellular substrates and/or products and fresh medium was added, which facilitated the self-cleansing of **6** during 24 h. After self-cleansing, a second addition of **5** (24 hours, 20 μM) were added to confirm that the spheroids were still catalytic and confirm reusability.

5.4. CONCLUSIONS

We have demonstrated for the first time the feasibility of using Pd/ZIF8 NCs as intracellular heterogeneous metallo-catalysts. In contrast to other MOF-metal hybrids which present active metals in their surface, our core-shell Pd/ZIF8 architecture ensures that the reaction occurs in the core reaction chamber, which

is critical for the biological application. Our polymer PMA post- functionalization provides our nanoreactors with robust colloidal stability even at the aqueous acidic medium of lysosomes. Therefore, the ZIF8-based shell plays a critical role to preserve the integrity of the catalytic chamber while providing for orthogonality (substrate selectivity) and biocompatibility. Excitingly, our heterogeneous nanoplatforms can process sequential batches of reactants when loaded in cells, both in the form of 2D monolayers or as 3D tumour spheroids. This represents a pioneering demonstration of intracellular recurrent nanoreactors and set the basis for the development of *catalytic cellular or tissue nanoimplants*.

The versatility of the nanobuilding technology promises a straightforward access to other related NCs (for instance, by integrating other metal(s) clusters or NPs, and/or metal-organic-framework based shells), which could operate as multifunctional nanoreactors in biological settings. These artificial nanoreactors featuring transition metal centres offer exotic possibilities for performing many other abiotic reactions in living environments, and therefore promise to have important applications in chemical and cell biology, and in biomedicine.

USC
UNIVERSIDADE
DE SANTIAGO
DE COMPOSTELA

6. APPENDIX

6.1. CHAPTER 2 APPENDIX

6.1.1. Synthesis of 808 nm-activable core-multishell upconversion nanoparticles

The injection sequence and volumes used to grow the shells are summarized in Table S2.1. Figure S2.1 shows the experimental setup.

$Shell_1$	**$NaYF_4$:$Yb_{10\%}$**	1 mL of Y,Yb-OA → 0.5 mL of Na-TFA-OA →1 mL of Y,Yb-OA → 0.5 mL of Na-TFA-OA
$Shell_2$	**$NaNdF_4$:$Yb_{10\%}$**	1 mL of Nd,Yb-OA→ 0.5 mL of Na-TFA-OA→1 mL of Nd,Yb-OA → 0.5 mL of Na-TFA-OA
$Shell_3$	**$NaYF_4$:$Yb_{10\%}$**	1 mL of Y,Yb-OA → 0.5 mL of Na-TFA-OA →1 mL of Y,Yb-OA → 0.5 mL of Na-TFA-OA

Table S2.1. Sequence of reactants injections.

Figure S2.1. Experimental setup for UCNP's synthesis

6.1.2. Characterization of 808 nm-activable upconversion core-multishell UCNPs

SEM and TEM. SEM images were acquired with a FESEM Zeiss Ultra Plus operated at 3 kV or 20 kV. TEM micrographs were obtained using a JEOL JEM-2010 electron microscope operated at an accelerating voltage of 120 kV. For SEM images, 5 μL of diluted samples were deposited onto a silicon wafer before air-drying. In order to prepare TEM samples, 3 μL of a diluted sample was deposited on a carbon film supported on a 400 mesh copper grid (Electric Microscopy

Sciences, CF400-CU) and was air-dried. Results confirmed that core and core-shell structures were perfectly monodispersed and all shells growth uniformly around the cores, keeping NPs morphology almost intact and producing a single population.

SEM and TEM micrographs from core and core@shell$_1$@shell$_2$@shell$_3$ structures are shown in Figure S2.2 and Figure S2.3. Using the free ImageJ software, the diameter (*d*) of at least 300 particles was measured

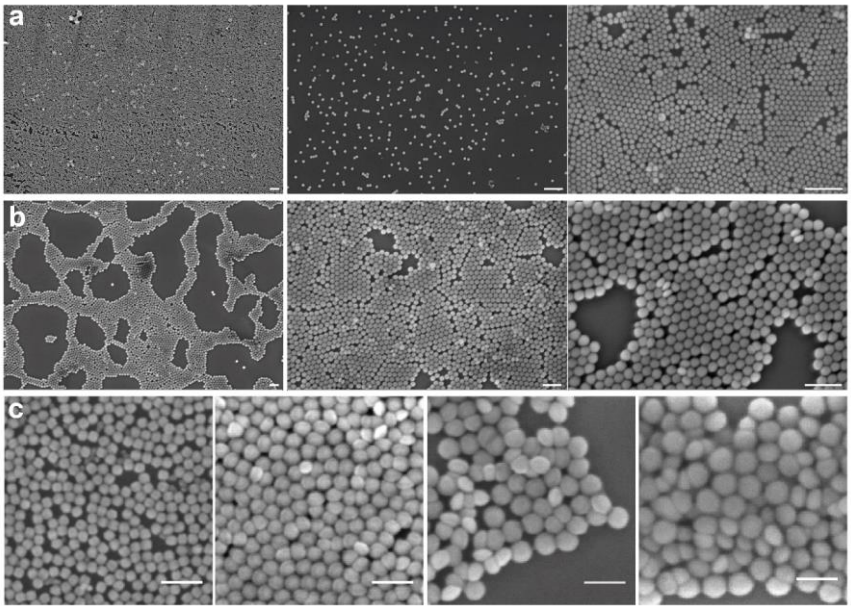

Figure S2.2. SEM characterization of UCNP cores and core@multishell.
a,b) SEM micrographs at different magnifications (50 kX, 100 kX and 200 kX) for cores (a) and core@multishell (b) structures. Scale bars represent 200 nm. c) SEM micrographs from the different growing steps. From left to right, core, core@shell1, core@shell1@shell2 and core@shell1@shell2@shell3. Scale bars represent 100 nm.

PXRD. Powder X-ray analysis were carried out in an X-ray diffractometer Philips to study the crystalline powder of samples; the samples were examined in the range of 2θ between 2° and 75°, with a passage of 0.02° and a time by step of 2s. The UCNPs cores showed a good correlation (red peaks) with the standard pattern for $NaFY_4$, (ICDD PDF #16-0334) which confirm the cores hexagonal crystalline structure. In Table S2.2 there is a list of the identified peaks in the cores sample.

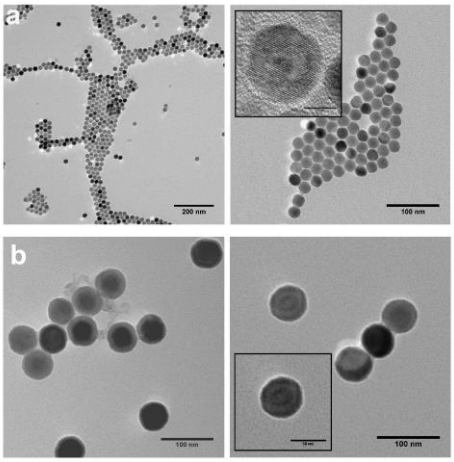

Figure S2.3. TEM characterization of UCNP cores and core@multishell.
TEM micrographs at different magnifications (50 kX, 100 kX and 200 kX) for a) 980 nm-UC cores and b) 808 nm-UC core@shell$_1$@shell$_2$@shell$_3$ structure.

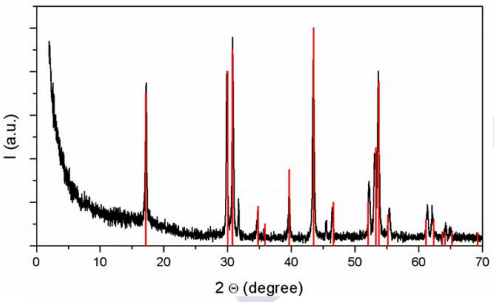

Figure S2.4. X-ray spectra from core UCNPs
Hexagonal structure and overlapping with the $NaYF_4$ standard pattern structure.

Pos. [°2Θ.]	d-spacing [Å]	Rel. Int. [%]	Height [cps]	Struct. FWHM [°2Θ]
17.183(3)	5.15646	66.57	84.99	0.159763
29.876(2)	2.98824	81.86	104.52	0.139381
30.796(2)	2.90106	91.94	117.39	0.152761
31.707(5)	2.81981	17.37	22.18	0.077344
34.67(1)	2.58553	11.95	15.26	0.126266
39.608(6)	2.27360	25.17	32.13	0.156949
43.436(2)	2.08166	100.00	127.68	0.163850
45.421(9)	1.99522	11.65	14.88	0.075171
46.394(7)	1.95562	15.97	20.39	0.123563
52.167(5)	1.75195	30.77	39.29	0.152546
53.062(5)	1.72448	41.66	53.19	0.173181
53.625(4)	1.70770	87.82	112.13	0.151593

Table S2.2. List of major peaks identified x-ray spectra of the cores.

Inductively coupled plasma mass spectrometry. ICP-MS analysis was performed in order to determine the final concentration and composition of the NPs after and during the synthesis and the dopants percentage in each of the core or shells.

Three different and independent core synthesis were analysed via ICP-MS. Samples obtained during the shell growing steps from the same synthetic process were analysed in order to determine the individual shell composition.

20 µL of all the samples were digested overnight with 480 µL of aqua regia. Samples were diluted with 4.5 mL of HCl 2% v/v. The concentration in ppb (µg/L) of Y, Yb, Nd and Er was measured. Using the molecular formula of the matrix (1 mol Na : 1 mol Y : 4 mol F) and correcting by the dilution factor, the total mass in each sample was determined. Then, the mass of one nanoparticle (Eq. 4), the molecular weight of the NPs, the number of NPs per liter and the molarity were determined. For that, the NPs were considered spherical and the bulk densities for all the materials were applied: $\rho(NaYF_4)$ = 4.13 g/cm^3, $\rho(NaNdF_4)$ = 4.87 g/cm^3, $\rho(Yb)$ = 6.98 g/cm^3, $\rho(Er)$ = 9.05 g/cm^3, $\rho(Er)$ = 7.01 g/cm^3.

$$m_{core} = V_{core} \cdot \rho_{core}$$

$$m_{core} = \left[\frac{4}{3}\pi\frac{d^2}{2}\right] \cdot [\rho(Yb) \cdot Yb_{\%} + \rho(Er) \cdot Er_{\%} + \rho(NaYF_4) \cdot Y_{\%}] \qquad \textbf{Eq. 4}$$

To determine both core composition and cores concentration three independent synthesis were measured (Table S2.3). Using Eq. 4, the experimental percentage for each element (Table S2.4) and the measured diameter obtained by TEM (*d*, Table S2.5), the mass of an individual core (m_{NP}) and the MW was determined. Results confirmed that the concentration of the core solutions dispersed in 30 mL of chloroform is 302 ± 25 nM (c_{NP}, Table S2.5).

	C_Y [10^3 uM]	C_{Na} [10^3 uM]	C_F [10^3 uM]	C_{Yb} [10^3 uM]	C_{Er} [10^3 uM]
1	(44.89 ± 0.37)	(44.89 ± 0.37)	(179.6 ± 1.5)	(5.11 ± 0.11)	(1.372 ± 0.024)
2	(46.35 ± 0.84)	(46.35 ± 0.84)	(185.4 ± 3.7)	(5.21 ± 0.12)	(1.514 ± 0.041)
3	(40.86 ± 0.37)	(40.86 ± 0.37)	(163.4 ± 1.5)	(4.58 ± 0.89)	(1.286 ± 0.022)

Table S2.3. Experimental concentrations of each element in three different syntheses of core UCNPs.

	Y [%]	Yb [%]	Er [%]	d [nm]
1	(87.38 ± 0.43)	(9.95 ± 0.03)	(2.67 ± 0.24)	(21.9 ± 1.7)
2	(87.34 ± 0.51)	(9.81 ± 0.21)	(2.85 ± 0.30)	(22.0 ± 1.3)
3	(87.45 ± 0.22)	(9.80 ± 0.07)	(2.75 ± 0.13)	(21.12 ± 0.89)

Table S2.4. Experimental concentrations of each element.
Values from three different synthesis of core UCNPs which diameters were obtained from TEM micrographs.

$Y_{\%}$	$Yb_{\%}$	$Er_{\%}$	MW $[\cdot 10^7$ g/mol]	m_{NP} $[\cdot 10^{-17}$ g]	C_{NPs} [nM]
87.39 ± 0.06	9.85 ± 0.08	2.76 ± 0.09	(1.5 ± 0.1)	(2.32 ± 0.19)	660 ± 44

Table S2.5. Experimental values obtained by ICP-MS after performing statistical calculations.

In order to calculate the experimental element ratios in each shell, each synthetic step was analysed independently. The expected UCNPs structure is $NaYF_4$:$Yb_{18\%}Er_{2\%}$@$NaYF_4$:$Yb_{10\%}$@$NaNdF_4$:$Yb_{10\%}$@$NaYF_4$:$Yb_{10\%}$. Using the experimental element percentage, the matrixes molecular formula and the Eq. 5, the mass corresponding to each shell was determined ($m_{shell,x}$). These values, combined with the shell thickness and volumes, allowed for the total mass of the final core@$shell_1$@$shell_2$@$shell_3$ calculation (Eq. 5).

Eq. 5

$$m_{UCNP} = m_{core} + m_{shell1} + m_{shell2} + m_{shell3}$$

$$m_{shell1} = \frac{\pi}{6}(d^3_{shell1} - d^3_{core}) \cdot \left[\rho(Yb) \cdot Yb^{\%}_{shell1} + \rho(NaYF_4) \cdot Y^{\%}_{shell1}\right]$$

$$m_{shell2} = \frac{\pi}{6}(d^3_{shell2} - d^3_{shell1}) \cdot \left[\rho(Yb) \cdot Yb^{\%}_{shell2} + \rho(NaNdF_4) \cdot Nd^{\%}_{shell2}\right]$$

$$m_{shell3} = \frac{\pi}{6}(d^3_{shell3} - d^3_{shell2}) \cdot \left[\rho(Yb) \cdot Yb^{\%}_{shell3} + \rho(NaYF_4) \cdot Y^{\%}_{shell3}\right]$$

	CORE	SHELL$_1$	SHELL$_2$	SHELL$_3$
Y$_{\%}$	(83.79 ± 0.01)	(94.20 ± 0.64)	-	(95.30 ± 1.60)
Yb$_{\%}$	(13.59 ± 0.01)	(5.80 ± 0.10)	(6.15 ± 0.20)	(4.67 ± 0.19)
Er$_{\%}$	(2.62 ± 0.01)	-	-	-
Nd$_{\%}$	-	-	(93.85 ± 0.19)	-
Element Ratio	Y/Er = 31.91 ± 0.05 Yb/Er = 5.17 ± 0.01	Y/Yb = 16.25 ± 0.28 Y_{shell1}/Y_{core} = 1.66 ± 0.02	Nd/Yb = 15.25 ± 0.50	
Diameter [nm]	24.0 ± 1.1	42.1 ± 6.5	52.3 ± 2.1	59.3 ± 9.4
Mass [·10^{-18} g]	33.5 ± 4.8	137 ± 78	178 ± 100	147 ± 230

Table S2.6. Dopants percentages and dopants ratios within the shells.
Measurements by ICP-MS obtained for core, core@shell$_1$, core@shell$_1$@shell$_2$ and core@shell$_1$@shell$_2$@shell$_3$. Diameters of the samples as determined by TEM and the mass of an individual particle of each sample.

d [nm]	MW [·10^7 g/mol]	m_{NP} [10^{-16} g]	$m_{Er/NP}$ [10^{-18} g]	$m_{Nd/NP}$ [10^{-18} g]	C_{NPs} [nM]
59.3 ± 9.4	(30 ± 16)	(4.9 ± 2.6)	(1.71 ± 0.14)	(162.92 ± 0.56)	**160 ± 14**

Table S2.7. Characteristic values for the final core@shell$_1$@shell$_2$@shell$_3$ UCNPs.

	$M_{Er/NP}$ [10^{-17} g]	C_{NPs} [nM]
core	(0.128 ± 0.014)	**670 ± 44**
core@multishell	(0.128 ± 0.014)	**160 ± 14**

Table S2.8. NPs concentration for final samples.
Values for cores and core@shell$_1$@shell$_2$@shell$_3$ structures. Comparison of concentrations.

Absorbance measurements. A Biochrom Libra S60 UV-Vis spectrophotometer was used to record UV-Vis absorption spectrum of the final solutions of cores and core@shell$_1$@shell$_2$@shell$_3$ (core@multishell) diluted in chloroform to a final concentration of 25 nM of NPs.

Photoluminescence measurements. The photoluminescent properties of the UCNPs, cores and core@multishell, were studied in a Horiba FluoroMax-3 spectrometer equipped with an optical fibre attached to a 980 nm or an 808 nm laser. When a laser was used as light source, the spectrometer lamp was disabled. 5 nM solutions of the samples were measured using a laser power of 1 W·cm^{-2}.

6.1.3. Synthesis and characterization of water dispersable UCNPs after click chemistry onto the surface

6.1.3.1. Polymer synthesis and previous modification of photosensitizers

Absorbance spectrum of PS-N$_3$. A Biochrom Libra S60 UV-Vis spectrophotometer was used to record UV-Vis absorption spectrum of the final solutions of the modified dyes. Stocks in DMSO were diluted in water to a final concentration of 20 μM (10% of DMSO) and placed in a quartz cuvette with 1 mL of sample.

DBCO-modified PMA preparation. An amphiphilic polymer was synthesized to further modify the UCNPs to make them colloidally stable and to provide them with reactive groups to carry out click chemistry reactions (see Figure 2.14). The amphiphilic polymer dodecyl grafted-poly(isobutylene-alt-maleic-anhydride), herein after referred to as PMA, was synthesized as described previously with some modifications.[183] Briefly, 1.85 mmol of poly-isobutylene-alt-maleic-anhydride (285 mg, $M_w \simeq 6000$ g/mol, 39 monomer units per polymer chain), 1.39 mmol DDA (265.8 mg, 75% of the monomers) and 0.04 mmol of DBCO-NH$_2$ (2% of the monomers) (10.2 mg) were mixed together in 50 mL of THF. The solution was kept under magnetic stirring and reflux overnight. In less than 30 min the solution became clear and light yellowish. When reaction is complete, THF was evaporated under vacuum and the dried polymer was redispersed with 3.7 mL of chloroform to obtain a final monomer concentration of 0.5 M.

6.1.3.2. PMA functionalization of oleic acid caped UCNPs

PMA coating of UCNPs. The UCNP diameter (*d*) (Table S2.6) was used to determine the amount of required PMA monomers per cm^2 (R). Thus, to calculate the amount of polymer (V_P) needed to stabilize a determine volume of a solution

of UCNPs (V_{NP}) with a determine concentration (C_{NP}), the Eq. 6 was used. Based on our previous work [50], an R of 500 monomers/cm^2 was selected. The effective diameter, d_{eff}, corresponds to the experimental diameter plus twice the length of the organic ligands (*ca.* 1.2 x 2 nm, *i.e.*, oleic acid).

$$V_P = \frac{R \cdot \pi \cdot d_{eff} \cdot C_{NP} \cdot V_{NP}}{C_P} \qquad \textbf{Eq. 6}$$

Experimentally, the coating procedure was performed by mixing 100 mL of ~ 300 nM UCNPs in chloroform with 150 µL of PMA(bare) or PMA(with DBCO) in chloroform at 0.25 M, and 1 mL of chloroform. After this, the solvent was evaporated under vacuum in a round bottom flask with rotavapor system. Once the mixture was completely dried, the polymer was hydrolysed using a basic buffer (SBB, 0.1M, pH 12) in order to open the anhydride rings. Samples were sonicated until a completely transparent and colourless solution was obtained. The empty PMA micelles formed during the process were cleaned by centrifugation (30 min, 30000 RCF at 10°C). Final solutions of UCNP@PMA (bare and with DBCO) were obtained after pellets dispersion in milli-Q water.

Emission spectra. Fluorescence spectroscopy measurements were carried out, with an 808 nm laser as excitation source to characterize the UCNPs photoluminescence properties in water and using xenon lamp to quantify the PS attached to the UCNPs. Measures were done in a quartz cuvette with 1 mL of sample at 5 nM of NPs. Figure S2.5 shows the emission spectra of a 5 nM solution of UCNPs before and after water transfer.

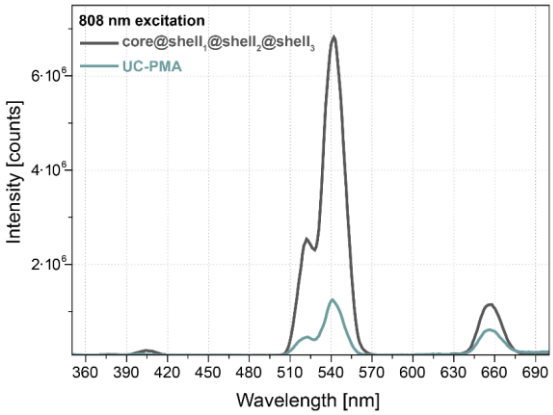

Figure S2.5.Fluorescence spectra of UCNPs.
Before (core@multishell) and after (UC-PMA) UCNPs water transfer.

6.1.3.3. Copper free click chemistry onto the UC-PMA

Conjugation of PS-N_3 and UC-PMA NPs. Figure S2.6 shows a photograph of UC-PMA NPs conjugated with one or both PS.

Figure S2.6. UC-PMA-RB,Ce6.
UC-PMA NPs conjugated with one PS type: Ce6 (UC-PMA-Ce6) or RB (UC-PMA-RB) or both PSs. (UC-PMA-RB,Ce6)

Quantification of PS per UCNP. Calibration curves to determine the concentration of RB and Ce6 attached to the NPs were collected in water exciting at 540 nm and 400 nm, respectively. The emitted fluorescence at 567 nm and 658 nm for RB and Ce6, respectively, versus dye concentration was plotted (Figure S2.7). These curves were used to quantify the number of PS per UCNP.

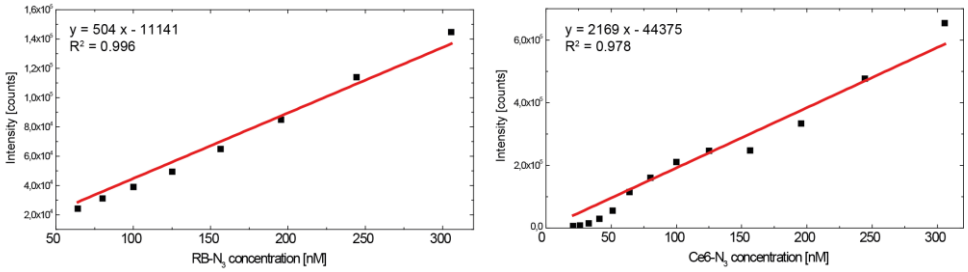

Figure S2.7. Calibration curves of modified PS.
(left)RB (λ_{ex} = 540 nm, λ_{em} = 567 nm) and (right) Ce6 (λ_{ex} = 400 nm, λ_{em} = 658 nm) in water.

6.1.3.4. Characterization of UCNP nanoplatforms

SEM. UC-PMA-RB,Ce6 NPs in water were observed under SEM to check their size and monodispersity. Micrographs are shown in Figure S2.8. Morphology and colloidal monodispersity were kept after the water transfer and the bioconjugation of the PSs.

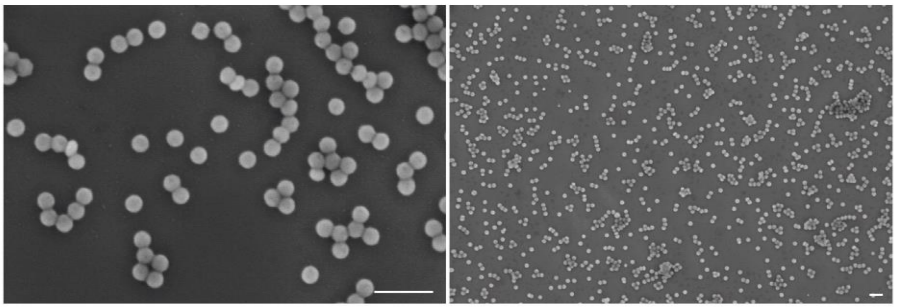

Figure S2.8. SEM micrographs of the final nanoplatform dispersed in water.
UC-PMA-RB,Ce6 at different magnifications (scale bars represent 200 nm).

Dynamic light scattering and ξ-potential measurements. Hydrodynamic diameter and surface zeta potential (mean ± standard deviation) were measured in a Zetasizer Nano ZSP. Disposable cells for DLS and disposable capillary zeta cell for ξ-potential were used. 5 nM UCNPs solutions in water were used. Results are summarized in Figure S2.9.

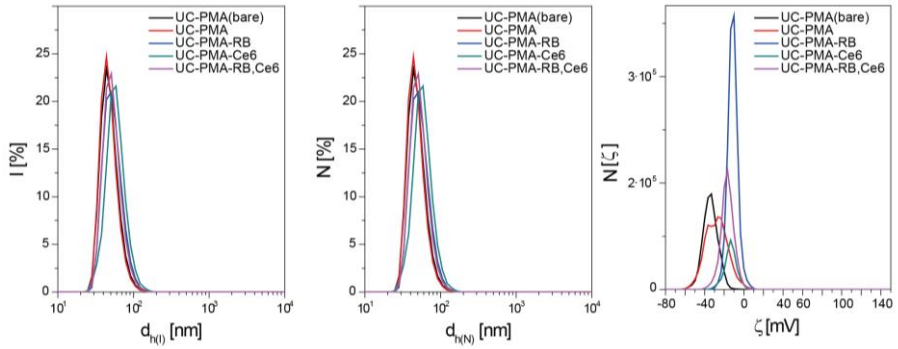

Figure S2.9. Intensity/number DLS population and ξ-potential distributions for different platforms.
UC-PMA(bare), UC-PMA, UC-PMA-RB, UC-PMA-Ce6 and UC-PMA-RB,Ce6 NPs in MilliQ water.

The stability of UCNPs in different biological relevant media was evaluated over time, up to seven days. Four different media were tested: i) water, ii) ALF, iii) ALF supplemented with a10% of FBS, iv) complete cell culture medium (DMEM, supplemented with 10% of FBS). Number mean values at each time are summarized in Table S2.9. Intensity and number distribution curves for the different media are summarized in Figure S2.10.

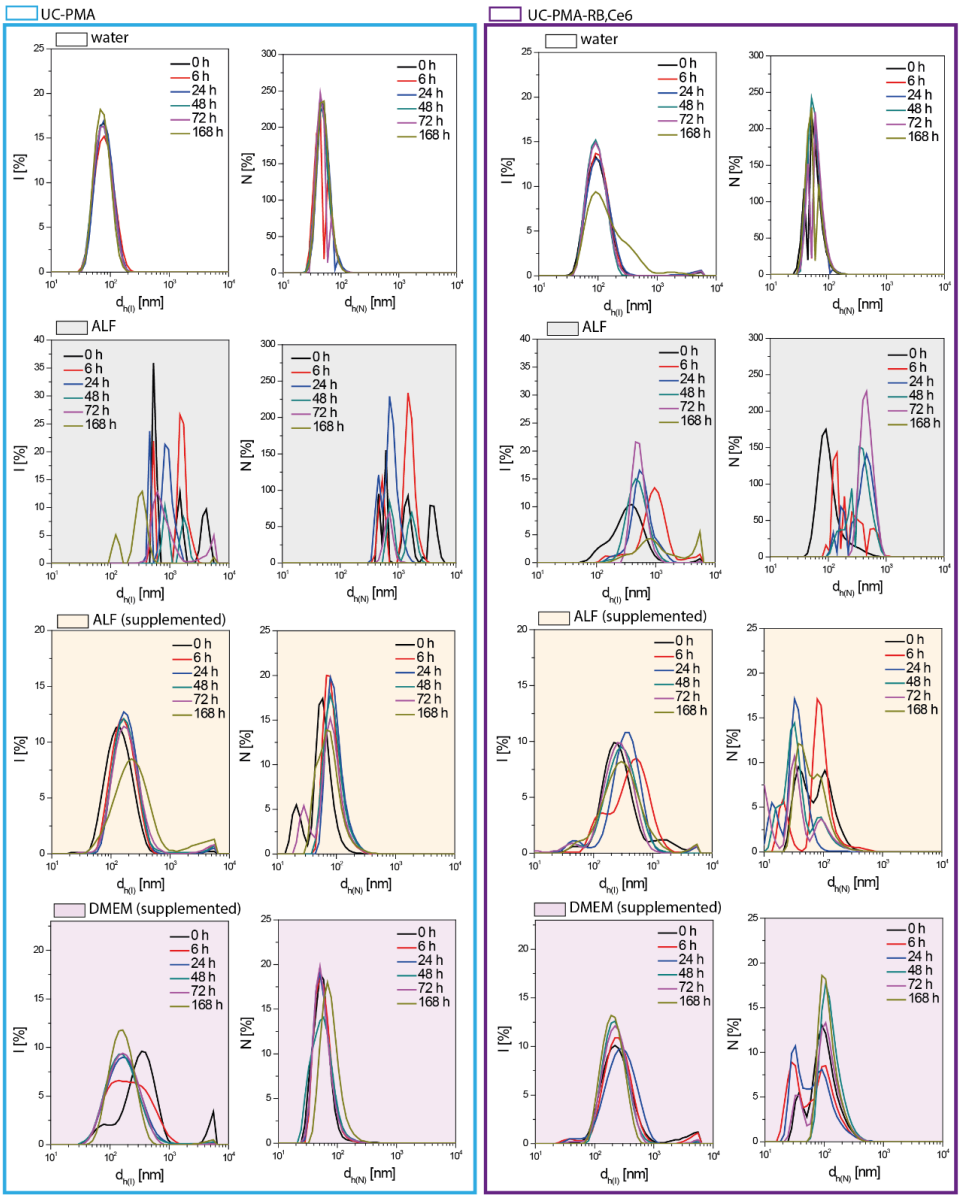

Figure S2.10. Raw intensity and number DLS values for UC platforms.
UC-PMA and UC-PMA-RB,Ce6 during 7 days in different media (water, ALF, ALF supplemented and DMEM supplemented).

	UC-PMA			
	water	ALF	ALF_{suppl}	$DMEM_{suppl}$
0 h	62.90 ± 2.10	1614 ± 1580	65.80 ± 2.20	58.60 ± 14.40
6 h	48.54 ± 5.37	1348 ± 567	83.80 ± 5.70	60.88 ± 11.05
24 h	52.69 ± 4.70	728 ± 220	98.00 ± 6.65	60.80 ± 10.30
48 h	48.96 ± 3.50	188.5 ± 376.0	94.40 ± 16.80	59.70 ± 19.60
72 h	49.50 ± 1.60	139.6 ± 311.0	94.40 ± 12.90	59.65 ± 7.70
7 days	51.20 ± 4.30	0.00 ± 0.02	98.60 ± 8.20	57.45 ± 28.74
	UC-PMA-RB,Ce6			
	water	ALF	ALF_{suppl}	$DMEM_{suppl}$
0 h	54.80 ± 5.80	125.60 ± 15.98	100.10 ± 43.60	102.50 ± 46.24
6 h	58.30 ± 6.20	212.50 ± 54.45	108.50 ± 14.00	118.20 ± 30.90
24 h	58.80 ± 5.80	383.80 ± 129.70	115.30 ± 43.60	110.20 ± 37.00
48 h	59.20 ± 3.50	361.50 ± 61.90	117.00 ± 35.3p	131.50 ± 11.60
72 h	60.04 ± 4.80	471.20 ± 55.29	122.00 ± 43.60	131.00 ± 21.80
7 days	56.80 ± 5.00	0.70 ± 0.02	107.50 ± 13.64	124.90 ± 5.90

Table S2.9. Raw hydrodynamic diameter values (number-weighted).
Size evolution in different media (water, ALF and ALF and DMEM both supplemented with a 10% FBS) of UC-PMA and UC-PMA-RB,Ce6.

6.1.4. Photodynamic therapy activation by 808 nm irradiation and ROS production

Nanoparticles internalization studies: ICP-MS. Table S2.10 summarized the total number of internalized NPs by cell as determined via ICP-MS.

	Total NP/cell
Control cells	0.44 ± 0.14
Cells + 5 nM of NPs	$(13.38 \pm 0.47) \cdot 10^3$

Table S2.10. Internalized UCNPs per cell determined by ICP-MS analysis.

Nanoparticles internalization studies: Confocal imaging of living cells. In Figure S2.11 and Figure S2.12, cells were incubated with UC-PMA-RB,Ce6 under strict dark conditions. Also, a different experiment was performed (Figure S2.13) using only UC-PMA-RB to avoid overlapping between channels.

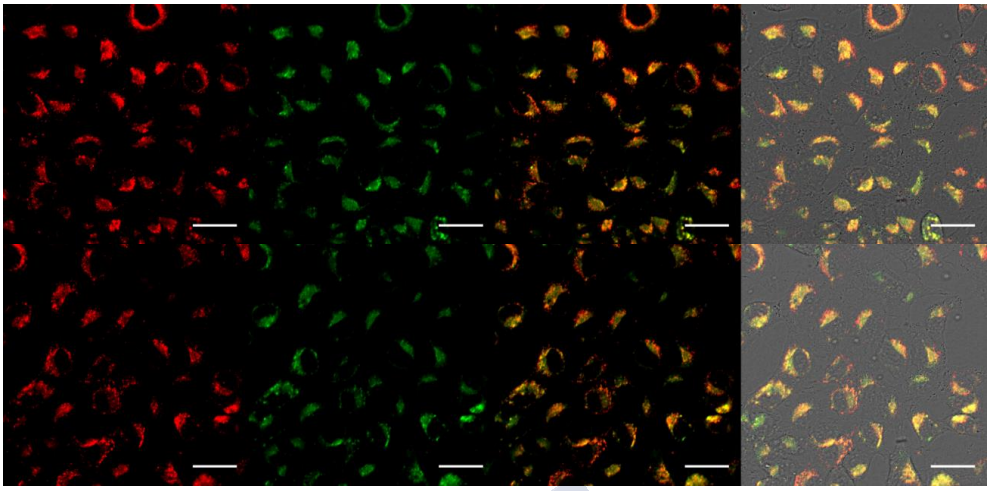

Figure S2.11. Intracellular location of UC-PMA-RB,Ce6 in HeLa cells after 3 h of incubation (2.5 nM of NPs).

From left to right: red (RB, Ex. 561, Em 620/60), green (Ce6, Ex. 405, Em. 725/40), red + green (yellow colour indicated colocalization of RB and Ce6), merged image of bright field (BF) + red + green. Scale bars represent 40 μm (60X magnification images).

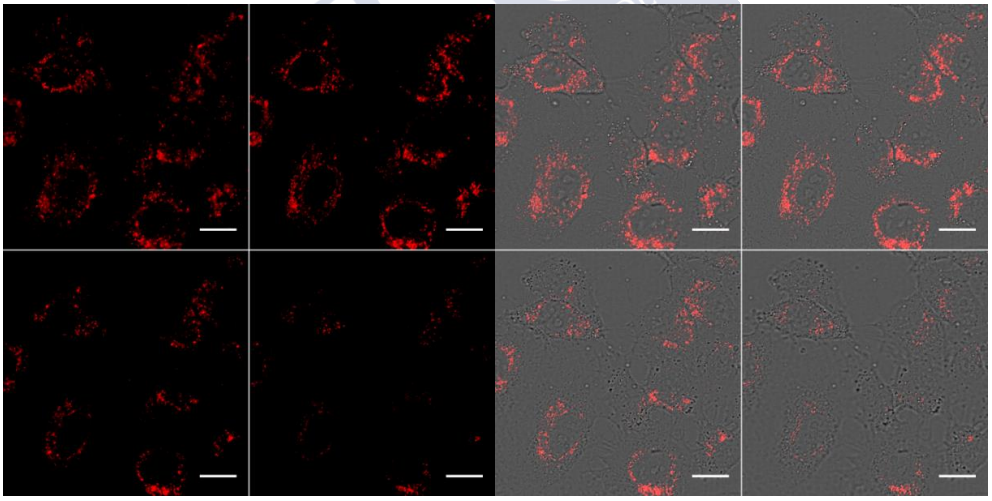

Figure S2.12. Intracellular location of UC-PMA-RB,Ce6 in HeLa cells (z-scan, 4 images) after 3 h of incubation (2.5 nM of NPs).

(Left) RB fluorescence (red, Ex. 561, Em 620/60) and (right) merged image of BF + red. Scale bars represent 20 μm (100X).

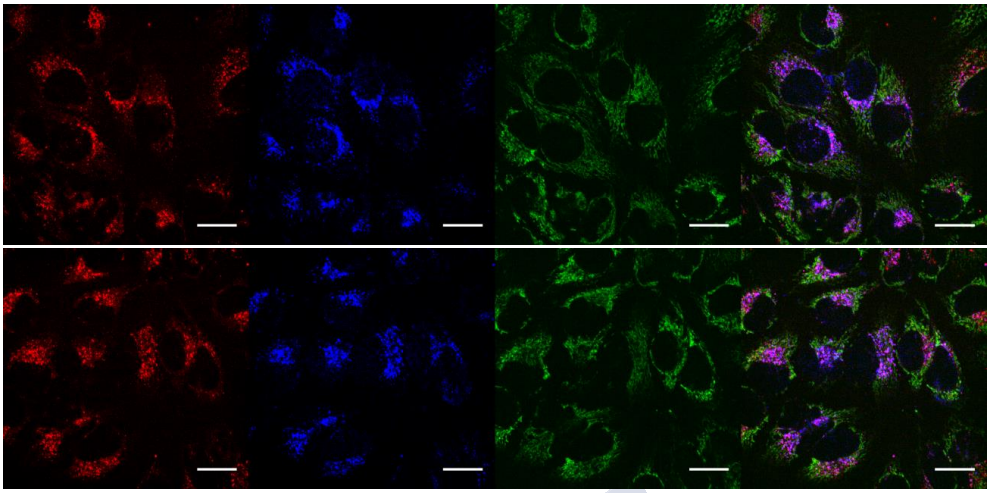

Figure S2.13. Intracellular colocation of UC-PMA-RB and lysosomes and mitochondria in HeLa cells after 3 h of incubation.

From left to right: red (RB, Ex. 561, Em. 620/60), blue (Lysotracker Blue, Ex. 405, Em. 450/50), green (Mitotracker Green, Ex. 488, Em. 525/50), merged image of blue + red + green. Purple indicates lysosomes and UCNPs colocalization. Scale bars represent 20 μm (100X).

Confocal microscopy TMRE studies.

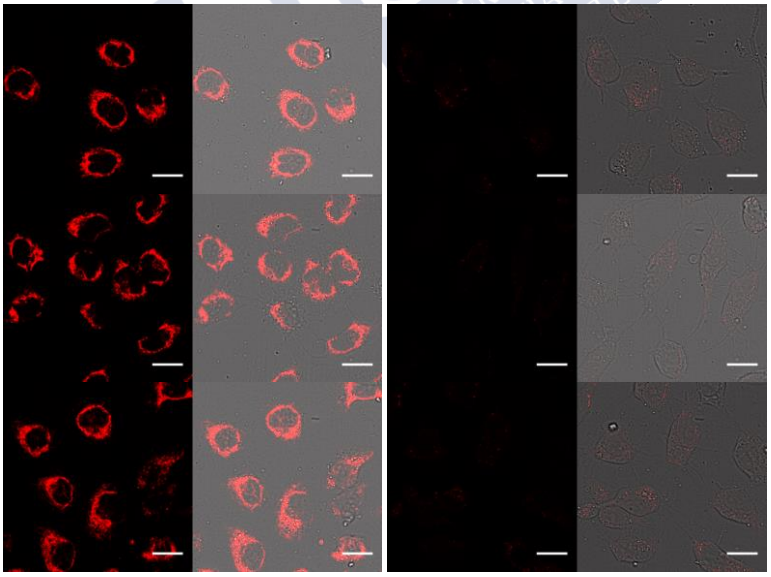

Figure S2.14. TMRE confocal experiments for PDT efficiency evaluation.

(left) Cells treated with UC-PMA-RB,Ce6; 2.5 nM during 3 hours under dark conditions after TMRE exposure (red, Ex. 561, Em. 620/60). (right) Cells treated in the same way but after 40 minutes of 5 $W \cdot cm^{-2}$ irradiation (right). Scales bars represent 40 μm (60X).

6.2. CHAPTER 3 APPENDIX

6.2.1. Synthesis and characterization of gold nanostars

CTAB-coated NSs were synthesized according to a previously reported protocol,[50] using spherical citrate-stabilized gold NPs with an average core diameter of *ca*. 11 nm as seeds, Ag^+ ions as blocking facet agents, and AA as reducing agent. All glassware was first cleaned with detergent followed by *aqua regia* and carefully rinsed with MilliQ water and acetone to guarantee an extremely cleaned glass surface.

Synthesis of NPs seeds. The seed NPs were synthesized following the citrate-reduction procedure reported by Schulz *et al*.[301] First, 144 mL of Milli-Q water were placed in a 250 mL three-necked round-bottomed flask connected with a condenser and heated up until boiling (*ca*. 100 °C) with a heating mantle. Then, a mixture of sodium citrate (3.5 mL, 60 mM; Sigma Aldrich #W302600) and citric acid (1.5 mL, 60 mM; Acros #A0350656) was added and kept under vigorous stirring (450 RPM) for 30 min. After that, 0.1 mL of 30 mM ethylenediaminetetraacetic acid (EDTA, Sigma Aldrich #EDS) was injected, followed by the quick addition of addition of 1 mL aqueous solution of 25 mM hydrogen tetrachloroaurate (III) ($HAuCl_4$, Alfa Aesar #12325). After 60 s the color of the mixture changed from pale yellow to dull blue and then to wine-red, indicating the growth of spherical NPs. The heating was then switched off, while the solution was kept under magnetic stirring. When the temperature dropped to 95 °C (*ca*. 5 min), the three-neck flask was immersed in a cold-ice water bath in order to arrest the NP growth.

Synthesis of NSs. In a glass flask, 20 mL of an aqueous $HAuCl_4$ solution (0.25 mM) were mixed with 0.03 mL of HCl (1 M) and 1.5 mL of the previously prepared NPs seeds, stirring the solution (350 RPM) at RT. To this mixture, 0.15 mL of 1 mM $AgNO_3$ (Sigma Aldrich #209139) and 0.15 mL of 66.67 mM AA (Sigma Aldrich #255564) were added simultaneously. After 10 min, 5 mL of 0.2 M CTAB (Sigma Aldrich #H9151) were added to arrest the NS growth. The solution was kept under stirring for 2 min, and the flask was then immersed in a cold-ice water bath for 10 min. Finally, the NSs were collected by centrifugation (4000 RCF,10 min), washed twice with diluted CTAB solution ($5 \cdot 10^{-4}$ M), and finally redispersed in CTAB solution ($5 \cdot 10^{-4}$ M) to ensure the stability of NSs during their storage.

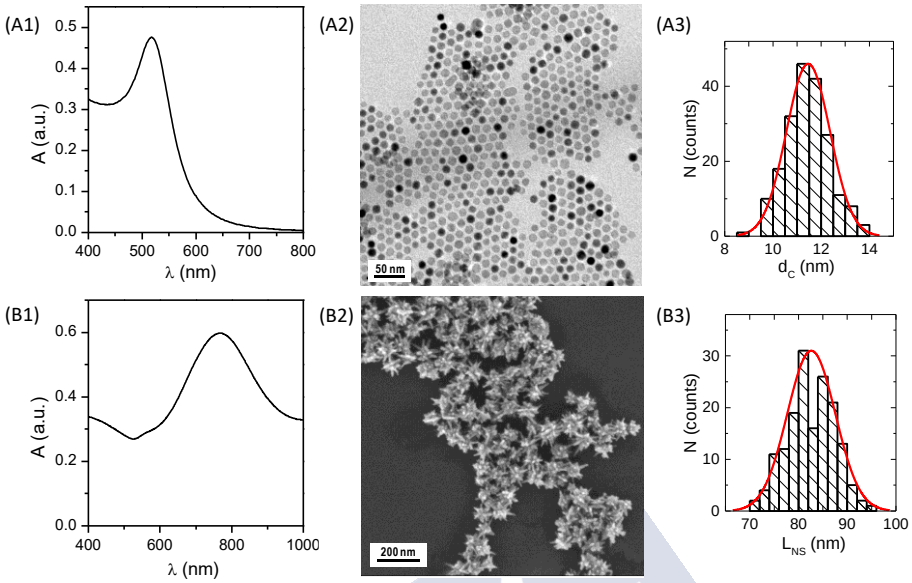

Figure S3.1. NS characterization.
A) Optical characterization of the as-prepared NPs seeds: A1) UV-Vis absorption spectrum showing their Surface Plasmon Resonance (SPR) peak at λ = 517 nm; A2) Representative TEM image (scale bar corresponds to 50 nm); and A3) the corresponding histogram of the number distribution N of the NP core diameter d_C as determined from TEM images, d_C = (11.4 ± 0.9) nm. B) Optical characterization of the as-prepared NSs: B1) UV-Vis absorption spectrum showing their SPR peak at λ = 768 nm; B2) Representative SEM image (scale bar corresponds to 200 nm); and B3) the corresponding histogram of the number distribution N of the tip-to-tip length L_{NS} of the NSs as determined from SEM images, L_{NS} = (82.6 ± 4.9) nm.

Optical characterization. UV-Vis absorption spectra of the NPs seeds and the NSs as recorded in aqueous solution are provided in Figure S3.1 (A1 and B1, respectively). The concentration of the seed NPs was determined from UV-Vis spectra by using the Lambert-Beer law.[50] Hereby an extinction coefficient at 450 nm of ε(450) = 8.27×10^7 $M^{-1} \cdot cm^{-1}$ was assumed,[302] taking into account that the average (± standard deviation) core diameter of the seed NPs was d_C = (11.4 ± 0.9) nm as determined by TEM analysis (Figure S3.1, A2-A3). In a typical synthesis of Au seed NPs as previously described, without concentration or purification steps, the concentration of NPs was c_{NP} = 3.7 nM. Since these NPs were used as seeds for NSs growth, the number of NSs is assumed to be the same as that of the added NP seeds. The purified NSs were finally diluted in CTAB solution ($5 \cdot 10^{-4}$ M) at a molar concentration of 2 nM for their storage and further use. SEM analysis of the as-prepared NSs (Figure S3.1, B2-B3) presented the typical star-shaped morphology with an average (± standard deviation) tip-to-tip length of L_{NS} = (82.6 ± 4.9) nm.

6.2.2. Synthesis of core-shell NS/ZIF8 NC (NC)

Nanosized ZIF8 particles were successfully prepared in water at RT using zinc nitrate hexahydrate ($Zn(NO_3)_2{\cdot}6H_2O$; Sigma Aldrich #96482) and 2-methylimidazole (MeIm; Sigma Aldrich #M50850) as zinc and organic ligand sources, respectively, and CTAB as size-controlling and structural-directing agent. We followed previous protocols with modifications.[213, 216] The molar ratio of ligand to zinc ion ($MeIm/Zn^{2+}$) in the reaction mixture was fixed at 54.

Synthesis of pristine ZIF8 particles. 1 mL of 1.3 M MeIm aqueous solution was placed in a glass vial under magnetic stirring at RT. Then 1 mL of 0.025 M $Zn(NO_3)_2{\cdot}6H_2O$ aqueous solution was added, and immediately after, 1 mL of $5{\cdot}10^{-4}$ M CTAB aqueous solution was added. The mixture was stirred for 2 min and left undisturbed for 3 h at RT, observing during this time the gradually appearance of whitish turbidity, which indicated the formation of the ZIF8 particles. Finally, the particles were collected by centrifugation (7000 RCF, 5 min), washed twice with MeOH and finally, redispersed in 3 mL of MeOH.

Synthesis of NS/ZIF8 NC. The synthetic and purification protocol for the NCs was equivalent to the one previously described for pristine ZIF8 particles, but a NP solution (NSs at a concentration of 2 nM in $5{\cdot}10^{-4}$ M CTAB aqueous solution) was added instead of the CTAB solution. In this case the appearance of bluish turbidity was gradually observed during the formation of ZIF8. The resulting NCs redispersed in 3 mL of MeOH were assumed to have a particle concentration of 0.67 nM, since this is the final concentration of NSs in the solution and we assume that one NC was formed per NS (*i.e.*, NSs acted as seeds and under optimized conditions almost all the ZIF8 particles contained a NS in the centre, *cf.* Figure S3.2).

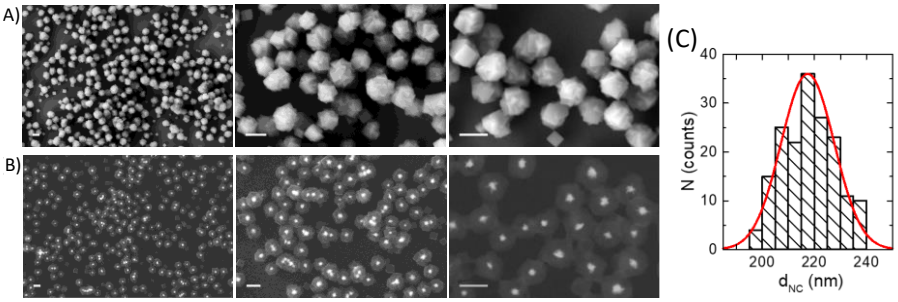

Figure S3.2. SEM images of the NC particles taken at different magnifications and at two different voltages.

A) low voltage (3 kV) to obtain surface information, and B) high voltage (20 kV) to penetrate further into the sample (see increased contrast of the core NSs). Scale bars correspond to 200 nm. C) Histogram of the number distribution N of the diameter (*i.e.*, vertex-to-vertex distance) d_{NC} of the NCs (idealized as spherical particles) as determined from SEM images, d_{NC} = (218 ± 24) nm.

Scanning Electron Microscopy. The morphology and size of NC particles was investigated with SEM (Figure S3.2). Images were acquired with a FESEM Zeiss Ultra Plus operated at 3 kV or 20 kV.

6.2.3. Encapsulation of HOE molecules in NS/ZIF8 nanocomposite (NC-HOE)

Loading procedure. NC were loaded with Hoechst (HOE, a fluorescent dye widely used to stain the cell nucleus; Hoechst 33258; Sigma Aldrich #96482) just by mixing the NC as dispersed in MeOH (1 mL, 0.67 nM) with a solution of HOE in MeOH (100 µL, 1.87 mM), having thus $3.10 \cdot 10^5$ HOE/NC during the incubation. The mixture was incubated overnight at RT to ensure that the maximum loading was reached regardless of the diffusion kinetic of the dye molecules through the NC pores. Then, the excess of the dye was removed by centrifugation and the NC-HOE was washed twice with MeOH in order to remove the HOE weakly adsorbed onto the ZIF8 surface.

Quantification by fluorescence measurements. Fluorescence characterization in solution was performed using a Horiba FluoroMax-3 spectrometer. The amount of HOE molecules loaded into the NC as dispersed in MeOH was quantified by fluorescence ($\lambda_{exc}/\lambda_{em}$=350/480 nm) indirectly, by measuring the HOE remaining in the supernatants after centrifugation and washing steps of the NC particles. The HOE concentration in the supernatant was determined by interpolation of the measured fluorescence intensity (I) to a previously constructed analytical calibration curve (Figure S3.3). This led to a value (mean ± standard deviation, n=2) of $2.94 \cdot 10^5 \pm 5.64 \cdot 10^2$ HOE per NC. It is worth noting that direct fluorescence measurements of the HOE molecules loaded into the NC led to underestimation of the loaded amount, which is likely due to fluorescence quenching of HOE trapped in the ZIF8 pores.

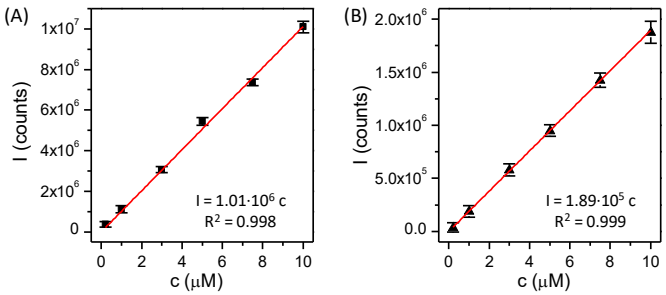

Figure S3.3. Calibration curves of HOE in MeOH (A) and water (B).
Plots were obtained from fluorescence measurements under excitation at 350 nm. Fluorescence intensity (I) at the maximum emission peak as a function of HOE concentration c is plotted, and the calibration equation is obtained by fitting a linear regression line to the collected data; R2 is the coefficient of determination.

6.2.4. Post-functionalization of the NC with poly[isobutylene–alt–maleic anhydride]–graft–dodecyl (NC-HOE-PMA)

NC and NC-HOE were functionalized with a PMA-based amphiphilic polymer in order to provide them with long-term stability in aqueous solution. The synthesis of the PMA as well as the protocol for the PMA-functionalization was performed as described previously,[50] and used herein with an optimized ratio (R) of 150 monomers of PMA polymer per nm^2 surface of NC particle (R = 150). The PMA optimization was based on achieving an optimum functionalization, that is, producing NC-PMA particles which are colloidally stable in aqueous solution, while using the minimum amount of PMA for avoiding the formation of a large excess of free PMA micelles together with the sample. Anyhow these free polymer micelles were removed by centrifugation.

PMA-functionalization procedure. NC or NC-HOE as dispersed in MeOH (1 mL, 2 nM) were mixed with PMA in chloroform solution (0.05 M; 150 monomers per nm^2 surface area of NC, assuming a spherical particle of diameter 218 nm), and the solvent (3:1 MeOH:$CHCl_3$) was slowly evaporated in a rotary evaporator. Then the dried product was resuspended by adding *ca*. 5 mL of SBB (0.1 M, pH 12), aided by sonication (1 min). The resulting NCs (NC-PMA or NC-HOE-PMA) were collected by centrifugation (7000 RCF, 10 min), washed twice with water, and finally redispersed in water (*cf.,* Figure S3.4). The morphology and size of the produced PMA-functionalized particles remains the same as the original NCs (*cf.,* Figure S3.5, Figure S3.6 and Figure S3.7).

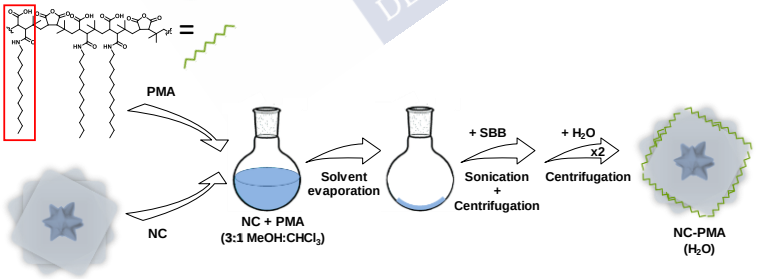

Figure S3.4. Scheme of PMA–functionalization procedure of NC.
PMA–functionalization procedure of NC. PMA polymer (the red box shows one monomer unit) and NCs are mixed in a round flask (3:1 MeOH:$CHCl_3$) in a ratio of 150 monomers per nm^2 of NC, the solvent is evaporated using a rotary evaporator, and the final dried product is redispersed in sodium borate buffer (SBB pH=9) by mild sonication. Purification of the resulting NC-PMA is carried out by centrifugation and washing with water.

Quantification by fluorescence measurements. The quantification of the HOE after the PMA-functionalization was carried out by fluorescence measurements as described previously, but here the measurements and calibration were

performed only in water, *cf*. Figure S3.3B. Importantly, the amount of HOE after the PMA-functionalization decreased to ~2/5 ($1.25 \cdot 10^5 \pm 6.11 \cdot 10^2$ dyes molecules per NC) of the original HOE content in NC-HOE, which may indicate that there is some HOE-leakage during the PMA-functionalization process and/or PMA was encapsulated, partially occupying the HOE's voids.

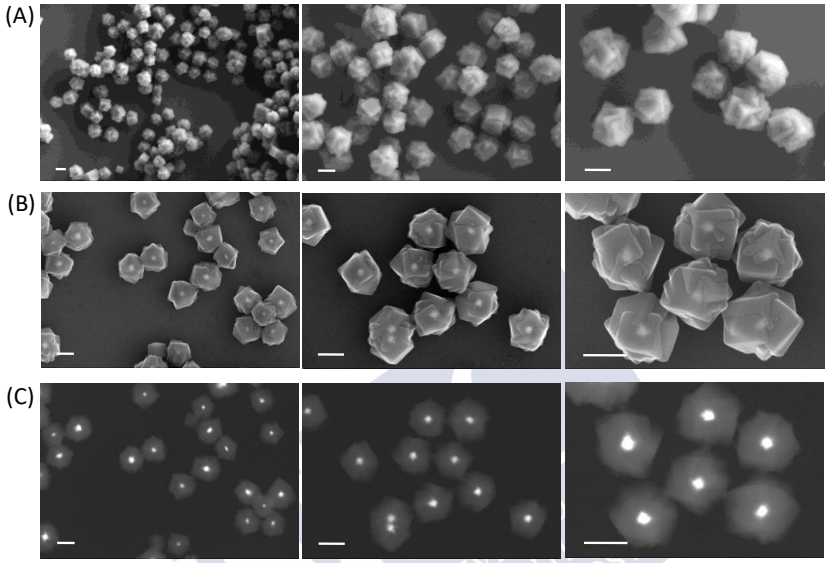

Figure S3.5. SEM images of NC-PMA particles.
Representative SEM images of the NC-PMA particles taken at different magnifications, and with different detectors at several voltages to get different structural information. A) Images collected with Everhart-Thornley detector (SE2, secondary electrons) at 3 Kv; B) InLens detector (SE1, secondary electrons) at 20 kV; and C) AsB detector (backscattered electrons) at 20 kV. Scale bars correspond to 200 nm.

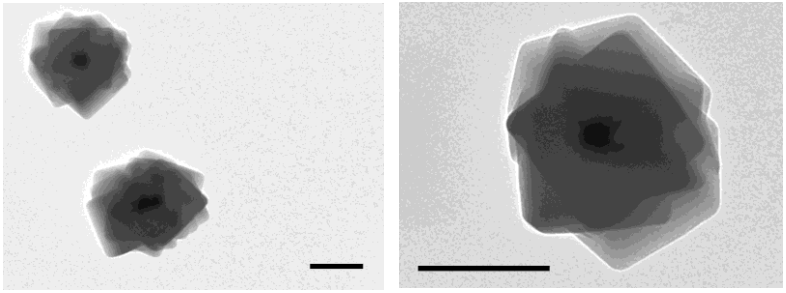

Figure S3.6.TEM images of NC-HOE-PMA particles.
Scale bars correspond to 200 nm.

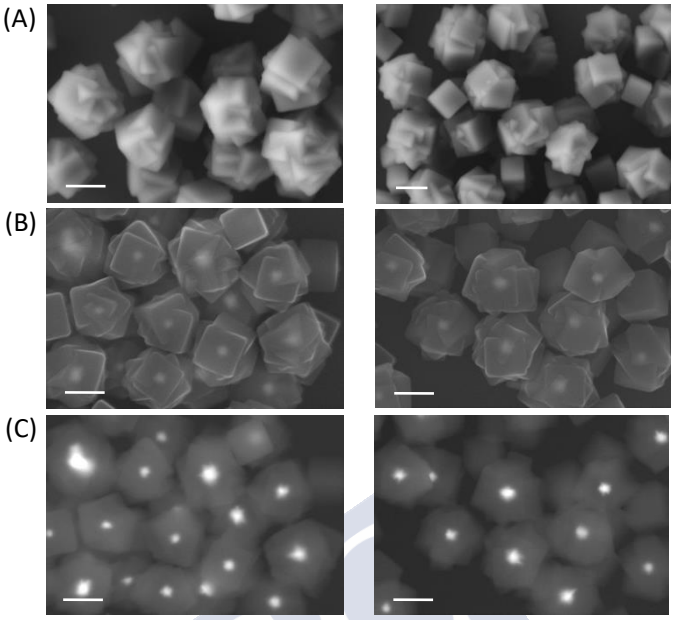

Figure S3.7. SEM images of NC-HOE and NC-HOE-PMA.
Representative SEM images of NC-HOE (left) and NC-HOE-PMA (right) particles taken with different detectors and voltages to get different structural information. (A) Images collected with Everhart-Thornley detector (SE2, secondary electrons) at 3 kV, (B) InLens detector (SE1, secondary electrons) at 20 kV, and (C) AsB detector (backscattered electrons) at 20 kV. Scale bars correspond to 200 nm.

6.2.5. Characterization of the NC particles

The different as-prepared NC particles, *i.e.* before and after dye loading as well as before (*cf*. Figure S3.8A) and after PMA-functionalization, were extensively characterized by using diverse and complementary characterization techniques as follows.

UV-Vis spectroscopy. A Biochrom Libra S60 UV–Vis spectrophotometer was used to record UV-Vis absorption spectrum of the NC in water, which is presented in Figure S3.8B showing a LSPR band centred at 790 nm.

Fluorescence spectroscopy. Figure S3.8C shows the fluorescence spectra of the HOE before encapsulation (*i.e*. free dye) and after their loading into the NC. A significant shift of the maximum emission peak was observed (from 472 nm to 480 nm), which could be attributed to the interaction of the HOE molecules with the ZIF8 and/or the change of the surrounding medium inside the ZIF8 pores. The PMA functionalization led to further redshift of the HOE emission (from 480 nm to 492 nm).

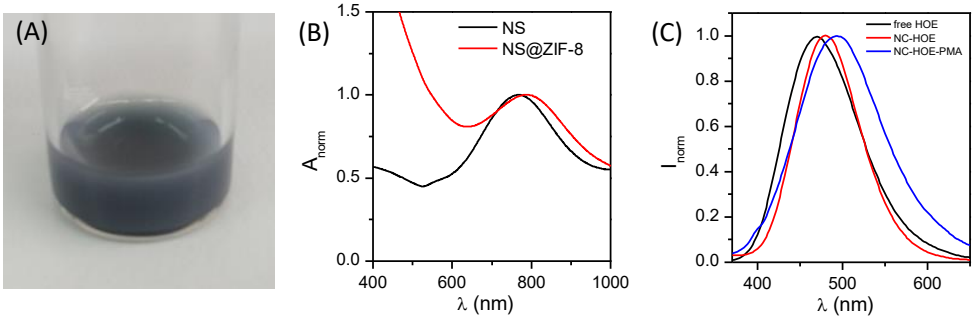

Figure S3.8. Characterization of NC particles.

A) Photograph of the as-prepared NC. B) Normalized UV-Vis absorption spectrum A_{norm} of the NC particles showing their SPR peak at λ = 790 nm. Note that the UV-Vis spectrum of the bare gold nanostars (NS) is also shown for comparison. C) Normalized fluorescence spectra I_{norm} of the HOE before (free dye molecules) and after their encapsulation into the NC (NC-HOE) as well as after PMA-functionalization (NC-HOE-PMA).

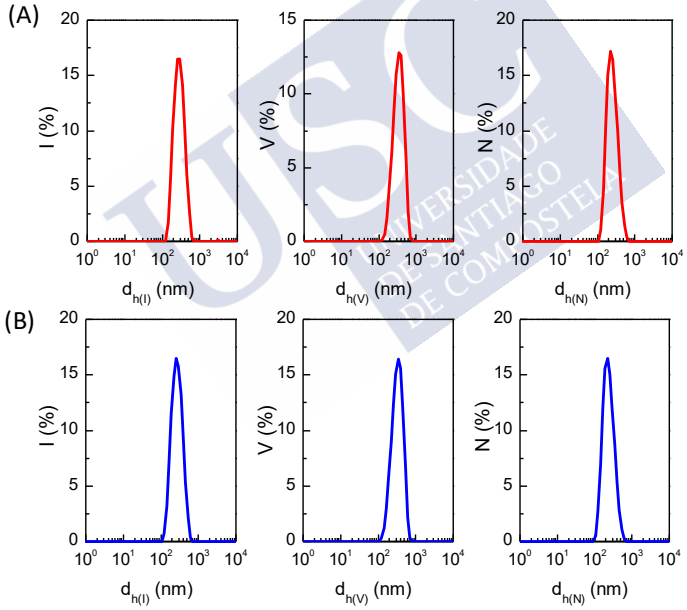

Figure S3.9. DLS characterization of NC-HOE and NC-HOE-PMA.

DLS intensity (I), volume (V) and number (N) distributions of the hydrodynamic diameter d_h of NC-HOE before (A) and after PMA-functionalization (NC-HOE-PMA) (B). Note that the NC-HOE sample was dispersed in MeOH while the NC-HOE-PMA was dispersed in water.

Dynamic light scattering (DLS) and ξ-Potential . The hydrodynamic diameter (d_h) and polydispersity index (PDI) of the NCs were determined by DLS using a Malvern Zetasizer Nano ZSP equipped with a 10 mW He–Ne laser operating at a wavelength of 633 nm and fixed scattering angle of 173°. DLS d_h values of the NC

particles before (NC-HOE, MeOH) and after PMA-functionalization (NC-HOE-PMA, water) are presented in Figure S3.9 and Table S3.1. It is worth noting that the loading of HOE molecules and PMA-functionalization did not significantly change the hydrodynamic diameter as measured by DLS. The ξ-potential of the particles after PMA functionalization as dispersed in MilliQ water was measured with LDA by using the same Malvern Zetasizer Nano ZSP instrument. The NC-HOE-PMA particles were negatively charged (ξ = –27.5 ± 0.3 mV) as expected due to the carboxyl groups of the PMA polymer.

Sample	$d_{h(I)}$ [nm]	$d_{h(V)}$ [nm]	$d_{h(N)}$ [nm]	PDI
NC-HOE	289 ± 92	356 ± 106	244 ± 88	0.09
NC-HOE-PMA	273 ± 98	348 ± 103	235 ± 85	0.26

Table S3.1.Hydrodynamic diameters of the NC-HOE and NC-HOE-PMA.
Hydrodynamic diameters d_h (mean value ± standard deviation SD) as derived from DLS measurements of the NC-HOE and NC-HOE-PMA. The PDI for each sample is also given. Data correspond to the raw data shown in Figure S3.9.

Powder x-ray diffraction. A Philips X-ray diffractometer Philips was used to study the crystalline powder of samples. These were examined in the range of 2θ between 2° and 75°, with a passage of 0.02° and a time by step of 2s. Table S3.2,Table S3.3 and Table S3.4 show major diffraction peaks of samples ZIF8, NC and NC-PMA, respectively (*cf.*, Figure S3.10).

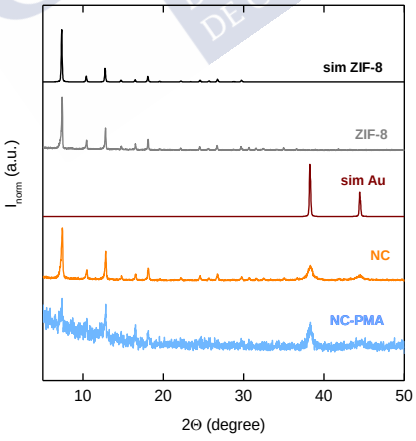

Figure S3.10. PXRD spectra of ZIF8 (grey), NC (orange) and NC-PMA (blue).
For comparison, simulations of ZIF8 (black, COD (Crystallography Open Database): 7111970) and Au-fcc (wine; COD: 9008463) are added. I_{norm} is the normalized intensity.

The relevant peaks identified by PXRD for each sample are summarized in the following tables:

Pos. [°2Θ)]	Height [cts]	FWHM Left [°2Θ]	d-spacing [Å]	Rel. Int. [%]
7.38	597	0.14	11.963	100.0
12.79	270	0.12	6.914	45.2
18.10	140	0.11	4.898	23.5
10.44	116	0.13	8.468	19.5
16.53	84	0.08	5.359	14.1
26.68	57	0.13	3.338	9.6
14.77	270	0.12	5.991	8.2
24.52	44	0.12	3.628	7.5
29.68	42	0.11	3.008	7.0

Table S3.2. Major peaks (relative intensity > 6%) identified in the ZIF8 diffractogram.

Pos. [2Θ]	Height [cts]	FWHM Left [°2Θ]	d-spacing [Å]	Rel. Int. [%]
7.39	531	0.19	11.948	100.0
12.81	264	0.16	6.904	49.6
38.28	132	0.65	2.349	24.9
18.13	127	0.17	4.891	23.9
10.46	94	0.17	8.452	17.7
26.73	65	0.10	3.332	12.2
16.54	60	0.16	5.354	11.2
14.81	43	0.12	5.977	8.2
24.55	43	0.18	3.623	8.2
29.73	37	0.10	3.002	6.9
44.38	35	0.87	2.039	6.6

Table S3.3. Major peaks (relative intensity > 6%) identified in the NC diffractogram.

Pos. [2Θ]	Height [cts]	FWHM Left [°2Θ]	d-spacing [Å]	Rel. Int. [%]
7.36	24	0.17	12.001	100.0
16.52	22	0.17	5.361	89.6
12.78	21	0.25	6.923	88.5
38.24	19	0.62	2.352	76.8
18.13	13	0.26	4.889	52.2
14.79	11	0.09	6.923	45.5
8.44	11	0.09	10.463	45.0
10.46	11	0.11	8.447	44.4
29.70	5	0.20	3.005	22.5
24.44	5	0.30	3.639	22.2
44.54	5	1.30	2.033	19.7
25.50	2	0.50	3.489	9.7

Table S3.4. Major peaks (relative intensity > 9%) identified in the NC-PMA diffractogram.

Thermogravimetric analysis. TGA of powder samples (freeze-dried) was performed using a TA Instruments Inc, SDT Q-600 thermobalance with a general heating profile from 30 to 600 °C with a heating rate of 5 °C·min^{-1} under air using a flux of 100 mL min^{-1} (*cf*. Figure 3.3B).

Recalculation of the inorganic and organic content (% wt = weight percentage) of the samples (*i.e.*, ZIF8, NC, NC-HOE, NC-PMA and NC-HOE-PMA), taking into account the evaporation of water and remaining solvents within the porosity T< 150 °C, is shown in the following (numerical values are provided in Table S3.5).

NS wt % in NC. Considering there is no loss of organic content of ZIF8 (MeIm) during the synthesis:

$$\text{Inorganic wt \% NC}_{\text{equivalent}} = \frac{\text{Organic wt \% NC}}{\text{Organic wt \% ZIF8}} \cdot \text{Inorganic wt \% ZIF8}$$

$$\text{NS wt \%} = \text{Total Inorganic wt \% NC} - \text{Inorganic wt \% NC}_{\text{equivalent}}$$

HOE wt % in NC-HOE. Considering the inorganic content (NS and Zn) remains constant:

$$\text{Organic wt \% NC-HOE}_{\text{equivalent}} = \frac{\text{Inorganic wt \% NC-HOE}}{\text{Inorganic wt \% NC}} \cdot \text{Organic wt \% NC}$$

$$\text{HOE wt \%} = \text{Total Organic wt \% NC-HOE} - \text{Organic wt \% NC-HOE}_{\text{equivalent}}$$

PMA wt % in NC-PMA. Considering the inorganic content (NS and Zn) remains constant:

$$\text{Organic wt \% NC-PMA}_{\text{equivalent}} = \frac{\text{Inorganic wt \% NC-PMA}}{\text{Inorganic wt \% NC}} \cdot \text{Organic wt \% NC}$$

$$\text{PMAwt \%} = \text{Total Organic wt \% NC-PMA} - \text{Organic wt \% NC-PMA}_{\text{equivalent}}$$

HOE & PMA wt % in NC-HOE-PMA. Considering the inorganic content (NS and Zn) remains constant and that 1/3 of HOE remains inside after PMA functionalization:

$$\text{Organic wt \% NC-HOE-PMA}_{\text{equivalent}} = \frac{\text{Inorganic wt \% NC-HOE-PMA}}{\text{Inorganic wt \% NC}} \cdot \text{Organic wt \% NC}$$

$$\text{PMA-HOE wt \%} = \text{Total Organic wt\% NC-HOE-PMA} - \text{Organic wt \% NC-HOE-PMA}_{\text{equivalent}}$$

$$\text{HOE wt \%} = (^{2}/_{5}) \frac{\text{Inorganic wt \% NC-HOE-PMA}}{\text{Inorganic wt \% NC-HOE}} \cdot \text{HOE wt \% in NC-HOE}$$

PMA wt % = (PMA+HOE) wt % - HOE wt %

Sample	Organic wt %	Inorganic wt %	Au wt %	HOE wt %	PMA wt %
ZIF8	63.92	36.08	n/a	n/a	n/a
NC	52.89	47.11	17.26	n/a	n/a
NC-HOE	60.57	39.43	14.44	16.30	n/a
NC-PMA	64.95	35.05	12.84	n/a	25.60
NC-HOE-PMA	70.10	29.90	10.95	4.94	31.59

Table S3.5. TGA characterization of selected samples.
Organic and inorganic weight percentage (wt %) derived from TGA measurements in selected samples, and estimated % wt of Au, HOE and PMA.

The residues generated by the TGA of selected samples were also investigated by PXRD, *cf.* Figure S3.11.

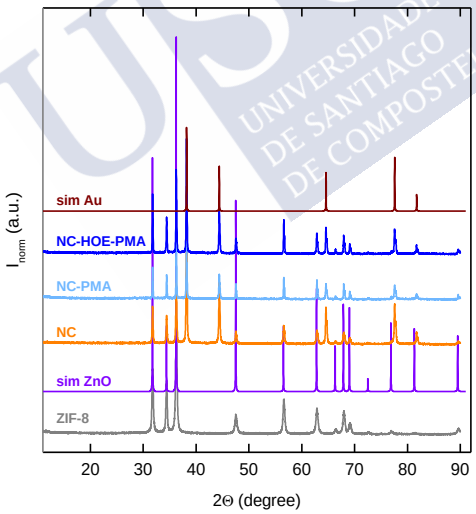

Figure S3.11. PXRD spectra of the TGA residues.
For comparison, simulations of ZnO (violet; COD: 2300112) and Au (wine; COD: 9008463) are added. I_{norm} is the normalized intensity.

N_2 isotherms analysis. N_2 sorption isotherms (77 K) were done in an AUTOSORB system (Quantachrome Instruments, Boynton Beach, FL, USA). Before the measurement, the sample was evacuated at 150 °C for 16 h. Specific surface area was determined by applying BET equation (Brunauer, Emmett & Teller) in the

pressure interval P/P_o = 0.01-0.3 (being P_0 the saturation pressure). Pore volume and pore size distribution were calculated by the NLDFT method (Non Localized Density Functional Theory) and the HK (Horvath-Kawazoe) methods, respectively, *cf*. Figure S3.12 and Table S3.6.

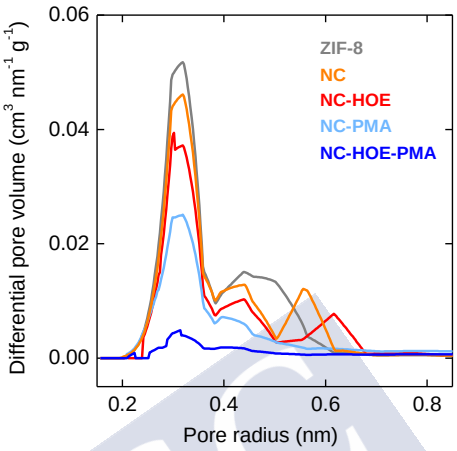

Figure S3.12. HK pore volume distribution of selected samples.

Sample	S_{BET} [m^2g^{-1}]	Micropore volume (P/P_0<0.3) [cm^3g^{-1}]	S_{BET} [m^2g^{-1}]*	Micropore volume (P/P_0<0.3) [cm^3g^{-1}]*	Mesopore Volume (P/P_0= 0.3-0.9) [cm^3g^{-1}]*
ZIF8	1800	0.68	-	-	0.06
NC	1570	0.61	1840	0.74	0.10
NC-HOE	1260	0.51	1510	0.61	0.12
NC-PMA	850	0.40	1440	0.67	0.25
NC-HOE-PMA	220	0.11	470	0.24	0.23

** corrected considering exclusively the ZIF8 weight*

Table S3.6. Data extracted from the N_2 isotherms analysis.

Comparative analysis of TGA, N_2 isotherms and fluorescence HOE quantification. HOE content in NC was estimated from different characterization data, providing values in the same order of magnitude. Notice that we had to take rough approximations such as the volume of one NC, the concentration of NC or the number of HOE per NC (from fluorescence data).

Thermogravimetric Analysis (TGA). Considering the % wt values in Table S3.5, the weight ratio HOE/ZIF8 is

$$R_{ZIF8}^{HOE} = \frac{g_{HOE}}{g_{ZIF8}} = \frac{\text{HOE wt \%}}{100 - \text{NS wt \%} - \text{HOE wt \%} - \text{NS wt \%}} = \mathbf{0.24}$$

then, taking the number of HOE molecules (MW_{HOE} = 424 g/mol) corresponding to HOE ratio above calculated, and the HOE volume (V_{HOE} = 18.5 · 4.1 · 8.6 Å = 0.65 ·10^{-21} cm^3, overestimated dimensions of HOE in vacuum) per g of ZIF8, allow to estimate pore volume occupied by the HOE load as

$$\text{Pore volume}_{HOE} = R_{ZIF8}^{HOE} \cdot MW_{HOE}^{-1} \cdot N_A \cdot V_{HOE} = \mathbf{0.22\ cm^3 g^{-1}}$$

N_2 isotherms. Considering the data (corrected) from Table S3.6, the pore volume occupied by the HOE load is

$$\text{Pore volume}_{HOE} = \text{Pore volume}_{NC} - \text{Pore volume}_{NC\text{-}HOE} = \mathbf{0.13\ cm^3 g^{-1}}$$

HOE loading estimated from fluorescence quantification. From the HOE load estimation based in fluorescence data (*i.e.*, N_{HOE} = 2.93 ·10^5 ± 6.20 ·10^2 HOE/NC-HOE), we can make an approximation of the pore volume occupied by the HOE load as

$$\text{Pore volume}_{HOE} = N_{HOE} \cdot V_{HOE} \cdot (V_{NC\text{-}HOE} - V_{NS})^{-1} \cdot \rho_{eff,NC} = \mathbf{0.15\ cm^3 g^{-1}}$$

where the volume of a NC-HOE was approximated to the one cube of edge L = 154 nm (which corresponds to a square of edge 154 nm circumscribed in a circle of diameter 218 nm, *cf*. Figure S3.2), and then

$$V_{NC\text{-}HOE} - V_{NS} = L^3 = 3.60 \cdot 10^{-15}\ cm^3$$

Also, we estimated the density of NC as

$$\rho_{eff,NC} = 0.012 \cdot \rho_{Au} + 0.988 \cdot \rho_{ZIF8} = 0.50\ g\ cm^{-3},$$

where ρ_{Au} = 19.3 g cm^{-3}, ρ_{ZIF8} = 0.35 g cm^{-3}, and we estimated from geometrical considerations and the TGA analysis (Au wt % in NC) that one NS occupies *ca*. 1.2 % of V_{NC}.

Colloidal stability. In order to evaluate their colloidal stability in aqueous solution, NC particles were centrifuged, MeOH (supernatant) was removed, and bare NC particles (precipitate) were redispersed in water. DLS measurements of the sample were performed at different time points. Results clearly show that the as-synthesized NC particles were not stable in water, *cf*. Figure S3.13, Table S3.7 and Figure 3.4). In contrast, NC-PMA particles (*i.e.*, after NC functionalization with PMA) were stable in water over time (at least, up to 7 days), *cf*. Figure S3.5. The stability of both samples, that is, before (NC) and after PMA-functionalization

(NC-PMA) in cell culture medium (DMEM) was also evaluated, a prerequisite to study their interaction with cells and, consequently, their cell internalization. Mean values (± SD) are listed in Table S3.7.

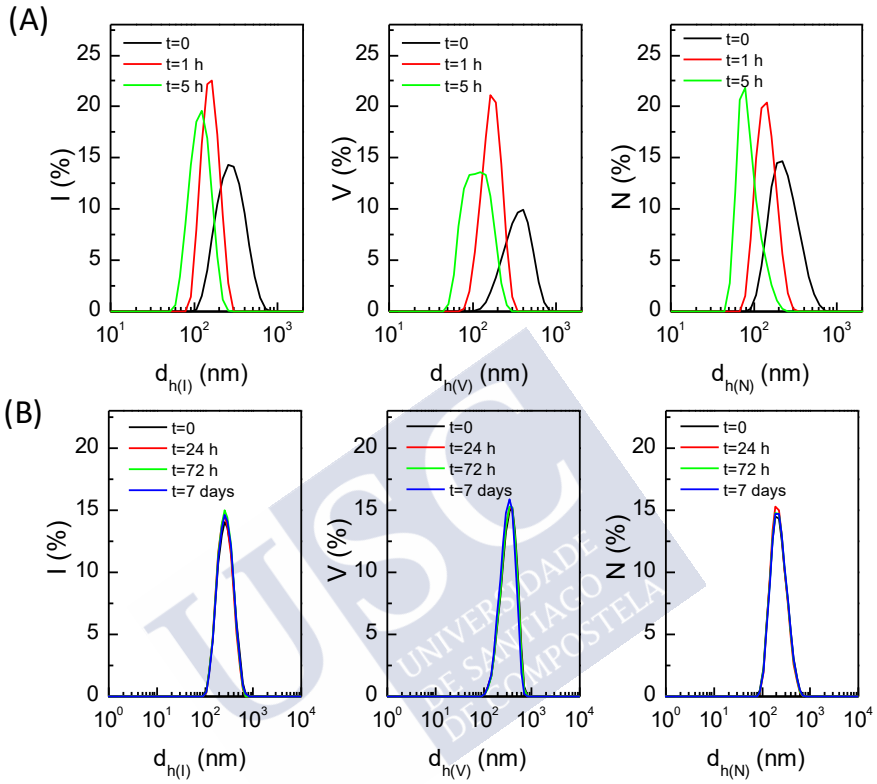

Figure S3.13. DLS characterization of NC-HOE and NC-HOE-PMA over time.
DLS intensity, volume, and number-weighted population distributions of the hydrodynamic diameter dh of NC before (A) and after PMA-functionalization, NC-PMA (B) as dispersed in water at different time points after their preparation. In case of the NC sample, longer times are not shown because of lack of reproducibility (particles were not colloidally stable).

Laser irradiation: To investigate the thermoplasmonic behaviour and encapsulation stability of the non-PMA (in methanol, see Figure S3.14) and the PMA (in water, see Figure 3.5; in PBS, see Figure S3.14 C) nanosystems, colloidal dispersions were irradiated during 1 min at 7 $W \cdot cm^{-2}$ with a NIR optical system, non-irradiated at RT or heated in a thermostatic batch (1 min, 50 °C). Immediately (0 h), and 8 h and 24 h after the corresponding treatment, samples were precipitated and the HOE content (released) was quantified by fluorescence. In Figure S3.14(B), Figure S3.14(C) and Figure 3.5B, HOE releases are expressed as % relative to the maximum HOE initial loading (2.94×10^5 and 1.25×10^5 HOE per NC or NC-PMA, respectively).

NC								
Time	water				cell medium			
	$d_{h(I)}$ [nm]	$d_{h(V)}$ [nm]	$d_{h(N)}$ [nm]	PDI	$d_{h(I)}$ [nm]	$d_{h(V)}$ [nm]	$d_{h(N)}$ [nm]	PDI
0 h	289 ± 7	356 ± 4	244 ± 3	0.09	297 ± 10	378 ± 12	271 ± 9	0.22
1 h	159 ± 4	172 ± 3	145 ± 2	0.17	219 ± 4	232 ± 5	201 ± 4	0.36
5 h	122 ± 4	119 ± 6	88 ± 7	0.25	154 ± 6	142 ± 7	118 ± 6	0.30
NC-PMA								
Time	water				cell medium			
	$d_{h(I)}$ [nm]	$d_{h(V)}$ [nm]	$d_{h(N)}$ [nm]	PDI	$d_{h(I)}$ [nm]	$d_{h(V)}$ [nm]	$d_{h(N)}$ [nm]	PDI
0 h	283 ± 5	359 ± 8	238 ± 7	0.21	292 ± 9	362 ± 12	245 ± 7	0.23
24 h	273 ± 8	349 ± 7	234 ± 5	0.26	315 ± 9	375 ± 15	260 ± 5	0.22
72 h	277 ± 6	346 ± 9	236 ± 5	0.24	321 ± 8	371 ± 13	258 ± 6	0.27
7 days	281 ± 5	345 ± 7	239 ± 9	0.24	318 ± 9	369 ± 13	252 ± 7	0.32

Table S3.7. Hydrodynamic diameters of NC-HOE and NC-HOE-PMA over time.
Hydrodynamic diameters d_h (mean value ± SD) as derived from DLS measurements of NC particles before (NC) and after PMA-functionalization (NC-PMA) dispersed in water or in cell culture medium at different time points. SD values correspond to the standard deviation of the diameter mean value as obtained from several repeats (n=3) of the measurement. The PDI for each sample is also given. Data correspond to the raw data depicted in Figure S3.13.

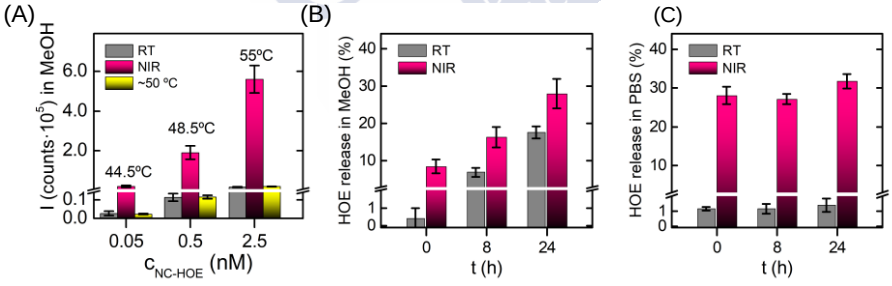

Figure S3.14. Study of HOE release under laser irradiation with NC-HOE-PMA.
A) HOE release in MeOH by fluorescence (I) after NIR illumination (1 min, 7 W·cm^{-2}) of the NC-HOE system (pink) at different concentrations (c); as controls, NC-HOE in MeOH was heated in a thermostatic batch (50 °C, 1 min, yellow) or non-heated (grey, RT); over the columns the bulk temperature reached by the solution after NIR irradiation is indicated B) HOE release (% of maximum HOE loading) in MeOH for the NC-HOE system (pink, c = 0.5 nM) immediately (0 h), 8 h and 24 h after NIR illumination; as controls, non-treated equivalent samples (grey, RT) are shown. C) HOE release (% of maximum HOE loading) in PBS for the NC-HOE-PMA system (pink, c = 0.5 nM) immediately (0 h), 8 h and 24 h after NIR illumination; as controls, non-treated equivalent samples (grey, RT) are shown (HOE's release ~ 1 %).

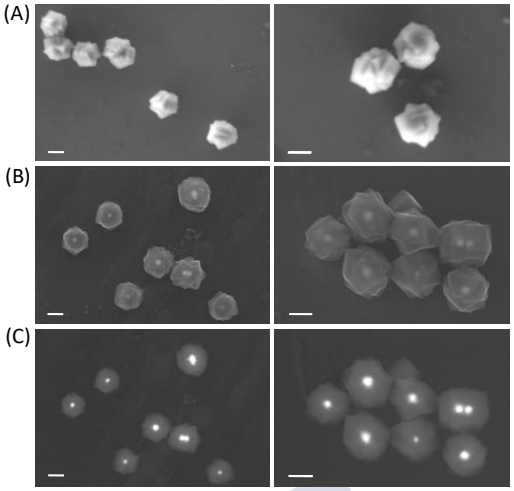

Figure S3.15. SEM images of NP-HOE-PMA after irradiation.
Laser irradiations were performed under 7 $W \cdot cm^{-2}$, 1 min. Images are taken with different detectors as well as voltages to get different morphological information. A) Images collected with Everhart-Thornley detector (SE2, secondary electrons) at 3 Kv; B) InLens detector (SE1, secondary electrons) at 20 kV; and C) AsB detector (backscattered electrons) at 20 kV. Scale bars correspond to 200 nm.

6.2.6. Cell studies

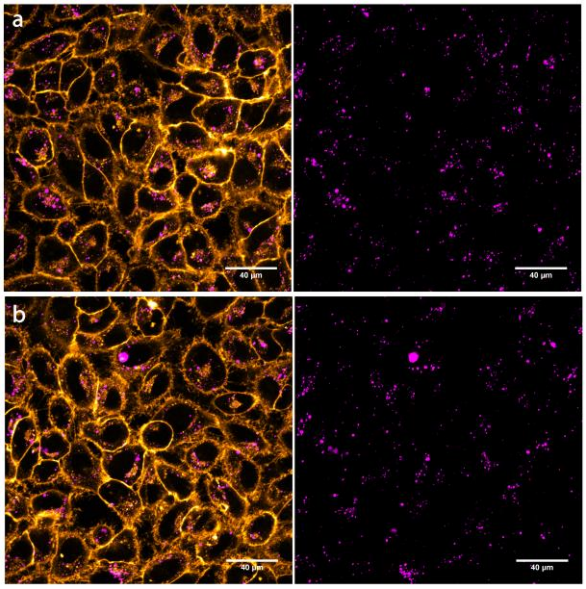

Figure S3.16. Collage confocal microscopy images for NC-HOE-PMA(rhodamine) system.
a-b) Images of NC-HOE-PMA(rhodamine) system (50 pM, overnight). Left: merged orange + pink channels; right: pink channel at 60X magnification. Pink and orange colours represent rhodamine and cell membrane staining, respectively (CellMaskTM Deep Red). Scale bar is 40 µm.

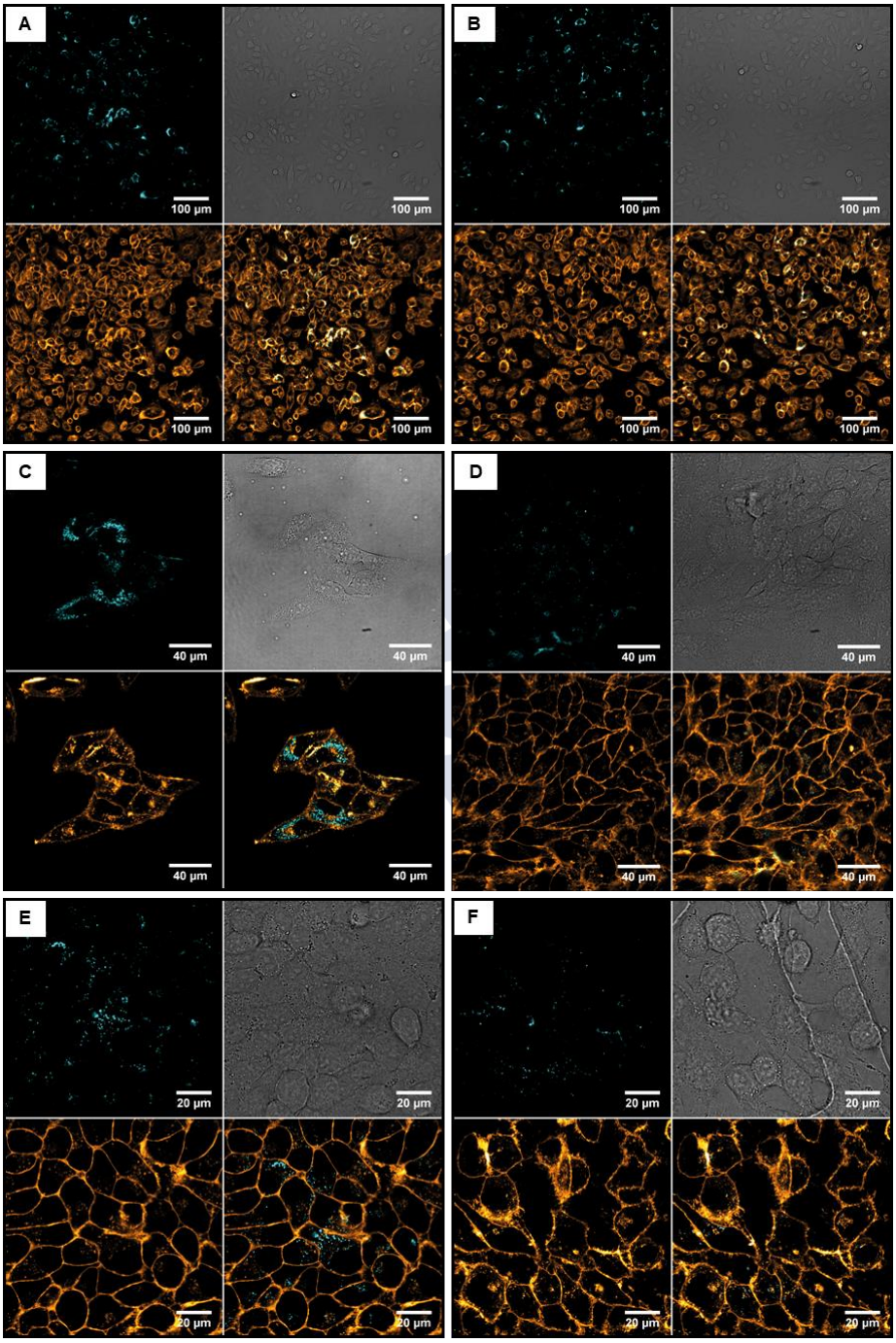

Figure S3.17. Collage confocal microscopy images for NC-HOE-PMA system.
Top-left: blue channel; top-right: bright field; bottom-left: orange channel; bottom-right: merged blue + orange) at different magnifications (A,B: 20X; C,D: 60X; E,F: 100X).

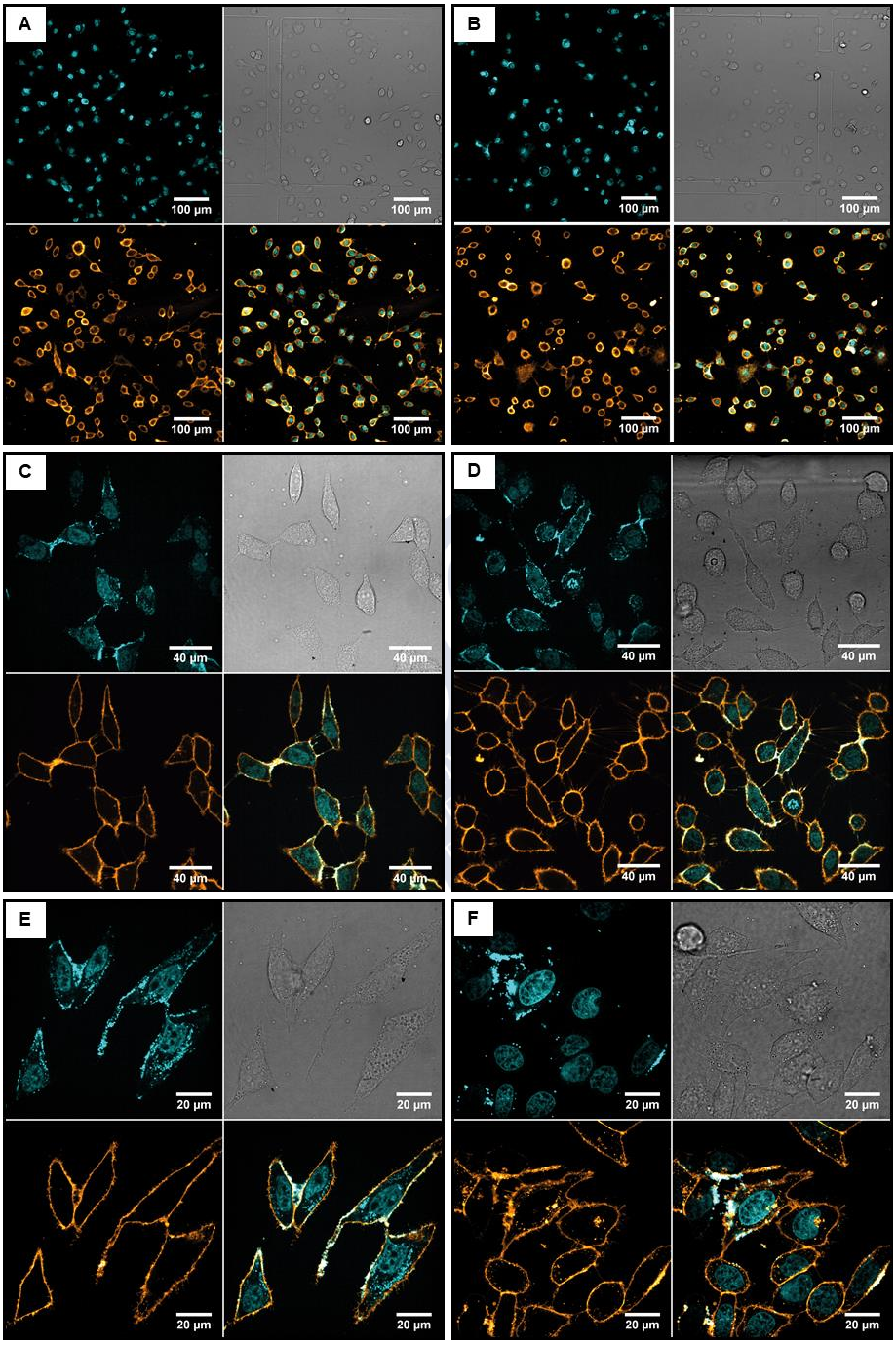

Figure S3.18. Collage confocal microscopy images for NC-HOE system.
Top-left: blue channel; top-right: bright field; bottom-left: orange channel; bottom-right: merged blue + orange) at different magnifications (A,B: 20X; C,D: 60X; E,F: 100X)

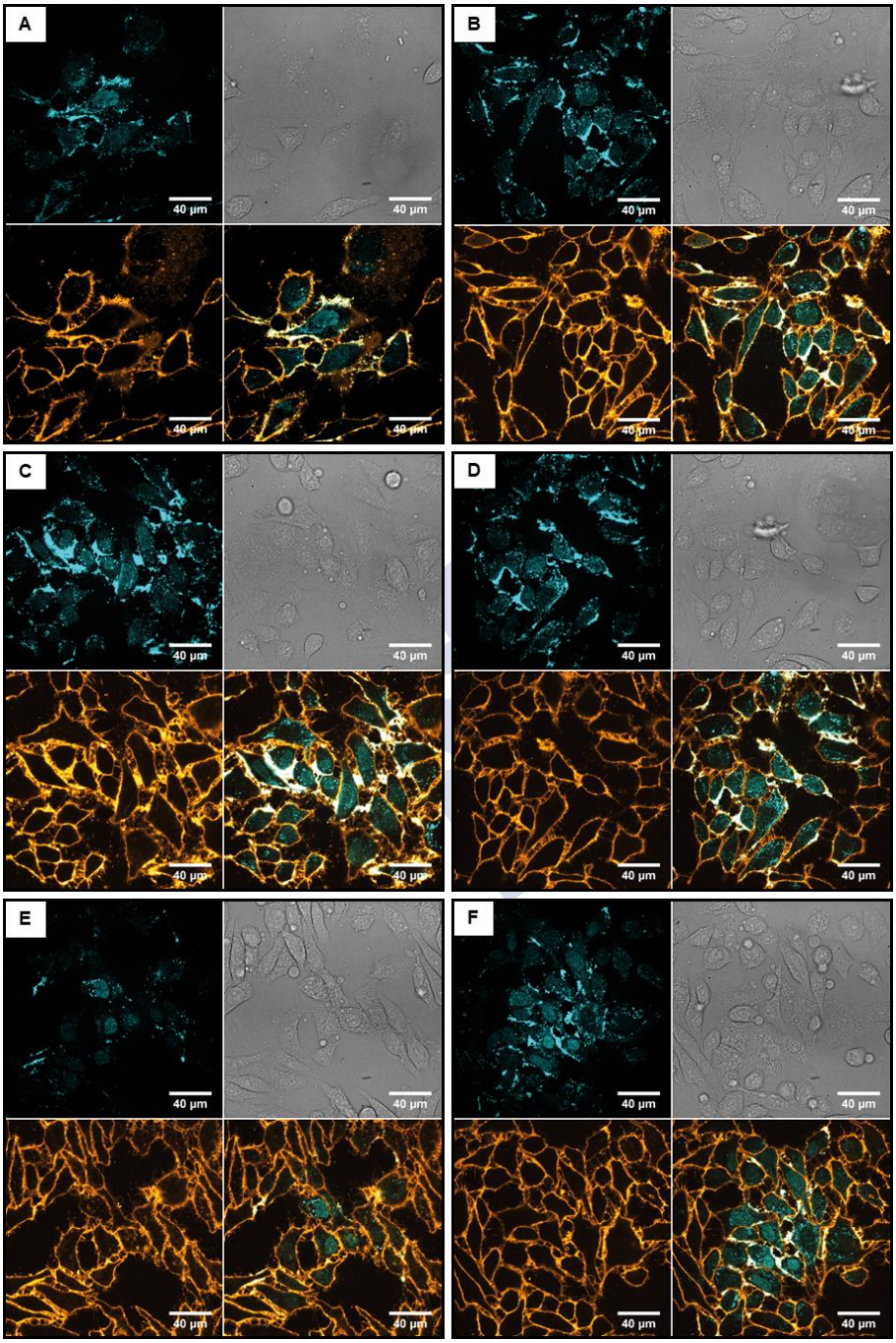

Figure S3.19. Collage confocal microscopy images for NC-HOE-PMA system after NIR treatment.

Top-left: blue channel; top-right: bright field; bottom-left: orange channel; bottom-right: merged blue + orange) at 60X magnification.

SERS imaging. To perform SERS imaging with living cells, A549 cells were seeded at a density of 60000 cells/cm^2 onto a Nunc™ Δ-Petri Dishes (Thermo Fisher Scientific) in DMEM medium without red phenol, 4.5 g/L D-glucose, 4 mM L-glutamine and 25 mM HEPES (DMEM, 1X, Gibco, #21063-029) supplemented with 10% heat-inactivated FBS (Gibco, #10270-106) and 1% P/S (Corning, 100X, #30-002-CI). After 16 h of culture, A549 cells displayed a semi-confluent (75%) phenotype under phase-contrast microscopy (IMT2 microscope by Olympus; Barcelona, Spain). Experiments were carried out at this semi-confluent state. NC-HOE and NC-HOE-PMA systems were redispersed in MeOH or in sterile Milli-Q water, respectively, at a concentration of 0.5 nM. NCs were added to A549 cells to a final concentration of 50 pM and kept in the incubator for 4 h. At the end of the experiment, culture media with non-internalized NCs was discarded, and cells were inspected in the SERS confocal microscope. A control consisting of a Petri dish with no cells but containing complete medium also incubated at 37°C, was included in this set of experiments to subtract the background signal caused by the Petri dish and the culture medium.

The laser was focused onto the samples with a 5x objective, providing an optical resolution of 1 μm. The inelastic radiation was collected with a Renishaw Invia system by using a high-resolution grating of 1200 g cm^{-1} and a NIR laser (785 nm). Samples were studied in single points or by mapping extended areas with the Renishaw StreaLine accessory. For the SERS characterization of the materials, samples were studied in powder. For quantitative analysis, bands were deconvoluted by curves of Lorentzian shape, where the band position and the full widths at half maxima were fixed after applying a linear baseline. Experiments with and without light were carried out as follows. For NIR illumination, cells were placed under the microscope and illuminated continuously with 3 mW of power at the sample. Spectra were collected every hour at 0.3 mW with acquisition times of 10 s. This difference of power was set to minimize the effect of the laser on the composites during the collection. In the case of the experiments without light, the same scheme was repeated but with no exposition of the sample to light (only for the spectral acquisition).

6.3. CHAPTER 4 APPENDIX

6.3.1. Synthesis and characterization of the probes

The compounds **1** and **3** were synthesized by adapting previously reported procedures aimed to derivatize carboxylic acids with thermolabile protecting groups;[248] both compounds include thermosensitive esters, which are subject of deprotection in neutral conditions only by increasing temperature (~ 90 °C). Thermocyclization of substrate **1** releases an aromatic carboxylic acid upon

nucleophilic intramolecular displacement by the pyridine group (product **2**). On the other hand, thermocyclization of substrate **3**, which holds a carbamate as leaving group, undergoes a concomitant decarboxylation reaction delivering an amine moiety, in this case the fluorogenic coumarine **4** in addition to the cyclization product **2**. The fluorogenic products **2** and **4** (Figure S4.1), resulting from the thermocyclization reactions depicted in Figure 4.2, were used herein to assess the efficiency of the thermal reactions (yield of the cyclized product **2** and/or release of **4**) in water and inside living cells. Figure 4.11 shows the general synthetic route followed to produce both substrates **1** and **3.**

All these molecules were synthesized and characterized in detail in the group of Mascareñas at CIQUS in Santiago de Compostela.

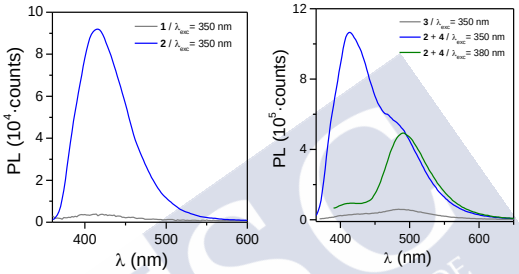

Figure S4.1. PL spectra of substrate 1 and 3.
(left) PL spectra of substrate **1** (20 μM, water) and the expected cyclized product (**2**) under excitation at λ_{exc} = 350 nm. (right) Photoluminescence (PL) spectra of substrate **3** (50 μM, water) under excitation at λ_{exc} = 350 nm, and the cyclized product **2** plus the released product **4** under different excitations.

6.3.2. Synthesis of PMA-modified NS/ZIF8 nanoreactors

Chemicals. All the reagents including zinc nitrate hexahydrate ($Zn(NO_3)_2{\cdot}6H_2O$; Sigma Aldrich #96482), 2-methylimidazole (MeIm; Sigma Aldrich #M50850), and CTAB (Sigma Aldrich #H5882) were used as purchased without any purification. CTAB-coated NSs were prepared by a seed-mediated growth method previously reported,[50] and the PMA-based amphiphilic polymer was synthesized as described previously.[50] Alternatively, the as synthesized CTAB coating on NSs was exchanged by serum proteins; to this aim, purified CTAB-coated NSs were mixed with FBS (10 $mg{\cdot}mL^{-1}$) and the mixture was stirred overnight at RT; finally, the FBS-stabilized NSs were collected by centrifugation (10000 RCF, 30 min), washed twice with water, and stored at 4 °C until use.

The modification of PMA polymer with a fluorophore, in particular here with amino-modified TAMRA (AnaSpec, #81506) in a ratio of 2 % (*i.e.* dye/PMA monomer ratio of 2/100) was performed according to a procedure already published.[50]

Synthesis of NS/ZIF8 nanocomposite. These core-shell particles were synthesized according to a previously reported protocol,[231] and consisted in growing a shell of ZIF8 around CTAB-coated NSs, which act as seed, in the presence of CTAB as a size-controlling and structural-directing agent. First, CTAB-coated NSs with a tip-to-tip length of *ca.* 80 nm were prepared and then stored at 4 °C in darkness until use. Then, for the formation of the ZIF8 onto the NSs, an aqueous solution of zinc nitrate (1 mL, 0.025 M) was added to an aqueous solution of 2-methylimidazole (1 mL, 1.3 M) under magnetic stirring (350 RPM) at RT, and immediately after a solution containing the NSs (1 mL, 2 nM of NSs dispersed in $5 \cdot 10^{-4}$ M of CTAB) was added. The mixture was stirred for 2 min and left then undisturbed for 3 h at RT, observing during this time the gradually appearance of bluish turbidity due to the formation of the NS/ZIF8 particles. Finally, the particles were collected by centrifugation (7000 RCF, 5 min), washed twice with MeOH and redispersed in 1 mL of MeOH. The concentration of particles in this solution was assumed to be 2 nM, taking into account that one NS/ZIF8 particle was formed per NS as confirmed by SEM. Note that NSs acted as seeds and that under the here described optimized conditions virtually all the ZIF8 particles contain a single NS in their geometric centre (*cf.,*Figure S4.2).

Post-functionalization of NS/ZIF8 NC with PMA polymer. The as-prepared NS/ZIF8 particles were functionalized with a PMA-based amphiphilic polymer by following a recently described protocol.[41] Briefly, the NS/ZIF8 particles dispersed in MeOH (1 mL, 2 nM) were mixed with the solution of the polymer in chloroform (0.05 M) in an optimized proportion; in particular 150 monomers of polymer per nm^2 of NS/ZIF8 particle, assuming a spherical particle of diameter ~ 220 nm, were added and the mixture was placed in a rotary evaporator. After complete evaporation of the solvent (3:1 MeOH:$CHCl_3$) the dried product was resuspended by addition of sodium borate buffer (0.1 M, pH 9) and aided by sonication (1-2 min). The resulting NS/ZIF8/PMA nanocomposite (or nanoreactor, NR from now) was collected and purified by centrifugation (7000 RCF, 10 min), washed twice with water, and finally redispersed in water (2 nM particle concentration). The same post-functionalization approach was carried out with a TAMRA-modified PMA polymer in order to obtain fluorescent-labelled NRs for their following tracing inside cells.

A scheme of the steps involved in the synthesis of these NRs is presented in Figure 4.3.

6.3.3. Morphological/structural characterization of NRs

Scanning Electron Microscopy and Transmission Electron Microscopy. The size and morphology of NRs was investigated with SEM and TEM (Figure S4.2). SEM images were acquired with a FESEM Zeiss Ultra Plus operated at 3 kV to get

surface information or 20 kV to penetrate deeper into the sample and obtain greater contrast of the NS nanoparticle into the NR. TEM images were acquired with a JEOL JEM-2010 microscope operated at 200 kV by deposition of the sample on top of a copper grid coated with a layer of carbon.

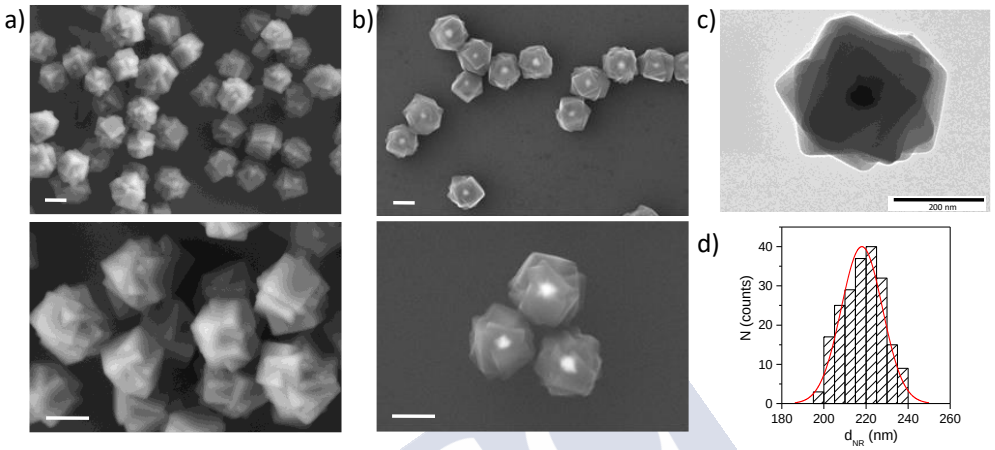

Figure S4.2. Representative SEM images of the NRs taken at different magnifications and different voltages.

a) 3 kV; b) 20 kV. c) Representative TEM image of the NRs. Scale bars correspond to 200 nm. d) Histogram of the number distribution N of the diameter (i.e., vertex-to-vertex distance) d_{NR} of the NRs (idealized as spherical particles) as determined from SEM images, d_{NR} = (218 ± 10) nm.

UV-Vis spectroscopy. A Biochrom Libra S60 UV–Vis spectrophotometer was used to record UV-Vis absorption spectrum of the NRs in water, which is presented in Figure S4.3 a showing a LSPR band centred at 790 nm.

Dynamic light scattering and ξ-*Potential.* The hydrodynamic diameter (d_h) and PDI of the NRs were determined by DLS using a Malvern Zetasizer Nano ZSP equipped with a 10 mW He–Ne laser operating at a wavelength of 633 nm and fixed scattering angle of 173˚. DLS histograms of NRs in water and the corresponding d_h values are presented in Figure S4.3b and Table S4.1, respectively. DLS measurements of NRs dispersed in either water or cell medium (i.e. DMEM supplemented with 10 % FBS) were performed at different time points (from 0 to 7 days) in order to evaluate the colloidal stability of NRs in both media (cf., Table S4.1). The ξ-potential of the NRs in water was measured with LDA using the same Malvern Zetasizer Nano ZSP instrument, indicating that NR particles were negatively charged (ξ = -27.5 ± 0.3 mV) as expected from the carboxyl groups of the PMA polymer.

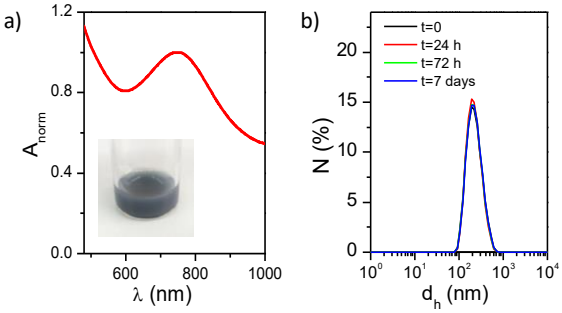

Figure S4.3. UV-Vis absorption spectrum and DLS number-weighted distribution of NR.
a) Normalized UV-Vis absorption spectrum (A_{norm}) of NR particles showing their SPR peak at λ = 790 nm. Inset shows a photograph of NR particles in water. b) DLS number-weighted distributions of the hydrodynamic diameter (d_h) of NR particles dispersed in water at different time points after their preparation.

Time	water		cell medium	
	d_h (nm) ± SD	PDI	d_h (nm) ± SD	PDI
0 h	238 ± 7	0.21	245 ± 7	0.23
24 h	234 ± 5	0.26	260 ± 5	0.22
72 h	236 ± 5	0.24	258 ± 6	0.27
7 days	239 ± 9	0.24	252 ± 7	0.32

Table S4.1. DLS measurements of the NRs dispersed in water and cell medium.
Time evolution of the hydrodynamic diameter d_h (mean value ± SD) given as number-weighted distributions from DLS measurements of NRs dispersed in water or in cell culture medium. SD values correspond to the standard deviation of the diameter mean value as obtained from several repeats (n=3) of the measurement. The PDI for each sample is also given. Data correspond to the raw data depicted in Figure S4.3b.

6.3.4. Thermoplasmonic properties of NRs

To evaluate the thermoplasmonic properties of the NR particles, solutions containing NRs in water (200 µL, 1 nM, placed in the wells of a 96-well plate) were irradiated with a 808 nm laser at different power densities (2, 4, and 8 $W \cdot cm^{-2}$) and for different irradiation times (from 0 to 10 min). The temperature of the solution after each irradiation condition was measured obtaining the ΔT versus-irradiation time curves presented in Figure S4.4. Water without NRs was used as control showing no obvious change of temperature (*i.e.* only an increase of 2 °C was observed after 10 min of irradiation at 8 $W \cdot cm^{-2}$). These results indicated that the NRs can rapidly absorb NIR light and efficiently convert the light energy into thermal one. Moreover, the stability/reproducibility of the photothermal conversion was investigated by performing repetitive irradiation

cycles, as shown in Figure 4.4. After each irradiation of 5 min at 8 W·cm^{-2} the cooling profile was recorded and once the solution reached the initial temperature (RT, ~ 22 °C), a new irradiation cycle was applied. No significant change was observed for the maximum temperature in the three laser on/off cycles in the case of the NRs. These results of successive "heating and cooling" cycles demonstrated the good reproducibility of the thermoplasmonic behaviour as well as the photostability of the NRs after irradiation. For comparison the same was done to pristine NSs (*i.e.*, CTAB-coated NSs; Figure S4.5a), which after just one cycle evidenced aggregation and a weaker thermoplasmonic response than that of NRs. In contrast, FBS-stabilized NSs retained their photothermal capabilities during three consecutive cycles (Figure S4.5b). The robust photostability of NR particles was also confirmed by SEM images of the NR after irradiation (*cf.,* Figure S4.6).

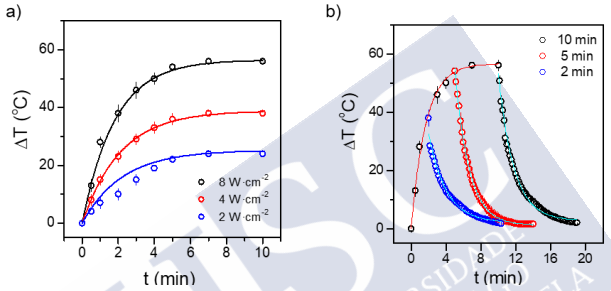

Figure S4.4. Test tube irradiation experiments.

a) Temperature-irradiation time profiles for NRs (1 nM) at different laser power densities. b) Heating and cooling profiles of the NRs (1 nM) after irradiation at 8 W·cm^{-2} for different times (2, 5, and 10 min). Error bars correspond to the standard deviations obtained from two repetitive experiments. Solid lines represent simulation curves for heating (Box-Lucas function) and cooling (exponential) using the fitting parameters shown in Table S4.2.

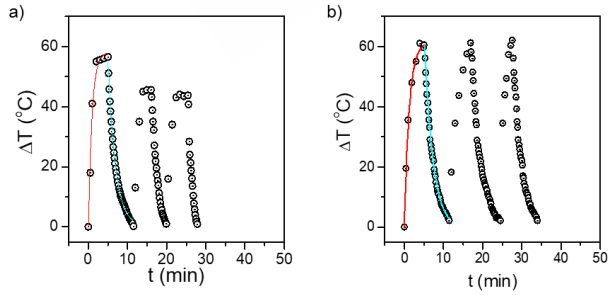

Figure S4.5. Reproducibility of the photothermal conversion in three successive cycles.

a) CTAB-coated NSs; b) FBS-stabilized NSs. Note that aggregation of the CTAB-coated NSs was observed after the first irradiation cycle, whereas FBS-stabilized NSs did not present any observable aggregation. The concentration of NSs particles was 1 nM. Irradiation conditions: 5 min at 8 W·cm^{-2}; solutions were left to cool down to RT (~22 °C), before starting a new 5 min irradiation cycle. Solid lines represent simulation curves for heating (Box-Lucas function) and cooling (exponential) using the fitting parameters shown in Table S4.3.

Irradiation time [min]	Irradiance [W·cm^{-2}]	fitting curves					
		Heating $\Delta T = T_{max} \cdot (1-e^{-b \cdot t})$			Cooling $\Delta T = T_0 + A \cdot e^{-b \cdot t}$		
		T_{max} [°C]	b [min^{-1}]	R^2	T_0 [°C]	b [min^{-1}]	R^2
10	2	25.22 ± 1.37	0.45 ± 0.09	0.97	-	-	-
	4	38.88 ± 0.39	0.47± 0.02	0.99	-	-	-
	8	56.51 ± 0.72	0.55 ± 0.72	0.99	-	-	-
2	8	56.62 ± 0.63	0.59 ± 0.03		2.79± 0.27	0.56 ± 0.01	0.99
4					1.20 ± 0.08	0.61 + 0.01	0.99
8					2.12 ± 0.33	0.50 + 0.02	0.98

Table S4.2. Fitting parameters for heating (Box-Lucas function) and cooling (exponential) simulation curves of NRs in water (Figure S4.4).

sample	fitting curves					
	Heating $\Delta T = T_{max} \cdot (1-e^{-b \cdot t})$			Cooling $\Delta T = T_0 + A \cdot e^{-b \cdot t}$		
	T_{max} [°C]	b [min^{-1}]	R^2	T_0 [°C]	b [min^{-1}]	R^2
CTAB-coated NS	58.08 ± 2.36	1.07 ± 0.16	0.98	0.30 ± 0.30	0.53 + 0.01	0.99
FBS-stabilized NS	61.44 ± 0.91	0.80± 0.04	0.99	0.00 ± 0.60	0.45 + 0.01	0.99
NR	55.58 ± 1.89	0.60 ± 0.05	0.99	1.21 + 0.09	0.62 ± 0.01	0.99

Table S4.3. Fitting parameters for heating (Box-Lucas function) and cooling (exponential) simulation curves in Figure S4.5 and Figure 4.4.

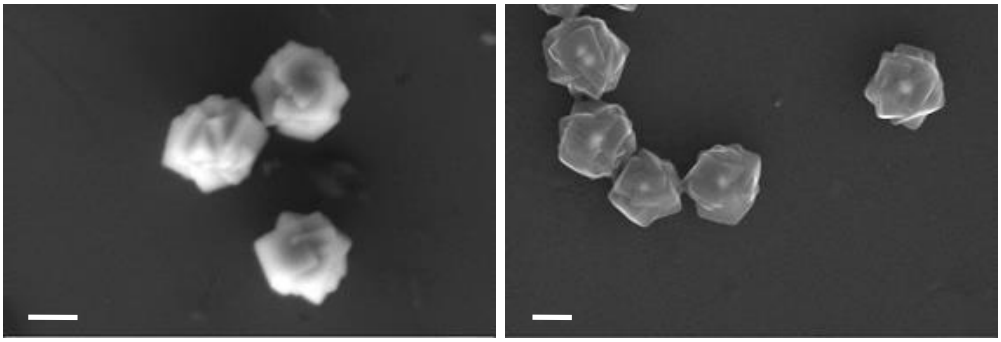

Figure S4.6. SEM images of NRs after irradiation.
808 nm laser at 8 W·cm^{-2} for 5 min. Scale bars correspond to 200 nm

6.3.5. Performance of NR particles as nanocontainer versus nanoreactor

Thanks to the high porosity of the MOFs, one of their outstanding properties is their ability for encapsulating large amounts of molecules inside their pores. In this way, the synthesized NRs can act as nanocontainer for a substrate (*i.e.* probe molecule). Therefore, if on the one hand the NRs can promote a reaction and, on the other, they can simultaneously host and carry such specific substrate, this dual role of the NRs opens the path for novel solutions in complex scenarios. Looking for example at the field of performing intracellular reactions, this could overcome problems of instability of the substrate in biological media or poor cellular uptake when the substrate is in a free form. The behaviour of our system for promoting a thermal reaction when the substrate is previously loaded inside the NRs (*i.e.* nanocontainer or loaded/filled nanoreactor), or when the NRs act simply as nanoreactor for substrate molecules diffusing freely in the surrounding environment was compared.

Loading of substrate (probe molecules) inside NRs. NRs were loaded with probe **1** before the post-functionalization with the PMA polymer. To this end, NS/ZIF8 particles dispersed in MeOH (0.5 mL, 2 nM) were mixed with a solution of the substrate **1** in methanol (150 µL, 1 mM), and the mixture was incubated overnight at RT to ensure the maximum loading, regardless of the diffusion kinetics of the molecules through the particles pores. Then, the excess of probe **1** was removed by centrifugation, and the particles were washed once with methanol in order to remove the molecules weakly adsorbed onto the surface of NS/ZIF8 particles. Afterwards, the NS/ZIF8 particles loaded with the probe were functionalized with the PMA polymer by following the procedure described above.

Quantification of the loaded probe by fluorescence. To quantify the amount of the substrate **1** loaded in NRs, the reaction was forced to achieve complete conversion of substrate **1** into its fluorescence product **2**. To this end, a solution of substrate **1** was heated in a thermostatic bath at 90 °C, and the amount of product formed was monitored by fluorescence. After 4 h, the fluorescence intensity did not further increase, which could be attributed to the complete conversion of the substrate, as previously demonstrated by Brzezinska *et* al.[248] The amount of the initial substrate loaded per NR was determined by interpolation in a previously obtained calibration curve of the fluorescent product (*cf.,* Figure S4.7a), resulting in $1.33 \cdot 10^5 \pm 4.20 \cdot 10^2$ molecules of probe per NR. In the case of probe **3**, quantification of **4** was performed using a calibration curve of the coumarin derivative (7-Amino-4-(trifluoromethyl)coumarin, Figure S4.7b).

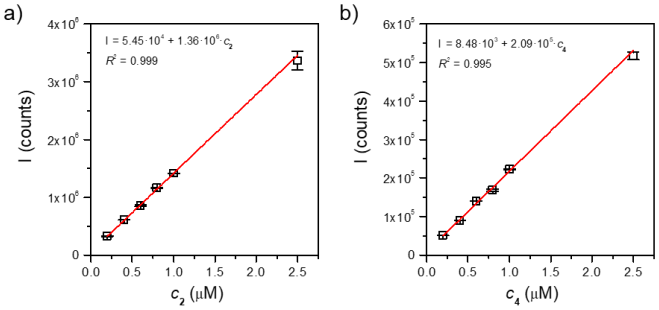

Figure S4.7. Calibration curves of fluorescent products.
a) Calibration curve of the fluorescent product from substrate **1** as obtained from fluorescence measurements under excitation (Ex.) at 350 nm. Fluorescence intensity (I) at the maximum emission (Em.) peak (λ=412 nm) as a function of the concentration is plotted, and the calibration equation is obtained by fitting a linear regression line to the collected data. b) Calibration curve of the fluorescent product from substrate **3** as obtained from fluorescence measurements under Ex. at 380 nm. Fluorescence intensity (I) at the maximum Em. peak (λ=490 nm) as a function of the concentration is plotted, and calibration equation is obtained by fitting a linear regression line to the collected data.

6.3.6. Thermal-promoted nucleophilic substitutions by NRs

The thermoplasmonic properties of NRs were used to promote the thermal reaction (nucleophilic substitution) depicted in Figure 4.11, leading to the transformation the non-fluorescent substrates (**1** and **3**) into the corresponding fluorescent products (**2** and **4**, respectively). An aqueous solution of NRs (200 μL, 1 nM) was mixed with the solution of the substrate (10 μL, 10 mM) in a well of a 96-well plate, and the mixture was irradiated with our 808 nm NIR set up (Figure 4.12). Different power densities (2, 4, and 8 $W \cdot cm^{-2}$) and irradiation times (from 0 to 10 min) were studied. After irradiation the temperature of the solution was measured (T_{max}), the NRs were then precipitated by centrifugation, and the generated product in the supernatant was quantified by fluorescence using the corresponding calibration curves (Figure S4.7). Data are presented in Figure 4.5, showing that the larger the exposure and/or irradiance were, the higher the yields of **2** were achieved. To compare the effect of irradiation with simply bulk heating using a bath, control experiments by heating the reaction mixture in a thermostatic bath at 80 °C during 5 min were carried out, leading to negligible yields (Table S4.5). Additionally, experiments involving varying NR-to-substrate molar ratios (%mol NR, Figure S4.8a), the transformation of **3** into **4** (Figure S4.8b), as well as manifold controls (*i.e.*, the performance of ZIF8 particles without NSs, FBS-stabilized NDs, and substrate without photocatalyst) were carried out, as summarized in Table S4.5.

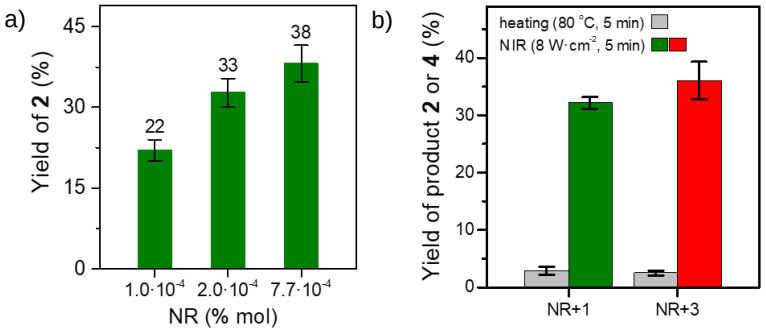

Figure S4.8. Yields of different reactions under different conditions and substrates.
a) Yield of **2** after NIR (8 W·cm^{-2}, 5 min) using different NR:**1** molar ratios: NRs dispersed in water (1 nM, 200 µl) with different concentrations of substrate **1** (1·10^{-4}, 2·10^{-4} and 7.7·10^{-4} %mol NR). b) Comparison of yield of **2** or **4** after NIR (8 W·cm^{-2}, 5 min); NRs dispersed in water (1 nM, 200 µl) with either **1** or **3**, respectively; molar ratio NR:substrate (**1** or **3**) = 2·10^{-4} %mol NR.

6.3.7. Photostability and reusability of the NRs

The photostability of the NRs after irradiation is a critical point for their potential reuse in successive cycles and, thus, it was investigated. As previously shown, SEM images of NR particles after irradiation were acquired, which showed that there were no changes on their morphology and size, *cf.*, Figure S4.6. Second, the performance of NRs for promoting the thermal reaction in five successive steps was studied as follows: for 1 cycle, a solution of NRs (200 µL, 1 nM) was mixed with the solution of the substrate (10 µL, 10 mM) in a well of a 96-well plate, and the mixture was irradiated with a 808 nm laser at 8 W·cm^{-2} for 5 min; then, the NRs were precipitated by centrifugation and the generated product in the supernatant was quantified by fluorescence. For 2 successive cycles, an identical mixture of NRs with substrate placed in a well was irradiated using 8 W·cm^{-2} for 5 min. The mixture was left to cool down until initial temperature conditions (*i.e.* waiting 10 min for assuring that RT was reached). Then, the irradiation was repeated for another 5 min, and after cooling the NRs were precipitated by centrifugation and the generated product in the supernatant was measured by fluorescence. The same was repeated up to a total of 3 cycles. Yields are presented in Figure S4.8, Figure S4.9a and Table S4.4, which indicate that NRs can act as a truly nanoreactor. Equivalent experiments using 8 W·cm^{-2} for 2 min, 5 consecutive irradiation/cooling cycles are presented in the main chapter (Figure 4.8, Table S4.4).

Finally, the reusability was also tested by performing the reaction using the same NRs (200 µL, 1 nM) mixed with the substrate 1 (10 µL, 10 mM) in five repetitive cycles at 8 W·cm^{-2} for 5 min. To this end and after each irradiation

cycle, *i.e.* after each use, the NRs were isolated by centrifugation and redispersed in a fresh aqueous solution containing the substrate for a new irradiation cycle (*i.e.* run). The supernatants from each use were measured by fluorescence to quantify the amount of generated product in each run. Data presented in Figure S4.9b and Table S4.4, clearly shows that negligible changes were observed after five reuses.

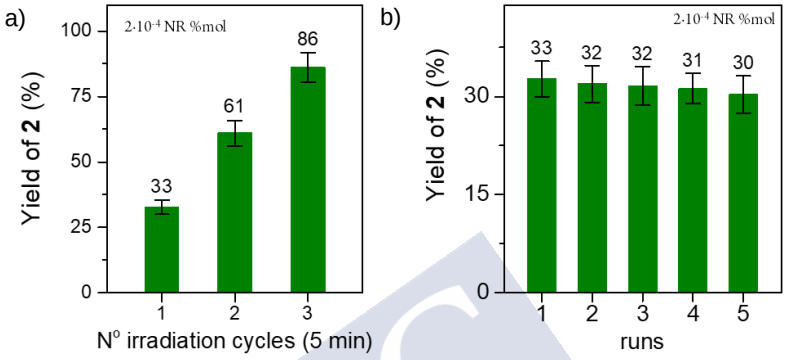

Figure S4.9. Cumulative yields of 2 and NR reusability experiments.
a) Cumulative yield of **2** after an increasing number of NIR cycles (8 W·cm^{-2}, 5 min NIR and 5 min cooling to RT); NRs dispersed in water (0.2 pmol in 200 µl) with 100 nmol substrate **1**; ratio NR:**1** = 2·10^{-4} %mol NR. b) Reusability of NRs; yield of **2** after different NIR cycles (8 W·cm^{-2}, 5 min NIR and washing); NRs dispersed in water (0.2 pmol in 200 µl) with 100 nmol substrate **1**; ratio NR:**1** = 2·10^{-4} %mol NR.

(i) Irradiation cycles		(ii) Irradiation cycles		(iii) Runs	
Nº cycles	Yield (%)*	Nº cycles	Yield (%)*	Run No.	Yield (%)
1	22.5 ± 1.4	1	32.7 ± 2.7	1	32.7 ± 2.7
2	43.6 ± 2.5	2	61.1 ± 4.9	2	31.9 ± 2.8
3	63.6 ± 2.8	3	86.3 ± 5.6	3	31.6 ± 2.9
4	81.5 ± 3.2	--	--	4	31.2 ± 2.3
5	96.0 ± 3.5	--	--	5	30.3 ± 2.8

*cumulative yield

Table S4.4. Thermal reaction yields of substrate 1 to generate the fluorescent product 2 promoted by NRs (1 nM).
i) Outcome of NCs as reactors by performing five successive irradiation cycles (8 W·cm^{-2}, 2 min each one, 20 nmol of **1**, 1·10^{-3} NR%) and neither the isolation of the NRs nor the reactants between one irradiation and the following one. Cumulative yields (%) are presented; ii) equivalent to (i) but with three successive irradiation cycles (8 W·cm^{-2}, 5 min each one, 100 nmol of **1**); iii) the reusability of NCs by performing five repetitive reuses, involving the isolation of the NCs after each use and redispersion in a fresh substrate (100 nmol of **1**, 2·10^{-4} NR%)) solution for a new irradiation (8 W·cm^{-2}, 5 min).

Particle (0.2 pmol)	NIR Irradiance [W·cm^{-2}]	Time [min]	T_{max} [°C]	T_{bath} [°C]	Substrate (100 nmol)	Product / Yield [%] ± SD**
NR	2	2	32	none	1	n.r.*
NR	2	5	45	none	1	n.r.*
NR	2	10	60	none	1	2 / 0.5 ± 0.3
NR	4	2	43	none	1	2 / 0.3 ± 0.1
NR	4	5	57	none	1	2 / 1.9 ± 0.1
NR	4	10	75	none	1	2 / 3.5 ± 0.3
NR	8	2	46	none	1	2 / 7.6 ± 1.4
NR	8	5	59	none	1	2 / 32.2 ± 1.9
NR	8	10	78	none	1	2 / 44.1 ± 2.4
none	8	5	22	none	1	2 / 2.9 ± 0.7
none	none	5	80	80	1	n.r.*
"bare" ZIF8#	none	5	80	80	1	n.r.*
"bare" ZIF8#	8	5	22	none	1	2 / 2.0 ± 0.8
NS/FBS$	8	5	81	none	1	2 / 5.0 ± 0.5
NR	none	5	80	80	1	2 / 2.9 ± 0.7
NR	8	5	59	none	3	4 / 36.1 ± 3.2
NR	none	5	80	80	3	4 / 2.5 ± 0.4

*n.r.: no reaction; # "bare" ZIF8 nanoparticles equivalent to NRs, but without the NS core; taking into account the reaction volume (200 µL), the absolute amounts of catalyst and substrate are 0.2 pmol and 100 nmol, respectively; $NS/FBS correspond to FBS-stabilized NSs; **SD values correspond to the standard deviation as obtained from several repetitions (n=3) of the measurement.

Table S4.5. Reaction yields of substrates (1 and 3) to generate the fluorescent products (2 and 4) promoted by NRs

Control experiments with FBS-stabilized NS and without catalyst are included. Reactions were performed under different conditions to study the following: i) Laser irradiation conditions (irradiance, irradiation time), and ii) thermoplasmonic heating versus conventional heating in a water bath.

6.3.8. Cell studies

Confocal imaging.

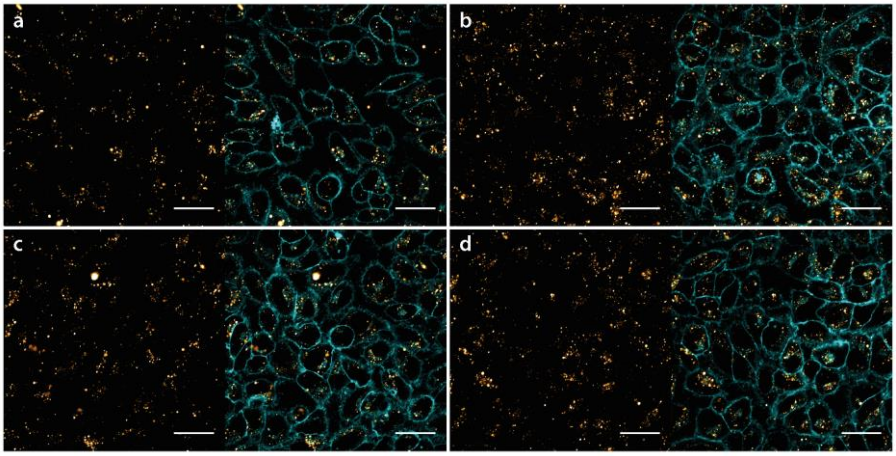

Figure S4.10. Internalization of TAMRA-labelled NRs.
a-d) Confocal microscopy images from TAMRA-labelled NRs internalized by Hela cells (orange; Ex./Em.: 561/620(60) nm); TAMRA-labelled NRs (orange) + cell plasma membrane staining using CellMask™ Deep Red (cyan; Ex./Em.: 637/725(40) nm). Scale bars correspond to 40 µm.

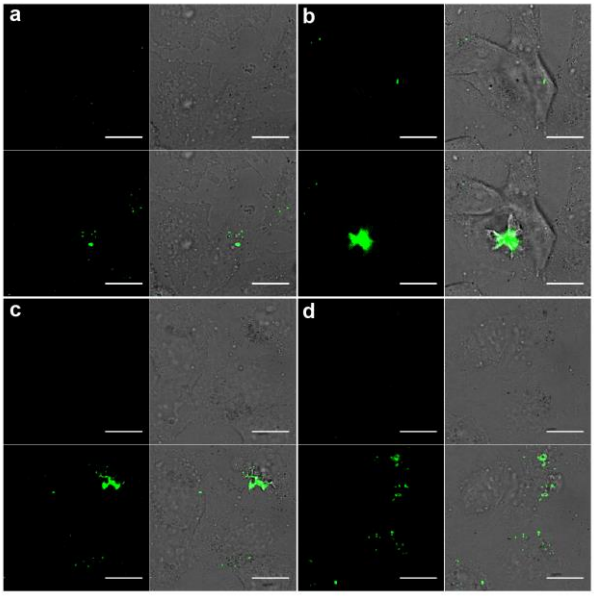

Figure S4.11. NR@1 preloaded cells before and after NIR pointer irradiation.
a-d) Different confocal microscopy images of NR@**1**-preloaded cells, before (top) and after (down) NIR pointer irradiation; fluorescence (left, Ex./Em. = 405/450(50) nm) and merged (right) bright field + fluorescence images are shown. Scale bars correspond to 20 µm.

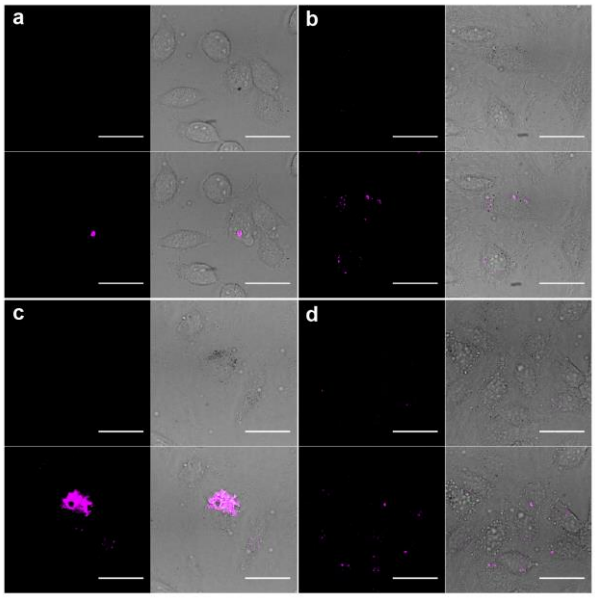

Figure S4.12. NR@3 preloaded cells before and after NIR pointer irradiation.
a-d) Different confocal microscopy images of NR@**3**-preloaded cells, before (top) and after (down) NIR pointer irradiation; fluorescence (left, Ex./Em. = 405/525(50) nm) and merged (right) bright field + fluorescence images are shown. Scale bars correspond to 20 μm.

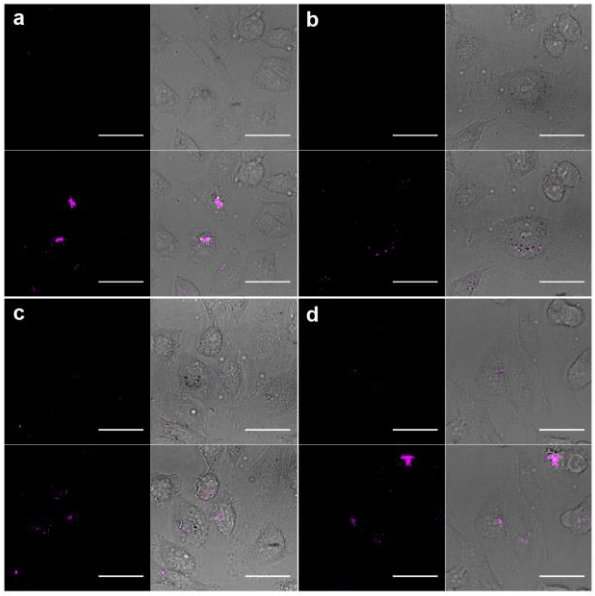

Figure S4.13. NR preloaded cells incubated with 3 before and after NIR pointer irradiation.
a-d) Different confocal microscopy images of NR-preloaded cells incubated with **3** (10 μM, 30 min), before (top) and after (down) NIR pointer irradiation; fluorescence (left, Ex./Em. = 405/525(50) nm) and merged bright field + fluorescence images are shown. Scale bars correspond to 20 μm.

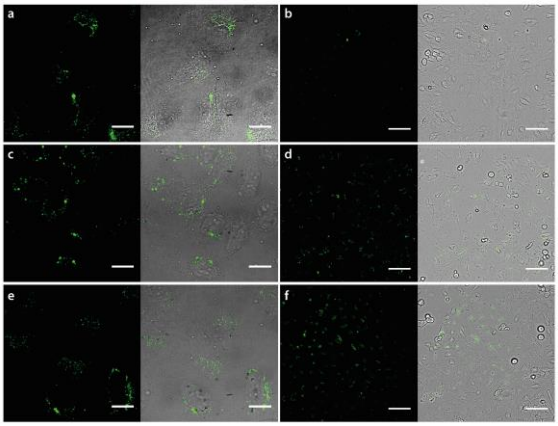

Figure S4.14. Controls with freely incubated probes 1 or 2 (10 μM, 30 min), and without NIR.

a,b) Control cells without NRs, incubated with **1**; c,d) control NR-preloaded cells (50 pM, overnight) incubated with **1**; e,f) control NR-preloaded cells (50 pM, overnight) incubated with **2** (10 mM, 30 min). Fluorescence (left, Ex./Em. = 488/525(50) nm) and merged bright field + fluorescence images are shown. Scale bars are 20 μm (a, c, e; 100X) or 100 μm (b, d, f; 20X).

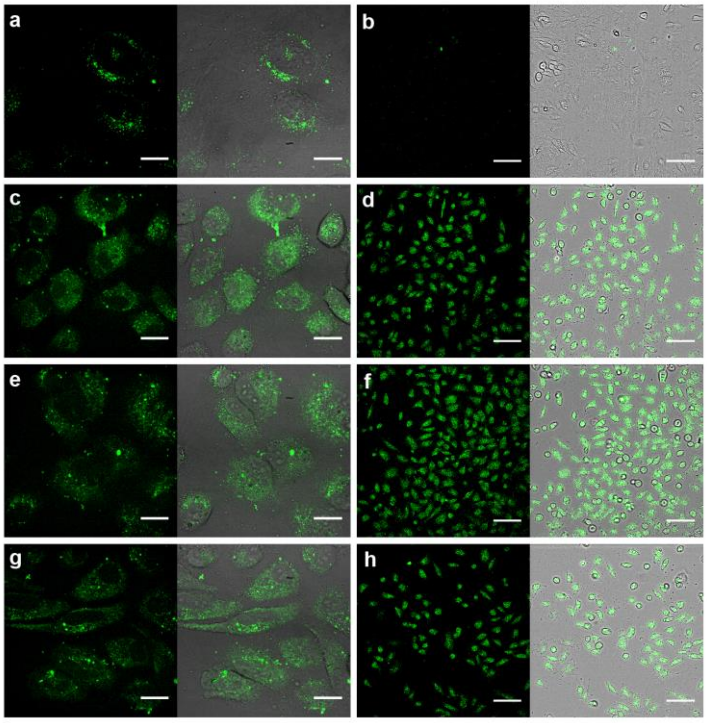

Figure S4.15. Particle-loaded cells with substrate 1 and NIR.

NS or NR (50 pM overnight)-loaded cells with substrate **1** (10 mM, 30 min) under NIR (10 $W \cdot cm^{-2}$, 1 min). a,b) NS-preloaded cells; c-h) NR-preloaded cells. Fluorescence (left, Ex./Em. = 488/525(50) nm) and merged bright field + fluorescence images are shown. Scale bars are 20 μm (a, c, e, g; 100X) or 100 μm (b, d, f, h; 20X).

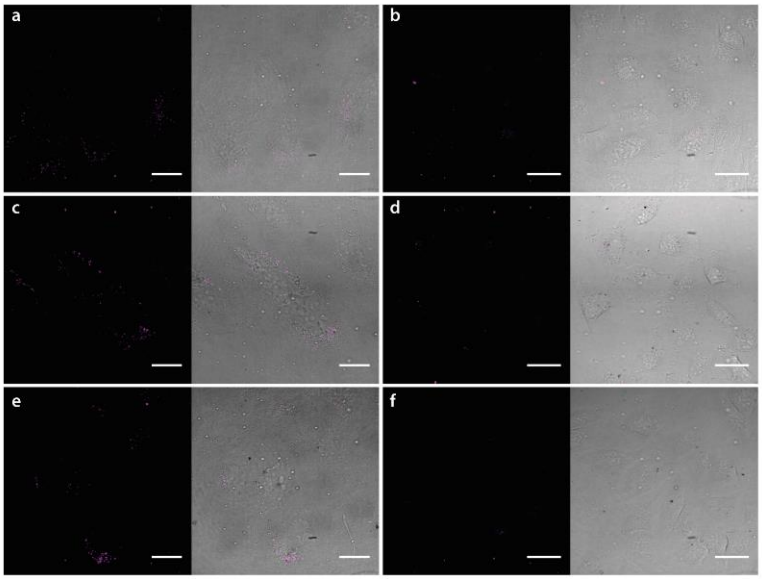

Figure S4.16. Controls with probes 3 or 4 (10 mM, 30 min), and without NIR.
a,b) Control cells without NRs, incubated with **3**. c,d) Control NR-preloaded cells (50 pM, overnight) incubated with free **3**. e,f) Control NR-preloaded cells (50 pM, overnight) incubated with free **4** (10 mM, 30 min). Fluorescence (left, Ex./Em. = 540/620(60) nm) and merged bright field + fluorescence images are shown. Scale bars are 20 μm (a, c, e; 100X) or 40 μm (b, d, f; 60X).

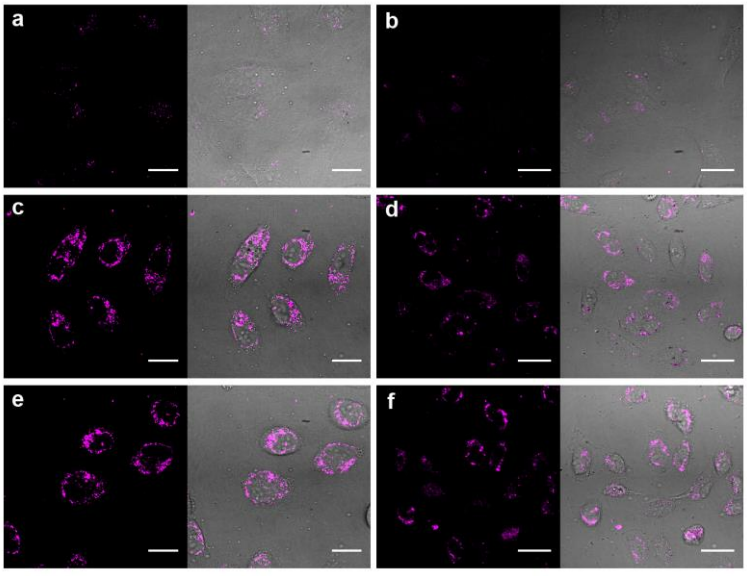

Figure S4.17. Particle-loaded cells with substrate 3 and NIR.
NS or NR (50 pM overnight)-loaded cells with substrate **3** (10 mM, 30 min) and NIR (10 $W \cdot cm^{-2}$, 1 min). a,b) NS-preloaded cells; c-f) NR-preloaded cells. Fluorescence (left, Ex./Em. = 540/620(60) nm) and merged bright field + fluorescence images are shown. Scale bars are 20 μm (a, c, e; 100X) or 40 μm(b, d, f; 60X).

6.4. CHAPTER 5 APPENDIX

6.4.1. Synthesis and characterization of the probes and palladium complexes

General procedures. The compounds propargyl-protected coumarin **1**,[167] propargyl-protected 2-(2'-hydroxyphenyl)benzothiazole **3**,[299] and bis-propargyl carbamate-protected cresyl violet **5**,[300] are known compounds and were synthesized and characterized according to those previously reported procedures. Compounds **2, 4** and **6** are commercially available and were purchased from Sigma-Aldrich.

Palladium complexes (**Pd-1** = $[Pd(allyl)Cl]_2$;[165] **Pd-2** = $[(PPh_3)Pd(allyl)Cl]$;[168] **Pd-3** = $[(PdCl_2(TFP)_2]$[270]) have been previously described and were synthesized from the corresponding ligands and palladium precursors following reported procedures. Their ^1H, ^{13}C and ^{31}P NMR data were in complete agreement with the reported values. Precursors $[Pd(allyl)Cl]_2$ and $[PdCl_2(CH_3CN)_2]$ are commercially available and were purchased from Sigma-Aldrich and Strem Chemicals, respectively. Ligands triphenylphosphine and tris(2-furyl)phosphine (TFP) were acquired from Sigma-Aldrich.

All these molecules were synthesized and characterized in detail in the group of Mascareñas at CIQUS in Santiago de Compostela. For characterization, mass spectra were acquired using IT-MS Bruker AmaZon SL at CiQUS and also using electrospray ionization (ESI) and were recorded at the CACTUS facility of the University of Santiago de Compostela. UV and fluorescence spectra were acquired using Jasco V-670 spectrometer and Varian Cary Eclipse fluorescence spectrofluorometer.

UV-Vis and Fluorescence spectra of synthesized molecules.

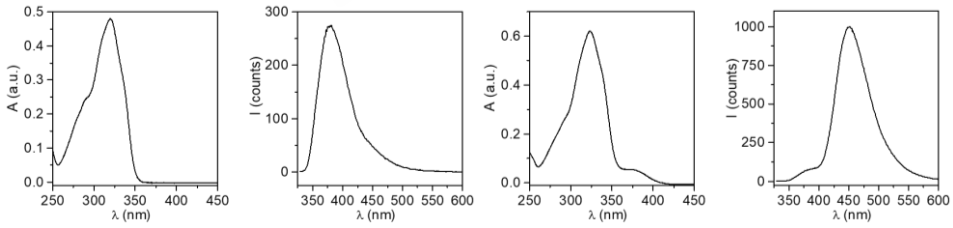

Figure S5.1.UV and fluorescence spectra of 1 and 2.
From left to right: UV spectrum of **1** (30 μM, 1:1 v/v mixture of DMSO:Tris buffer 200 mM, pH = 7.5); fluorescence spectrum of **1** (10 μM, 7:3 v/v mixture of DMSO:H_2O; λ_{ex} 323 nm, λ_{em} 380 nm, λ_{cut} 330 nm; UV spectrum of **2** (30 μM, 1:1 v/v mixture of DMSO:Tris buffer 200 mM, pH = 7.5) and fluorescence spectrum of **2** (10 μM, 7:3 v/v mixture of DMSO:H_2O; λ_{ex} 323 nm, λ_{em} 452 nm, λ_{cut} 330 nm.

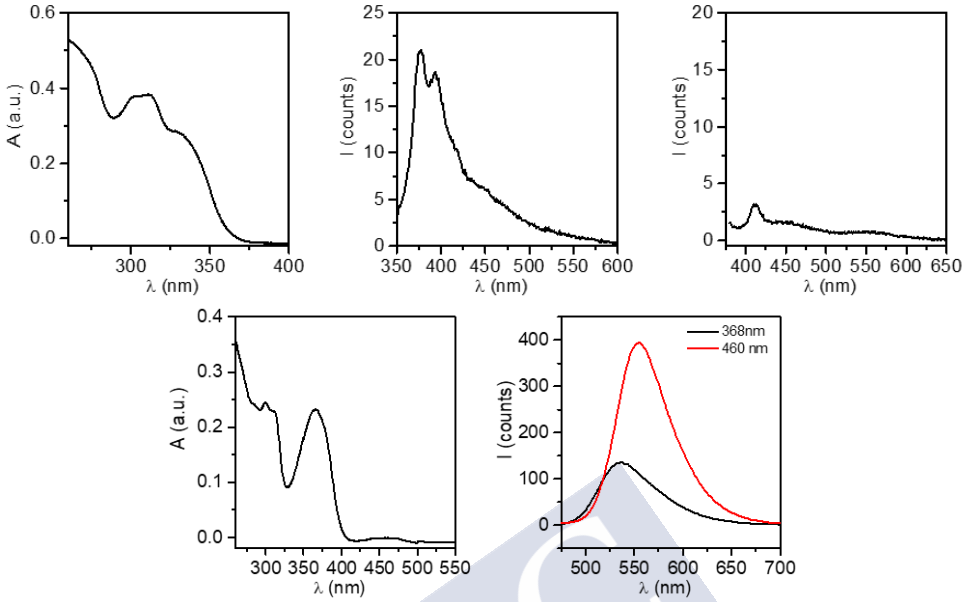

Figure S5.2. UV and fluorescence spectra of 3 (up) and 4. (down)

From left to right: UV spectrum of **3** (20 μM, 7:3 v/v DMSO:H_2O), fluorescence spectra of **3** (5 μM, 7:3 v/v DMSO:H_2O; λ_{ex} 335 nm, λ_{em} 377 nm, λ_{cut} 340 nm), fluorescence spectrum of **3** (5 μM, 7:3 v/v DMSO:H_2O; λ_{ex} 368 nm, λ_{em} 412 nm, λ_{cut} 380 nm), UV spectrum of **4** (20 μM, DMSO:H_2O 7:3) and fluorescence spectra of **4** (5 μM, 7:3 v/v mixture of DMSO:H_2O) at different wavelengths (λ_{ex} 368 nm, λ_{em} 558 nm, λ_{cut} 380 nm and λ_{ex} 460 nm, λ_{em} 535 nm, λ_{cut} 465 nm).

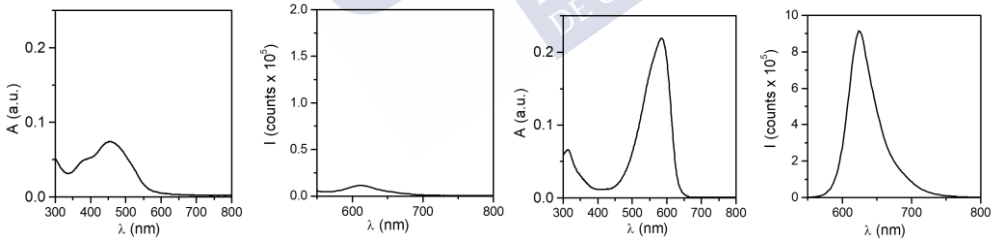

Figure S5.3. UV and fluorescence spectra of 5 and 6.

From left to right: UV spectrum of **5** (10 μM, 8:2 PBS:MeOH), fluorescence spectrum of **5** (1 μM, 8:2 PBS:MeOH) under excitation at λ_{ex}=540 nm; maximum emission at λ_{em}=610 nm (right), UV spectrum (left) of **6** (10 μM, 8:2 PBS:MeOH) and fluorescence spectrum of **6** (1 μM, 8:2 PBS:MeOH) under excitation at λ_{ex}=540 nm; maximum emission at λ_{em}=624 nm.

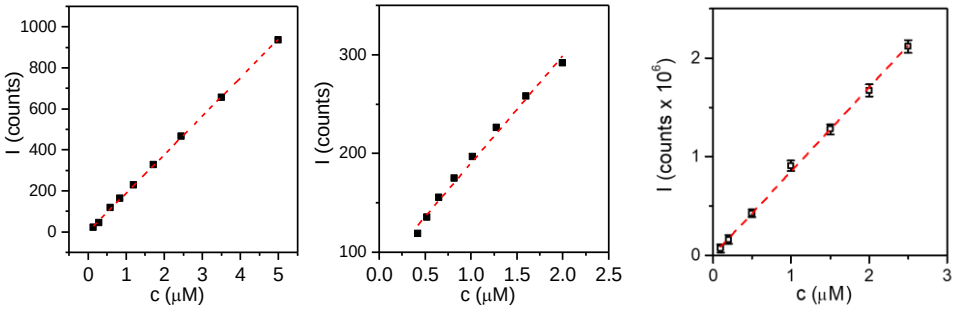

Figure S5.4. Calibration curves of 2, 4 and 6.
From left to right: calibration curve of **2** (9:1 v/v H_2O:MeOH), λ_{ex} 323 nm, λ_{em} 452 nm. Dashed red line: linear regression fitting I [counts] = 1+188 ·c [μM]; coefficient of determination R^2 = 0.999. Calibration curve of **4** (7:3 v/v DMSO:H_2O), λ_{ex} 460 nm, λ_{em} 535 nm, λ_{cut} 470 nm. Dashed red line: linear regression fitting I [counts] = 81 + 108 ·c [μM]; coefficient of determination R^2 = 0.990. Calibration curve of **6** (8:2 PBS:MeOH), λ_{ex}=540 nm, λ_{em}=624 nm. Dashed red line: linear regression fitting I ·10^5 [counts] = 0.006 + 8.504 ·c [μM]; coefficient of determination R^2 = 0.998.

6.4.2. Synthesis of PMA-modified Pd/ZIF8 NCs (NRs)

Chemicals. All the reagents including potassium tetrachloropalladium (II) (K_2PdCl_4; Sigma Aldrich #205796), AA (Sigma Aldrich #A5960), zinc nitrate hexahydrate ($Zn(NO_3)_2{\cdot}6H_2O$; Sigma Aldrich #96482), 2-methylimidazole (MeIm; Sigma Aldrich #M50850), and CTAB (Sigma Aldrich #H5882) were used as purchased without any purification. The PMA-based amphiphilic polymer was synthesized as described previously.[50]

Synthesis of Pd nanocubes. CTAB-coated Pd-NPs enclosed by {100} facets were synthesized according to a previously reported protocol,[292] using K_2PdCl_4 as precursor, AA as reducing agent, and CTAB as capping agent and stabilizer. In a typical synthesis, 0.5 mL of 0.1 M CTAB, 21.25 mL of deionized water and 2.5 mL of 0.01 M K_2PdCl_4 were placed in a 50 mL glass vial, and then 0.75 mL of 0.1 M AA was added while magnetic stirring. The mixture is stirred at RT for some minutes (~ 5 min) observing during this time that the solution turns into black colour, which indicates the formation of the Pd nanocubes (in the following referred to as Pd-NPs). Next, the black product was collected by centrifugation (7200 RCF, 10 min), washed twice with MilliQ water to remove the excess of CTAB (Figure S5.5), and finally the purified Pd-NPs were redispersed in 1.4 ·10^{-3} M CTAB.

Synthesis of Pd-ZIF8. These particles were synthesized according to a previously reported protocol with slight modifications.[231] The Pd-NPs were used as seeds onto which a shell of ZIF8 was grown, in the presence of CTAB as size-

controlling and structural-directing agent, obtaining in this way the core-shell NC. Briefly, an aqueous solution of zinc nitrate (1 mL, 0.025 M) was added to an aqueous solution of 2-methylimidazole (1 mL, 1.3 M) under magnetic stirring (350 RPM) at RT and immediately after, a solution containing the Pd-NPs (1mL, 2 nM of nanoparticles dispersed in $1.4 \cdot 10^{-3}$ M of CTAB) was added. After 2 min, the stirring was stopped, and the mixture was left undisturbed for 3 h at RT The gradual appearance of brownish turbidity indicated the formation of the Pd-ZIF8 particles. Finally, the particles were collected by centrifugation (7000 RCF, 5 min), washed twice with MeOH and redispersed in 1 mL of MeOH. The concentration of particles in this solution was assumed to be ~2 nM, considering that one Pd-ZIF8 particle was formed per Pd-NP (seed). Note that under optimized conditions virtually all the ZIF8 particles contained a Pd-NP as core (Figure S5.6).

Post-functionalization of Pd-ZIF8 with PMA polymer. The as-prepared Pd-ZIF8 particles were functionalized with a PMA-based amphiphilic polymer) by following a recently described protocol.[231] Briefly, the Pd-ZIF8 particles dispersed in methanol (2 nM) were mixed with the solution of the polymer in chloroform (0.05 M) in an optimized proportion; specifically, 150 monomers of polymer per nm^2 of Pd-ZIF8 particle, assuming a spherical particle with diameter of 250 nm; and the mixture was placed in a rotary evaporator. After complete evaporation of the solvent (3:1 MeOH:$CHCl_3$) the dried product was resuspended by addition of SBB (0.1 M, pH 9) and aided by sonication (1-2 min). The resulting PMA-modified Pd-ZIF8 NCs (in the following referred to as NRs) were collected and purified by centrifugation (7000 RCF, 10 min), washing twice with water, and finally redispersed in water.

6.4.3. Morphological/structural characterization of NRs

Scanning Electron Microscopy. The size and morphology of Pd-NPs and NRs were investigated with SEM (Figure S5.5 and Figure S5.6). SEM images were acquired with a FESEM Zeiss Ultra Plus operated at 3 kV or 20 kV.

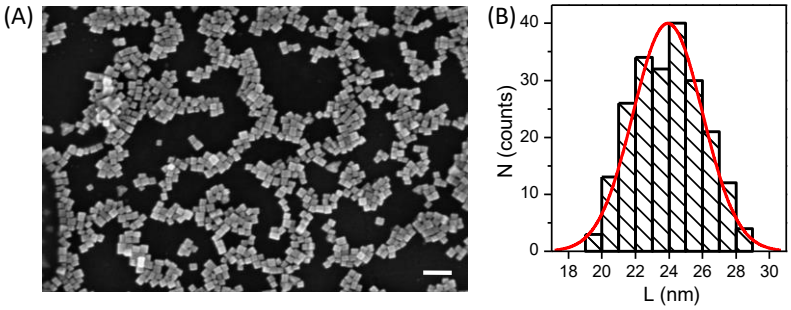

Figure S5.5. SEM characterization of Pd-NPs.
A) Representative SEM image (scale bar corresponds to 100 nm); and B) the corresponding histogram of the number-weighted distribution N of the side length L of the Pd-NPs (200 particles measured) as determined from SEM images, L = (23.9 ± 2.0) nm.

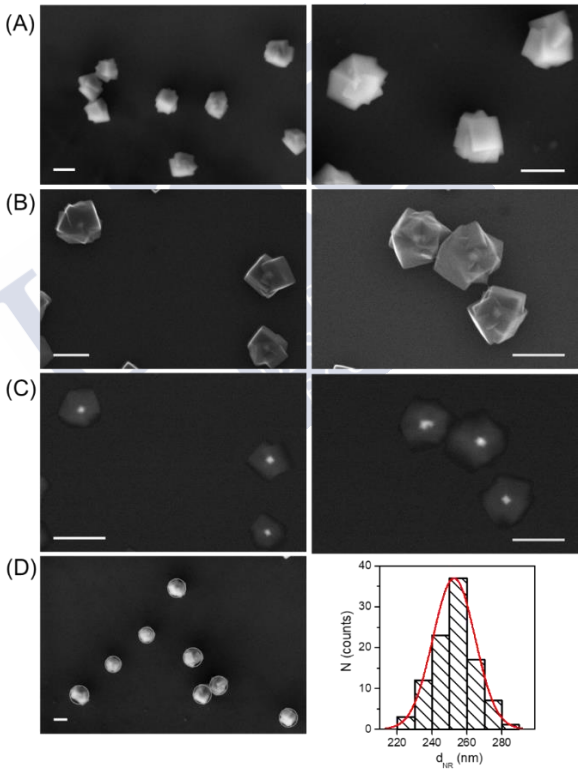

Figure S5.6. SEM characterization of NRs.
Representative SEM images of NRs acquired with different detectors and different voltages: A) Everhart-Thornley detector (SE2, secondary electrons) at 3 kV; B) InLens detector (SE1, secondary electrons) at 20 kV; and C) AsB detector (backscattered electrons) at 20 kV. Scale bars correspond to 200 nm. D) Histogram of the number-weighted distribution N of the diameter (i.e., vertex-to-vertex distance) d_{NR} of the NRs (idealized as spherical particles; 100 particles measured); regions of interest (ROIs, outlines) were drawn in the SEM images to estimate the size of the NRs, i.e., d_{NR} = (253 ± 12) nm.

Powder x-ray diffraction. A Philips x-ray diffractometer was used to study the crystallinity of the Pd-ZIF8 NCs. Sample was examined in the range of 2θ between 2^0 and 75^0 with a passage of 0.02^0 and a time by step of 2s. Table S5.1 shows the major diffraction peaks identified by PXRD (*cf.*, Figure S5.7).

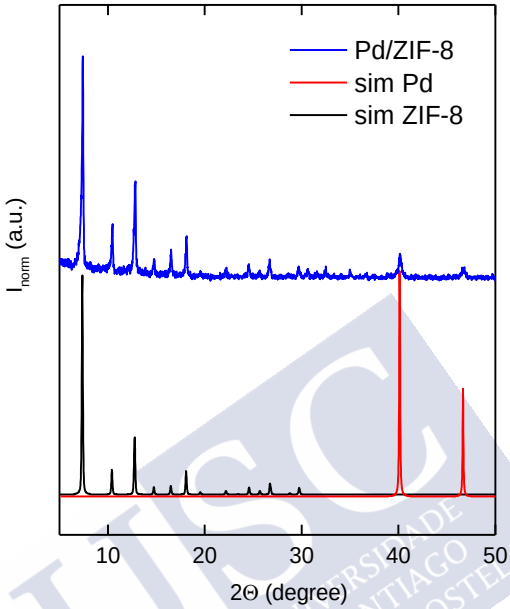

Figure S5.7. PXRD spectrum of Pd-ZIF8 NCs.
For comparison, simulations of ZIF8 (black, COD - Crystallography Open Database: 7111970) and Pd-fcc (red; COD: 9008478) are added. I_{norm} is the normalized intensity.

Pos. [°2Θ]	Height [cts]	FWHM Left [°2Θ]	d-spacing [Å]	Rel. Int. [%]
7.37	447	0.16	11.977	100.0
10.44	95	0.16	8.470	21.2
12.79	209	0.15	6.918	46.6
14.75	33	0.16	5.999	7.5
16.52	49	0.17	5.363	11.0
18.09	93	0.15	4.899	20.7
24.52	30	0.16	3.627	6.6
26.68	33	0.22	3.339	7.4
40.13	46	0.34	2.245	10.3

Table S5.1.PXRD peaks.
Major peaks (relative intensity > 6%) identified in the Pd/ZIF8 diffractogram.

Dynamic light scattering and ξ-Potential. The hydrodynamic diameter (d_h) and PDI of the NCs were determined by DLS using a Malvern Zetasizer Nano ZSP equipped with a 10 mW He–Ne laser operating at a wavelength of 633 nm and fixed scattering angle of 173°. DLS spectra of the NRs dispersed in water freshly prepared, as well as measured over time up to one week are presented in Figure S5.8, and the corresponding d_h values of the NRs both in water, cell medium (supplemented with 10% FBS) and ALF (10% FBS or without supplements) over time, are summarized in Table S5.2.

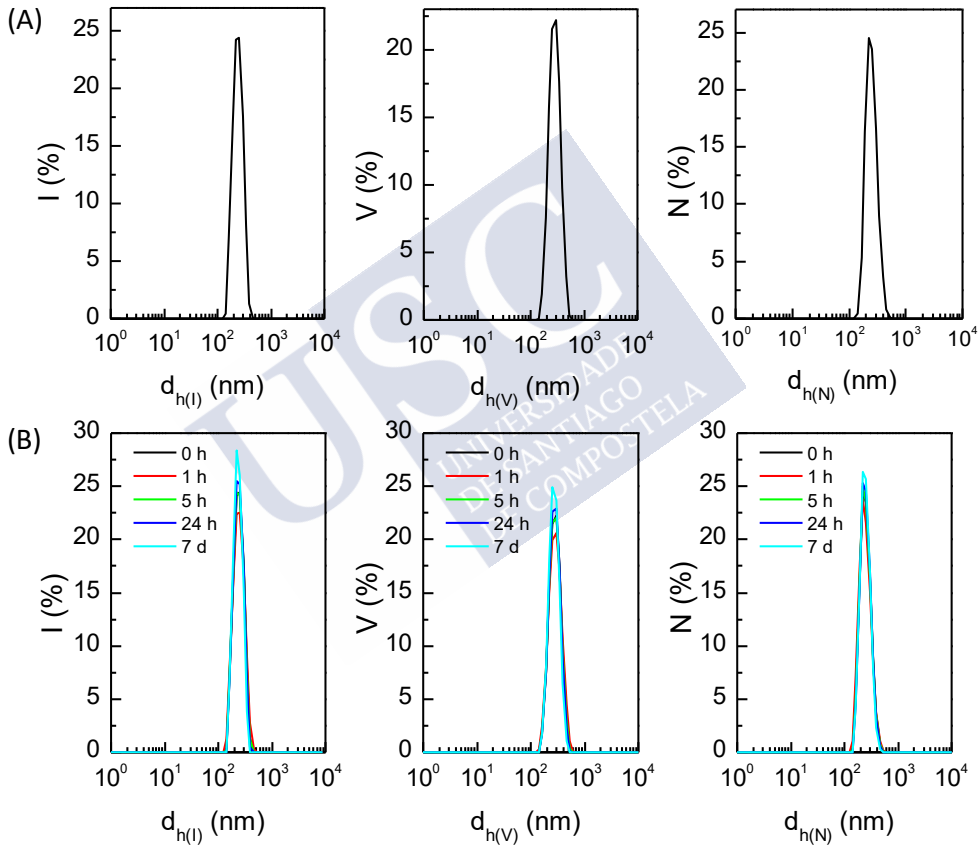

Figure S5.8. DLS spectra of NRs.

DLS population size distributions, given as intensity, volume and number-weighted distributions of NRs immediately dispersed in water (A), and (B) measured at different time points up to one week.

NRs								
Time	water		cell medium		ALF		ALF+10%FBS	
	$d_{h(N)}$ [nm]	PDI	$d_{h(N)}$ [nm]	PDI	$d_{h(N)}$ [nm]	PDI	$d_{h(N)}$ [nm]	PDI
0 h	252 ± 2	0.18	299 ± 8	0.22	268 ± 3	0.14	289 ± 6	0.12
1 h	249 ± 3	0.21	291 ± 9	0.24	273 ± 4	0.15	300 ± 7	0.21
5 h	251 ± 2	0.22	289 ± 11	0.24	278 ± 4	0.20	295 ± 7	0.20
24 h	252 ± 2	0.20	294 ± 10	0.30	292 ± 2	0.11	293 ± 9	0.19
7 days	250 ± 4	0.22	301 ± 10	0.35	296 ± 3	0.19	294 ± 8	0.22
Pd-NP								
Time	water		cell medium		ALF*		ALF+10%FBS	
	$d_{h(N)}$ [nm]	PDI	$d_{h(N)}$ [nm]	PDI	$d_{h(N)}$ [nm]	PDI	$d_{h(N)}$ [nm]	PDI
0 h	25 ± 1	0.16	50 ± 3	0.19	376 ± 15	0.23	58 ± 2	0.15
1 h	68 ± 2	0.20	53 ± 3	0.20	-		61 ± 3	0.21
5 h	113 ± 3	0.24	51 ± 3	0.20	-		61 ± 4	0.20
24 h	171 ± 10	0.27	49 ± 4	0.21	-		56 ± 3	0.19
48 h	362 ± 24	0.39	50 ± 3	0.22	-		54 ± 3	0.19
7 days	480 ± 25	0.41	49 ± 4	0.19	-		53 ± 4	0.20

**Pd-NPs aggregated immediately in ALF, leading to irreversible precipitation.*

Table S5.2. DLS measurements of the NRs and Pd-NPs overtime in different media. Hydrodynamic diameters d_h (mean value ± SD) as derived from DLS measurements of NRs and Pd-NPs dispersed in water, cell culture medium (DMEM supplemented with 10 % FBS), artificial lysosomal fluid (ALF), or ALF supplemented with 10 % FBS at different time points. SD values correspond to the standard deviation of the diameter mean value as obtained from several repetitions (n = 3) of the measurement. The PDI values are also given.

6.4.4. Quantification of Pd by inductively coupled plasma mass spectrometry (ICP-MS) and estimation of potentially active Pd

Quantification of Pd by ICP-MS. ICP-MS measurements were performed on an Agilent 7700x inductively coupled plasma mass spectrometer after acidic digestion of the particles in samples with aqua regia. To this end, 300 µL of fresh aqua regia (*i.e.* HCl 35 wt % and HNO_3 67 wt % in 3:1 volume ratio) was added to 50 µL of sample solution (NRs or Pd-NPs as control; both at the same concentration), and then the samples were left for digestion overnight. Afterwards 4.65 mL of HCl solution (2 wt % HCl) was added prior to their injection into ICP-MS being, thus, the total dilution sample in a factor of 100. External calibration was applied to quantify the amount of elemental Pd and Zn. External standards were prepared by diluting ICP-MS standards of all the ions in

the same background solution (2 wt % HCl) as the samples, measured by triplicate and used for obtaining the external calibration curves.

Results revealed that the total amount of Pd atoms used per reaction were: 8.9 μg (RSD = 1.0 %) for NRs and 9.1 μg (RSD = 1.4 %) for Pd-NPs (Table S5.3). This clearly indicates that when we are carrying out equivalent reactions with NRs and Pd-NPs (for comparison), we are using the same amount of Pd.

The amount of Pd per NR was determined from ICP-MS data; and considering that the empirical formula of ZIF8 is $C_8H_{10}N_4Zn$, which means that 1 mol of ZIF8 contains 1 mol of Zn. Therefore, the Pd amount in NR (i.e. Pd-ZIF8) could be determined by the following Eq. 7, where m_{Pd} = amount of ^{105}Pd obtained by ICP-MS; m_{Zn} = amount of ^{66}Zn obtained by ICP-MS; M_{Zn} = atomic mass of Zn (65.38 g/mol) and M_{ZIF8} = molecular mass of ZIF8 (227.58 g/mol).

$$\% \text{ Pd} = \frac{m_{Pd}}{m_{Pd} + m_{Zn} \cdot \frac{M_{ZIF8}}{M_{Zn}}} \cdot 100 \qquad \textbf{Eq. 7}$$

Applying this equation, we obtained that the percentage of total Pd in the NR is 3.8 wt%. It was also determined by ICP-MS that this wt% of Pd in the NR is the same after performing the reaction, which is a clear indication of the stability of the NRs during the catalytic reaction.

Cata-lyst	V_{cat} [μL]	$C_{particles}$ [nM]	V_{react} [μL]	c_{Zn} [μg/μL]*	c_{Pd} [μg/μL]*	m_{Zn} [μg]	$m_{Pd,total}$ [μg]	Pd total [wt %]
Pd-NPs	50	2	400	–	0.183	–	9.1	100
NRs	50	2	400	1.296	0.179	64.8	8.9	3.8

**Relative standard deviation (RSD) < 1.5%*

Table S5.3. Amount of Pd per reaction as derived from ICP-MS measurements.

Estimation of the Pd potentially active for catalysis. Whereas ICP-MS measurements give us the total amount of Pd contained in the NR, it is important to note that only the Pd atoms on the surface of the Pd-NP (located in the center of the NR) will be able to catalyse the reactions and therefore, only this fraction of Pd (hereinafter referred to as surface-Pd) is potentially active. We can estimate this surface-Pd as follows (*cf.,* Table S5.4).

First, we calculate the number of Pd atoms contained in a Pd-NP. The volume of a Pd-NP (V_{NP}) with a side length of 23.9 nm as determined from SEM images.

$V_{NP} = L^3 = (23.9 \text{ nm})^3 = 1.36 \cdot 10^4 \text{ nm}^3$

The structure is face-centered-cubic (fcc structure) with a lattice constant of 0.389 nm, being the volume of a unit cell ($V_{fcc\ cell}$).

$$V_{fcc\ cell} = (0.389\ nm)^3 = 0.059\ nm^3$$

Knowing that each unit cell contains 4 Pd atoms, the total number of Pd atoms in a single Pd-NP is

$$N_{Pd,\ cell} = (1.36 \cdot 10^4\ nm^3) / (0.059\ nm^3) \cdot 4 = 9.26 \cdot 10^5$$

2) Next, we calculate the number of Pd atoms on the surface of a Pd-NP. A Pd-NP is enclosed by 6 {100} facets, so the total surface area of a Pd-NP ($A_{nanocube}$) can be calculated as

$$A_{nanocube} = 6 \cdot L^2 = 6 \cdot (23.9\ nm)^2 = 3.43 \cdot 10^3\ nm^2$$

The lattice constant of the fcc unit cell is 0.389 nm, and each two-dimensional unit cell on the {100} facets contains two Pd atoms. Therefore, the total number of Pd atoms on the surface of a single nanocube ($N_{Pd,\ surface}$) can be calculated as

$$A_{fcc\ cell} = (0.389\ nm)^2 = 0.151\ nm^2$$
$$N_{Pd,\ surface} = (3.43 \cdot 10^3\ nm^2) / (0.151\ nm^2) \cdot 2 = 4.54 \cdot 10^4$$

3) Knowing the number of NRs used for the catalytic reaction we calculate the amount of surface-Pd per reaction. The total amount of Pd used per reaction is $8.94 \cdot 10^{-6}$ g as determined by ICP-MS. Thus, the total number of Pd atoms in the catalytic reaction is

$$N_{Pd} = (8.94 \cdot 10^{-6}\ g) / (106.42\ g/mol) \cdot (6.02 \cdot 10^{23}\ mol^{-1}) = 5.06 \cdot 10^{16}$$

The number of Pd-NPs involved in the catalytic reaction is (note that one nanocube contains $9.26 \cdot 10^5$ Pd atoms as calculated above)

$$N_{nanocube} = (5.06 \cdot 10^{16}) / (9.26 \cdot 10^5) = 5.46 \cdot 10^{10}$$

Note here that owing to the architecture of the NC particle (one Pd-NP in the center of one NR), the number of NRs involved in the reaction is the same as the number of Pd-NPs.

Thus, the actual concentration of NRs used per reaction (total volume 400 μL) is

n_{NR}= (5.46 ·10^{10}) / (6.022 ·10^{23}) = 9.07 ·10^{-14} mol of NR
C_{NR} = (9.07 ·10^{-14}) / (4 ·10^{-4}) = 2.3 ·10^{-10} M = **0.23 nM**

Regarding the fraction of Pd potentially active, the total number of Pd atoms on the surface of Pd-NPs used in the catalytic reaction is

$N_{total\ surface\text{-}Pd}$ = (5.46 ·10^{10}) · (4.54 ·10^{4}) = 2.71 ·10^{15}
$n_{total\ surface\text{-}Pd}$ = (2.71 ·10^{15}) / (6.022 ·10^{23}) = 4.5 ·10^{-9} mol

As the total volume of the reaction is 400 µL, the concentration of surface Pd in the reaction is ~ 10 µM.

Catalyst	V_{NP} [nm³]	$V_{fcc,cell}$ [nm³]	$N_{Pd,cell}$*	A_{NP} [nm²]	$A_{fcc,cell}$ [nm²]	$N_{Pd,surface}$#
Pd-NPs	1.36·10^{4}	0.059	9.26·10^{5}	3.43·10^{3}	0.151	4.54·10^{4}
NRs	1.36·10^{4}	0.059	9.26·10^{5}	3.43·10^{3}	0.151	4.54·10^{4}

Catalyst	$m_{Pd,total}$ [µg]	$m_{Surface\text{-}Pd}$ [µg]	$C_{Surface\text{-}Pd}$ [µM]
Pd-NPs	9.14	3.78·10^{-5}	10.1
NRs	8.94	3.69·10^{-5}	9.8

**Each unit cell with fcc structure contains 4 Pd atoms*
#Each two-dimensional unit cell on the {100} facets contains 2 Pd atoms
Table S5.4. Amounts of Pd (total and surface) per reaction as derived from ICP-MS measurements.

6.4.5. Evaluation of porous accessibility/porosity of NRs

The porosity and possibility of diffusion-controlled flow of molecules through the porous of the ZIF8 shell in NRs was evaluated using model fluorescent probes. To this end, NRs were incubated with two fluorescent probes: TAMRA and DOX (doxorubicin); and the amount loaded probes was quantified by fluorescence. NRs as dispersed in water (100 µL, 1 nM) were mixed with a solution of fluorescent probes in MeOH (10 µL, 1.5 mM), having thus 1.5 ·10^{5} probe/NC during the incubation, and the mixture was incubated for 4 h at RT Afterwards, NRs were quickly collected by centrifugation (1 min, 10,000 RCF), and the loaded fluorescent molecules were determined after digestion/destruction of the NRs in order to avoid errors in the quantification associated to potential fluorescence quenching and/or scattering/turbidity interference. For the digestion, the pellet of NR containing the fluorescent molecules were treated with 40 µL of 2% HCl solution for 15 min. Then, 10 µL of 2 M NaOH solution was added to neutralize the medium, plus 250 µL of water, and fluorescence measurement of this mixture was performed. The

concentration of TAMRA or DOX loaded was determined by interpolation of the measured fluorescence intensity (I) to a previously constructed analytical calibration curve (Figure S5.9). This led to a value (mean ± standard deviation, n = 2) of (4.24 ± 0.08) ·10^4 TAMRA per NR and (7.58 ± 0.06) ·10^4 DOXO per NR (Table S5.5).

probe	$N_{probe/NR}$ (incubated)	$N_{probe/NR}$ (loaded)	% loading
TAMRA	1.5·10^5	(4.24 ± 0.08) ·10^4	28.3 ± 0.8
DOX	1.5·10^5	(7.58 ± 0.06) ·10^4	50.5 ± 0.6

Table S5.5. Determination of loading percentage of two fluorescent probes into NRs after 4 h of incubation.

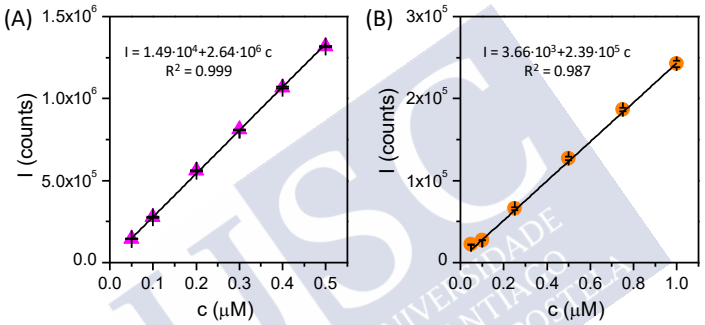

Figure S5.9. Calibration curves of TAMRA (A) and DOX (B)

Measurements were done in water from fluorescence measurements: for (A) TAMRA $\lambda_{exc}/\lambda_{em}$=550/580 nm and for (B) DOXO $\lambda_{exc}/\lambda_{em}$=480/588 nm. Fluorescence intensity (*I*) at the maximum emission peak as a function of probe concentration c is plotted and calibration equation is obtained by fitting a linear regression line to the collected data; R^2 is the coefficient of determination.

6.4.6. General procedures of the propargyl uncaging reactions

*Propargyl group uncaging of substrates **1** and **3** promoted by NR or Pd-NPs.* **1** or **3** (8 µL, 0.5 mM stock solution in MeOH) was added to a H_2O:MeOH 9:1 solution (342 µL) in a 1.5 mL vial (containing a stirring bar) followed by addition of an aqueous solution of Pd-NPs or NRs (50 µL, 2 nM; this corresponds to 10 µM of surface-Pd). The influence of the catalyst concentration was also evaluated by varying the amount of the aqueous solution of Pd-NPs or NRs added. The vial was sealed with a screw cap and the reaction mixture was stirred (400 RPM) at 37 °C. After overnight (15 h), NRs were collected by centrifugation (7000 RCF, 10 min), and the supernatant was separated. The precipitate was washed once with 400 µL of a 9:1 H_2O:MeOH solution, centrifuged again (7000 RCF, 10 min), and the supernatant was separated and mixed with the first supernatant. Finally, this

supernatant was analyzed by fluorescence to quantify the obtained amount of **2** or **4** respectively (Table S5.6, Figure 5.6), *cf.* calibration curves in Figure S5.4.

*Propargyl group uncaging of substrate **5** promoted by NR*. **5** (8 µL, 0.5 mM stock solution in MeOH) was added to a PBS:MeOH 8:2 solution (342 µL) in a 1.5 mL vial (containing a stirring bar) followed by addition of an aqueous solution of NRs (50 µL, 2 nM; this is the concentration of NRs). The vial was sealed with a screw cap and the reaction mixture was stirred (400 RPM) at 37 °C. After overnight (15 h), the NRs were collected by centrifugation (7000 RCF, 10 min), and the supernatant was separated. The precipitate was washed once with 400 µL of an 8:2 PBS:MeOH solution, centrifuged again (7000 RCF, 10 min), and the supernatant was separated and mixed with the first supernatant. Finally, this supernatant was analysed by fluorescence to quantify the amount of **6** obtained (Table S5.6, Figure 5.6), *cf.* calibration curve in Figure S5.4.

Catalyst	Surface Pd [µM]	Substrate	Substrate [µM]	Product	Product [µM]	Yield [%]
NRs	1	**1**	10	**2**	3.70 ± 0.08	37.0 ± 1.2
NRs	5	**1**	10	**2**	8.92 ± 0.14	89.2 ± 1.4
NRs	10	**1**	10	**2**	9.70 ± 0.13	97.0 ± 1.3
NRs	15	**1**	10	**2**	9.85 ± 0.15	98.5 ± 1.5
NRs	10	**1**	10	**2**	9.20 ± 0.14	92.0 ± 1.4
Pd-NPs	10	**1**	10	**2**	1.90 ± 0.45	19.0 ± 4.5
ZIF8#	0	**1**	0	n.r.*	n.r.*	n.r.*
NRs	10	**3**	10	n.r.*	n.r.*	n.r.*
Pd-NPs	10	**3**	10	**4**	1.54 ± 0.18	15.4 ± 1.8
NRs	10	**1+3**	10+10	**2**	5.40 ± 0.37	54.0 ± 3.7
NRs	10	**5**	10	**6**	8.23 ± 0.10	82.3 ± 1.0

**n.r. : no reaction; #ZIF8 nanoparticles equivalent to NRs, but without the Pd core.*

Table S5.6. Depropargylation reaction yields.
Reaction conditions and yields of the depropargylation of several substrates promoted by NRs or Pd-NPs; as control, we also used ZIF8 nanoparticles without the Pd core.

*Propargyl group uncaging of substrate **1** in the presence of **3** promoted by NR.* **1** (8 µL, 0.5 mM stock solution in MeOH) and **3** (8 µL, 0.5 mM stock solution in MeOH) were added to a H_2O:MeOH 9:1 solution (334 µL) in a 1.5 mL vial (containing a stirring bar) followed by addition of an aqueous solution of NRs (50 µL, 2 nM; this is the concentration of NRs). The vial was sealed with a screw cap and the reaction mixture was stirred (400 RPM) at 37 °C. After overnight (15 h),

the NRs were collected by centrifugation (7000 RCF, 10 min), and the supernatant was separated. The precipitate was washed once with 400 µL of a 9:1 H_2O:MeOH solution, centrifuged again (7000 RCF, 10 min), and the supernatant was separated and joined with the first supernatant. Finally, this supernatant was analysed by fluorescence to quantify the obtained amount of **2** and **4** (Table S5.6), *cf.* calibration curve in Figure S5.4.

Influence of the washing step after reaction. In order to minimize the number of steps in the general procedure from the reaction to the determination of the generated product, the influence of the washing step after the reaction was evaluated. As described above, the general separation and purification procedure consisted of separating NRs by centrifugation after the reaction, washing the particles once with the same medium as used for carrying out the reaction, and finally determining the amount of product formed by measuring the fluorescence in the total supernatant. The need of this washing step was evaluated by performing the procedure with and without this The obtained data are presented in Table S5.7, in which it is clear that depending on the substrate (**1** or **5**), and thus of the affinity of the generated product with the pores of the ZIF8 structure (*i.e.*, hydrophobicity/hydrophilicity, polarity, and so on), this step of washing is important for achieving a quantitative determination or not.

Catalyst	SurfacePd [µM]	Substrate	Substrate [µM]	Product	Yield (%)	
					without washing	with washing
NRs	10	**1**	10	**2**	93.0 ± 3.8	97.0 ± 1.3
NRs	10	**5**	10	**6**	60.0 ± 6.1	85.7 ± 2.8

Table S5.7. Influence of the washing step after reaction.
Effect of the washing step on the quantitative yield determination of the depropargylation of two different substrates promoted by NRs.

*Leakage of Pd during the uncaging of coumarin **2***. The stability of the Pd-NPs inside the ZIF8 structure was studied by evaluating the potential leakage of Pd from the NRs during the reaction. To this end, the reaction was performed under the optimized conditions described above (used during the reaction of **1** as a model) and the amount of Pd released to the supernatant after the reaction was quantified by ICP-MS. For comparison, the same was done with the CTAB-protected Pd-NPs. Data presented in Table S5.8 are expressed in ppm (i.e., mg/L), showing that the amount of Pd released was much higher in the case of working with Pd-NPs whilst the leaching in the case of NRs was negligible. As we know the amount of total Pd in both Pd-NPs and NRs, the amount of released Pd was also expressed as the percentage of the total Pd. These results clearly indicate that the Pd-NPs are well protected inside the ZIF8 structure, avoiding not only

their potential passivation by biomolecules as demonstrated above, but also their surface damage leading to the irreversible leaching of Pd from the catalyst.

Catalyst	Surface Pd [μM]	Pd released [ppm]	% Pd released
NRs	10	0.146 ± 0.011	0.081 ± 0.008
Pd-NPs	10	30.4 ± 2.0	16.6 ± 1.1

Table S5.8. Leakage of Pd during the depropargylation reaction of 1.
Dependency on the catalyst used as derived from ICP-MS analysis. Pd leaking is represented in ppm of Pd released.

Calculation of turnover number. As calculated in a previous section, the concentration of the catalyst (surface-Pd) used in the reaction under the optimized conditions was 10 μM. Knowing that the total volume of the reaction is 400 μL, this corresponds to $4 \cdot 10^{-9}$ mol of catalyst per reaction. The calculation of the yield of the reactions, and therefore, the amount of substrate converted to the desired product, allows us to calculate the TON by using the following Eq. 8.

$$\text{TON} = \frac{\text{moles of desired product formed}}{\text{moles of catalyst}} \qquad \textbf{Eq. 8}$$

We determined the TON values as function of the amount of catalyst used and maintaining constant the amount of substrate (see Table S5.9).

Catalyst SurfacePd [μM]	Substrate	Substrate [μM]	Yield [%]	Product [μM]	TON
15	**1**	10	98.5 ± 1.5	9.85 ± 0.15	0.66 ± 0.01
10	**1**	10	97.0 ± 1.3	9.70 ± 0.13	0.97 ± 0.01
5	**1**	10	89.2 ± 1.4	8.92 ± 0.14	1.78 ± 0.04
1	**1**	10	37.0 ± 1.2	3.70 ± 0.08	3.70 ± 0.11
1	**1**	10	99.6 ± 1.1	9.96 ± 0.11	9.96 ± 0.15
15	**5**	10	90.8 ± 1.5	9.08 ± 0.15	0.60 ± 0.01
10	**5**	10	82.3 ± 1.0	8.23 ± 0.10	0.82 ± 0.01
5	**5**	10	65.6 ± 1.2	6.56 ± 0.12	1.31 ± 0.03
1	**5**	10	26.6 ± 0.9	2.66 ± 0.09	2.66 ± 0.13

Table S5.9. TON values for the depropargylation reaction of 1 and 5.
Different amounts of NRs were used. In all cases, the reactions were carried out overnight at 37 °C, except in one case in which the reaction was performed for 7 days.

*Kinetics of the propargyl uncaging reaction **1**→**2***: To study the kinetics of the reaction of substrate **1**, this was evaluated as a function of time. Several reactions

were carried out in parallel under identical conditions and each one was stopped at different time points. To this end, **1** (8 µL, 0.5 mM stock solution in MeOH) was added to a H_2O:MeOH 9:1 solution (342 µL) in a 1.5 mL HPLC vial (containing a stirring bar) followed by addition of an aqueous solution of NRs (50 µL, 2 nM; this is the concentration of NRs). The vial was sealed with a screw cap and the reaction mixture was stirred (400 RPM) at 37 °C. After different times, the reaction was stopped and the NRs were collected by centrifugation (7000 RCF, 10 min), and washed once with 400 µL of a H_2O:MeOH 9:1 solution. All the supernatants were collected and the fluorescence from product **2** was measured. The fluorescence intensity of **2** was plotted versus time (see Figure S5.10) to obtain the kinetics curve. Moreover, the kinetics of the reaction of substrate **1** was evaluated also in the presence of **3** as interference, knowing that the uncaging of substrate **3** is not promoted by the NRs. In this case, 10 µM of **3** (8 µL, 0.5 mM stock solution in MeOH) was added together with 10 µM of **1** (8 µL, 0.5 mM stock solution in MeOH) to the reaction mixture.

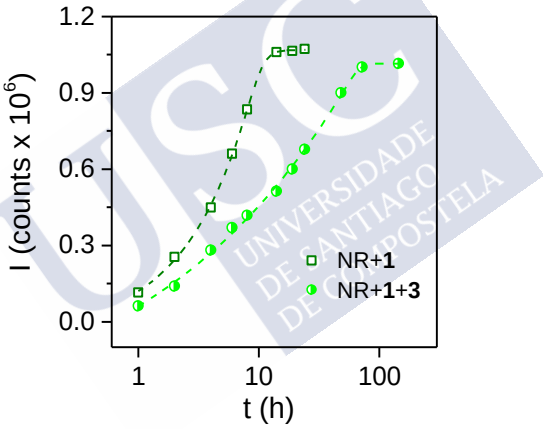

Figure S5.10. Kinetics of the coumarin 2 uncaging reaction.
Experiments were done either by mixing NR with **1** in the absence (green) or presence of **1** eq. of **3** (light green). Dashed lines correspond to logistic fitting curves obtained with Originlab; $R^2 > 0.99$.

In order to figure out a potential reason why substrate **3** is not catalysed by NRs, and additionally not only slows down the reaction kinetics of **1** but also a change of the slope in the kinetic curve takes place from 10 h, we carried out studies of NRs after reaction by DLS and ξ-potential. As shown in Table S5.10, after the reaction of NRs with substrate **3** the hydrodynamic size of NRs increased, and a decrease of the negative charge was also observed. This could be attributed to a binding of some molecules of substrate **3** on the surface of NRs, avoiding their diffusion into the NR core, and also partially blocking the diffusion of substrate **1**. In contrast, substrate **1** did not cause any significant change in the NRs.

Parameter	Before reaction	After reaction with	
		1	3
d_h [nm]	249 ± 3	252 ± 4	306 ± 3
PDI	0.10	0.12	0.11
ξ [mV]	-34.5 ± 0.5	-34.4 ± 0.8	-26.5 ± 0.7

Table S5.10. Hydrodynamic diameters of NR after uncaging reactions.
Data shown, d_h (mean value ± SD), are derived from DLS measurements of NRs dispersed in the reaction mixture before and after reaction with substrate **1** or **3**. SD values correspond to the standard deviation of the diameter mean value as obtained from several repetitions (n = 3) of the measurement. The PDI and ξ-potential values are also given.

Reusability of NRs: In order to investigate the potential reuse of NRs, after a reaction NRs were collected by centrifugation, washed twice with water to remove potential remaining substrate/products, and redispersed in a fresh aqueous solution containing the substrate for a new run. The supernatants from each use were measured by fluorescence to quantify the amount of generated product. Using substrate **1** the same procedure was carried out with Pd-NPs in order to compare the stability of NRs with that of Pd-NPs. Data presented in Table S5.11 clearly shows that the loss of efficiency of NRs for promoting the depropargylation reaction was negligible after four runs.

Catalyst	Surface Pd [μM]	Substrate	Substrate [μM]	Product	Yield (%) / Run number			
					1	2	3	4
NRs	10	**1**	10	**2**	97.0 ± 3.1	96.1 ± 2.5	98.0 ± 2.1	95.4 ± 3.4
Pd-NPs	10	**1**	10	**2**	19.0 ± 1.5	9.2 ± 2.1	5.0 ± 2.8	2.1 ± 2.7
NRs	10	**5**	10	**6**	80.3 ± 2.9	81.1 ± 3.2	77.9 ± 4.7	71.0 ± 6.1

Table S5.11. Depropargylation yields of two different substrates promoted by NRs or Pd-NPs after successive runs of the catalyst.

Performance of the NRs as "continuous" nanoreactors. The performance of the NRs for promoting the depropargylation reaction of **5** in three successive steps was studied as follows: for 1 cycle, **5** (8 μL, 0.5 mM stock solution in MeOH) was added to a PBS:MeOH 8:2 solution (342 μL) in a 1.5 mL HPLC vial (containing a stirring bar) followed by addition of an aqueous solution of NRs (50 μL, 2 nM; this is the concentration of NRs). The vial was sealed with a screw cap and the reaction mixture was stirred (400 RPM) at 37 °C. After 18 h, the NRs were collected by centrifugation (7000 RCF, 10 min), and the supernatant was

separated. The precipitate was washed once with 400 µL of a 8:2 PBS:MeOH solution, centrifuged again (7000 RCF, 10 min), and the supernatant was separated and mixed with the first supernatant. The generated product in the supernatant was measured by fluorescence. For two successive cycles, the reaction was carried out in identical conditions and after 18 h, instead of purified the product, another shot of **5** (8 µL, 0.5 mM stock solution in MeOH) was added to the reaction mixture. The mixture was left to react 18 h, with stirring and at 37 °C, and afterwards the total generated product was separated and quantify as described in first cycle. The same was repeated with one more addition for 3 cycles. Results are presented in Table S5.12.

Catalyst	surfacePd [µM]	Cycles Number	Substrate [µM]	Product	Cumulative Yield [%]
NRs	10	1	10	**2**	94.6 ± 5.3
NRs	10	2	10 + 10	**2**	178.4 ± 6.8
NRs	10	3	10 + 10 + 10	**2**	250.6 ± 8.1

Table S5.12. Cumulative depropargylation yield of 5 promoted by NRs after successive reuses of the catalyst.

6.4.7. Performance of the reactions in the presence of bio-additives

*Reaction of substrate **1** in the presence of additives.* The reaction was carried out as described in the previous section, but adding the following additives (Table S5.13): (i) different amounts of BSA (for a final concentration in the total volume of 40 µM, 80 µM, or 150 µM); (ii) 10% DMEM (supplemented with 10 % FBS), and in this case the reaction was studied after 15 h and 72 h; (iii) 5 mg/mL of cell lysate.

*Reaction of substrate **5** in the presence of additives.* The reaction was carried out as described in the previous section, but adding the following additives (Table S5.13): (i) different amounts of BSA (for a final concentration in the total volume of 40 µM, 80 µM, or 150 µM); (ii) 5 mg/mL of cell lysate.

Cell lysate preparation. For the preparation of the HeLa cells lysates, $3 \cdot 10^6$ exponentially growing HeLa cells were washed twice with PBS, scrapped with a rubber policeman in 0.5 mL of PBS, and sonicated intensely for 2 rounds of 1 min with a 30 second cooling period in between. The protein concentration of the lysates was quantified by DCTM Protein Assay (BioRad) and equalised to 10 mg/mL for reproducibility among experiments.

Catalyst	Surface Pd [μM]	Additive	Substrate	Substrate [μM]	Product	Yield [%]
NRs	10	-	**1**	10	**2**	97.0 ± 1.3
NRs	10	BSA, 40 μM	**1**	10	**2**	55.0 ± 3.0
NRs	10	BSA, 80 μM	**1**	10	**2**	53.0 ± 2.9
NRs	10	BSA, 150 μM	**1**	10	**2**	33.0 ± 3.5
Pd-NPs	10	-	**1**	10	**2**	19.0 ± 1.5
Pd-NPs	10	BSA, 40 μM	**1**	10	**2**	9.0 ± 1.6
Pd-NPs	10	BSA, 80 μM	**1**	10	**2**	7.0 ± 2.0
Pd-NPs	10	BSA, 150 μM	**1**	10	**2**	7.0 ± 2.1
NRs	10	DMEM, 10%, 15h	**1**	10	**2**	22.0 ± 3.2
NRs	10	DMEM, 10%, 72h	**1**	10	**2**	47.0 ± 3.7
NRs	10	Lysate, 5 mg/mL	**1**	10	**2**	19.0 ± 2.8
NRs	10	-	**5**	10	**6**	84.8 ± 2.5
NRs	10	BSA, 20 μM	**5**	10	**6**	62.8 ± 2.3
NRs	10	BSA, 40 μM	**5**	10	**6**	54.1 ± 2.9
NRs	10	BSA, 8 μM	**5**	10	**6**	23.8 ± 3.9
NRs	10	Lysate, 5 mg/mL	**5**	10	**6**	22.5 ± 4.1

Table S5.13.Depropargylation reaction yields of 5 and 6 promoted by NRs or Pd-NPs in the presence of different bioadditives.

6.4.8. Cells studies

Pd content per cell. ICP-MS was used to quantify the average Pd content per cell, which we used to estimate the number of Pd-NPs or NRs per cell (Table S5.14); see calculations in section 6.4.4.

Particle	Pd per particle [μg]*	Cells [No.]	Particles per cell (added)	ICP-MS		
				Pd per cell [μg]	Particle per cell [No.]	% particle internalization#
Pd-NPs	$1.7 \cdot 10^{10}$	$6.5 \cdot 10^{5}$	$5.6 \cdot 10^{3}$	$1.2 \cdot 10^{-8} \pm 8.9 \cdot 10^{-11}$	71 ± 1	**0.5**
NRs	$1.7 \cdot 10^{10}$	$6.3 \cdot 10^{5}$	$5.8 \cdot 10^{3}$	$2.0 \cdot 10^{-8} \pm 2.5 \cdot 10^{-10}$	120 ± 1	**0.8**

**See section IV. #Assuming particles retain their Pd original content inside cells.*

Table S5.14. Amounts of Pd per cell and particle uptake % (measured-to-added) as derived from ICP-MS measurements.

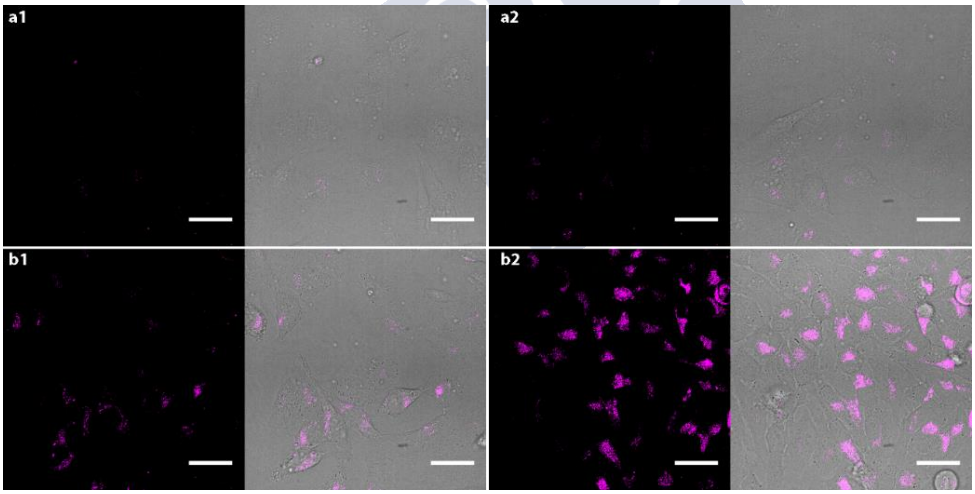

Figure S5.11. 6 production with NR-preloaded cells (using 2.5 μM of 5).
Collage of confocal microscopy images (left: pink channel; right: merged pink + bright-field) for the production of **6** after 6 h incubation with NR-preloaded cells (using 2.5 μM of **5**). a1,a2) Controls without NRs. b1,b2) Two examples using NR-preloaded cells as previously discussed. Scale bars correspond to 40 μm (60X).

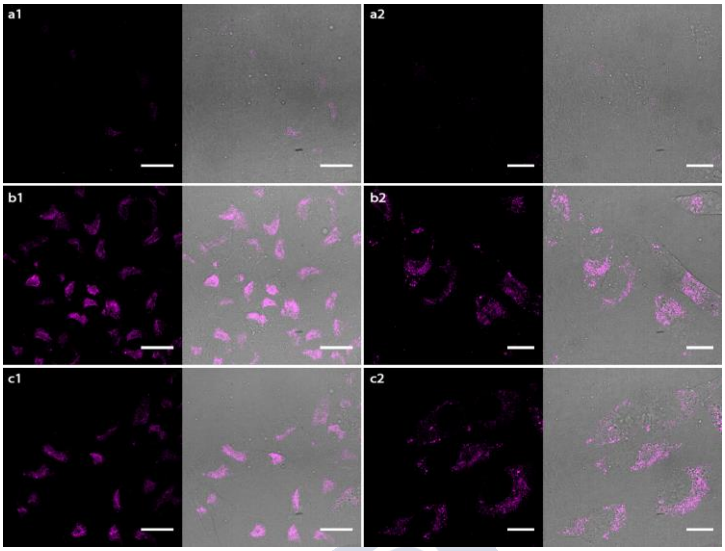

Figure S5.12. 6 production with NR-preloaded cells (using 10 μM of 5).
Collage of confocal microscopy images (left: pink channel; right: merged pink + bright-field) for the production of **6** after 1 h incubation with NR-preloaded cells (using 10 μM of **5**). a1,a2)Controls without NRs (a1: 60X; a2: 100X). b1,c1) Two examples using NR-preloaded cells as previously discussed (60X). b2,c2) Two examples using NR-preloaded cells as previously discussed (100X). Scale bars correspond to 20 μm (100X) or 40 μm (60X).

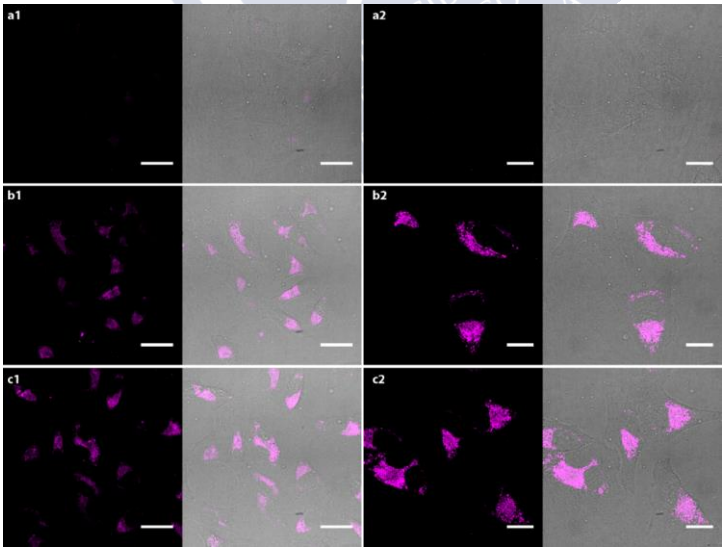

Figure S5.13. 6 production with NR-preloaded cells after 3 hours of incubation.
Collage of confocal microscopy images (left: pink channel; right: merged pink + bright-field; 60X) for the production of **6** after 3 h incubation with NR-preloaded cells (using 10 μM of **5**). a1,a2) Controls without NRs (a1: 60X; a2: 100X). b1-c1) Two examples using NR-preloaded cells as previously discussed (60X). b2-c2) Two examples using NR-preloaded cells as previously discussed (100X). Scale bars correspond to 20 μm (100X) or 40 μm (60X).

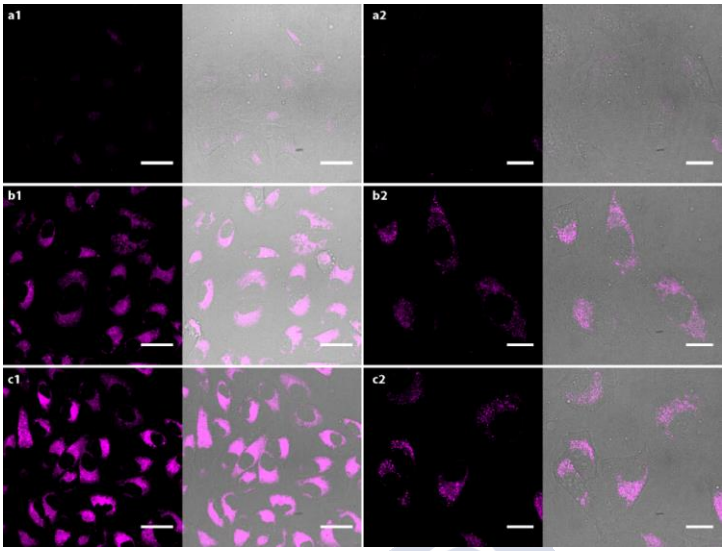

Figure S5.14. 6 production with NR-preloaded cells after 6 hours of incubation.
Collage of confocal microscopy images (left: pink channel; right: merged pink + bright-field) for the production of **6** after 6 h incubation with NR-preloaded cells (using 10 μM of **5**). a1,a2) Controls without NRs (a1: 60X; a2: 100X). b1-c1) Two examples using NR-preloaded cells as previously discussed (60X). b2-c2) Two examples using NR-preloaded cells as previously discussed (100X). Scale bars correspond to 20 μm (100X) or 40 μm (60X).

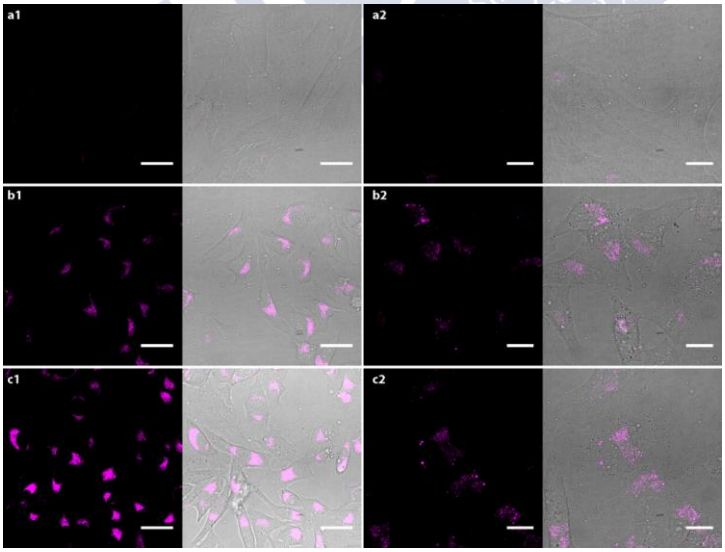

Figure S5.15. 6 production with NR-preloaded cells after 24 hours of incubation.
Collage of confocal microscopy images (left: pink channel; right: merged pink + bright-field) for the production of **6** after 24 h incubation with NR-preloaded cells (using 10 μM of **5**). a1-a2) Controls without NRs (a1: 60X; a2: 100X). b1-c1) Two examples using NR-preloaded cells as previously discussed (60X). b2-c2) Two examples using NR-preloaded cells as previously discussed (100X). Scale bars correspond to 20 μm (100X) or 40 μm (60X).

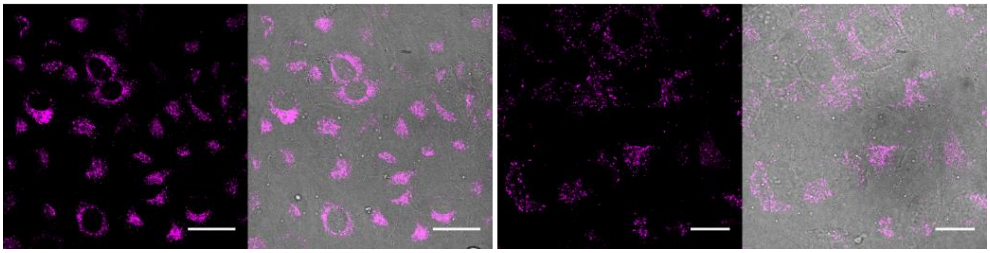

Figure S5.16. Cell controls incubated with 6.

Collage of confocal microscopy images (left: fluorescence channel; right: merged fluorescence + bright field; left, 60X, and right, 100X) for the incubation of **6** with Pd-free cells; cells were incubated with **6** (0.2 μM) for ~1 h. Before microscope inspection, cells were washed to remove extracellular probes. Scale bars correspond to 20 μm (100X) or 40 μm (60X)

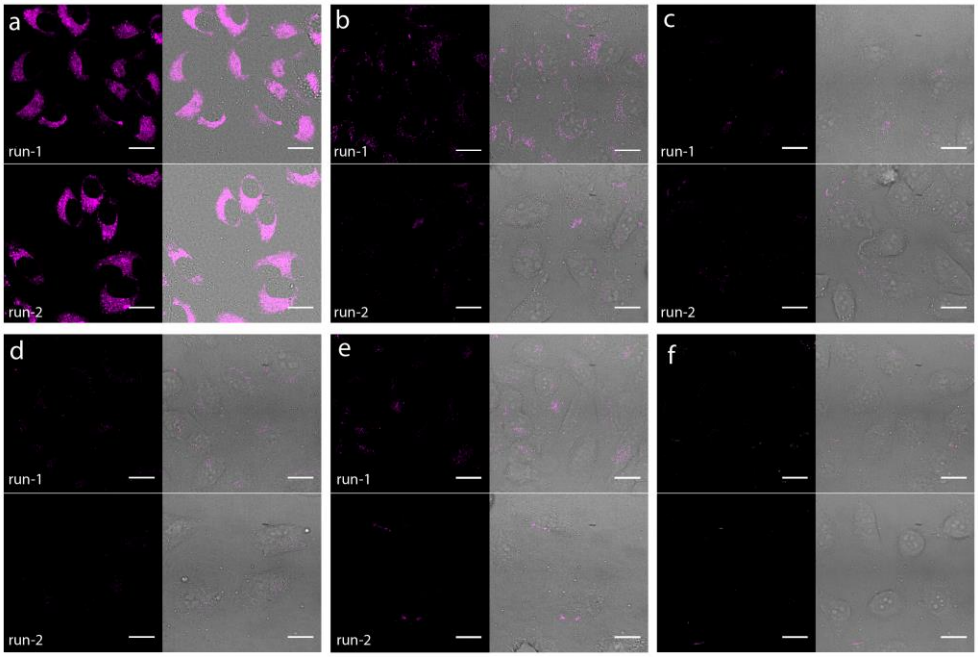

Figure S5.17. 6 production comparison with different catalysts.

Collage of confocal microscopy images (left: pink channel; right: merged pink + bright-field; top: first generation run; bottom: second generation run using the same catalyst-preloaded cells) for the production of **6**, using cells preloaded with a) NR (50 pM ≈ 2 μM in surface Pd, overnight); b) Pd-NP (50 pM ≈ 2 μM in surface Pd, overnight); of discrete Pd complexes c) **Pd-1**; d) **Pd-2**; or e) **Pd-3**, which were incubated with **5** (10 μM) for ~ 6 h before microscope inspection. f) Control experiments using "empty" cells (Pd "free" cells). Scale bars correspond to 20 μm. All these experiments were carried out using the same experimental conditions.

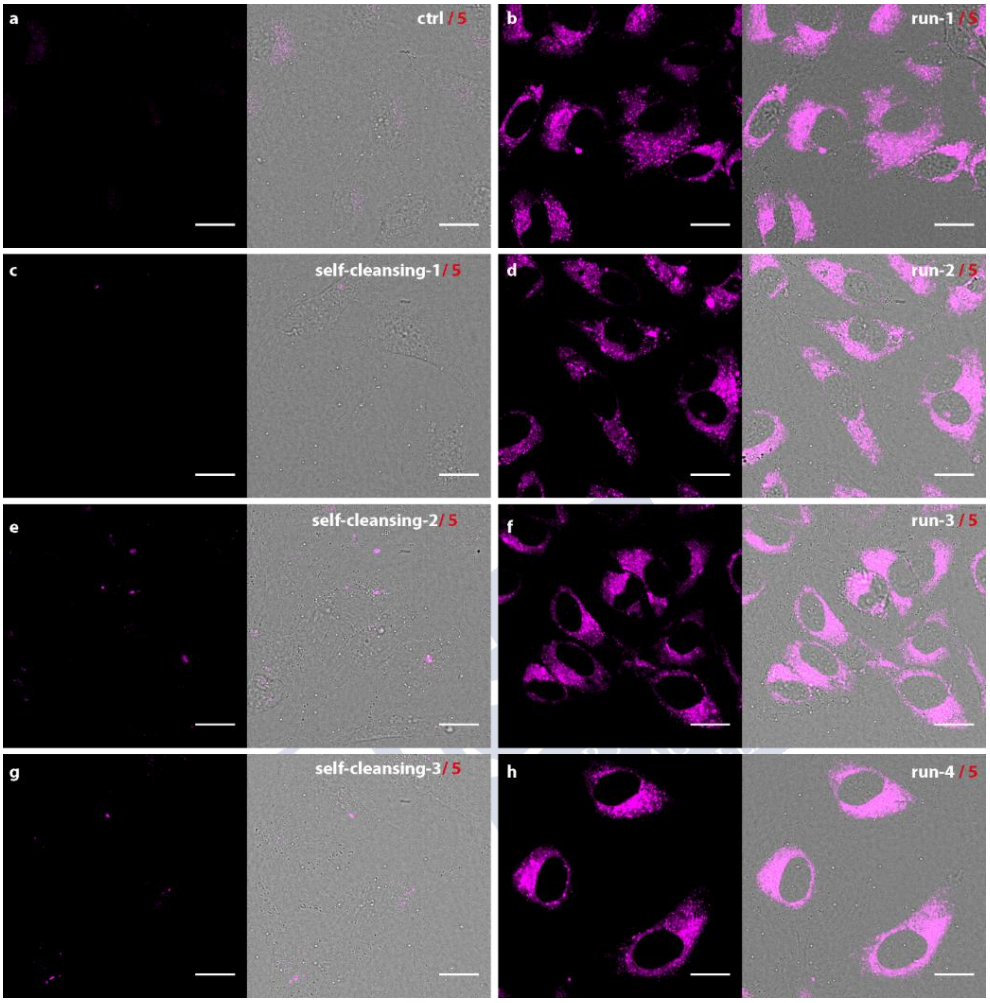

Figure S5.18. Intracellular recycling.

Collage of confocal microscopy images (left: pink channel; right: merged pink + bright-field). a) Control without NRs and the addition of substrate **5** (20 μM). b-g) First, second and third generation runs using the same NR-preloaded cells and recorded by confocal microscopy. b,d,f) Generation of **6** after 3 h incubation of **5** (20 M). c,e,g) 3 h self-cleansing. h) Fourth reaction cycle. Scale bars correspond to 20 μm.

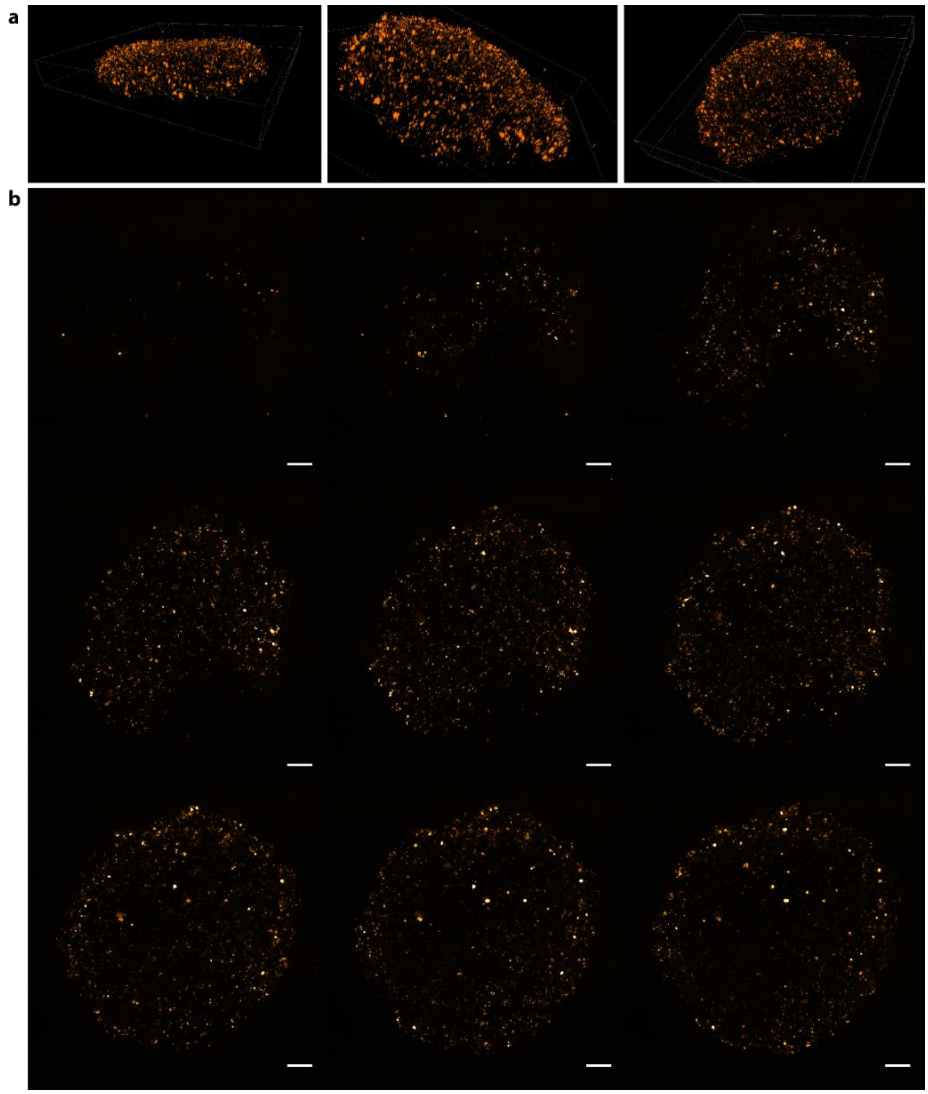

Figure S5.19. NR-TAMRA labeled loaded cell spheroid

Collage of confocal images of 3D spheroids of HeLa cells loaded with TAMRA-labelled NRs. a) Three different views of a 3D reconstruction of a NR-loaded spheroid with diameter ~ 1 μm. b) Different stacks of the same spheroid. Scale bars correspond to 100 μm

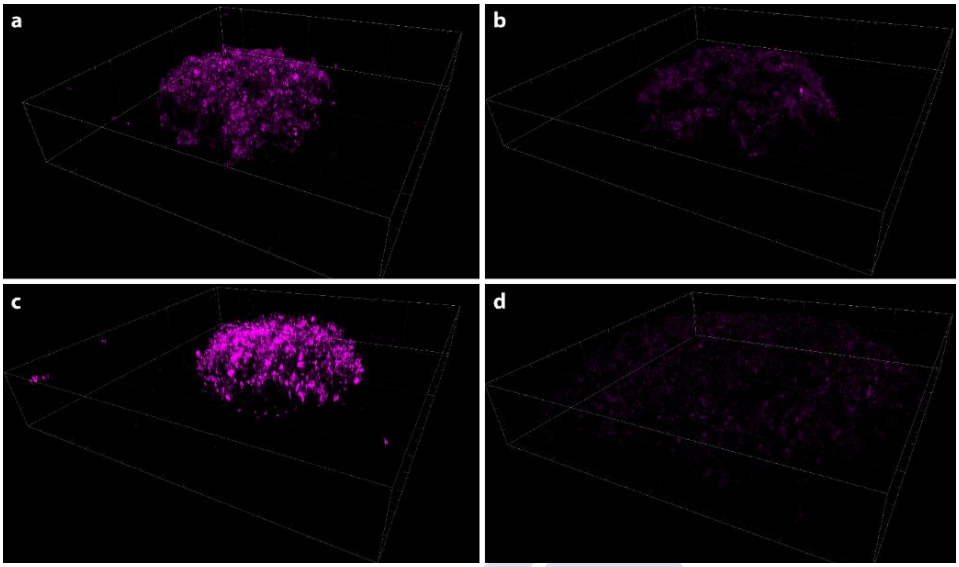

Figure S5.20. Intracellular recycling in 3D cell spheroids.
3D reconstructions of spheroids of NR-preloaded HeLa cells treated with the substrate **5**. a) First generation of **6** after 24 h incubation of **5** (20 μM). b) 24 h self-cleansing. c) Second generation of **6** after 24 h incubation of **5** (20 μM). d) Control experiment of "empty" (Pd "free") spheroids incubated during 24 h with substrate **5** (20 μM). All these experiments were carried out using the same experimental conditions and acquisition settings.

7. REFERENCES

1. NASA Nanotechnology.
2. Alexander T. Florence, D. A., Colloidal and coarse lyophobic dispersions. In *Physiochemical Principles of Pharmacy*, Macmillan International Higher Education: 1988.
3. Feynman, R. P., There's Plenty of Room at the Bottom American Physical Society: 1959.
4. Yoffe, A. D., Low-dimensional systems: Quantum size effects and electronic properties of semiconductor microcrystallites (zero-dimensional systems) and some quasi-two-dimensional systems. *Advances in Physics* **2002,** *51* (2), 799-890.
5. Noginov, M. A.; Zhu, G.; Gavrilenko, V. I., Sensitized nonlinear emission of gold nanoparticles. *Opt. Express* **2007,** *15* (24), 15648-15655.
6. Ramsden, J. J.; Freeman, J., The nanoscale. *Nanotechnology Perceptions* **2009,** *5*, 3-25.
7. Liong, M.; Lu, J.; Kovochich, M.; Xia, T.; Ruehm, S. G.; Nel, A. E.; Tamanoi, F.; Zink, J. I., Multifunctional Inorganic Nanoparticles for Imaging, Targeting, and Drug Delivery. *ACS Nano* **2008,** *2* (5), 889-896.
8. Nam, J.; Won, N.; Bang, J.; Jin, H.; Park, J.; Jung, S.; Jung, S.; Park, Y.; Kim, S., Surface engineering of inorganic nanoparticles for imaging and therapy. *Advanced Drug Delivery Reviews* **2013,** *65* (5), 622-648.
9. Jaiswal, J. K.; Simon, S. M., Potentials and pitfalls of fluorescent quantum dots for biological imaging. *Trends in Cell Biology* **2004,** *14* (9), 497-504.
10. Porov, P.; Chandel, V. S.; Manohar, R., Dielectric and Electro-Optical Properties of Ceramic Nanoparticles Doped Liquid Crystals. *Transactions on Electrical and Electronic Materials* **2016,** *17* (2), 69-78.
11. Wilhelm, S., Perspectives for Upconverting Nanoparticles. *ACS Nano* **2017,** *11* (11), 10644-10653.
12. Marinho, T.; Costa, P.; Lizundia, E.; Costa, C. M.; Corona-Galván, S.; Lanceros-Méndez, S., Ceramic nanoparticles and carbon nanotubes reinforced thermoplastic materials for piezocapacitive sensing applications. *Composites Science and Technology* **2019,** *183*, 107804.
13. E. Rokhvarger, A.; A. Chigirinsky, L. Sintered ceramic composite lead with superconductive nano-architecture. 2004.
14. Polo, E.; Araban, V.; Pelaz, B.; Alvarez, A.; Taboada, P.; Mahmoudi, M.; del Pino, P., Photothermal effects on protein adsorption dynamics of PEGylated gold nanorods. *Applied Materials Today* **2019,** *15*, 599-604.
15. Zhang, T.; Hartl, C.; Frank, K.; Heuer-Jungemann, A.; Fischer, S.; Nickels, P. C.; Nickel, B.; Liedl, T., 3D DNA Origami Crystals. *Advanced Materials* **2018,** *30* (28), 1800273.
16. Lambert, K.; Geyter, B. D.; Moreels, I.; Hens, Z., PbTe|CdTe Core|Shell Particles by Cation Exchange, a HR-TEM study. *Chemistry of Materials* **2009,** *21* (5), 778-780.
17. Carrillo-Carrión, C.; Martínez, R.; Navarro Poupard, M. F.; Pelaz, B.; Polo, E.; Arenas-Vivo, A.; Olgiati, A.; Taboada, P.; Soliman, M. G.; Catalán, Ú.; Fernández-Castillejo, S.; Solà, R.; Parak, W. J.; Horcajada, P.; Alvarez-Puebla, R. A.; del Pino, P., Aqueous Stable Gold Nanostar/ZIF-8 Nanocomposites for Light-Triggered Release of Active Cargo Inside Living Cells. *Angewandte Chemie International Edition* **2019,** *58* (21), 7078-7082.
18. He, P.; Fang, Y.; Yu, X.-Y.; Lou, X. W., Hierarchical Nanotubes Constructed by Carbon-Coated Ultrathin SnS Nanosheets for Fast Capacitive Sodium Storage. *Angewandte Chemie International Edition* **2017,** *56* (40), 12202-12205.
19. Saccà, B.; Meyer, R.; Erkelenz, M.; Kiko, K.; Arndt, A.; Schroeder, H.; Rabe, K. S.; Niemeyer, C. M., Orthogonal Protein Decoration of DNA Origami. *Angewandte Chemie International Edition* **2010,** *49* (49), 9378-9383.
20. Martínez-González, R.; Estelrich, J.; Busquets, A. M., Liposomes Loaded with Hydrophobic Iron Oxide Nanoparticles: Suitable T2 Contrast Agents for MRI. *Int J Mol Sci* **2016,** *17* (8).

21. Soprano, E.; Alvarez, A.; Pelaz, B.; del Pino, P.; Polo, E., Plasmonic Cell-Derived Nanocomposites for Light-Controlled Cargo Release inside Living Cells. *Advanced Biosystems* **2020,** *4* (3), 1900260.
22. Troyano, J.; Carné-Sánchez, A.; Avci, C.; Imaz, I.; Maspoch, D., Colloidal metal–organic framework particles: the pioneering case of ZIF-8. *Chemical Society Reviews* **2019,** *48* (23), 5534-5546.
23. Xu, K.; Kalantari, A.; Qian, X., Efficient AFM-Based Nanoparticle Manipulation Via Sequential Parallel Pushing. *IEEE Transactions on Nanotechnology* **2012,** *11* (4), 666-675.
24. Polo, E.; del Pino, P.; Pelaz, B.; Grazu, V.; de la Fuente, J. M., Plasmonic-driven thermal sensing: ultralow detection of cancer markers. *Chemical Communications* **2013,** *49* (35), 3676-3678.
25. Wilhelmi, O.; Reyntjens, S.; Mitterbauer, C.; Roussel, L.; Stokes, D. J.; Hubert, D. H. W., Rapid Prototyping of Nanostructured Materials with a Focused Ion Beam. *Japanese Journal of Applied Physics* **2008,** *47* (6), 5010-5014.
26. Pelaz, B.; Grazu, V.; Ibarra, A.; Magen, C.; del Pino, P.; de la Fuente, J. M., Tailoring the Synthesis and Heating Ability of Gold Nanoprisms for Bioapplications. *Langmuir* **2012,** *28* (24), 8965-8970.
27. Dekkers, J. F.; Alieva, M.; Wellens, L. M.; Ariese, H. C. R.; Jamieson, P. R.; Vonk, A. M.; Amatngalim, G. D.; Hu, H.; Oost, K. C.; Snippert, H. J. G.; Beekman, J. M.; Wehrens, E. J.; Visvader, J. E.; Clevers, H.; Rios, A. C., High-resolution 3D imaging of fixed and cleared organoids. *Nature Protocols* **2019,** *14* (6), 1756-1771.
28. Müller, D. J.; Hand, G. M.; Engel, A.; Sosinsky, G. E., Conformational changes in surface structures of isolated connexin 26 gap junctions. *EMBO J* **2002,** *21* (14), 3598-3607.
29. Ahopelto, J.; Ardila, G.; Baldi, L.; Balestra, F.; Belot, D.; Fagas, G.; De Gendt, S.; Demarchi, D.; Fernandez-Bolaños, M.; Holden, D.; Ionescu, A. M.; Meneghesso, G.; Mocuta, A.; Pfeffer, M.; Popp, R. M.; Sangiorgi, E.; Sotomayor Torres, C. M., NanoElectronics roadmap for Europe: From nanodevices and innovative materials to system integration. *Solid-State Electronics* **2019,** *155*, 7-19.
30. Koledov, V.; Gratowski, S. v.; Shelyakov, A.; Lega, P.; Cotta, M.; Orlov, A.; Frolov, A.; Irzhak, A.; Smolovich, A. In *3D Nano-Manipulation and Nano-assembling by the smallest and the fastest shape memory alloy nano-tools*, 2019 International Conference on Manipulation, Automation and Robotics at Small Scales (MARSS), 1-5 July 2019; 2019; pp 1-4.
31. Pelaz, B.; Jaber, S.; de Aberasturi, D. J.; Wulf, V.; Aida, T.; de la Fuente, J. M.; Feldmann, J.; Gaub, H. E.; Josephson, L.; Kagan, C. R.; Kotov, N. A.; Liz-Marzán, L. M.; Mattoussi, H.; Mulvaney, P.; Murray, C. B.; Rogach, A. L.; Weiss, P. S.; Willner, I.; Parak, W. J., The State of Nanoparticle-Based Nanoscience and Biotechnology: Progress, Promises, and Challenges. *ACS Nano* **2012,** *6* (10), 8468-8483.
32. Pelaz, B.; Alexiou, C.; Alvarez-Puebla, R. A.; Alves, F.; Andrews, A. M.; Ashraf, S.; Balogh, L. P.; Ballerini, L.; Bestetti, A.; Brendel, C.; Bosi, S.; Carril, M.; Chan, W. C. W.; Chen, C.; Chen, X.; Chen, X.; Cheng, Z.; Cui, D.; Du, J.; Dullin, C.; Escudero, A.; Feliu, N.; Gao, M.; George, M.; Gogotsi, Y.; Grünweller, A.; Gu, Z.; Halas, N. J.; Hampp, N.; Hartmann, R. K.; Hersam, M. C.; Hunziker, P.; Jian, J.; Jiang, X.; Jungebluth, P.; Kadhiresan, P.; Kataoka, K.; Khademhosseini, A.; Kopeček, J.; Kotov, N. A.; Krug, H. F.; Lee, D. S.; Lehr, C.-M.; Leong, K. W.; Liang, X.-J.; Ling Lim, M.; Liz-Marzán, L. M.; Ma, X.; Macchiarini, P.; Meng, H.; Möhwald, H.; Mulvaney, P.; Nel, A. E.; Nie, S.; Nordlander, P.; Okano, T.; Oliveira, J.; Park, T. H.; Penner, R. M.; Prato, M.; Puntes, V.; Rotello, V. M.; Samarakoon, A.; Schaak, R. E.; Shen, Y.; Sjöqvist, S.; Skirtach, A. G.; Soliman, M. G.; Stevens, M. M.; Sung, H.-W.; Tang, B. Z.; Tietze, R.; Udugama, B. N.; VanEpps, J. S.; Weil, T.; Weiss, P. S.; Willner, I.; Wu, Y.; Yang, L.; Yue, Z.; Zhang, Q.; Zhang, Q.; Zhang, X.-E.; Zhao, Y.; Zhou, X.; Parak, W. J., Diverse Applications of Nanomedicine. *ACS Nano* **2017,** *11* (3), 2313-2381.
33. Unterweger, H.; Dézsi, L.; Matuszak, J.; Janko, C.; Poettler, M.; Jordan, J.; Bäuerle, T.; Szebeni, J.; Fey, T.; Boccaccini, A. R.; Alexiou, C.; Cicha, I., Dextran-coated superparamagnetic iron oxide nanoparticles for magnetic resonance imaging: evaluation of size-dependent imaging properties, storage stability and safety. *Int J Nanomedicine* **2018,** *13*, 1899-1915.

34. Rivera-Gil, P.; Jimenez De Aberasturi, D.; Wulf, V.; Pelaz, B.; Del Pino, P.; Zhao, Y.; De La Fuente, J. M.; Ruiz De Larramendi, I.; Rojo, T.; Liang, X.-J.; Parak, W. J., The Challenge To Relate the Physicochemical Properties of Colloidal Nanoparticles to Their Cytotoxicity. *Accounts of Chemical Research* **2013,** *46* (3), 743-749.
35. Feliu, N.; Docter, D.; Heine, M.; del Pino, P.; Ashraf, S.; Kolosnjaj-Tabi, J.; Macchiarini, P.; Nielsen, P.; Alloyeau, D.; Gazeau, F.; Stauber, R. H.; Parak, W. J., In vivo degeneration and the fate of inorganic nanoparticles. *Chemical Society Reviews* **2016,** *45* (9), 2440-2457.
36. Li, K.; Schneider, M., Quantitative evaluation and visualization of size effect on cellular uptake of gold nanoparticles by multiphoton imaging-UV/Vis spectroscopic analysis. (1560-2281 (Electronic)).
37. Chithrani, B. D.; Chan, W. C., Elucidating the mechanism of cellular uptake and removal of protein-coated gold nanoparticles of different sizes and shapes. (1530-6984 (Print)).
38. Zhang, L.; Cao, Z.; Li, Y.; Ella-Menye, J.-R.; Bai, T.; Jiang, S., Softer Zwitterionic Nanogels for Longer Circulation and Lower Splenic Accumulation. *ACS Nano* **2012,** *6* (8), 6681-6686.
39. Abdelmonem, A. M.; Pelaz, B.; Kantner, K.; Bigall, N. C.; Del Pino, P.; Parak, W. J., Charge and agglomeration dependent in vitro uptake and cytotoxicity of zinc oxide nanoparticles. *Journal of Inorganic Biochemistry* **2015,** *153*, 334-338.
40. Del Pino, P.; Yang, F.; Pelaz, B.; Zhang, Q.; Kantner, K.; Hartmann, R.; Martinez de Baroja, N.; Gallego, M.; Moller, M.; Manshian, B. B.; Soenen, S. J.; Riedel, R.; Hampp, N.; Parak, W. J., Basic Physicochemical Properties of Polyethylene Glycol Coated Gold Nanoparticles that Determine Their Interaction with Cells. *Angewandte Chemie (International ed. in English)* **2016,** *55* (18), 5483-7.
41. Parak, W. J., Complex Colloidal Assembly. *Science* **2011,** *334* (6061), 1359.
42. Del Pino, P., Tailoring the interplay between electromagnetic fields and nanomaterials toward applications in life sciences: a review. *Journal of biomedical optics* **2014,** *19* (10), 101507.
43. Polo, E.; Navarro Poupard, M. F.; Guerrini, L.; Taboada, P.; Pelaz, B.; Alvarez-Puebla, R. A.; del Pino, P., Colloidal bioplasmonics. *Nano Today* **2018,** *20*, 58-73.
44. Zhang, Q.; Castellanos-Rubio, I.; Munshi, R.; Orue, I.; Pelaz, B.; Gries, K. I.; Parak, W. J.; del Pino, P.; Pralle, A., Model Driven Optimization of Magnetic Anisotropy of Exchange-Coupled Core–Shell Ferrite Nanoparticles for Maximal Hysteretic Loss. *Chemistry of Materials* **2015,** *27* (21), 7380-7387.
45. Ashraf, S.; Carrillo-Carrion, C.; Zhang, Q.; Soliman, M. G.; Hartmann, R.; Pelaz, B.; del Pino, P.; Parak, W. J., Fluorescence-based ion-sensing with colloidal particles. *Current Opinion in Pharmacology* **2014,** *18*, 98-103.
46. Gavia, D. J.; Shon, Y. S., Catalytic Properties of Unsupported Palladium Nanoparticle Surfaces Capped with Small Organic Ligands. *ChemCatChem* **2015,** *7* (6), 892-900.
47. Fratila, R. M.; Mitchell, S. G.; del Pino, P.; Grazu, V.; de la Fuente, J. M., Strategies for the Biofunctionalization of Gold and Iron Oxide Nanoparticles. *Langmuir* **2014,** *30* (50), 15057-15071.
48. Conde, J.; Dias, J. T.; Grazú, V.; Moros, M.; Baptista, P. V.; de la Fuente, J. M., Revisiting 30 years of biofunctionalization and surface chemistry of inorganic nanoparticles for nanomedicine. *Front Chem* **2014,** *2*, 48-48.
49. Lin, C.-A. J.; Sperling, R. A.; Li, J. K.; Yang, T.-Y.; Li, P.-Y.; Zanella, M.; Chang, W. H.; Parak, W. J., Design of an Amphiphilic Polymer for Nanoparticle Coating and Functionalization. *Small* **2008,** *4* (3), 334-341.
50. Hühn, J.; Carrillo-Carrion, C.; Soliman, M. G.; Pfeiffer, C.; Valdeperez, D.; Masood, A.; Chakraborty, I.; Zhu, L.; Gallego, M.; Yue, Z.; Carril, M.; Feliu, N.; Escudero, A.; Alkilany, A. M.; Pelaz, B.; del Pino, P.; Parak, W. J., Selected Standard Protocols for the Synthesis, Phase Transfer, and Characterization of Inorganic Colloidal Nanoparticles. *Chemistry of Materials* **2017,** *29* (1), 399-461.
51. Castellón, E.; Martínez, M.; Madrigal-Carballo, S.; Arias, M. L.; Vargas, W. E.; Chavarría, M., Scattering of Light by Colloidal Aluminosilicate Particles Produces the Unusual Sky-Blue Color of Río Celeste (Tenorio Volcano Complex, Costa Rica). *PLOS ONE* **2013,** *8* (9), e75165.

52. Borghei, Y. S.; Hosseini, M.; Dadmehr, M.; Hosseinkhani, S.; Ganjali, M. R.; Sheikhnejad, R., Visual detection of cancer cells by colorimetric aptasensor based on aggregation of gold nanoparticles induced by DNA hybridization. *Analytica chimica acta* **2016,** *904*, 92-7.
53. Liu, T.-M.; Conde, J.; Lipiński, T.; Bednarkiewicz, A.; Huang, C.-C., Revisiting the classification of NIR-absorbing/emitting nanomaterials for in vivo bioapplications. *Npg Asia Materials* **2016,** *8*, e295.
54. de Mello, J. C.; Wittmann, H. F.; Friend, R. H., An improved experimental determination of external photoluminescence quantum efficiency. *Advanced Materials* **1997,** *9* (3), 230-232.
55. Boyer, J.-C.; van Veggel, F. C. J. M., Absolute quantum yield measurements of colloidal NaYF4: Er3+, Yb3+ upconverting nanoparticles. *Nanoscale* **2010,** *2* (8), 1417-1419.
56. Stephens, D. J.; Allan, V. J., Light Microscopy Techniques for Live Cell Imaging. *Science* **2003,** *300* (5616), 82.
57. Adrian, M.; Dubochet, J.; Lepault, J.; McDowall, A. W., Cryo-electron microscopy of viruses. *Nature* **1984,** *308* (5954), 32-36.
58. Dubochet, J.; Adrian, M.; Chang, J.-J.; Homo, J.-C.; Lepault, J.; McDowall, A. W.; Schultz, P., Cryo-electron microscopy of vitrified specimens. *Quarterly Reviews of Biophysics* **2009,** *21* (2), 129-228.
59. Dufrêne, Y. F.; Ando, T.; Garcia, R.; Alsteens, D.; Martinez-Martin, D.; Engel, A.; Gerber, C.; Müller, D. J., Imaging modes of atomic force microscopy for application in molecular and cell biology. *Nature Nanotechnology* **2017,** *12* (4), 295-307.
60. L'Azou, B.; Passagne, I.; Mounicou, S.; Tréguer-Delapierre, M.; Puljalté, I.; Szpunar, J.; Lobinski, R.; Ohayon-Courtès, C., Comparative cytotoxicity of cadmium forms (CdCl2, CdO, CdS micro- and nanoparticles) in renal cells. *Toxicology Research* **2014,** *3* (1), 32-41.
61. Cedervall, T.; Lynch, I.; Lindman, S.; Berggård, T.; Thulin, E.; Nilsson, H.; Dawson, K. A.; Linse, S., Understanding the nanoparticle–protein corona using methods to quantify exchange rates and affinities of proteins for nanoparticles. *Proceedings of the National Academy of Sciences* **2007,** *104* (7), 2050-2055.
62. Gianneli, M.; Polo, E.; Lopez, H.; Castagnola, V.; Aastrup, T.; Dawson, K. A., Label-free in-flow detection of receptor recognition motifs on the biomolecular corona of nanoparticles. *Nanoscale* **2018,** *10* (12), 5474-5481.
63. Polo, E.; Collado, M.; Pelaz, B.; Del Pino, P., Advances toward More Efficient Targeted Delivery of Nanoparticles in Vivo: Understanding Interactions between Nanoparticles and Cells. *ACS Nano* **2017,** *11* (3), 2397-2402.
64. Jung, S.-Y.; Lim, S.-M.; Albertorio, F.; Kim, G.; Gurau, M. C.; Yang, R. D.; Holden, M. A.; Cremer, P. S., The Vroman Effect: A Molecular Level Description of Fibrinogen Displacement. *Journal of the American Chemical Society* **2003,** *125* (42), 12782-12786.
65. Hadjidemetriou, M.; McAdam, S.; Garner, G.; Thackeray, C.; Knight, D.; Smith, D.; Al-Ahmady, Z.; Mazza, M.; Rogan, J.; Clamp, A.; Kostarelos, K., The Human In Vivo Biomolecule Corona onto PEGylated Liposomes: A Proof-of-Concept Clinical Study. *Advanced materials (Deerfield Beach, Fla.)* **2019,** *31* (4), e1803335.
66. Weber, C.; Morsbach, S.; Landfester, K., Possibilities and Limitations of Different Separation Techniques for the Analysis of the Protein Corona. *Angewandte Chemie International Edition* **2019,** *58* (37), 12787-12794.
67. Cruje, C.; Chithrani, D. B., Polyethylene Glycol Functionalized Nanoparticles for Improved Cancer Treatment. *Reviews in Nanoscience and Nanotechnology* **2014,** *3* (1), 20-30.
68. Bertrand, N.; Grenier, P.; Mahmoudi, M.; Lima, E. M.; Appel, E. A.; Dormont, F.; Lim, J.-M.; Karnik, R.; Langer, R.; Farokhzad, O. C., Mechanistic understanding of in vivo protein corona formation on polymeric nanoparticles and impact on pharmacokinetics. *Nature Communications* **2017,** *8* (1), 777.
69. Pozzi, D.; Colapicchioni, V.; Caracciolo, G.; Piovesana, S.; Capriotti, A. L.; Palchetti, S.; De Grossi, S.; Riccioli, A.; Amenitsch, H.; Laganà, A., Effect of polyethyleneglycol (PEG) chain length on

the bio–nano-interactions between PEGylated lipid nanoparticles and biological fluids: from nanostructure to uptake in cancer cells. *Nanoscale* **2014,** *6* (5), 2782-2792.
70. Pelaz, B.; del Pino, P.; Maffre, P.; Hartmann, R.; Gallego, M.; Rivera-Fernández, S.; de la Fuente, J. M.; Nienhaus, G. U.; Parak, W. J., Surface Functionalization of Nanoparticles with Polyethylene Glycol: Effects on Protein Adsorption and Cellular Uptake. *ACS Nano* **2015,** *9* (7), 6996-7008.
71. Puertas, A. M.; de las Nieves, F. J., Colloidal Stability of Polymer Colloids with Variable Surface Charge. *Journal of Colloid and Interface Science* **1999,** *216* (2), 221-229.
72. Loeb, J., THE INFLUENCE OF ELECTROLYTES ON THE CATAPHORETIC CHARGE OF COLLOIDAL PARTICLES AND THE STABILITY OF THEIR SUSPENSIONS : II. EXPERIMENTS WITH PARTICLES OF GELATIN, CASEIN, AND DENATURED EGG ALBUMIN. *The Journal of general physiology* **1923,** *5* (3), 395-413.
73. Kirchner, C.; Liedl, T.; Kudera, S.; Pellegrino, T.; Muñoz Javier, A.; Gaub, H. E.; Stölzle, S.; Fertig, N.; Parak, W. J., Cytotoxicity of Colloidal CdSe and CdSe/ZnS Nanoparticles. *Nano letters* **2005,** *5* (2), 331-338.
74. Villar-Alvarez, E.; Leal, B. H.; Martínez-González, R.; Pardo, A.; Al-Qadi, S.; Juárez, J.; Váldez, M. A.; Cambón, A.; Barbosa, S.; Taboada, P., siRNA Silencing by Chemically Modified Biopolymeric Nanovectors. *ACS Omega* **2019,** *4* (2), 3904-3921.
75. Chen, X.; Tong, R.; Shi, Z.; Yang, B.; Liu, H.; Ding, S.; Wang, X.; Lei, Q.; Wu, J.; Fang, W., MOF Nanoparticles with Encapsulated Autophagy Inhibitor in Controlled Drug Delivery System for Antitumor. *ACS applied materials & interfaces* **2018,** *10* (3), 2328-2337.
76. Wolfram, J.; Ferrari, M., Clinical cancer nanomedicine. *Nano Today* **2019,** *25*, 85-98.
77. Gradishar, W. J.; Tjulandin, S.; Davidson, N.; Shaw, H.; Desai, N.; Bhar, P.; Hawkins, M.; O'Shaughnessy, J., Phase III Trial of Nanoparticle Albumin-Bound Paclitaxel Compared With Polyethylated Castor Oil–Based Paclitaxel in Women With Breast Cancer. *Journal of Clinical Oncology* **2005,** *23* (31), 7794-7803.
78. Correa-Paz, C.; Navarro Poupard, M. F.; Polo, E.; Rodríguez-Pérez, M.; Taboada, P.; Iglesias-Rey, R.; Hervella, P.; Sobrino, T.; Vivien, D.; Castillo, J.; del Pino, P.; Campos, F.; Pelaz, B., In vivo ultrasound-activated delivery of recombinant tissue plasminogen activator from the cavity of sub-micrometric capsules. *Journal of Controlled Release* **2019,** *308*, 162-171.
79. Ediriwickrema, A.; Saltzman, W. M., Nanotherapy for Cancer: Targeting and Multifunctionality in the Future of Cancer Therapies. *ACS Biomaterials Science & Engineering* **2015,** *1* (2), 64-78.
80. Solomon, R.; Gabizon, A. A., Clinical Pharmacology of Liposomal Anthracyclines: Focus on Pegylated Liposomal Doxorubicin. *Clinical Lymphoma and Myeloma* **2008,** *8* (1), 21-32.
81. Shen, H.; Sun, T.; Ferrari, M., Nanovector delivery of siRNA for cancer therapy. *Cancer Gene Therapy* **2012,** *19*, 367.
82. Rodriguez, P. L.; Harada, T.; Christian, D. A.; Pantano, D. A.; Tsai, R. K.; Discher, D. E., Minimal "Self" peptides that inhibit phagocytic clearance and enhance delivery of nanoparticles. *Science (New York, N.Y.)* **2013,** *339* (6122), 971-975.
83. Pasut, G.; Veronese, F. M., State of the art in PEGylation: The great versatility achieved after forty years of research. *Journal of Controlled Release* **2012,** *161* (2), 461-472.
84. Dicko, A.; Kwak, S.; Frazier, A. A.; Mayer, L. D.; Liboiron, B. D., Biophysical characterization of a liposomal formulation of cytarabine and daunorubicin. *International Journal of Pharmaceutics* **2010,** *391* (1), 248-259.
85. Allen, T. M., Ligand-targeted therapeutics in anticancer therapy. *Nature Reviews Cancer* **2002,** *2* (10), 750-763.
86. Singh, N.; Nayak, J.; Sahoo, S. K.; Kumar, R., Glutathione conjugated superparamagnetic Fe3O4-Au core shell nanoparticles for pH controlled release of DOX. *Materials Science and Engineering: C* **2019,** *100*, 453-465.

87. Ni, D.; Jiang, D.; Valdovinos, H. F.; Ehlerding, E. B.; Yu, B.; Barnhart, T. E.; Huang, P.; Cai, W., Bioresponsive Polyoxometalate Cluster for Redox-Activated Photoacoustic Imaging-Guided Photothermal Cancer Therapy. *Nano letters* **2017,** *17* (5), 3282-3289.
88. Gustafson, H. H.; Holt-Casper, D.; Grainger, D. W.; Ghandehari, H., Nanoparticle uptake: The phagocyte problem. *Nano Today* **2015,** *10* (4), 487-510.
89. Soo Choi, H.; Liu, W.; Misra, P.; Tanaka, E.; Zimmer, J. P.; Itty Ipe, B.; Bawendi, M. G.; Frangioni, J. V., Renal clearance of quantum dots. *Nature Biotechnology* **2007,** *25*, 1165.
90. Ferrari, M., Frontiers in cancer nanomedicine: directing mass transport through biological barriers. *Trends in Biotechnology* **2010,** *28* (4), 181-188.
91. Koay, E. J.; Ferrari, M., Transport Oncophysics in silico, in vitro, and in vivo. *Physical Biology* **2014,** *11* (6), 060201.
92. Michor, F.; Liphardt, J.; Ferrari, M.; Widom, J., What does physics have to do with cancer? *Nature Reviews Cancer* **2011,** *11*, 657.
93. Gimbrone, M. A.; Leapman, S. B.; Cotran, R. S.; Folkman, J., TUMOR DORMANCY IN VIVO BY PREVENTION OF NEOVASCULARIZATION. *The Journal of Experimental Medicine* **1972,** *136* (2), 261.
94. Yuan, F.; Dellian, M.; Fukumura, D.; Leunig, M.; Berk, D. A.; Torchilin, V. P.; Jain, R. K., Vascular Permeability in a Human Tumor Xenograft: Molecular Size Dependence and Cutoff Size. *Cancer Research* **1995,** *55* (17), 3752.
95. Iyer, A. K.; Khaled, G.; Fang, J.; Maeda, H., Exploiting the enhanced permeability and retention effect for tumor targeting. *Drug Discovery Today* **2006,** *11* (17), 812-818.
96. Gerlowski, L. E.; Jain, R. K., Microvascular permeability of normal and neoplastic tissues. *Microvascular Research* **1986,** *31* (3), 288-305.
97. Matsumura, Y.; Maeda, H., A New Concept for Macromolecular Therapeutics in Cancer Chemotherapy: Mechanism of Tumoritropic Accumulation of Proteins and the Antitumor Agent Smancs. *Cancer Research* **1986,** *46* (12 Part 1), 6387.
98. Gentile, E.; Cilurzo, F.; Di Marzio, L.; Carafa, M.; Anna Ventura, C.; Wolfram, J.; Paolino, D.; Celia, C., Liposomal chemotherapeutics. *Future Oncology* **2013,** *9* (12), 1849-1859.
99. Maeda, H., SMANCS and polymer-conjugated macromolecular drugs: advantages in cancer chemotherapy. *Advanced Drug Delivery Reviews* **2001,** *46* (1), 169-185.
100. Prabhakar, U.; Maeda, H.; Jain, R. K.; Sevick-Muraca, E. M.; Zamboni, W.; Farokhzad, O. C.; Barry, S. T.; Gabizon, A.; Grodzinski, P.; Blakey, D. C., Challenges and Key Considerations of the Enhanced Permeability and Retention Effect for Nanomedicine Drug Delivery in Oncology. *Cancer Research* **2013,** *73* (8), 2412.
101. Harrington, K. J.; Rowlinson-Busza, G.; Syrigos, K. N.; Abra, R. M.; Uster, P. S.; Peters, A. M.; Stewart, J. S. W., Influence of tumour size on uptake of111In-DTPA-labelled pegylated liposomes in a human tumour xenograft model. *British Journal of Cancer* **2000,** *83* (5), 684-688.
102. Koukourakis, M. I.; Koukouraki, S.; Giatromanolaki, A.; Archimandritis, S. C.; Skarlatos, J.; Beroukas, K.; Bizakis, J. G.; Retalis, G.; Karkavitsas, N.; Helidonis, E. S., Liposomal Doxorubicin and Conventionally Fractionated Radiotherapy in the Treatment of Locally Advanced Non–Small-Cell Lung Cancer and Head and Neck Cancer. *Journal of Clinical Oncology* **1999,** *17* (11), 3512-3521.
103. Sindhwani, S.; Syed, A. M.; Ngai, J.; Kingston, B. R.; Maiorino, L.; Rothschild, J.; MacMillan, P.; Zhang, Y.; Rajesh, N. U.; Hoang, T.; Wu, J. L. Y.; Wilhelm, S.; Zilman, A.; Gadde, S.; Sulaiman, A.; Ouyang, B.; Lin, Z.; Wang, L.; Egeblad, M.; Chan, W. C. W., The entry of nanoparticles into solid tumours. *Nature Materials* **2020**.
104. Adriani, G.; de Tullio, M. D.; Ferrari, M.; Hussain, F.; Pascazio, G.; Liu, X.; Decuzzi, P., The preferential targeting of the diseased microvasculature by disk-like particles. *Biomaterials* **2012,** *33* (22), 5504-5513.
105. Sevick, E. M.; Jain, R. K., Viscous Resistance to Blood Flow in Solid Tumors: Effect of Hematocrit on Intratumor Blood Viscosity. *Cancer Research* **1989,** *49* (13), 3513.
106. Lee, S.-Y.; Ferrari, M.; Decuzzi, P., Shaping nano-/micro-particles for enhanced vascular interaction in laminar flows. *Nanotechnology* **2009,** *20* (49), 495101.

107. Decuzzi, P.; Ferrari, M., The adhesive strength of non-spherical particles mediated by specific interactions. *Biomaterials* **2006,** *27* (30), 5307-5314.
108. Hemmer, E.; Venkatachalam, N.; Hyodo, H.; Hattori, A.; Ebina, Y.; Kishimoto, H.; Soga, K., Upconverting and NIR emitting rare earth based nanostructures for NIR-bioimaging. *Nanoscale* **2013,** *5* (23), 11339-11361.
109. Hemmer, E.; Benayas, A.; Légaré, F.; Vetrone, F., Exploiting the biological windows: current perspectives on fluorescent bioprobes emitting above 1000 nm. *Nanoscale Horizons* **2016,** *1* (3), 168-184.
110. *Active Plasmonic Nanomaterials*. Jenny Stanford Publishing: 2015.
111. Jain, P. K.; Huang, X.; El-Sayed, I. H.; El-Sayed, M. A., Noble Metals on the Nanoscale: Optical and Photothermal Properties and Some Applications in Imaging, Sensing, Biology, and Medicine. *Accounts of Chemical Research* **2008,** *41* (12), 1578-1586.
112. Bruzzone, S.; Malvaldi, M.; Arrighini, G. P.; Guidotti, C., Comparative study of near and far field e.m. scattering response by Au/Ag alloy and core-shell nanoparticles. *Materials Science and Engineering: C* **2007,** *27* (5), 1015-1021.
113. Schuller, J. A.; Barnard, E. S.; Cai, W.; Jun, Y. C.; White, J. S.; Brongersma, M. L., Plasmonics for extreme light concentration and manipulation. *Nature Materials* **2010,** *9*, 193.
114. van der Zee, J., Heating the patient: a promising approach? *Annals of Oncology* **2002,** *13* (8), 1173-1184.
115. Millikan, R. C.; White, D. R., Systematics of Vibrational Relaxation. *The Journal of Chemical Physics* **1963,** *39* (12), 3209-3213.
116. Jaffe, H. H.; Miller, A. L., The fates of electronic excitation energy. *Journal of Chemical Education* **1966,** *43* (9), 469.
117. Zheng, J.; Zhang, C.; Dickson, R. M., Highly Fluorescent, Water-Soluble, Size-Tunable Gold Quantum Dots. *Physical Review Letters* **2004,** *93* (7), 077402.
118. Sychugov, I.; Juhasz, R.; Valenta, J.; Linnros, J., Narrow Luminescence Linewidth of a Silicon Quantum Dot. *Physical Review Letters* **2005,** *94* (8), 087405.
119. He, Y.; Zhong, Y.; Su, Y.; Lu, Y.; Jiang, Z.; Peng, F.; Xu, T.; Su, S.; Huang, Q.; Fan, C.; Lee, S.-T., Water-Dispersed Near-Infrared-Emitting Quantum Dots of Ultrasmall Sizes for In Vitro and In Vivo Imaging. *Angewandte Chemie International Edition* **2011,** *50* (25), 5695-5698.
120. Chen, X.; Peng, D.; Ju, Q.; Wang, F., Photon upconversion in core–shell nanoparticles. *Chemical Society Reviews* **2015,** *44* (6), 1318-1330.
121. Ji, D.-K.; Ménard-Moyon, C.; Bianco, A., Physically-triggered nanosystems based on two-dimensional materials for cancer theranostics. *Advanced Drug Delivery Reviews* **2019,** *138*, 211-232.
122. Hou, Z.; Deng, K.; Wang, M.; Liu, Y.; Chang, M.; Huang, S.; Li, C.; Wei, Y.; Cheng, Z.; Han, G.; Al Kheraif, A. A.; Lin, J., Hydrogenated Titanium Oxide Decorated Upconversion Nanoparticles: Facile Laser Modified Synthesis and 808 nm Near-Infrared Light Triggered Phototherapy. *Chemistry of Materials* **2019,** *31* (3), 774-784.
123. Tao, K.; Sun, K., Chapter 7 - Imaging and therapy with upconversion nanoparticles. In *Photonanotechnology for Therapeutics and Imaging*, Choi, S. k., Ed. Elsevier: 2020; pp 177-204.
124. Wilhelm, S.; del Barrio, M.; Heiland, J.; Himmelstoß, S. F.; Galbán, J.; Wolfbeis, O. S.; Hirsch, T., Spectrally Matched Upconverting Luminescent Nanoparticles for Monitoring Enzymatic Reactions. *ACS applied materials & interfaces* **2014,** *6* (17), 15427-15433.
125. Wang, Z.; Hu, M.; Ai, X.; Zhang, Z.; Xing, B., Near-Infrared Manipulation of Membrane Ion Channels via Upconversion Optogenetics. *Advanced Biosystems* **2019,** *3* (1), 1800233.
126. Huang, P.; Zheng, W.; Zhou, S.; Tu, D.; Chen, Z.; Zhu, H.; Li, R.; Ma, E.; Huang, M.; Chen, X., Lanthanide-Doped LiLuF4 Upconversion Nanoprobes for the Detection of Disease Biomarkers. *Angewandte Chemie International Edition* **2014,** *53* (5), 1252-1257.
127. Auzel, F., Upconversion and anti-Stokes processes with f and d ions in solids. (0009-2665 (Print)).

128. Xu, C. T.; Zhan, Q.; Liu, H.; Somesfalean, G.; Qian, J.; He, S.; Andersson-Engels, S., Upconverting nanoparticles for pre-clinical diffuse optical imaging, microscopy and sensing: Current trends and future challenges. *Laser & Photonics Reviews* **2013,** *7* (5), 663-697.
129. Skripka, A.; Benayas, A.; Marin, R.; Canton, P.; Hemmer, E.; Vetrone, F., Double rare-earth nanothermometer in aqueous media: opening the third optical transparency window to temperature sensing. *Nanoscale* **2017,** *9* (9), 3079-3085.
130. Estelrich, J.; Escribano, E.; Queralt, J.; Busquets, M. A., Iron oxide nanoparticles for magnetically-guided and magnetically-responsive drug delivery. *Int J Mol Sci* **2015,** *16* (4), 8070-8101.
131. Ester Polo, P. d. P., Alberto Pardo, Pablo Taboada and Beatriz Pelaz, Magnetic Nanoparticles for Cancer Therapy and Bioimaging. In *Nanooncology. Nanomedicine and Nanotoxicology*, Gonçalves G., T. G., Ed. Springer, Cham: 2018; pp 239-279.
132. Estelrich, J.; Sánchez-Martín, M. J.; Busquets, M. A., Nanoparticles in magnetic resonance imaging: from simple to dual contrast agents. *Int J Nanomedicine* **2015,** *10*, 1727-1741.
133. Mahmoudi, M.; Hosseinkhani, H.; Hosseinkhani, M.; Boutry, S.; Simchi, A.; Journeay, W. S.; Subramani, K.; Laurent, S., Magnetic Resonance Imaging Tracking of Stem Cells in Vivo Using Iron Oxide Nanoparticles as a Tool for the Advancement of Clinical Regenerative Medicine. *Chemical Reviews* **2011,** *111* (2), 253-280.
134. Paul M. Parizel, L. v. d. H., Frank De Belder, J. Van Goethem, Caroline Venstermans, Rodrigo Salgado, Maurits Voormolen, Wim Van Hecke, Magnetic Resonance Imaging of the Brain. In *Clinical MR Imaging*, Reimer P., P. P. M., Meaney J.F.M., Stichnoth F.A., Ed. Springer, Berlin, Heidelberg: 2010; pp 107-195.
135. Lu, A.-H.; Salabas, E. L.; Schüth, F., Magnetic Nanoparticles: Synthesis, Protection, Functionalization, and Application. *Angewandte Chemie International Edition* **2007,** *46* (8), 1222-1244.
136. Budde, J.; Shajan, G.; Scheffler, K.; Pohmann, R., Ultra-high resolution imaging of the human brain using acquisition-weighted imaging at 9.4T. *NeuroImage* **2014,** *86*, 592-598.
137. Wocik-Piotrowicz, K.; Kaszuba-Zwoinska J Fau - Rokita, E.; Rokita E Fau - Thor, P.; Thor P Fau - Chrobik, P.; Chrobik P Fau - Nieckarz, Z.; Nieckarz Z Fau - Michalski, J.; Michalski, J., Influence of static and alternating magnetic fields on U937 cell viability. (0015-5616 (Print)).
138. Guidelines on limits of exposure to static magnetic fields. (1538-5159 (Electronic)).
139. Chopra, R.; Shaikh, S.; Chatzinoff, Y.; Munaweera, I.; Cheng, B.; Daly, S. M.; Xi, Y.; Bing, C.; Burns, D.; Greenberg, D. E., Employing high-frequency alternating magnetic fields for the non-invasive treatment of prosthetic joint infections. *Sci Rep* **2017,** *7* (1), 7520-7520.
140. Périgo, E. A.; Hemery, G.; Sandre, O.; Ortega, D.; Garaio, E.; Plazaola, F.; Teran, F. J., Fundamentals and advances in magnetic hyperthermia. *Applied Physics Reviews* **2015,** *2* (4), 041302.
141. Plank, C.; Zelphati, O.; Mykhaylyk, O., Magnetically enhanced nucleic acid delivery. Ten years of magnetofection—Progress and prospects. *Advanced Drug Delivery Reviews* **2011,** *63* (14), 1300-1331.
142. Bobo, D.; Robinson, K. J.; Islam, J.; Thurecht, K. J.; Corrie, S. R., Nanoparticle-Based Medicines: A Review of FDA-Approved Materials and Clinical Trials to Date. *Pharmaceutical Research* **2016,** *33* (10), 2373-2387.
143. Wang, Z. L., Nanopiezotronics. *Advanced Materials* **2007,** *19* (6), 889-892.
144. Chiriacò, F.; Soloperto, G.; Greco, A.; Conversano, F.; Ragusa, A.; Menichetti, L.; Casciaro, S., Magnetically-coated silica nanospheres for dual-mode imaging at low ultrasound frequency. *World J Radiol* **2013,** *5* (11), 411-420.
145. Gai, S.; Li, C.; Yang, P.; Lin, J., Recent Progress in Rare Earth Micro/Nanocrystals: Soft Chemical Synthesis, Luminescent Properties, and Biomedical Applications. *Chemical Reviews* **2014,** *114* (4), 2343-2389.
146. Wang, F.; Xue, X.; Liu, X., Multicolor Tuning of (Ln, P)-Doped YVO4 Nanoparticles by Single-Wavelength Excitation. *Angewandte Chemie International Edition* **2008,** *47* (5), 906-909.

147. Weissleder, R., A clearer vision for in vivo imaging. *Nature Biotechnology* **2001,** *19* (4), 316-317.
148. Xie, X.; Li, Z.; Zhang, Y.; Guo, S.; Pendharkar, A. I.; Lu, M.; Huang, L.; Huang, W.; Han, G., Emerging ≈800 nm Excited Lanthanide-Doped Upconversion Nanoparticles. *Small* **2017,** *13* (6), 1602843.
149. Liu, B.; Chen, Y.; Li, C.; He, F.; Hou, Z.; Huang, S.; Zhu, H.; Chen, X.; Lin, J., Poly(Acrylic Acid) Modification of Nd3+-Sensitized Upconversion Nanophosphors for Highly Efficient UCL Imaging and pH-Responsive Drug Delivery. *Advanced Functional Materials* **2015,** *25* (29), 4717-4729.
150. Wang, Y.-F.; Liu, G.-Y.; Sun, L.-D.; Xiao, J.-W.; Zhou, J.-C.; Yan, C.-H., Nd3+-Sensitized Upconversion Nanophosphors: Efficient In Vivo Bioimaging Probes with Minimized Heating Effect. *ACS Nano* **2013,** *7* (8), 7200-7206.
151. Li, X.; Shen, D.; Yang, J.; Yao, C.; Che, R.; Zhang, F.; Zhao, D., Successive Layer-by-Layer Strategy for Multi-Shell Epitaxial Growth: Shell Thickness and Doping Position Dependence in Upconverting Optical Properties. *Chemistry of Materials* **2013,** *25* (1), 106-112.
152. Punjabi, A.; Wu, X.; Tokatli-Apollon, A.; El-Rifai, M.; Lee, H.; Zhang, Y.; Wang, C.; Liu, Z.; Chan, E. M.; Duan, C.; Han, G., Amplifying the Red-Emission of Upconverting Nanoparticles for Biocompatible Clinically Used Prodrug-Induced Photodynamic Therapy. *ACS Nano* **2014,** *8* (10), 10621-10630.
153. Ai, F.; Ju, Q.; Zhang, X.; Chen, X.; Wang, F.; Zhu, G., A core-shell-shell nanoplatform upconverting near-infrared light at 808 nm for luminescence imaging and photodynamic therapy of cancer. *Sci Rep* **2015,** *5* (1), 10785.
154. Hamblin, M. R., Upconversion in photodynamic therapy: plumbing the depths. *Dalton Transactions* **2018,** *47* (26), 8571-8580.
155. Maurin, G.; Serre, C.; Cooper, A.; Férey, G., The new age of MOFs and of their porous-related solids. *Chemical Society Reviews* **2017,** *46* (11), 3104-3107.
156. Luzuriaga, M. A.; Benjamin, C. E.; Gaertner, M. W.; Lee, H.; Herbert, F. C.; Mallick, S.; Gassensmith, J. J., ZIF-8 degrades in cell media, serum, and some—but not all—common laboratory buffers. *Supramolecular Chemistry* **2019,** *31* (8), 485-490.
157. Yu, J.; Mu, C.; Yan, B.; Qin, X.; Shen, C.; Xue, H.; Pang, H., Nanoparticle/MOF composites: preparations and applications. *Materials Horizons* **2017,** *4* (4), 557-569.
158. Völker, T.; Meggers, E., Transition-metal-mediated uncaging in living human cells—an emerging alternative to photolabile protecting groups. *Current Opinion in Chemical Biology* **2015,** *25*, 48-54.
159. Yang, M.; Yang, Y.; Chen, P. R., Transition-Metal-Catalyzed Bioorthogonal Cycloaddition Reactions. *Topics in Current Chemistry* **2015,** *374* (1), 2.
160. Soldevila-Barreda, J. J.; Sadler, P. J., Approaches to the design of catalytic metallodrugs. *Current Opinion in Chemical Biology* **2015,** *25*, 172-183.
161. Martínez-Calvo, M.; Mascareñas, J. L., Organometallic catalysis in biological media and living settings. *Coordination Chemistry Reviews* **2018,** *359*, 57-79.
162. Rebelein, J. G.; Ward, T. R., In vivo catalyzed new-to-nature reactions. *Current Opinion in Biotechnology* **2018,** *53*, 106-114.
163. Bai, Y.; Chen, J.; Zimmerman, S. C., Designed transition metal catalysts for intracellular organic synthesis. *Chemical Society Reviews* **2018,** *47* (5), 1811-1821.
164. Soldevila-Barreda, J. J.; Metzler-Nolte, N., Intracellular Catalysis with Selected Metal Complexes and Metallic Nanoparticles: Advances toward the Development of Catalytic Metallodrugs. *Chemical Reviews* **2019,** *119* (2), 829-869.
165. Li, J.; Yu, J.; Zhao, J.; Wang, J.; Zheng, S.; Lin, S.; Chen, L.; Yang, M.; Jia, S.; Zhang, X.; Chen, P. R., Palladium-triggered deprotection chemistry for protein activation in living cells. *Nat. Chem.* **2014,** *6*, 352.
166. Wang, J.; Cheng, B.; Li, J.; Zhang, Z.; Hong, W.; Chen, X.; Chen, P. R., Chemical Remodeling of Cell-Surface Sialic Acids through a Palladium-Triggered Bioorthogonal Elimination Reaction. *Angewandte Chemie International Edition* **2015,** *54* (18), 5364-5368.

167. Wang, J.; Zheng, S.; Liu, Y.; Zhang, Z.; Lin, Z.; Li, J.; Zhang, G.; Wang, X.; Li, J.; Chen, P. R., Palladium-Triggered Chemical Rescue of Intracellular Proteins via Genetically Encoded Allene-Caged Tyrosine. *Journal of the American Chemical Society* **2016,** *138* (46), 15118-15121.
168. Martínez-Calvo, M.; Couceiro, J. R.; Destito, P.; Rodríguez, J.; Mosquera, J.; Mascareñas, J. L., Intracellular Deprotection Reactions Mediated by Palladium Complexes Equipped with Designed Phosphine Ligands. *ACS Catal.* **2018,** *8* (7), 6055-6061.
169. Dahal, E.; Curtiss, J.; Subedi, D.; Chen, G.; Houston, J. P.; Smirnov, S., Evaluation of the Catalytic Activity and Cytotoxicity of Palladium Nanocubes: The Role of Oxygen. *ACS applied materials & interfaces* **2015,** *7* (18), 9364-9371.
170. Kotov, N., The only way is up. *Nature Materials* **2011,** *10* (12), 903-904.
171. Wang, X.-d.; Achatz, D. E.; Hupf, C.; Sperber, M.; Wegener, J.; Bange, S.; Lupton, J. M.; Wolfbeis, O. S., Imaging of cellular oxygen via two-photon excitation of fluorescent sensor nanoparticles. *Sensors and Actuators B: Chemical* **2013,** *188*, 257-262.
172. Wilhelm, S.; Kaiser, M.; Wuerth, C.; Heiland, J.; Carrillo-Carrion, C.; Muhr, V.; Wolfbeis, O. S.; Parak, W. J.; Resch-Genger, U.; Hirsch, T., Water dispersible upconverting nanoparticles: effects of surface modification on their luminescence and colloidal stability. *Nanoscale* **2015,** *7* (4), 1403-1410.
173. He, S.; Johnson, N. J. J.; Nguyen Huu, V. A.; Huang, Y.; Almutairi, A., Leveraging Spectral Matching between Photosensitizers and Upconversion Nanoparticles for 808 nm-Activated Photodynamic Therapy. *Chemistry of Materials* **2018,** *30* (12), 3991-4000.
174. Jayakumar, M. k. g.; Idris, N. M.; Huang, K.; Zhang, Y., A paradigm shift in the excitation wavelength of upconversion nanoparticles. *Nanoscale* **2014,** *6* (15), 8441-8443.
175. Arboleda, C.; He, S.; Stubelius, A.; Johnson, N. J. J.; Almutairi, A., High Nd(III)-Sensitizer Concentrations for 800 nm Wavelength Excitation Using Isotropic Core–Shell Upconversion Nanoparticles. *Chemistry of Materials* **2019,** *31* (9), 3103-3110.
176. Xie, X.; Gao, N.; Deng, R.; Sun, Q.; Xu, Q.-H.; Liu, X., Mechanistic Investigation of Photon Upconversion in Nd3+-Sensitized Core–Shell Nanoparticles. *Journal of the American Chemical Society* **2013,** *135* (34), 12608-12611.
177. Dong, A.; Ye, X.; Chen, J.; Kang, Y.; Gordon, T.; Kikkawa, J. M.; Murray, C. B., A Generalized Ligand-Exchange Strategy Enabling Sequential Surface Functionalization of Colloidal Nanocrystals. *Journal of the American Chemical Society* **2011,** *133* (4), 998-1006.
178. Chen, D.; Tao, R.; Tao, K.; Chen, B.; Choi, S. K.; Tian, Q.; Xu, Y.; Zhou, G.; Sun, K., Efficacy Dependence of Photodynamic Therapy Mediated by Upconversion Nanoparticles: Subcellular Positioning and Irradiation Productivity. *Small* **2017,** *13* (13), 1602053.
179. Li, F.; Du, Y.; Liu, J.; Sun, H.; Wang, J.; Li, R.; Kim, D.; Hyeon, T.; Ling, D., Responsive Assembly of Upconversion Nanoparticles for pH-Activated and Near-Infrared-Triggered Photodynamic Therapy of Deep Tumors. *Advanced Materials* **2018,** *30* (35), 1802808.
180. Liu, K.; Liu, X.; Zeng, Q.; Zhang, Y.; Tu, L.; Liu, T.; Kong, X.; Wang, Y.; Cao, F.; Lambrechts, S. A. G.; Aalders, M. C. G.; Zhang, H., Covalently Assembled NIR Nanoplatform for Simultaneous Fluorescence Imaging and Photodynamic Therapy of Cancer Cells. *ACS Nano* **2012,** *6* (5), 4054-4062.
181. Jiang, G.; Pichaandi, J.; Johnson, N. J. J.; Burke, R. D.; van Veggel, F. C. J. M., An Effective Polymer Cross-Linking Strategy To Obtain Stable Dispersions of Upconverting NaYF4 Nanoparticles in Buffers and Biological Growth Media for Biolabeling Applications. *Langmuir* **2012,** *28* (6), 3239-3247.
182. Wen, H.; Zhu, H.; Chen, X.; Hung, T. F.; Wang, B.; Zhu, G.; Yu, S. F.; Wang, F., Upconverting Near-Infrared Light through Energy Management in Core–Shell–Shell Nanoparticles. *Angewandte Chemie International Edition* **2013,** *52* (50), 13419-13423.
183. Hühn, J.; Carrillo-Carrion, C.; Soliman, M. G.; Pfeiffer, C.; Valdeperez, D.; Masood, A.; Chakraborty, I.; Zhu, L.; Gallego, M.; Zhao, Y.; Carril, M.; Feliu, N.; Escudero, A.; Alkilany, A. M.; Pelaz, B.; Pino, P. d.; Parak, W. J., Selected Standard Protocols for the Synthesis, Phase Transfer, and Characterization of Inorganic Colloidal Nanoparticles. *Chemistry of Materials* **2017,** *29*, 399−461.

184. Dukhno, O.; Przybilla, F.; Collot, M.; Klymchenko, A.; Pivovarenko, V.; Buchner, M.; Muhr, V.; Hirsch, T.; Mély, Y., Quantitative assessment of energy transfer in upconverting nanoparticles grafted with organic dyes. *Nanoscale* **2017,** *9* (33), 11994-12004.
185. Lin, X.; Chen, X.; Zhang, W.; Sun, T.; Fang, P.; Liao, Q.; Chen, X.; He, J.; Liu, M.; Wang, F.; Shi, P., Core–Shell–Shell Upconversion Nanoparticles with Enhanced Emission for Wireless Optogenetic Inhibition. *Nano Letters* **2018,** *18* (2), 948-956.
186. Idris, N. M.; Gnanasammandhan, M. K.; Zhang, J.; Ho, P. C.; Mahendran, R.; Zhang, Y., In vivo photodynamic therapy using upconversion nanoparticles as remote-controlled nanotransducers. *Nature Medicine* **2012,** *18* (10), 1580-1585.
187. Liu, J.; Zhang, T.; Song, X.; Xing, J., Enhanced red emission of 808 nm excited upconversion nanoparticles by optimizing the composition of shell for efficient generation of singlet oxygen. *Optical Materials* **2018,** *75*, 79-87.
188. Li, Y.; Tang, J.; Pan, D.-X.; Sun, L.-D.; Chen, C.; Liu, Y.; Wang, Y.-F.; Shi, S.; Yan, C.-H., A Versatile Imaging and Therapeutic Platform Based on Dual-Band Luminescent Lanthanide Nanoparticles toward Tumor Metastasis Inhibition. *ACS Nano* **2016,** *10* (2), 2766-2773.
189. Wang, D.; Xue, B.; Kong, X.; Tu, L.; Liu, X.; Zhang, Y.; Chang, Y.; Luo, Y.; Zhao, H.; Zhang, H., 808 nm driven Nd3+-sensitized upconversion nanostructures for photodynamic therapy and simultaneous fluorescence imaging. *Nanoscale* **2015,** *7* (1), 190-197.
190. Kumar, B.; Murali, A.; Bharath, A. B.; Giri, S., Guar gum modified upconversion nanocomposites for colorectal cancer treatment through enzyme-responsive drug release and NIR-triggered photodynamic therapy. *Nanotechnology* **2019,** *30* (31), 315102.
191. Wei, Y.; Lu, F.; Zhang, X.; Chen, D., Synthesis of Oil-Dispersible Hexagonal-Phase and Hexagonal-Shaped NaYF4:Yb,Er Nanoplates. *Chemistry of Materials* **2006,** *18* (24), 5733-5737.
192. Mackenzie, L. E.; Goode, J. A.; Vakurov, A.; Nampi, P. P.; Saha, S.; Jose, G.; Millner, P. A., The theoretical molecular weight of NaYF4:RE upconversion nanoparticles. *Scientific Reports* **2018,** *8* (1), 1106.
193. Feliu, N.; Pelaz, B.; Zhang, Q.; del_Pino, P.; Nyström, A.; Parak, W. J., Nanoparticle dosage-a nontrivial task of utmost importance for quantitative nanosafety research. *Wiley Interdiscip Rev Nanomed Nanobiotechnol* **2016,** *8*, 479-492.
194. Himmelstoß, S. F.; Hirsch, T., Long-Term Colloidal and Chemical Stability in Aqueous Media of NaYF4-Type Upconversion Nanoparticles Modified by Ligand-Exchange. *Particle & Particle Systems Characterization* **2019,** *36* (10), 1900235.
195. Soliman, M. G.; B, B. P.; Parak, W. J.; Pino, P. d., Phase transfer and polymer coating methods toward improving the stability of metallic nanoparticles for biological applications. *Chemistry of Materials* **2015,** *27*, 990-997.
196. Carrillo-Carrión, C.; del Pino, P.; Pelaz, B., Aqueous stable luminescent perovskite-polymer composites. *Applied Materials Today* **2019,** *15*, 562-569.
197. Xu, M.; Soliman, M. G.; Sun, X.; Pelaz, B.; Feliu, N.; Parak, W. J.; Liu, S., How Entanglement of Different Physicochemical Properties Complicates the Prediction of in Vitro and in Vivo Interactions of Gold Nanoparticles. *ACS Nano* **2018,** *accepted based on minor revision* (12), 10104-10113.
198. Zhu, L.; Pelaz, B.; Chakraborty, I.; Parak, W. J., Investigating Possible Enzymatic Degradation on Polymer Shells around Inorganic Nanoparticles. *International Journal of Molecular Sciences* **2019,** *20* (4), 935.
199. Pelaz, B.; Del Pino, P.; Maffre, P.; Hartmann, R.; Gallego, M.; Rivera-Fernandez, S.; de la Fuente, J. M.; Nienhaus, G. U.; Parak, W. J., Surface Functionalization of Nanoparticles with Polyethylene Glycol: Effects on Protein Adsorption and Cellular Uptake. *ACS Nano* **2015,** *9* (7), 6996-7008.
200. del_Pino, P.; Pelaz, B.; Zhang, Q.; Maffre, P.; Nienhaus, G. U.; Parak, W. J., Protein corona formation around nanoparticles-from the past to the future. *Materials Horizons* **2014,** *1*, 301-313.
201. Manshian, B. B.; Abdelmonem, A. M.; Kantner, K.; Pelaz, B.; Klapper, M.; Tirroni, C. N.; Parak, W. J.; Himmelreich, U.; Soenen, S. J., Evaluation of quantum dot cytotoxicity: interpretation

of nanoparticle concentrations versus intracellular nanoparticle numbers. *Nanotoxicology* **2016,** *10*, 1318-1328.
202. Ma, X.; Hartmann, R.; Aberasturi, D. J. d.; Yang, F.; Soenen, S. J. H.; Manshian, B. B.; Franz, J.; Valdeperez, D.; Pelaz, B.; Feliu, N.; Hampp, N.; Riethmüller, C.; Vieker, H.; Frese, N.; Gölzhäuser, A.; Simonich, M.; Tanguay, R. L.; Liang, X.-J.; Parak, W. J., Colloidal Gold Nanoparticles Induce Changes in Cellular and Subcellular Morphology. *ACS Nano* **2017,** *11*, 7807−7820.
203. Li, Z.; Zhang, Y., An efficient and user-friendly method for the synthesis of hexagonal-phase NaYF4:Yb, Er/Tm nanocrystals with controllable shape and upconversion fluorescence. *Nanotechnology* **2008,** *19* (34), 345606.
204. Qian, H.-S.; Zhang, Y., Synthesis of Hexagonal-Phase Core−Shell NaYF4 Nanocrystals with Tunable Upconversion Fluorescence. *Langmuir* **2008,** *24* (21), 12123-12125.
205. McKinlay, A. C.; Morris Re Fau - Horcajada, P.; Horcajada P Fau - Ferey, G.; Ferey G Fau - Gref, R.; Gref R Fau - Couvreur, P.; Couvreur P Fau - Serre, C.; Serre, C., BioMOFs: metal-organic frameworks for biological and medical applications. (1521-3773 (Electronic)).
206. Park, K. S.; Ni, Z.; Côté, A. P.; Choi, J. Y.; Huang, R.; Uribe-Romo, F. J.; Chae, H. K.; O'Keeffe, M.; Yaghi, O. M., Exceptional chemical and thermal stability of zeolitic imidazolate frameworks. *Proceedings of the National Academy of Sciences* **2006,** *103* (27), 10186.
207. Nabipour, H.; Sadr, M. H.; Bardajee, G. R., Synthesis and characterization of nanoscale zeolitic imidazolate frameworks with ciprofloxacin and their applications as antimicrobial agents. *New Journal of Chemistry* **2017,** *41* (15), 7364-7370.
208. Yan, L.; Chen, X.; Wang, Z.; Zhang, X.; Zhu, X.; Zhou, M.; Chen, W.; Huang, L.; Roy, V. A. L.; Yu, P. K. N.; Zhu, G.; Zhang, W., Size Controllable and Surface Tunable Zeolitic Imidazolate Framework-8–Poly(acrylic acid sodium salt) Nanocomposites for pH Responsive Drug Release and Enhanced in Vivo Cancer Treatment. *ACS applied materials & interfaces* **2017,** *9* (38), 32990-33000.
209. Tran, T. T. D.; Tran, P. H. L., Controlled Release Film Forming Systems in Drug Delivery: The Potential for Efficient Drug Delivery. *Pharmaceutics* **2019,** *11* (6), 290.
210. Liu, X.; Li, Y.; Ban, Y.; Peng, Y.; Jin, H.; Bux, H.; Xu, L.; Caro, J.; Yang, W., Improvement of hydrothermal stability of zeolitic imidazolate frameworks. *Chemical Communications* **2013,** *49* (80), 9140-9142.
211. Zhang, H.; Liu, D.; Yao, Y.; Zhang, B.; Lin, Y. S., Stability of ZIF-8 membranes and crystalline powders in water at room temperature. *Journal of Membrane Science* **2015,** *485*, 103-111.
212. Karimi, M.; Ghasemi, A.; Sahandi Zangabad, P.; Rahighi, R.; Moosavi Basri, S. M.; Mirshekari, H.; Amiri, M.; Shafaei Pishabad, Z.; Aslani, A.; Bozorgomid, M.; Ghosh, D.; Beyzavi, A.; Vaseghi, A.; Aref, A. R.; Haghani, L.; Bahrami, S.; Hamblin, M. R., Smart micro/nanoparticles in stimulus-responsive drug/gene delivery systems. *Chemical Society Reviews* **2016,** *45* (5), 1457-1501.
213. Zheng, G.; de Marchi, S.; López-Puente, V.; Sentosun, K.; Polavarapu, L.; Pérez-Juste, I.; Hill, E. H.; Bals, S.; Liz-Marzán, L. M.; Pastoriza-Santos, I.; Pérez-Juste, J., Encapsulation of Single Plasmonic Nanoparticles within ZIF-8 and SERS Analysis of the MOF Flexibility. *Small* **2016,** *12* (29), 3935-3943.
214. Wang, Z.; Tang, X.; Wang, X.; Yang, D.; Yang, C.; Lou, Y.; Chen, J.; He, N., Near-infrared light-induced dissociation of zeolitic imidazole framework-8 (ZIF-8) with encapsulated CuS nanoparticles and their application as a therapeutic nanoplatform. *Chemical Communications* **2016,** *52* (82), 12210-12213.
215. He, L.; Brasino, M.; Mao, C.; Cho, S.; Park, W.; Goodwin, A. P.; Cha, J. N., DNA-Assembled Core-Satellite Upconverting-Metal–Organic Framework Nanoparticle Superstructures for Efficient Photodynamic Therapy. *Small* **2017,** *13* (24), 1700504.
216. Hu, P.; Morabito, J. V.; Tsung, C.-K., Core−Shell Catalysts of Metal Nanoparticle Core and Metal–Organic Framework Shell. *ACS Catalysis* **2014,** *4* (12), 4409-4419.
217. Kuo, C.-H.; Tang, Y.; Chou, L.-Y.; Sneed, B. T.; Brodsky, C. N.; Zhao, Z.; Tsung, C.-K., Yolk–Shell Nanocrystal@ZIF-8 Nanostructures for Gas-Phase Heterogeneous Catalysis with Selectivity Control. *Journal of the American Chemical Society* **2012,** *134* (35), 14345-14348.

218. Bucevicius, J.; Lukinavicius, G.; Gerasimaite, R., The Use of Hoechst Dyes for DNA Staining and beyond. *Chemosensors* **2018,** *6*, 18.
219. Kumari, G.; Jayaramulu, K.; Maji, T. K.; Narayana, C., Temperature Induced Structural Transformations and Gas Adsorption in the Zeolitic Imidazolate Framework ZIF-8: A Raman Study. *The Journal of Physical Chemistry A* **2013,** *117* (43), 11006-11012.
220. Knebel, A.; Geppert, B.; Volgmann, K.; Kolokolov, D. I.; Stepanov, A. G.; Twiefel, J.; Heitjans, P.; Volkmer, D.; Caro, J., Defibrillation of soft porous metal-organic frameworks with electric fields. *Science* **2017,** *358* (6361), 347.
221. Fairen-Jimenez, D.; Moggach, S. A.; Wharmby, M. T.; Wright, P. A.; Parsons, S.; Düren, T., Opening the Gate: Framework Flexibility in ZIF-8 Explored by Experiments and Simulations. *Journal of the American Chemical Society* **2011,** *133* (23), 8900-8902.
222. Rivera_Gil, P.; Vazquez-Vazquez, C.; Giannini, V.; Callao, M. P.; Parak, W. J.; Correa-Duarte, M. A.; Alvarez-Puebla, R. A., Plasmonic Nanoprobes for Real-Time Optical Monitoring of Nitric Oxide inside Living Cells. *Angewandte Chemie International Edition* **2013,** *52* (51), 13694-13698.
223. Arnold, F. H., Directed Evolution: Bringing New Chemistry to Life. *Angew. Chem. Int. Ed.* **2018,** *57* (16), 4143-4148.
224. Martínez-Calvo, M.; Mascareñas, J. L., Organometallic catalysis in biological media and living settings. *Coord. Chem. Rev.* **2018,** *359*, 57-79.
225. Ji, X.; Pan, Z.; Yu, B.; De La Cruz, L. K.; Zheng, Y.; Ke, B.; Wang, B., Click and release: bioorthogonal approaches to "on-demand" activation of prodrugs. *Chem. Soc. Rev.* **2019,** *48* (4), 1077-1094.
226. Yang, M.; Li, J.; Chen, P. R., Transition metal-mediated bioorthogonal protein chemistry in living cells. *Chem. Soc. Rev.* **2014,** *43* (18), 6511-6526.
227. Unciti-Broceta, A., Bioorthogonal catalysis: Rise of the nanobots. *Nat. Chem.* **2015,** *7* (7), 538-9.
228. Del Pino, P.; Pelaz, B.; Zhang, Q.; Maffre, P.; Nienhaus, G. U.; Parak, W. J., Protein corona formation around nanoparticles - from the past to the future. *Materials Horizons* **2014,** *1* (3), 301-313.
229. Tian, F.; Clift, M. J. D.; Casey, A.; del Pino, P.; Pelaz, B.; Conde, J.; Byrne, H. J.; Rothen-Rutishauser, B.; Estrada, G.; de la Fuente, J. M.; Stoeger, T., Investigating the role of shape on the biological impact of gold nanoparticles in vitro. *Nanomedicine* **2015,** *10* (17), 2643-2657.
230. Bao, C.; Conde, J.; Polo, E.; del Pino, P.; Moros, M.; Baptista, P. V.; Grazu, V.; Cui, D.; de la Fuente, J. M., A promising road with challenges: where are gold nanoparticles in translational research? *Nanomedicine* **2014,** *9* (15), 2353-2370.
231. Carrillo-Carrion, C.; Martinez, R.; Navarro Poupard, M. F.; Pelaz, B.; Polo, E.; Arenas-Vivo, A.; Olgiati, A.; Taboada, P.; Soliman, M. G.; Catalan, U.; Fernandez-Castillejo, S.; Sola, R.; Parak, W. J.; Horcajada, P.; Alvarez-Puebla, R. A.; Del Pino, P., Aqueous Stable Gold Nanostar/ZIF-8 Nanocomposites for Light-Triggered Release of Active Cargo Inside Living Cells. *Angew. Chem. Int. Ed. Engl.* **2019,** *58* (21), 7078-7082.
232. Perez-Hernandez, M.; Del Pino, P.; Mitchell, S. G.; Moros, M.; Stepien, G.; Pelaz, B.; Parak, W. J.; Galvez, E. M.; Pardo, J.; de la Fuente, J. M., Dissecting the molecular mechanism of apoptosis during photothermal therapy using gold nanoprisms. *ACS Nano* **2015,** *9* (1), 52-61.
233. Zhou, L.; Swearer, D. F.; Zhang, C.; Robatjazi, H.; Zhao, H.; Henderson, L.; Dong, L.; Christopher, P.; Carter, E. A.; Nordlander, P.; Halas, N. J., Quantifying hot carrier and thermal contributions in plasmonic photocatalysis. *Science* **2018,** *362* (6410), 69-72.
234. Christopher, P.; Xin, H.; Marimuthu, A.; Linic, S., Singular characteristics and unique chemical bond activation mechanisms of photocatalytic reactions on plasmonic nanostructures. *Nat. Mater.* **2012,** *11* (12), 1044-1050.
235. Zhang, X.; Li, X.; Zhang, D.; Su, N. Q.; Yang, W.; Everitt, H. O.; Liu, J., Product selectivity in plasmonic photocatalysis for carbon dioxide hydrogenation. *Nature Communications* **2017,** *8* (1), 14542.

236. Zhang, Y.; He, S.; Guo, W.; Hu, Y.; Huang, J.; Mulcahy, J. R.; Wei, W. D., Surface-Plasmon-Driven Hot Electron Photochemistry. *Chem. Rev.* **2018,** *118* (6), 2927-2954.
237. González-Rubio, G.; Díaz-Núñez, P.; Rivera, A.; Prada, A.; Tardajos, G.; González-Izquierdo, J.; Bañares, L.; Llombart, P.; Macdowell, L. G.; Alcolea Palafox, M.; Liz-Marzán, L. M.; Peña-Rodríguez, O.; Guerrero-Martínez, A., Femtosecond laser reshaping yields gold nanorods with ultranarrow surface plasmon resonances. *Science* **2017,** *358* (6363), 640-644.
238. Nguyen, S. C.; Zhang, Q.; Manthiram, K.; Ye, X.; Lomont, J. P.; Harris, C. B.; Weller, H.; Alivisatos, A. P., Study of Heat Transfer Dynamics from Gold Nanorods to the Environment via Time-Resolved Infrared Spectroscopy. *ACS Nano* **2016,** *10* (2), 2144-2151.
239. Kumar, A.; Kumar, S.; Kumari, N.; Lee, S. H.; Han, J.; Michael, I. J.; Cho, Y.-K.; Lee, I. S., Plasmonically Coupled Nanoreactors for NIR-Light-Mediated Remote Stimulation of Catalysis in Living Cells. *ACS Catal.* **2018,** *9* (2), 977-990.
240. Weiss, J. T.; Dawson, J. C.; Macleod, K. G.; Rybski, W.; Fraser, C.; Torres-Sánchez, C.; Patton, E. E.; Bradley, M.; Carragher, N. O.; Unciti-Broceta, A., Extracellular palladium-catalysed dealkylation of 5-fluoro-1-propargyl-uracil as a bioorthogonally activated prodrug approach. *Nat. Commun.* **2014,** *5*, 3277.
241. Perez-Lopez, A. M.; Rubio-Ruiz, B.; Sebastian, V.; Hamilton, L.; Adam, C.; Bray, T. L.; Irusta, S.; Brennan, P. M.; Lloyd-Jones, G. C.; Sieger, D.; Santamaria, J.; Unciti-Broceta, A., Gold-Triggered Uncaging Chemistry in Living Systems. *Angew. Chem. Int. Ed. Engl.* **2017,** *56* (41), 12548-12552.
242. Vázquez-Vázquez, C.; Vaz, B.; Giannini, V.; Pérez-Lorenzo, M.; Alvarez-Puebla, R. A.; Correa-Duarte, M. A., Nanoreactors for Simultaneous Remote Thermal Activation and Optical Monitoring of Chemical Reactions. *J. Am. Chem. Soc.* **2013,** *135* (37), 13616-13619.
243. Xiao, J.-D.; Jiang, H.-L., Metal–Organic Frameworks for Photocatalysis and Photothermal Catalysis. *Acc. Chem. Res.* **2019,** *52* (2), 356-366.
244. Gai, S.; Yang, G.; Yang, P.; He, F.; Lin, J.; Jin, D.; Xing, B., Recent advances in functional nanomaterials for light–triggered cancer therapy. *Nano Today* **2018,** *19*, 146-187.
245. Hu, M.; Wang, X.; Hartland, G. V.; Salgueiriño-Maceira, V.; Liz-Marzán, L. M., Heat dissipation in gold–silica core-shell nanoparticles. *Chem. Phys. Lett.* **2003,** *372* (5), 767-772.
246. Cui, B.; Audu, C. O.; Liao, Y.; Nguyen, S. T.; Farha, O. K.; Hupp, J. T.; Grayson, M., Thermal Conductivity of ZIF-8 Thin-Film under Ambient Gas Pressure. *ACS Appl. Mater. Interfaces* **2017,** *9* (34), 28139-28143.
247. Lesniak, A.; Fenaroli, F.; Monopoli, M. P.; Åberg, C.; Dawson, K. A.; Salvati, A., Effects of the Presence or Absence of a Protein Corona on Silica Nanoparticle Uptake and Impact on Cells. *ACS Nano* **2012,** *6* (7), 5845-5857.
248. Brzezinska, J.; Witkowska, A.; Bałabańska, S.; Chmielewski, M. K., 2-Pyridinyl-N-(2,4-difluorobenzyl)aminoethyl Group As Thermocontrolled Implement for Protection of Carboxylic Acids. *Org. Lett.* **2016,** *18* (13), 3230-3233.
249. Völker, T.; Meggers, E., Transition-metal-mediated uncaging in living human cells—an emerging alternative to photolabile protecting groups. *Curr. Opin. Chem. Biol.* **2015,** *25*, 48-54.
250. Yang, M.; Yang, Y.; Chen, P. R., Transition-Metal-Catalyzed Bioorthogonal Cycloaddition Reactions. *Top. Curr. Chem.* **2015,** *374* (1), 2.
251. Soldevila-Barreda, J. J.; Sadler, P. J., Approaches to the design of catalytic metallodrugs. *Curr. Opin. Chem. Biol.* **2015,** *25*, 172-183.
252. Rebelein, J. G.; Ward, T. R., In vivo catalyzed new-to-nature reactions. *Curr. Opin. Biotechnol.* **2018,** *53*, 106-114.
253. Bai, Y.; Chen, J.; Zimmerman, S. C., Designed transition metal catalysts for intracellular organic synthesis. *Chem. Soc. Rev.* **2018,** *47* (5), 1811-1821.
254. Link, A. J.; Tirrell, D. A., Cell Surface Labeling of Escherichia coli via Copper(I)-Catalyzed [3+2] Cycloaddition. *J. Am. Chem. Soc.* **2003,** *125* (37), 11164-11165.
255. Link, A. J.; Vink, M. K. S.; Tirrell, D. A., Presentation and Detection of Azide Functionality in Bacterial Cell Surface Proteins. *J. Am. Chem. Soc.* **2004,** *126* (34), 10598-10602.

256. Beatty, K. E.; Xie, F.; Wang, Q.; Tirrell, D. A., Selective Dye-Labeling of Newly Synthesized Proteins in Bacterial Cells. *J. Am. Chem. Soc.* **2005,** *127* (41), 14150-14151.
257. Tiwari, V. K.; Mishra, B. B.; Mishra, K. B.; Mishra, N.; Singh, A. S.; Chen, X., Cu-Catalyzed Click Reaction in Carbohydrate Chemistry. *Chem. Rev.* **2016,** *116* (5), 3086-3240.
258. Mahdavi, A.; Hamblin, G. D.; Jindal, G. A.; Bagert, J. D.; Dong, C.; Sweredoski, M. J.; Hess, S.; Schuman, E. M.; Tirrell, D. A., Engineered Aminoacyl-tRNA Synthetase for Cell-Selective Analysis of Mammalian Protein Synthesis. *J. Am. Chem. Soc.* **2016,** *138* (13), 4278-4281.
259. Miguel-Ávila, J.; Tomás-Gamasa, M.; Olmos, A.; Pérez, P. J.; Mascareñas, J. L., Discrete Cu(i) complexes for azide–alkyne annulations of small molecules inside mammalian cells. *Chem. Sci.* **2018,** *9* (7), 1947-1952.
260. Völker, T.; Dempwolff, F.; Graumann, P. L.; Meggers, E., Progress towards Bioorthogonal Catalysis with Organometallic Compounds. *Angew. Chem. Int. Ed.* **2014,** *53* (39), 10536-10540.
261. Williams, D. S.; Atilla, G. E.; Bregman, H.; Arzoumanian, A.; Klein, P. S.; Meggers, E., Switching on a Signaling Pathway with an Organoruthenium Complex. *Angew. Chem. Int. Ed.* **2005,** *44* (13), 1984-1987.
262. Streu, C.; Meggers, E., Ruthenium-Induced Allylcarbamate Cleavage in Living Cells. *Angew. Chem. Int. Ed.* **2006,** *45* (34), 5645-5648.
263. Tomás-Gamasa, M.; Martínez-Calvo, M.; Couceiro, J. R.; Mascareñas, J. L., Transition metal catalysis in the mitochondria of living cells. *Nat. Commun.* **2016,** *7*, 12538.
264. Vidal, C.; Tomás-Gamasa, M.; Destito, P.; López, F.; Mascareñas, J. L., Concurrent and orthogonal gold(I) and ruthenium(II) catalysis inside living cells. *Nat. Commun.* **2018,** *9* (1), 1913.
265. Vidal, C.; Tomás-Gamasa, M.; Gutiérrez-González, A.; Mascareñas, J. L., Ruthenium-Catalyzed Redox Isomerizations inside Living Cells. *J. Am. Chem. Soc.* **2019,** *141* (13), 5125-5129.
266. Tsubokura, K.; Vong, K. K. H.; Pradipta, A. R.; Ogura, A.; Urano, S.; Tahara, T.; Nozaki, S.; Onoe, H.; Nakao, Y.; Sibgatullina, R.; Kurbangalieva, A.; Watanabe, Y.; Tanaka, K., In Vivo Gold Complex Catalysis within Live Mice. *Angew. Chem. Int. Ed.* **2017,** *56* (13), 3579-3584.
267. Bose, S.; Ngo, A. H.; Do, L. H., Intracellular Transfer Hydrogenation Mediated by Unprotected Organoiridium Catalysts. *J. Am. Chem. Soc.* **2017,** *139* (26), 8792-8795.
268. Coverdale, J. P. C.; Romero-Canelón, I.; Sanchez-Cano, C.; Clarkson, G. J.; Habtemariam, A.; Wills, M.; Sadler, P. J., Asymmetric transfer hydrogenation by synthetic catalysts in cancer cells. *Nat. Chem.* **2018,** *10*, 347.
269. Jbara, M.; Maity, S. K.; Brik, A., Palladium in the Chemical Synthesis and Modification of Proteins. *Angew. Chem. Int. Ed.* **2017,** *56* (36), 10644-10655.
270. Miller, M. A.; Askevold, B.; Mikula, H.; Kohler, R. H.; Pirovich, D.; Weissleder, R., Nano-palladium is a cellular catalyst for in vivo chemistry. *Nat. Commun.* **2017,** *8*, 15906.
271. Feliu, N.; Docter, D.; Heine, M.; del Pino, P.; Ashraf, S.; Kolosnjaj-Tabi, J.; Macchiarini, P.; Nielsen, P.; Alloyeau, D.; Gazeau, F.; Stauber, R. H.; Parak, W. J., In vivo degeneration and the fate of inorganic nanoparticles. *Chem. Soc. Rev.* **2016**.
272. Gavia, D. J.; Shon, Y.-S., Catalytic Properties of Unsupported Palladium Nanoparticle Surfaces Capped with Small Organic Ligands. *ChemCatChem* **2015,** *7* (6), 892-900.
273. Yusop, R. M.; Unciti-Broceta, A.; Johansson, E. M. V.; Sánchez-Martín, R. M.; Bradley, M., Palladium-mediated intracellular chemistry. *Nat. Chem.* **2011,** *3*, 239.
274. Unciti-Broceta, A.; Johansson, E. M. V.; Yusop, R. M.; Sánchez-Martín, R. M.; Bradley, M., Synthesis of polystyrene microspheres and functionalization with Pd0 nanoparticles to perform bioorthogonal organometallic chemistry in living cells. *Nat. Protoc.* **2012,** *7*, 1207.
275. Destito, P.; Sousa-Castillo, A.; Couceiro, J. R.; López, F.; Correa-Duarte, M. A.; Mascareñas, J. L., Hollow nanoreactors for Pd-catalyzed Suzuki–Miyaura coupling and O-propargyl cleavage reactions in bio-relevant aqueous media. *Chem. Sci.* **2019,** *10* (9), 2598-2603.
276. Giménez-Marqués, M.; Hidalgo, T.; Serre, C.; Horcajada, P., Nanostructured metal–organic frameworks and their bio-related applications. *Coord. Chem. Rev.* **2016,** *307*, 342-360.

277. Li, G.; Zhao, S.; Zhang, Y.; Tang, Z., Metal-Organic Frameworks Encapsulating Active Nanoparticles as Emerging Composites for Catalysis: Recent Progress and Perspectives. *Adv. Mater.* **2018,** *30* (51), e1800702.
278. Pascanu, V.; Gonzalez Miera, G.; Inge, A. K.; Martin-Matute, B., Metal-Organic Frameworks as Catalysts for Organic Synthesis: A Critical Perspective. *J. Am. Chem. Soc.* **2019**.
279. Wan, M.; Zhang, X.; Li, M.; Chen, B.; Yin, J.; Jin, H.; Lin, L.; Chen, C.; Zhang, N., Hollow Pd/MOF Nanosphere with Double Shells as Multifunctional Catalyst for Hydrogenation Reaction. *Small* **2017,** *13* (38), 1701395.
280. Dhakshinamoorthy, A.; Asiri, A. M.; Garcia, H., Metal–Organic Frameworks as Catalysts for Oxidation Reactions. *Chem.: Eur. J.* **2016,** *22* (24), 8012-8024.
281. Yuan, N.; Pascanu, V.; Huang, Z.; Valiente, A.; Heidenreich, N.; Leubner, S.; Inge, A. K.; Gaar, J.; Stock, N.; Persson, I.; Martín-Matute, B.; Zou, X., Probing the Evolution of Palladium Species in Pd@MOF Catalysts during the Heck Coupling Reaction: An Operando X-ray Absorption Spectroscopy Study. *J. Am. Chem. Soc.* **2018,** *140* (26), 8206-8217.
282. Liu, X.; Li, Y.; Ban, Y.; Peng, Y.; Jin, H.; Bux, H.; Xu, L.; Caro, J.; Yang, W., Improvement of hydrothermal stability of zeolitic imidazolate frameworks. *Chem. Commun.* **2013,** *49* (80), 9140-2.
283. Howarth, A. J.; Liu, Y. Y.; Li, P.; Li, Z. Y.; Wang, T. C.; Hupp, J.; Farha, O. K., Chemical, thermal and mechanical stabilities of metal-organic frameworks. *Nat. Rev. Mater.* **2016,** *1* (3).
284. Yan, L.; Chen, X.; Wang, Z.; Zhang, X.; Zhu, X.; Zhou, M.; Chen, W.; Huang, L.; Roy, V. A. L.; Yu, P. K. N.; Zhu, G.; Zhang, W., Size Controllable and Surface Tunable Zeolitic Imidazolate Framework-8-Poly(acrylic acid sodium salt) Nanocomposites for pH Responsive Drug Release and Enhanced in Vivo Cancer Treatment. *ACS Appl. Mater. Interfaces* **2017,** *9* (38), 32990-33000.
285. Yang, S.; Peng, L.; Sun, D. T.; Asgari, M.; Oveisi, E.; Trukhina, O.; Bulut, S.; Jamali, A.; Queen, W. L., A new post-synthetic polymerization strategy makes metal–organic frameworks more stable. *Chem. Sci.* **2019,** *10* (17), 4542-4549.
286. Luzuriaga, M. A.; Benjamin, C. E.; Gaertner, M. W.; Lee, H.; Herbert, F. C.; Mallick, S.; Gassensmith, J. J., ZIF-8 degrades in cell media, serum, and some—but not all—common laboratory buffers. *Supramol. Chem.* **2019**, 1-6.
287. Gao, Q.; Xu, J.; Bu, X.-H., Recent advances about metal–organic frameworks in the removal of pollutants from wastewater. *Coord. Chem. Rev.* **2019,** *378*, 17-31.
288. Llabrés i Xamena, F. X.; Abad, A.; Corma, A.; Garcia, H., MOFs as catalysts: Activity, reusability and shape-selectivity of a Pd-containing MOF. *J. Catal.* **2007,** *250* (2), 294-298.
289. Pascanu, V.; Yao, Q.; Bermejo Gómez, A.; Gustafsson, M.; Yun, Y.; Wan, W.; Samain, L.; Zou, X.; Martín-Matute, B., Sustainable Catalysis: Rational Pd Loading on MIL-101Cr-NH2 for More Efficient and Recyclable Suzuki–Miyaura Reactions. *Chem.: Eur. J.* **2013,** *19* (51), 17483-17493.
290. Wang, F.; Zhang, Y.; Liu, Z.; Du, Z.; Zhang, L.; Ren, J.; Qu, X., A Biocompatible Heterogeneous MOF-Cu Catalyst for In Vivo Drug Synthesis in Targeted Subcellular Organelles. *Angew. Chem. Int. Ed. Engl.* **2019,** *58* (21), 6987-6992.
291. Zhang, H.; Jin, M.; Xiong, Y.; Lim, B.; Xia, Y., Shape-Controlled Synthesis of Pd Nanocrystals and Their Catalytic Applications. *Acc. Chem. Res.* **2013,** *46* (8), 1783-1794.
292. Xie, X.; Gao, G.; Pan, Z.; Wang, T.; Meng, X.; Cai, L., Large-Scale Synthesis of Palladium Concave Nanocubes with High-Index Facets for Sustainable Enhanced Catalytic Performance. *Sci. Rep.* **2015,** *5*, 8515.
293. Hu, P.; Zhuang, J.; Chou, L.-Y.; Lee, H. K.; Ling, X. Y.; Chuang, Y.-C.; Tsung, C.-K., Surfactant-Directed Atomic to Mesoscale Alignment: Metal Nanocrystals Encased Individually in Single-Crystalline Porous Nanostructures. *J. Am. Chem. Soc.* **2014,** *136* (30), 10561-10564.
294. Zheng, G.; de Marchi, S.; Lopez-Puente, V.; Sentosun, K.; Polavarapu, L.; Perez-Juste, I.; Hill, E. H.; Bals, S.; Liz-Marzan, L. M.; Pastoriza-Santos, I.; Perez-Juste, J., Encapsulation of Single Plasmonic Nanoparticles within ZIF-8 and SERS Analysis of the MOF Flexibility. *Small* **2016,** *12* (29), 3935-43.

295. Kaur, H.; Mohanta, G. C.; Gupta, V.; Kukkar, D.; Tyagi, S., Synthesis and characterization of ZIF-8 nanoparticles for controlled release of 6-mercaptopurine drug. *J. Drug Deliv. Sci. Technol.* **2017,** *41*, 106-112.
296. Chen, X.; Tong, R.; Shi, Z.; Yang, B.; Liu, H.; Ding, S.; Wang, X.; Lei, Q.; Wu, J.; Fang, W., MOF Nanoparticles with Encapsulated Autophagy Inhibitor in Controlled Drug Delivery System for Antitumor. *ACS Appl. Mater. Interfaces* **2018,** *10* (3), 2328-2337.
297. Jin, M.; Zhang, H.; Xie, Z.; Xia, Y., Palladium nanocrystals enclosed by {100} and {111} facets in controlled proportions and their catalytic activities for formic acid oxidation. *Energy Environ. Sci.* **2012,** *5* (4), 6352-6357.
298. Weiswald, L.-B.; Bellet, D.; Dangles-Marie, V., Spherical Cancer Models in Tumor Biology. *Neoplasia* **2015,** *17* (1), 1-15.
299. Chen, T.; Wei, T.; Zhang, Z.; Chen, Y.; Qiang, J.; Wang, F.; Chen, X., Highly sensitive and selective ESIPT-based fluorescent probes for detection of Pd2+ with large Stocks shifts. *Dyes Pigm.* **2017,** *140*, 392-398.
300. Clavadetscher, J.; Indrigo, E.; Chankeshwara, S. V.; Lilienkampf, A.; Bradley, M., In-Cell Dual Drug Synthesis by Cancer-Targeting Palladium Catalysts. *Angew. Chem. Int. Ed.* **2017,** *56* (24), 6864-6868.
301. Schulz, F.; Homolka, T.; Bastús, N. G.; Puntes, V.; Weller, H.; Vossmeyer, T., Little Adjustments Significantly Improve the Turkevich Synthesis of Gold Nanoparticles. *Langmuir* **2014,** *30* (35), 10779-10784.
302. Haiss, W.; Thanh, N. T. K.; Aveyard, J.; Fernig, D. G., Determination of Size and Concentration of Gold Nanoparticles from UV−Vis Spectra. *Analytical Chemistry* **2007,** *79* (11), 4215-4221.
303. Tsoulos, T. V.; Han, L.; Weir, J.; Xin, H. L.; Fabris, L., A closer look at the physical and optical properties of gold nanostars: an experimental and computational study. *Nanoscale* **2017,** *9* (11), 3766-3773.
304. Kantner, K.; Rejman, J.; Kraft, K. V. L.; Soliman, M. G.; Zyuzin, M. V.; Escudero, A.; Del Pino, P.; Parak, W. J., Laterally and Temporally Controlled Intracellular Staining by Light-Triggered Release of Encapsulated Fluorescent Markers. *Chem. Eur. J* **2018,** *24* (9), 2098-2102.
305. del Pino, P.; Yang, F.; Pelaz, B.; Zhang, Q.; Kantner, K.; Hartmann, R.; Martinez de Baroja, N.; Gallego, M.; Möller, M.; Manshian, B. B.; Soenen, S. J.; Riedel, R.; Hampp, N.; Parak, W. J., Basic Physicochemical Properties of Polyethylene Glycol Coated Gold Nanoparticles that Determine Their Interaction with Cells. *Angew. Chem. Int. Ed.* **2016,** *55* (18), 5483-5487.